DSPACE

https://dspace.org/

Prediction of DC current flow between the Otjiwarongo and Katima Mulilo regions, Namibia

Share, Pieter-Ewald

2013-02-14
http://hdl.handle.net/10539/12429

Downloaded from a DSpace repository. https://dspace.org/

Prediction of DC current flow between the Otjiwarongo and Katima Mulilo regions, Namibia

Pieter-Ewald Share

A dissertation submitted to the Faculty of Science, University of the Witwatersrand, Johannesburg, in fulfilment of the requirements for the degree of

Master of Science

School of Geoscience, University of the Witwatersrand and the School of Cosmic Physics, Dublin Institute for Advanced Studies

Johannesburg, 2012

I declare that this dissertation is my own, unaided work. It is being submitted for the Degree of Master of Science in the University of the Witwatersrand, Johannesburg. It has not been submitted for any degree or examination in any other University.

_____

Pieter-Ewald Share

30th day of October 2012

Abstract

As an additional opportunistic component to the Southern African Magnetotelluric Experiment (SAMTEX), audio-magnetotelluric (AMT) data were acquired during the most recent phase of the experiment (Phase IV) to investigate the local-scale conductivity substructure in the Otjiwarongo and Katima Mulilo regions (Namibia), as to aid in the installation of high-voltage direct current (HVDC) earth electrodes that has since taken place. Both of the AMT surveys are situated close to the edge of the orogenic Neo-Proterozoic Damara Mobile Belt (DMB). Previous studies all point to the existence of a highly conductive mid-crustal zone which correlates well with the spatial location of the DMB. Two-dimensional (2D) inverse modelling of the Otjiwarongo AMT data confirms the existence of the high conductive zone at mid-crustal depths (10-15 km). The high conductivity of the DMB is explained by the presence of interconnected graphite in the marble units present. The Katima Mulilo inversion results are characterized by a conductive upper crustal layer that does not form part of the DMB conductive belt. It is deduced that at the uppermost subsurface Kalahari sediments are responsible for the high conductivity observed while at greater depth it is due to ironstone within the Ghanzi Group. In contrast to the conductive DMB, the lithospheric structure of the neighbouring Archaean cratons, the Congo and Kalahari, are generally found to be electrically resistive. Therefore, it is hypothesized that ground return current, if present, will flow along a path between the Otjiwarongo and Katima Mulilo regions that lies either exclusively, or almost entirely within the DMB. The hypothesis is tested by inputting a three dimensional (3D) conductivity model (calculated using available magnetotelluric (MT) data and geological information) of the region into a DC resistivity forward modelling code. Forward modelling shows that the return current is only confined to, and follows regional trends characteristic of, the conductive DMB for approximately 200-300 km away from the injection point, after which there is no preferential flow.

To my family at home and at DIAS

Acknowledgements

Firstly to my supervisors, Prof. Alan G Jones and Dr. Susan J. Webb, thank you for your encouragement and critique throughout the completion of my Masters degree, each at the exact right time when it was needed. In particular, thank you Alan for giving me the opportunity to come to Dublin, it was a highly knowledgeable experience and very enjoyable. Also, my thanks and appreciation to Dr. Hans Thunehed and Dr. Johan De Beer for very insightful discussion regarding my research.

To the post-docs and senior staff at DIAS, thank you for great discussions and to those who aided me in my research. In particular, I would like to acknowledge Dr. Mark Muller. Mark you were always there when I had questions and always had a welcoming attitude. I never hesitated to step into your office and talk about work or life. You were always encouraging of me and my abilities and I am truly grateful for that!

My sponsors, the CSIR and Wits University (through the AfricaArray program), without the funding I received from you, this whole learning curve would definitely not have been possible.

My parents, stepdad and brother, I am truly grateful for your continuous love and support not only during my time of study but throughout my entire life. You believed in me when in many cases I did not believe in myself.

I would also like to acknowledge my second family in Centurion, the De Witt's: you gave me accommodation, food and love whenever I needed it. Thank you Uncle Delano for your support and the reading of my dissertation several times to help me improve the script.

All my fellow MT students in the "kindergarten". What can I say? What a

fantastic experience! The friendships I made during my time there will stay with me forever. I am ashamed to admit that at times we had so much fun we actually forgot to do some work.

Phil and Jennie, my housemates. You made my Dublin house a home! Thanks for all the good laughs, even if it was sometimes at my expense. Thanks for making it a low-stress environment where I could just always be myself.

Contents

Declaration i

Abstract ii

Dedication iii

Acknowledgements iv

List of Figures xiv

List of Tables xv

List of Symbols xvi

Nomenclature xvii

1 Introduction 1

1.1 The SAMTEX project 1
1.2 Purpose of the current study 3
1.3 HVDC transmission 6
1.4 Tectonics and geology of northern Namibia and Botswana . . 8
1.5 Study outline 13

2 Electrical conductivity of the Earth 16

2.1 Factors controlling conductivity 16
2.2 Conductivity of the crust 18
2.3 Conductivity of the mantle 22
2.4 Previous conductivity studies in the study regions 24

3 The MT method 29

3.1 Assumptions of the MT method 29
3.2 Electromagnetic induction within the Earth 31

3.2.1 Maxwell's equations and the quasi-static assumption . 31
3.2.2 Diffusive EM energy propagation 34
3.2.3 The MT impedance tensor 37
3.2.3.1 The uniform and one-dimensional (1D) impedance tensor 38
3.2.3.2 The 2D impedance tensor 39
3.2.3.3 The 3D impedance tensor 41
3.2.3.4 Apparent resistivity and phase 41
3.2.4 The tipper 43
3.3 The MT source fields 44
3.3.1 Causes and characteristics of the external magnetic field variations 44
3.3.2 Effects of non-uniform sources on MT data 46
3.4 MT data acquisition 48
3.5 MT data processing 50
3.5.1 Data pre-conditioning 51
3.5.2 Time domain to frequency domain 51
3.5.3 Estimation of impedance tensor and tipper 52
3.6 Distortion 56
3.6.1 Distortion effects on the impedance tensor and tipper . 56
3.6.2 Decomposition of the MT impedance tensor 58
3.7 Inversion of MT data 60
3.7.1 1D Inversion 61
3.7.2 2D Inversion 62
3.7.3 3D Inversion 63

4 Data processing and strike analysis 64
4.1 Data processing 64
4.2 Strike analysis 68
4.2.1 Single site strike analysis 68
4.2.2 Multisite strike analysis 71
4.2.2.1 Otjiwarongo region 71
4.2.2.2 Katima Mulilo region 74

5 2D inversion of MT data 78
5.1 Creating a mesh 80
5.2 L-curve 82
5.3 Regularization settings 83

5.4 TE and TM mode inversion 84
5.5 Joint TE and TM mode inversion 87
5.6 Sensitivity testing 91
5.6.1 Otjiwarongo inversion 91
5.6.2 Katima Mulilo inversion 93

6 3D interpolation of inversion results 98
6.1 Interpolation strategy 99
6.2 Interpolation testing 100
6.3 Profile projections 107
6.3.1 Crustal depths 107
6.3.2 Lithospheric mantle depths 110
6.4 Interpolation results 117

7 DC forward modelling 122
7.1 Program input 122
7.2 Modelling results 123

8 Discussion and conclusions 128
8.1 Placement of earth electrodes 128
8.1.1 Otjiwarongo region 128
8.1.2 Katima Mulilo region 129
8.2 Interpretation of 2D inversion results 131
8.2.1 Otjiwarongo inversion 131
8.2.2 Katima Mulilo inversion 133
8.3 Interpolation results 136
8.4 DC return current flow 136

9 Summary and recommendations 139

A Acquisition parameters 143

B Recorded MT data 145

C 2D inversion results 153

D Interpolation material 157

E Interpolation code 163

References 187

List of Figures

1.1 SAMTEX sites and southern Africa's geological provinces. . . 2
1.2 13 AMT sites installed close to Otjiwarongo. 5
1.3 9 AMT sites installed close to Katima Mulilo. 6
1.4 A cost versus distance plot for a HVDC system. 8
1.5 The three HVDC configurations. 9
1.6 Map of the exposed Archaean cratons and surrounding orogenic belts in southern Africa. 10
1.7 An aeromagnetic map of central and northern Namibia and Botswana. 11
1.8 Geological map of the Otjiwarongo region. 14

2.1 Electrical resistivity of rocks and other common Earth materials. 19
2.2 Regional conductivity models of the Earth obtained by various authors. 20
2.3 The proposed three-layer conductivity model of the crust. . . . 21
2.4 Results from laboratory and EM studies showing conductivity variations in the transition zone. 23
2.5 Location of the 1972 magnetometer array (de Beer et al., 1976) in southern Africa. 25
2.6 The 1977 magnetometer array (a) and proposed crustal conductor crossing Namibia and Botswana(b). 26
2.7 Location of the Ritter et al. (2003) MT profiles (a) and 2D inversion results (b) 27

3.1 EM induction cycle within the Earth. 35
3.2 The fault model and decoupling of the EM wave into TE and TM modes. 40
3.3 An observed high frequency spectrum at California, 14 July 1980 (Labson et al., 1985). 46

3.4 The effect of decreasing the spatial wavelength of the overhead source on MT responses. 47
3.5 A '+'-shaped BBMT site layout. 50
3.6 The recorded electric and magnetic field components for site ELZ291 over 16 seconds. 52
3.7 The frequency dependence of galvanic and inductive distortion effects. 58

4.1 MT response curves of site ELG091A before and after manual editing. 66
4.2 Poor MT responses in the AMT dead-band of site ELG014A. . 67
4.3 Strike angles computed over all frequencies for each individual MT site in the Otjiwarongo region. 69
4.4 Strike angles computed over all frequencies for each individual MT site in the Katima Mulilo region. 70
4.5 GB-errors (RMS) and phase differences computed after assigning strike angles of 0°, 20°, 40°, 60° and 80° to the Otjiwarongo data. 72
4.6 Plots of GB-error versus strike angle for the available decades of the 8 selected Otjiwarongo sites. 73
4.7 Strike angles computed over higher dimensional decades for the 8 selected MT site in the Otjiwarongo region. 75
4.8 Plots of GB-error versus strike angle for the available decades of the 7 selected Katima Mulilo sites. 76
4.9 Strike angles computed over higher dimensional decades for the 7 selected MT sites in the Katima Mulilo region. 77

5.1 2D inversion profiles for the Otjiwarongo (a) and Katima Mulilo (b) regions, respectively, and the sites included in each. 80
5.2 L-curves generated for the Otjiwarongo (top) and Katima Mulilo (bottom) data by plotting τ versus RMS error. 83
5.3 Inversions of the individual TM (left) and TE (right) modes of the Otjiwarongo data. 86
5.4 Inversions of the individual TM (left) and TE (right) modes of the Katima Mulilo data. 87
5.5 Standard grid (top) and uniform grid (bottom) Laplacian joint inversions of the TM and TE modes of the Otjiwarongo data. 89

5.6 Standard grid (top) and uniform grid (bottom) Laplacian joint inversions of the TM and TE modes of the Katima Mulilo data. 90
5.7 Uniform grid Laplacian joint inversion of the TM and TE modes of the Otjiwarongo data with $\tau = 7$. 92
5.8 Sensitivity tests done on the mid-crustal conductor in the Otjiwarongo inversion result. 94
5.9 NB-depths of the Otjiwarongo data and removal of parts of the mid-crustal conductor that the data are insensitive to (right). 95
5.10 Inversion result (right) after locking only parts of the conductor that the Otjiwarongo data are sensitive to. 95
5.11 Sensitivity tests done on the shallow conductive layer in the Katima Mulilo inversion result. 96
5.12 NB-depths of the Katima data and removal of parts of the surface conductive layer that the data are insensitive to (right). 97
5.13 Inversion result (right) after locking only parts of the conductive layer that the Katima Mulilo data are sensitive to. 97

6.1 2D inversion profiles of SAMTEX data acquired in central and northern Namibia and Botswana. 99
6.2 Resistivity model used as input for the first interpolation test. 101
6.3 Projected profiles (a) used as input in the first interpolation test and subsequent interpolation results (b and c). 102
6.4 Interpolation results for the first test with $b = 1$ (a and b) and $b = 9$ (c and d). 103
6.5 Resistivity model used as input for the second interpolation test. 104
6.6 Projected profiles (a) and interpolation results (b, c and d) for the second test. 105
6.7 Projected profiles used in the third interpolation test with strike on the right side equal to 60° (a) and 30° (b). 107
6.8 Interpolation results using Figure 6.7a as input. 108
6.9 Interpolation results using Figure 6.7b as input. 109
6.10 Interpolation results using the profile arrangement in Figure 6.6a and setting $a = 4$ and $b = 9$. 110
6.11 Strike angles and projection directions of selected SAMTEX profiles for crustal depths. 110
6.12 Tipper strike angles calculated at 100 seconds and associated penetration depths. 112

6.13 Tipper strike angles calculated at 200 seconds and associated penetration depths. 113
6.14 Tipper strike angles calculated at 333 seconds and associated penetration depths. 113
6.15 Tipper strike angles calculated at 500 seconds and associated penetration depths. 114
6.16 Tipper strike angles calculated at 1000 seconds and associated penetration depths. 114
6.17 Tipper strike angles obtained after averaging the five values calculated at 100, 200, 333, 500 and 1000 seconds at each site. 115
6.18 Impedance (yellow) and tipper (blue) strike angles calculated for sites in northern Namibia and Botswana. 116
6.19 Nine regions identified where strike appears approximately consistent over a number of sites. 117
6.20 Strike angles and projection directions of selected SAMTEX profiles for lithospheric mantle depths. 118
6.21 Resistivity values associated with the projected SAMTEX profiles at a depth of 20 km. 119
6.22 Resistivity values associated with the projected SAMTEX profiles at a depth of 120 km. 119
6.23 Interpolation results at 20 km depth (a) and the number of resistivity values used in each calculation (b). 120
6.24 Interpolation results at 120 km depth (a) and the number of resistivity values used in each calculation (b). 121

7.1 A histogram of the interpolated resistivity values and division of the values into 10 groups. 123
7.2 Comparison of the potential drop-off with current injected in the Otjiwarongo region and the size of the input grid varied. . 125
7.3 Potential values after current was injected in the Otjiwarongo region and structure at different depths included in calculation. 126
7.4 Potential values after current was injected in the Katima Mulilo region and structure at different depths included in calculation. 127

8.1 Uniform grid Laplacian inversion result (right) after placing a 5 km thick resistive layer at the top of the original Otjiwarongo inversion model (left). 129

8.2 Uniform grid Laplacian inversion result (right) after placing a thin 1 km resistive layer at the top of the original Katima Mulilo inversion model (left). 131
8.3 NB-resistivities calculated for the Katima Mulilo AMT sites at depths of 100 m, 200 m, 500 m, 900 m and 1000 m. 132
8.4 The Otjiwarongo (left square) and Katima Mulilo (right square) study regions relative to the proposed conductive belt (van Zijl and de Beer, 1983). 133
8.5 Regional geology of central and northern Namibia (Gray et al., 2006) and the Autseib Fault crossing the Otjiwarongo region. . 134

B.1 MT apparent resistivity and phase curves for sites ELG001m, ELG002m, ELG003A and ELG004B. 145
B.2 MT apparent resistivity and phase curves for sites ELG005A, ELG007m, ELG008A and ELG009A. 146
B.3 MT apparent resistivity and phase curves for sites ELG010A, ELG011A, ELG012B and ELG013m. 147
B.4 MT apparent resistivity and phase curves for site ELG014m. . 148
B.5 MT apparent resistivity and phase curves for sites ELZ001A, ELZ002A, ELZ003A and ELZ101m. 149
B.6 MT apparent resistivity and phase curves for sites ELZ102m, ELZ103A, ELZ201m and ELZ294A. 150
B.7 MT apparent resistivity and phase curves for sites ELZ555A, CPV027, CPV028 and CPV029. 151
B.8 MT apparent resistivity and phase curves for sites RAK053 and RAK054. 152

C.1 Standard grid Laplacian inversion results of the Otjiwarongo data with $\alpha = 1$ and β varied from 1 to 3. 153
C.2 Standard grid Laplacian inversion results of the Otjiwarongo data with $\alpha = 2$ and β varied from 1 to 3. 154
C.3 Standard grid Laplacian inversion results of the Otjiwarongo data with $\alpha = 3$ and β varied from 1 to 3. 155
C.4 Standard grid Laplacian inversion results of the Katima Mulilo data with α and β varied. 156

D.1 Results of the first interpolation test, at 40 km depth, with $b = 9$ and a varied from 1 to 3. 157

D.2 Results of the first interpolation test, at 40 km depth, with $b = 9$ and a varied from 4 to 9. 158
D.3 Real and imaginary induction arrows at 100 seconds for the MT sites in profiles ETO, DMB, NEN, OKAWIN and ZIM. . 159
D.4 Real and imaginary induction arrows at 200 seconds for the MT sites in profiles ETO, DMB, NEN, OKAWIN and ZIM. . 159
D.5 Real and imaginary induction arrows at 333 seconds for the MT sites in profiles ETO, DMB, NEN, OKAWIN and ZIM. . 160
D.6 Real and imaginary induction arrows at 500 seconds for the MT sites in profiles ETO, DMB, NEN, OKAWIN and ZIM. . 160
D.7 Real and imaginary induction arrows at 1000 seconds for the MT sites in profiles ETO, DMB, NEN, OKAWIN and ZIM. . 161
D.8 Impedance strike angles calculated for the MT sites in northern Namibia and Botswana over the $50 - 200$ km depth range. 161
D.9 Plots of standard deviation versus number of strike values removed for 8 of the 9 groups of consistent strike. 162

List of Tables

3.1 Dielectric constants and relative magnetic permeabilities of some rocks and minerals. 33
3.2 Classification of regular and irregular geomagnetic variations. . 45

4.1 Higher dimensional frequency ranges for the Otjiwarongo and Katima Mulilo sites and the strike angles computed for the ranges. 74

5.1 RMS errors for Otjiwarongo and Katima Mulilo inversions where weighting parameters α and β were varied. 85
5.2 RMS errors of joint inversions of TE and TM modes of the Otjiwarongo and Katima Mulilo data, where the order in which components were added was varied. 91

A.1 Data acquisition parameters for sites close to Otjiwarongo. . . 143
A.2 Data acquisition parameters for sites close to Katima Mulilo. . 144

List of Symbols

Symbol	Description(units)	Relationship
∇	the vector differential	
$\times$	cross product operator	
$\cdot$	dot product operator	
i	imaginary number ($\sqrt{-1}$)	
$\vec{A}$	first-order tensor (vector) A	
$\boldsymbol{A}$	second-order tensor A	
$\vec{H}$	magnetic intensity ($\mathrm{A.m^{-1}}$)	
$\vec{B}$	magnetic field (T)	$\vec{B} = \mu\vec{H}$
μ	magnetic permeability ($\mathrm{H.m^{-1}}$)	
μ_0	permeability of free space ($4\pi \times 10^{-7}$ $\mathrm{H.m^{-1}}$)	$\mu = \mu_r\mu_0$
μ_r	relative magnetic permeability (unitless)	
$\vec{J_f}$	current density ($\mathrm{A.m^{-2}}$)	
$\vec{E}$	electric field ($\mathrm{V.m^{-1}}$)	$\vec{J_f} = \sigma\vec{E}$
σ	electrical conductivity ($\mathrm{S.m^{-1}}$)	
ρ	electrical resistivity (Ω.m)	$\rho = 1/\sigma$
$\vec{D}$	electrical displacement ($\mathrm{C.m^{-2}}$)	$\vec{D} = \epsilon\vec{E}$
ϵ	electrical permittivity ($\mathrm{F.m^{-1}}$)	
ϵ_0	permittivity of free space (8.85×10^{-12} $\mathrm{F.m^{-1}}$)	$\epsilon = \epsilon_r\epsilon_0$
ϵ_r	relative electrical permittivity (unitless)	
ρ_f	free charge per unit volume ($\mathrm{C.m^{-3}}$)	
σ_f	free charge per unit area ($\mathrm{C.m^{-2}}$)	
f	frequency (Hz)	
ω	angular frequency ($\mathrm{rad.s^{-1}}$)	$\omega = 2\pi f$
T	period (s)	$T = 1/f$
λ	wavelength (m)	

Nomenclature

Abbreviation	Description
1D	one-dimensional
2D	two-dimensional
3D	three-dimensional
AC	Alternating-current
AEJ	Auroral Electrojet
AMT	Audio-magnetotelluric(s)
BBMT	Broad-band Magnetotelluric(s)
DC	Direct-current
DMB	Damara Mobile Belt
EEJ	Equatorial Electrojet
ELF	extremely low frequency
EM	electromagnetic
ERC	Equatorial ring current
FFT	Fast Fourier Transform
GB	Groom-Bailey
GDS	Geomagnetic Depth Sounding
GPS	Global Positioning System
HVAC	High-voltage Alternating-current
HVDC	High-voltage Direct-current
LMT	Long-period Magnetotellurics
MT	Magnetotelluric(s)
NACP	North American Central Plains
NB	Niblett-Bostick
RMS	root mean square
RMT	Radio-magnetotellurics
SADC	Southern African Development Community
SAMTEX	Southern African Magnetotelluric Experiment
SASE	Southern African Seismic Experiment
SCCB	Southern Cape Conductive Belt
TE	transverse electric
TM	transverse magnetic
ULF	ultra low frequency
VLF	very low frequency

Chapter 1

Introduction

The purpose of chapter one is to introduce the Southern African Magnetotelluric Experiment (SAMTEX) and the initial aims of the project. Following that is a description of how the project has expanded over the last decade to finally include the current localized study. The chapter concludes with a geological description of northern Namibia and Botswana, an area over which several magnetotelluric (MT) sites, including the sites of the current study, were installed during SAMTEX.

1.1 The SAMTEX project

SAMTEX is a multi-national project that was initiated in 2003 to study the electrical conductivity subsurface structure of southern Africa and to infer from it the tectonic processes involved in the formation of the southern African subcontinent (Figure 1.1). At present, data have been recorded at over 730 MT sites covering an area that exceeds 1 000 000 km^2 (Jones et al., 2009), making SAMTEX the largest land-based MT experiment ever conducted. The consortium members[1] that form part of SAMTEX come from academia, government and industry.

The Kaapvaal Craton, due to its old age ($3.7 - 2.6$ Ga, de Wit et al., 1992) and excellent preservation, provides Earth scientists with one of the best natural laboratories to explore in their quest to better understand the formation and evolution of continental lithosphere (de Wit et al., 2004). Both seismological (Silver and Chan, 1988) and electromagnetic (EM) methods (Jones,

[1] see `http://www.geophysics.dias.ie/projects/samtex/Consortium_Members.html`

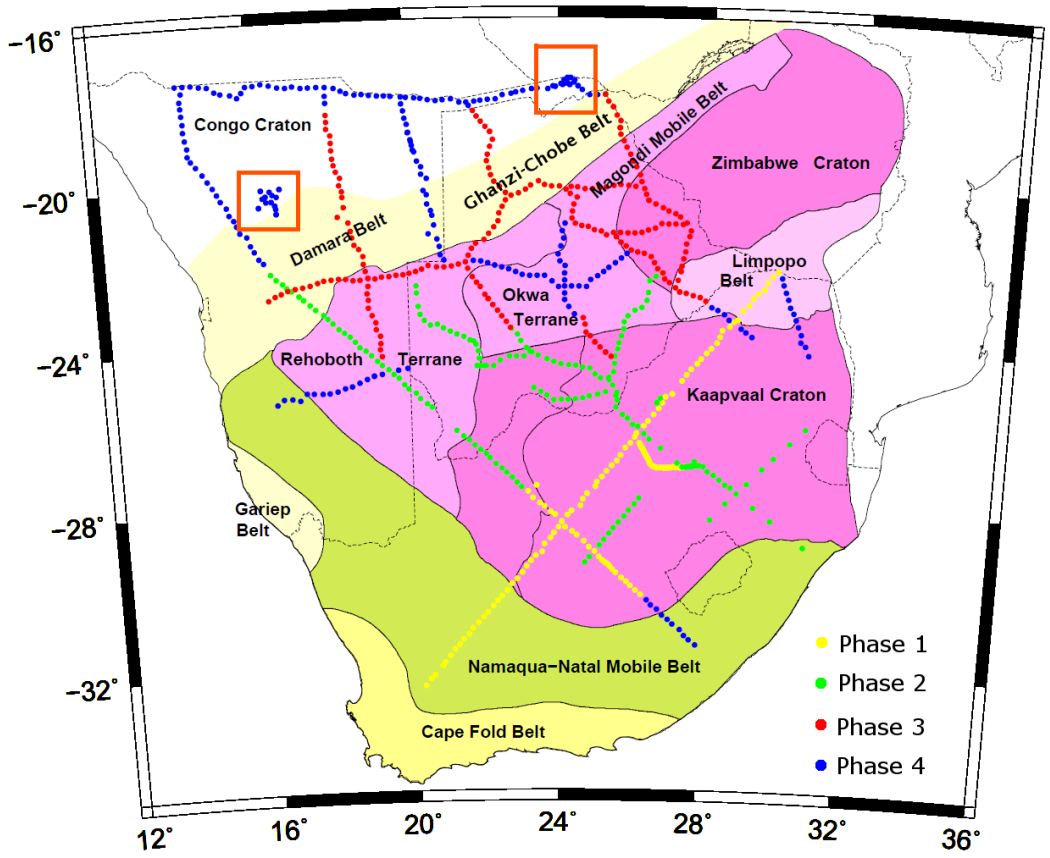


Figure 1.1: *The more than 730 MT sites installed during SAMTEX plotted on a map of southern Africa's geological provinces (after Nguuri et al., 2001). The two squares indicate the Audio-magnetotelluric arrays installed close to the towns of Otjiwarongo (left) and Katima Mulilo (right) that are central to the current study.*

1999) have been shown to be invaluable tools in broadening the understanding of processes involved in the deformation of continental lithosphere. In combination, where results of one method are used as constraints in interpreting results of the other, or through joint inversion of the two datasets, an even greater understanding of lithospheric processes is achieved. Due to the added knowledge obtained when combining EM and seismological methods the project SAMTEX was proposed to cover an area coincident with the earlier installed Southern African Seismic Experiment (SASE) array (Carlson et al., 1996). In addition to seismological data, EM results can also be combined with other geoscientific results such as geochemical, petrological and geochronological results that are available in southern Africa. Following subsequent approval and funding by the U.S. National Science Foundation, Phase 1 of SAMTEX commenced in 2003 with the installation of three planned MT profiles, the longest of which traverses the Kaapvaal Craton in

a south-west north-east direction (Figure 1.1).

After realizing the unique information gained through knowledge of the electrical structure of the southern African lithosphere, the interest and number of consortium members increased, leading to an expansion of the SAMTEX project through the planning and installation of several other MT profiles (Phases $2-4$, Figure 1.1). Data acquisition for Phase 4 of SAMTEX ended in 2008, completing a network of MT profiles that cross geological terranes varying in age from the Archaean to Phanerozoic.

SAMTEX data have been used by various researchers in their scientific endeavours. There has been a comparison of electric and seismic anisotropy at lithospheric depths by means of analysis of MT data from SAMTEX and shear wave splitting of teleseismic events from SASE (Hamilton et al., 2006), leading to a new model explaining the anisotropy observed at lithospheric depths in the Kaapvaal region. More recently, lithospheric two-dimensional (2D) conductivity models have been produced for parts of South Africa, Namibia and Botswana that indicate variations in conductivity between the older cratonic regions and younger surrounding mobile belts (Muller et al., 2009; Evans et al., 2011; Khoza et al., 2011; Miensopust et al., 2010). Furthermore, the conductivity models were used to make inferences about the thermal, mechanical and chemical properties of the geological terranes (Fullea et al., 2011). The correlation between diamond prospectivity and regional resistive/conductive boundaries in Namibia and South Africa has also been examined with SAMTEX results (Jones et al., 2009 and Muller et al., 2009).

1.2 Purpose of the current study

In the most recent phase of SAMTEX (Phase 4), in conjunction with deeper probing of the Earth, a study with shallower imaging objectives was undertaken in north and north-eastern Namibia. Two localized surveys were undertaken after a new consortium member, ABB of Sweden for NamPower of Namibia, expressed specific interest in the shallow subsurface in the regions close to the towns of Otjiwarongo and Katima Mulilo. The conductivity information in the Otjiwarongo and Katima Mulilo regions is needed for the optimal placement of High-voltage Direct-current (HVDC) earth electrodes.

Because of the shallow target depths under investigation, a high frequency counterpart of MT (typically $1 - 10\ 000$ Hz), the Audio-magnetotelluric (AMT) method was used. An AMT survey requires a dense spacing of sites to best define the extent of structures within the shallow subsurface (to about 5 km). In the current study the inter-site spacing ranged from 5 to 20 km (Figures 1.2 and 1.3), in contrast to the minimum 20 km spacing for SAMTEX MT sites. Data were recorded at a total of 22 locations, of which 13 were situated in the Otjiwarongo region (Figure 1.2) and 9 in the Katima Mulilo region (Figure 1.3). To provide greater depth resolution Broad-band Magnetotelluric (BBMT) data ($0.001 - 100$ Hz) were also acquired at 6 of the 13 locations in the Otjiwarongo region and 4 of the 9 locations in the Katima Mulilo region.

The aim of the current study is to use the data from the two AMT arrays and existing modelling tools to find the best possible model of the subsurface conductivity structure for each area, up to mid-crustal depths (20 km). Where available, BBMT data will be used to resolve subsurface conductivity structure to even greater crustal depths. Modelling of MT data involves processing of the recorded electric and magnetic time-varying fields and obtaining appropriate frequency response curves for each site. From the calculated responses, galvanic distortion of the electric field is removed and geoelectric strike angles are obtained that best approximate the two three-dimensional (3D) regions as 2D ones. The corrected responses are derived in the obtained strike angles and used as input to a 2D inversion algorithm (incorporated in the program WinGLink™) to obtain the subsurface conductivity models. After robust models with low misfit errors are obtained, the results, together with models derived from other geophysical datasets, are correlated with existing geological data to facilitate in constraining interpretation where the geology is unknown. The conductivity models will also be used in recommending locations for the placement of the HVDC earth electrodes in the Otjiwarongo and Katima Mulilo regions. The Otjiwarongo and Katima Mulilo models will then be used, together with geology and results from previous conductivity studies, including SAMTEX profiles crossing the Damara Mobile Belt (DMB, see Section 1.4 for composition), to create an interpolated 3D conductivity model. The 3D model is, in turn, used as input to a 3D Direct-current (DC) forward modelling code, written by Dr. M. H. Loke, to try to predict the return path that the DC current will follow

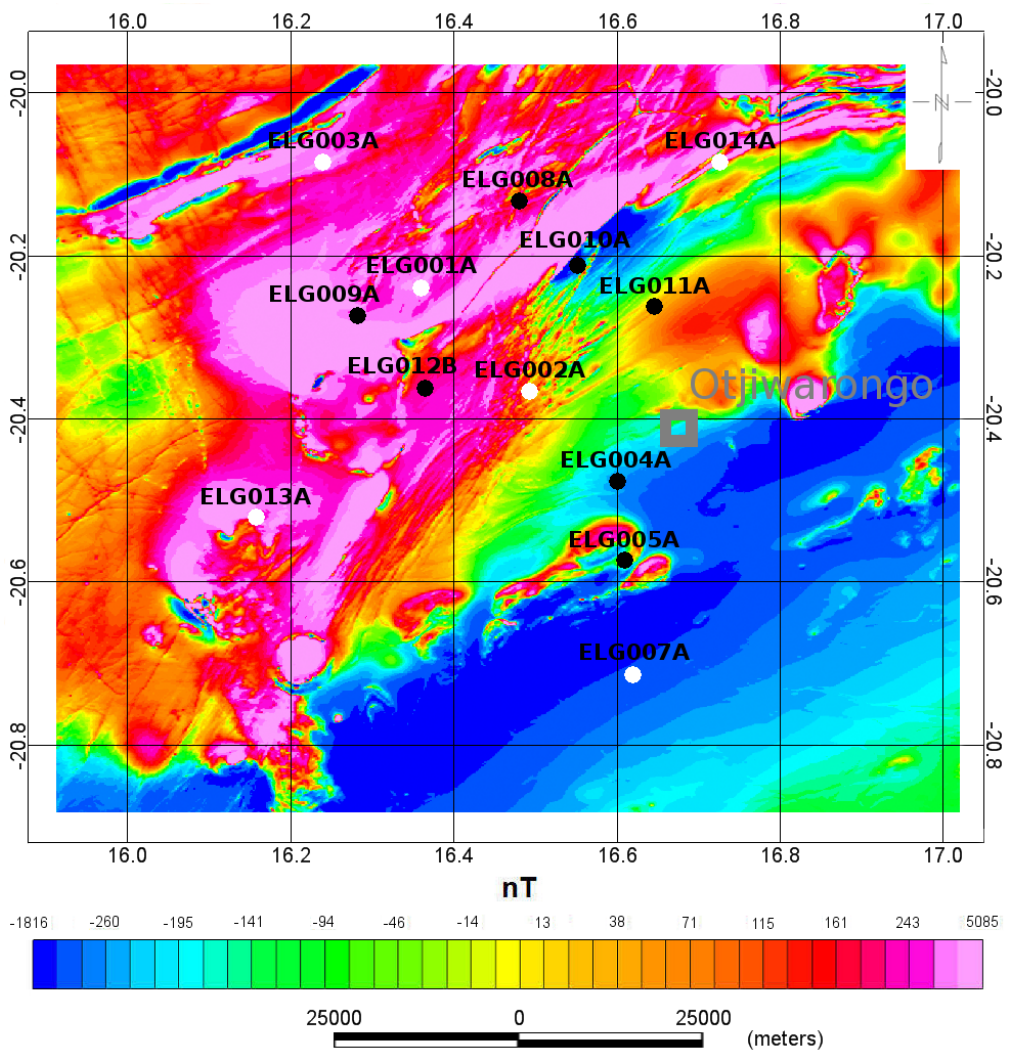


Figure 1.2: *Locations of the 13 AMT sites installed during SAMTEX Phase 4 close to the town of Otjiwarongo, plotted on top of a magnetic map of the area (courtesy of the Ministry of Mines and Energy, Geological Survey of Namibia). Sites ELG001A, ELG002A, ELG003A, ELG007A, ELG013A and ELG014A have collocated BBMT and AMT data.*

between the Katima Mulilo and Otjiwarongo regions. The current injection point is varied between the Otjiwarongo and Katima Mulilo regions as more conductivity information is added at depth with the aim of examining the effects that changing the conductive geometries around the injection point and enlarging the 3D conductivity model have on return current flow.

Previous studies suggest that there is a continuous region of higher conductivity in northern Namibia that coincides with the location of the Central Zone of the DMB (see Section 2.4). In contrast, on either side of the DMB

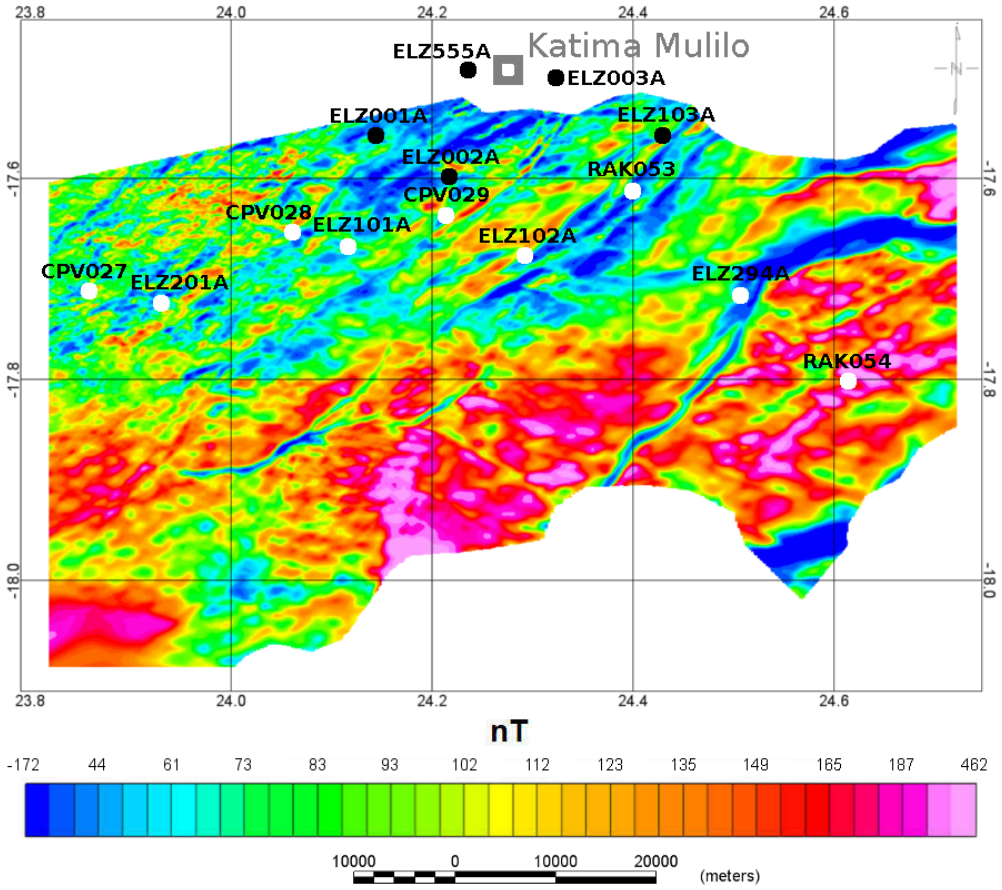


Figure 1.3: *Locations of the 9 AMT sites (sitenames starting with ELZ) installed during SAMTEX Phase 4 close to the town of Katima Mulilo, plotted on top of a magnetic map of the area (courtesy of the Ministry of Mines and Energy, Geological Survey of Namibia). Sites ELZ101A, ELZ102A, ELZ201A and ELZ204A have collocated BBMT and AMT data. The other sites shown; CPV027, CPV028, CPV029, RAK053 and RAK054, are BBMT sites also used in the current study and were installed prior to, or during the installation of the AMT array.*

there are two cratons which are more resistive: the Kalahari (see Section 1.4 for composition) and the Congo. It is therefore hypothesized that return flow of DC current, in between Otjiwarongo and Katima Mulilo, will follow a path that lies either exclusively, or almost entirely within the DMB.

1.3 HVDC transmission

High-voltage Direct-current (HVDC) is one of the most efficient methods of transmitting power over large distances (Woodford, 1998 and Rudervall et al., 2000). HVDC systems have been successfully installed and operated

in many countries, including Brazil (Itaipu), Phillipines (Leyte), India (Rihand), Sweden (Gotland), Australia (Direct Link) and Mozambique - South Africa (Cahora Bassa)(Rudervall et al., 2000). At present, the demand for electricity in South Africa and other Southern African Development Community (SADC) countries is rapidly increasing. In most cases the areas of demand and areas of potential power generation are separated by hundreds and even thousands of kilometres (Tuson, 2007). Therefore, HVDC powerlines form an integral part in present and future plans for supplying many African countries with adequate power (Tuson, 2007). One of the planned HVDC powerlines is the one between Gerus (Otjiwarongo region) and Katima Mulilo (Katima Mulilo region) in Namibia.

A HVDC system is preferred over a High-voltage Alternating-current (HVAC) system (Woodford, 1998), because it is more cost effective over large distances. The initial cost and operation of the DC converter stations on either end of the line are more expensive than the terminating stations of a HVAC line. However, an overhead HVDC transmission line is less costly per unit length than an equivalent HVAC line designed to transmit the same level of power (Woodford, 1998). Therefore, there will be some breakeven distance after which the HVDC powerline becomes cheaper to manage than an equivalent HVAC powerline (Figure 1.4). In some cases the frequencies of the Alternating-current (AC) used in neighbouring countries or neighbouring parts of a country (for example, Japan) are dissimilar (Woodford, 1998), making the use of a HVDC line, even over short distances, more viable, because of the converter stations installed on either end of the line.

The three typical HVDC configurations are (Tuson, 2007); (1) a monopole with earth or metallic return (Figure 1.5a), (2) a bipole with earth or metallic return (Figure 1.5b) and (3) a bipole without earth or metallic return (Figure 1.5c). A pole consists of a single DC line with converter stations on either end. Most land schemes operate in bipolar mode without any return current (Figure 1.5c), but are manufactured in such a way that operation in monopolar mode with return current is possible when needed (for example, when one of the poles fail)(Thunehed et al., 2007). In the case of monopolar operation, large amounts of DC current are injected into the ground at the electrode locations. If the Earth is used as a return path a subsurface with resistivities (inverse of conductivity) of approximately 10 Ω.m is needed at

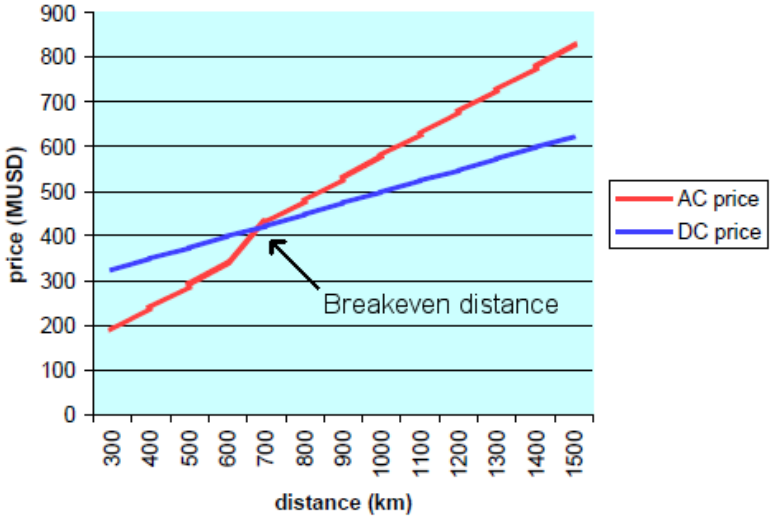


Figure 1.4: *A cost versus distance plot for a 2000 Megawatt powerline pointing out the breakeven distance where above HVDC systems become more economically viable than their HVAC counterparts (modified from Rudervall et al., 2000).*

the electrode locations so that the current can flow into the Earth unobstructed. If the electrodes are incorrectly placed (that is, on a subsurface with resistivities of the order of 1000 and 10 000 Ω.m), the injected current will create intense electric fields that can be hazardous to humans and animals in close proximity (Thunehed et al., 2007 and Koshcheev, 2003). Today, pre-investigation of an area to find the most suitable conductivity region for electrode placement is done with an EM technique (such as the AMT arrays installed in the current study).

1.4 Tectonics and geology of northern Namibia and Botswana

The crust of southern Africa consists of a network of Proterozoic orogenic belts that wrap around and separate older, Archaean cratonic nuclei and, to a lesser extent, Paleoproterozoic terranes (Singletary et al., 2003)(Figure 1.6). Where exposed, the geological terranes (cratons and orogenic belts) of southern Africa are well documented. However, there are extensive regions underlying the vast expanses of Phanerozoic sediment cover (Figure 1.6). Geophysical data (Figure 1.7) have, in the past (Hutchins and Reeves, 1980) and present (SAMTEX), been used to investigate structures to lithospheric depths in the poorly exposed areas, and inferences about the geology under-

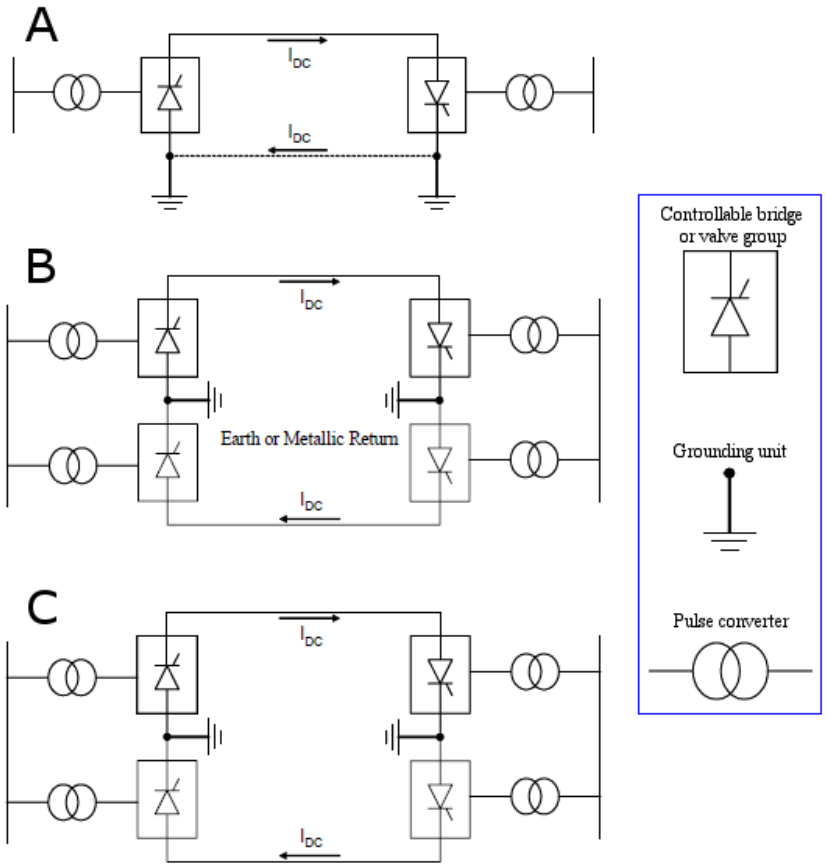


Figure 1.5: *The three HVDC configurations; a) monopole with earth or metallic return, b) bipole with earth or metallic return and c) bipole without earth or metallic return (modified from Tuson, 2007).*

neath the sedimentary cover have been made. The region underneath the Kalahari Desert in central and northern Namibia and Botswana is of particular importance. It is an area where the interconnected (Key and Rundle, 1981) Neo-Proterozoic Ghanzi-Chobe and Damara Belts (collectively termed the DMB, Figure 1.1) converge.

The Kalahari Craton (Jacobs et al., 2008) includes the Kaapvaal craton and $3.5 - 2.6$ Ga old Zimbabwe Craton (Kusky, 1998), the Early Proterozoic (<2.3 Ga old, Muller et al., 2009) Rehoboth and Okwa Terranes, and the Magondi Belt ($2.0 - 1.8$ Ga, Majaule et al., 2001) and Limpopo Belt (formed during the collision of the Kaapvaal and Zimbabwe cratons $2.7 - 2.6$ Ga ago, van Reenen et al., 1987)(Figure 1.1). The Congo Craton comprises various Archaean shields (Begg et al., 2009), of which the southernmost one is the Angolan shield. The DMB separates the two cratons in northern Namibia

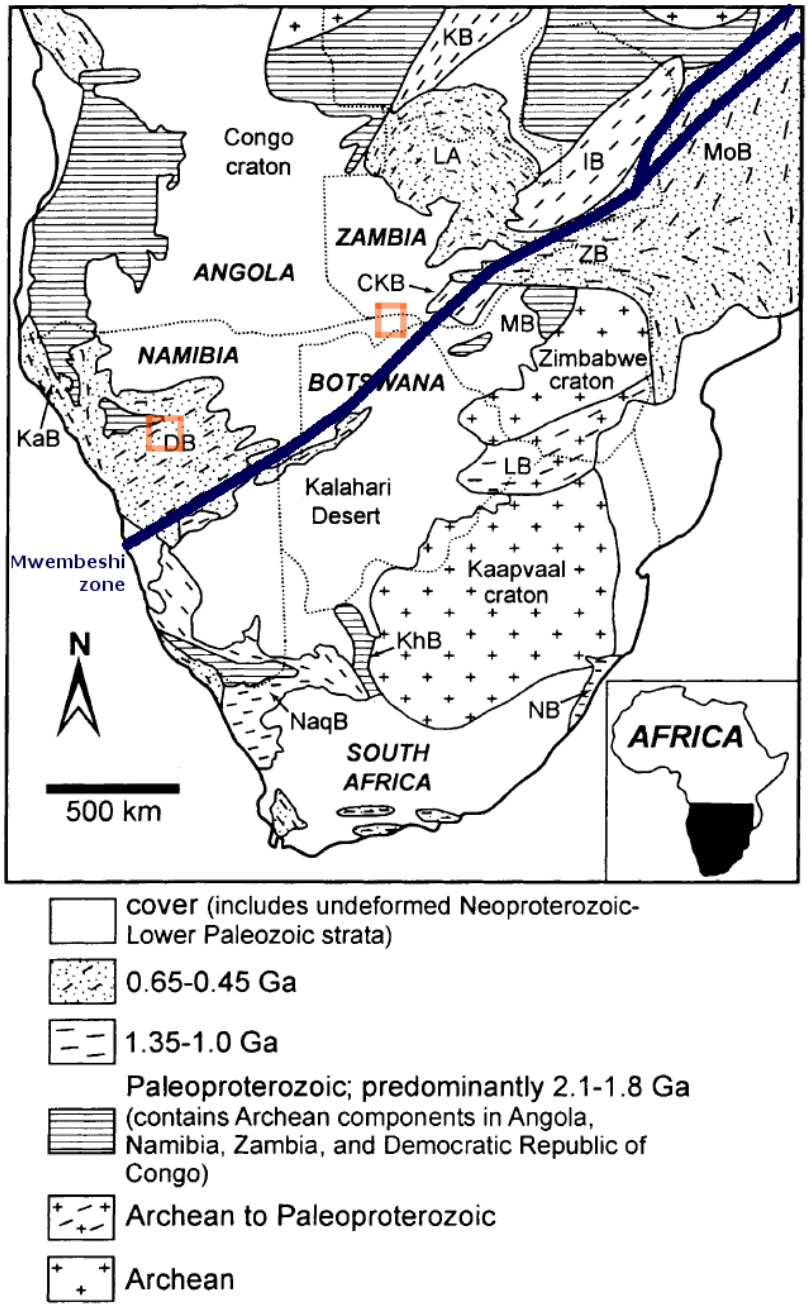


Figure 1.6: *Map of the exposed Archaean cratons and surrounding orogenic belts in southern Africa. The belts are; CKB - Choma-Kalomo Block, DB - Damara Belt, IB - Irumide Belt, KaB - Kaoko Belt, KB - Kibaran Belt, KhB - Kheis Belt, LA - Lufilian Arc, LB - Limpopo Belt, MB - Magondi Belt, MoB - Mozambique Belt, NaqB - Namaqua Belt, NB - Natal Belt, ZB - Zambezi Belt (Singletary et al., 2003). The locations of the two AMT arrays and the Mwembeshi shear zone (after Daly, 1986) are indicated.*

and Botswana. Large parts of the Damara Belt is exposed in Namibia (Figure 1.6) but the Ghanzi-Chobe Belt, except for a few sparse outcrops (Single-

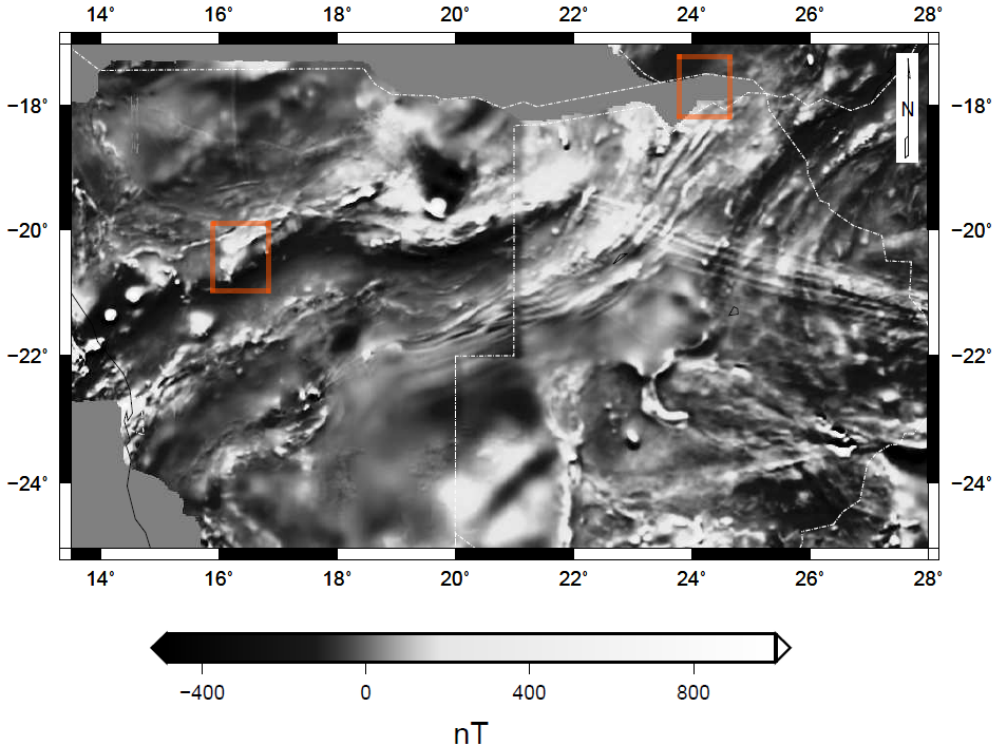


Figure 1.7: *An aeromagnetic map of central and northern Namibia and Botswana showing clearly, even under sedimentary cover, crustal remnants of the deformation and movement that dominated during the formation of southern Africa (Courtesy of the Council for Geosciences, South Africa).*

tary et al., 2003), is totally covered by Kalahari sediments. The Damara Belt constitutes the intracontinental branch, together with southern and northern (Kaoko Belt) coastal branches, of a three-armed asymmetric orogenic junction, called the Damara Province (Tankard et al., 1982, p. 314). The Damara Province, in turn, is one of several other orogens, including the Gariep (southern Africa), Dom Feliciano and Ribiera Belts (in South America) that, during Gondwanan assembly, bound together different supercontinents and now contain remnants (most evident in large-scale geophysical surveys, Figure 1.7) of past deformation and movement (Gray et al., 2006).

Extensive rifting between the stable Congo, Kalahari, Rio de la Plata and São Francisco Cratons resulted in deposition of Ghanzi-Chobe sediments (Modie, 2000) and later deposition of Damara Province sediments from $1000-900$ Ma (Tankard et al., 1982, p. 316) to at least 600 Ma (Miller, 1983). It is evident from their shallow-water or terrestrial sedimentary affinities and the presence of pre-Damara sialic basement within the Damara Province (for example, the

Kamanjab Inlier located north-west of the Otjiwarongo study region, Figure 1.6), that deposition of the Damara sequence took place on continental crust (Tankard et al., 1982, p. 314). At 650 Ma rifting ceased through tectonic inversion and subduction of the Kalahari beneath the Congo Craton followed (Miller, 1983), leading to the Late Neoproterozoic/Early Palaeozoic Damara Orogeny (Modie, 2000). The formations of the Damara/Ghanzi-Chobe, Kaoko and Gariep Belts did not occur simultaneously. Most recent geochronological and thermochronological data point to the formation of the Kaoko Belt first (Adamastor Ocean closure), followed by the Gariep Belt (southern Adamastor Ocean closure), and finally the DMB (Khomas Ocean closure)(Gray et al., 2006). Continental convergence was accompanied by varying levels of deformation and metamorphism that reached a maximum at $580 - 550$ Ma in the Kaoko Belt (high-grade amphibolite to granulite facies metamorphics), $545 - 530$ Ma in the Gariep Belt (low-grade metamorphics) and $530 - 500$ Ma in the DMB (high-grade thermal metamorphism in the centre and intermediate-grade metamorphics in the sides, Gray et al., 2006). Jurassic breakup of Gondwana followed stabilization of the various orogenic belts, separating the Gariep and Kaoka Belts and the southern coastal branch of the Damara Province (southern Africa) from the Dom Feliciano and Ribeira Belts (South America) to form the present-day southern Atlantic Ocean. The DMB was affected by extension and widespread igneous intrusion but, due to north-westward subduction of the Kalahari Craton below the Congo Craton (Miller, 1983), it never developed to the rift stage.

Extensional faults that formed during rifting between the Kalahari and Congo Cratons were partly reactivated as thrusts during later continental collision (Miller, 1983). Today the collisional thrusts manifest themselves as lineaments on the surface, and in southern Africa many observed regional lineaments are shear zones with large displacement (Coward and Daly, 1984). The Mwembeshi shear zone (Daly, 1986), that extends across northern Namibia, Botswana, Zambia and Malawi, is one of the largest shear zones in southern Africa (Figure 1.6). In the Damara Belt, shear zones separate regions of different stratigraphic and structural evolutions, where its variability is primarily related to the different stages of deformation and metamorphism that took place across the belt (Miller, 1983 and Daly, 1986). The four main zones identified in the Damara Belt are the Northern Zone, Central Zone, Southern Zone and Southern Margin Zone (Gray et al., 2006)(Figure 8.5).

One of the major shear zones, separating the Central and Northern Zones of the Damara Belt, crosses the southern edge of the Otjiwarongo study region (compare Figures 1.8 and 8.5).

The Damara sequence consists of Archaean-Proterozoic basement outcrops, clastic sediments and minor volcanics of the Nosib Group (1000−830 Ma) filling the fault-bounded troughs of rifted basement (Martin and Porada, 1977), carbonates of the Otavi Group (830 − 760 Ma) rimming the ocean basins between cratons, turbidites of the Swakop Group (830 − 760 Ma) within the ocean basins and foreland basin deposits of the Mulden and Nama Groups (approximately 650 Ma ago, Gray et al., 2006)(Figure 1.8). The clastic sediments and carbonates of the Nosib and Otavi Groups can be correlated with sequences in the Ghanzi Group in northern Botswana (Ghanzi-Chobe Belt). The Ghanzi Group, together with volcanics of the Kgwebe Formation (1100 Ma) which it disconformably overlies (Modie, 2000), constitute the rifted zone in northern Botswana. Due to the up to 300 m thick sedimentary cover in northern Namibia and Botswana (Thomas and Shaw, 1990) it is difficult to state the exact basement composition beneath the Katima Mulilo study region. According to sparse outcrops, borehole data and geophysical results in northern Botswana, the study region is estimated to lie within the north-western edge of the rifted zone in the Caprivi Strip (a narrow eastward protrusion of Namibia separating Angola and Zambia from Botswana)(Singletary et al., 2003). The northeast-trending metasedimentary and meta-igneous rocks west of the rifted zone in Botswana are considered as extensions of the main part of the Damara Belt in Botswana (Singletary et al., 2003).

1.5 Study outline

The next chapter explains how the conductivity of rock is largely controlled by the presence of interconnected minor conductive phases and also by external factors such as pressure and temperature. Chapter 3 continues with a description of the MT method. Focus is placed on the physics behind the method, its limitations, how data are acquired, possible sources of noise and data processing. In Chapter 4 results of processing of data from the Otjiwarongo and Katima Mulilo arrays are presented, with emphasis on galvanic distortion removal from the data in addition to the geoelectric strike angle

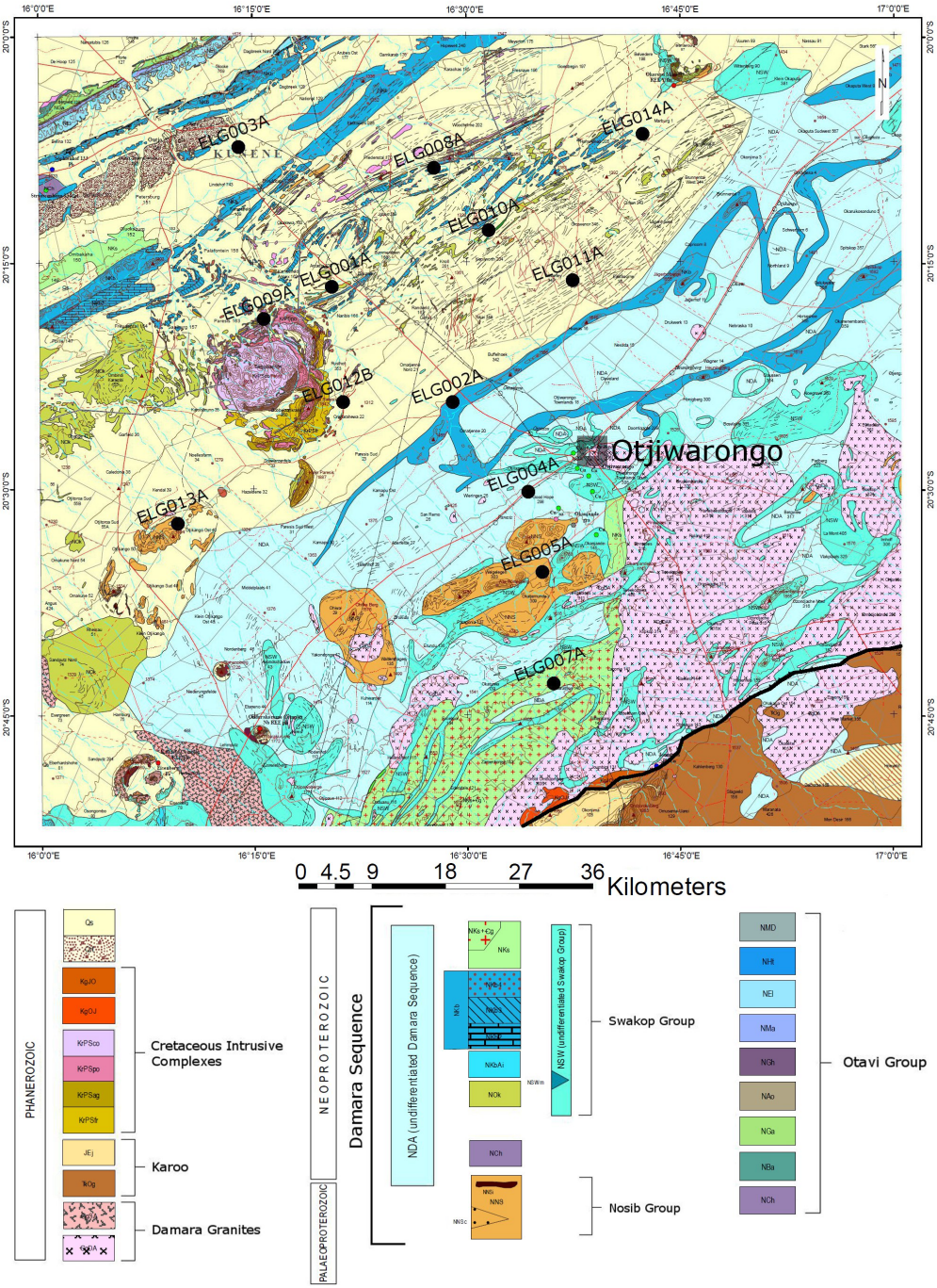


Figure 1.8: *Locations of the 13 AMT sites installed in the Otjiwarongo region, plotted on top of a geological map of the area (courtesy of the Ministry of Mines and Energy, Geological Survey of Namibia). The solid line in the south-eastern corner of the map depicts a major shear zone in the Damara Belt.*

determination for each region. Chapter 5 then follows with 2D inversions of the distortion-free data where the strike angles calculated in Chapter 4 are used to derive the distortion-corrected region data in appropriate angles prior

to inversion. Chapter 6 describes how the Otjiwarongo and Katima Mulilo inversion results are used, in conjunction with other geological and geophysical information, to create a 3D conductivity model representative of northern Namibia and Botswana. The 3D model is subsequently utilized in Chapter 7 to model the behaviour of ground return currents when injected in either the Otjiwarongo or Katima Mulilo regions. In the penultimate chapter, Chapter 8, results from the study are interpreted and discussed at length. The final chapter contains an encapsulation of the entire study in addition to possible areas of interest for future research being pointed out.

Chapter 2

Electrical conductivity of the Earth

The electrical conductivity of the various materials found in the Earth depends on the amount of free particle charges found in the rocks and minerals, and their mobility (Schwarz, 1990). All the materials that comprise the mechanically different divisions of the Earth (crust, mantle and core) have different intrinsic microscopic structures, therefore the amount and mobility of their free charged particles will be different. Apart from the intrinsic properties of rocks there are also extrinsic factors prevailing within the Earth that affect the number of free particles and their mobility that are, in fact, of greater importance to the geophysics community owing to the higher degree to which it dictates measured conductivity.

2.1 Factors controlling conductivity

The extrinsic petrological and physical factors, on which conductivity is greatly dependant, are more easily explained and distinguished when coupled with the four conduction mechanisms (charge transport processes) present in the Earth. The first conduction mechanism, electronic conduction, is present when highly conductive minerals (for example, graphite, iron, or any metallic ore) form an interconnected or partially interconnected network within the host rock matrix (Nover, 2005). Another factor that influences conductivity is the presence of partial melt (Nover, 2005), which generally explains the high conductivities associated with volcanic areas. Its contribution to the total conductivity is directly related to the amount (melt fraction is dependent on temperature, Roberts and Tyburczy, 1999) and interconnectivity of

the melts.

The third conduction type, electrolytic conduction, dominates in fluid-filled porous rocks and varies with the petrophysical factors within the rock, namely; size, orientation, interconnectivity, etc. of the pores and on the chemistry of the fluid and its interaction with the host rock (Nover, 2005). Conductivity anywhere within the Earth is a function of the amount and interconnectivity of the conducting phase (Jones, 1999). In the case of electrolytic conduction an empirical relationship, called Archie's law, between the total conductivity σ_m of the medium and that of the conducting phase σ_f is given by (Jones, 1999):

$$\sigma_m = \sigma_f \eta^n, \tag{2.1}$$

where η is the porosity of the rock and exponent n varies between 1 for well connected and 2 for weakly connected porous rocks (Keller, 1988, pp. 40-42). For electronic and partial melt conduction more complicated calculations need to be made to determine its effects on bulk conductivity (Pommier et al., 2008) but can easily be accomplished using a new freely available web application (SIGMELTS, Pommier and Le-Trong, 2011).

Host rock conductivity does not appear in equation (2.1) because it is assumed to be too small to have any effect on total conductivity. Therefore, when no conductive phase is present, Archie's law fails, and the final charge transport process is introduced, namely semiconduction. Semiconduction is most prominent in the Earth's lower crust and upper mantle and depends on thermodynamical factors such as temperature, oxygen fugacity (partial pressure of oxygen) and pressure to a lesser extent (Shankland, 1975). The temperature dependence is best described by Arrhenius-type behaviour (Nover, 2005):

$$\sigma = \sigma_0 e^{\left(-\frac{E_a}{kT}\right)}, \tag{2.2}$$

where σ is the material conductivity, σ_0 is the limiting value of conductivity as the absolute temperature T approaches infinity, E_a is the activation energy and k is the Boltzmann constant. Equation (2.2) has been used to estimate the conductivities of rocks exposed to lower mantle temperatures (that is, 1600 ℃ to 3700 ℃, Shankland et al., 1993). In contrast, electrolytic and electronic conduction are in general less dependent on temperature and pressure (Nover, 2005).

Combining results from other geophysical methods, such as seismology and studies on the elasticity and density of rocks, estimates of how mineralogy, composition and temperatures within the Earth change, have long been obtained, but new information forces corrections to be continuously made (Xu et al., 1998). In an attempt to further understand how all conditions vary within the Earth, results from MT and other EM techniques, such as Geomagnetic Depth Soundings (GDS), are compared with laboratory experiments conducted under approximate conditions that are representative of the Earth at different depths. Researchers have obtained conductivity results for rocks and minerals, including and excluding conducting phases in the bulk rock (electrolytic and electronic conduction and partial melt)(Figure 2.1), under mostly crustal and mantle P-T conditions (Hinze, 1982; Laštovičková, 1983; Schwarz, 1990; Nover, 2005). Owing to lack of penetration of EM energy into the Earths conductive core (see "skin depth", page 37), comparisons between results from laboratory (Gardner and Stacey, 1971 and Stacey and Anderson, 2001) and deep EM studies are impossible.

The variability of conductivity-depth profiles obtained recently in EM studies in and around the Pacific Ocean and Europe confirm the heterogeneous nature of the Earth (Figure 2.2a). One of the models obtained (Utada et al., 2003)(bold line in Figure 2.2a), is termed the semi-global model by the authors and is predicted to be a good estimate of the conductivity-depth structure for the quarter of the Earth covered by the Pacific Ocean. The semi-global model has been reanalysed with improved inversion schemes (Kuvshinov et al., 2005) and the result obtained is the most reliable model to date of regional conductivity variations up to mid mantle depths beneath the Pacific Ocean (Yoshino et al., 2008)(Figure 2.2b). The following is a more specific discussion of conductivity and conduction mechanisms in the crust and mantle.

2.2 Conductivity of the crust

The heterogeneous crust of the Earth has been explored through many geophysical and scientific tools. Studies show that the conductivity of the crust and Earth can range from 0.00001 to 10 $S.m^{-1}$ (Schwarz, 1990). Knowledge of reasons for the large variation in conductivity has grown immensely over

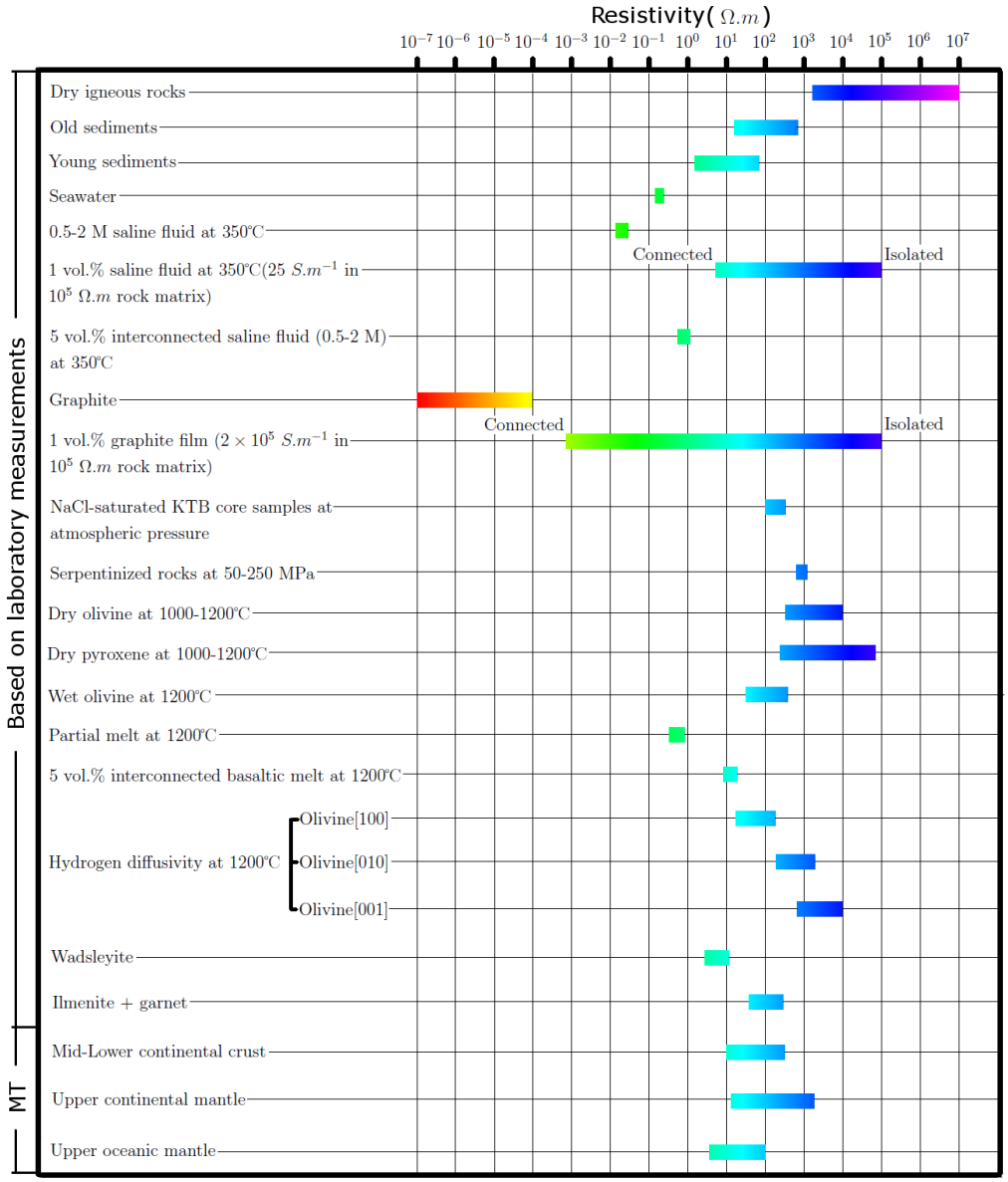


Figure 2.1: *Experimentally determined electrical resistivities (inverse of conductivity) of rocks and other common Earth materials that determine conductivity. The labels "Connected" and "Isolated" refers to the two extremities of interconnectivity of the material (modified from Simpson and Bahr, 2005, p. 11).*

the past century (Simpson, 1999 and Nover, 2005). Schwarz (1990) summarizes crustal conductivity studies collected on several continents and where conductive anomalies were observed.

Temperature and pressure in the Earth both increase monotonically with depth. The low temperatures (20 ℃ to 30 ℃) at the uppermost kilometre of the crust means an Arrhenius-type behaviour (equation 2.2) is generally

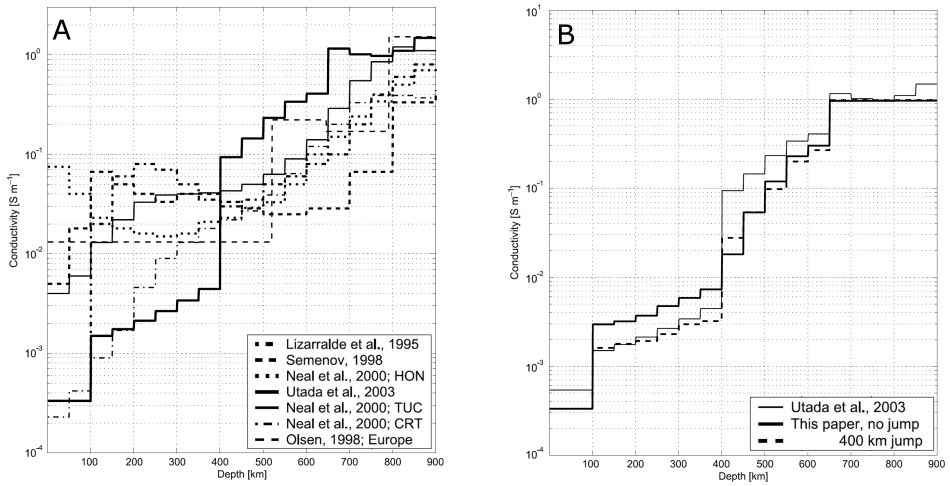


Figure 2.2: *Regional conductivity models, up to mid mantle depths, obtained by inversion of long period EM data by different authors (a), and Kuvshinov et al. (2005)(b) using the data of Utada et al. (2003)(Kuvshinov et al., 2005 and references therein).*

not observed. The conduction mechanism that most often dominates is electrolytic conduction. Electrolytic conduction can occur through the fluids that become trapped in the highly porous (due to low pressure) and fractured (rigid rocks under tectonic stress) rocks of the upper crust. Furthermore, in specific geological settings highly conducting phases (graphite or partial melt) may be present, and electronic and partial melt conduction can easily, depending on the interconnectivity of the phases, dominate over the effects of electrolytic conduction (Figure 2.1).

Deeper in the crust temperature increases with depth at $10\,^{\circ}\mathrm{C.km^{-1}}$ or less, after the initial increase of $15 - 50\,^{\circ}\mathrm{C.km^{-1}}$ in the upper crust, meaning temperature-induced semiconduction gradually becomes dominant as depth increases and porosity decreases (Nover, 2005). However, similar to the upper crust, anomalous regions also exist in the middle and lower crust, and electronic, electrolytic and partial melt conduction can dominate. The crust in general, as studied with EM methods, can be divided into at least three regions; a highly conductive surface layer consisting of sediments and groundwater, a resistive crystalline middle layer and a conductive lower layer (Shankland and Ander, 1983)(Figure 2.3).

There is still debate about why the lower crust is, in many places especially Phanerozoic in age, so highly conductive but amongst the possible reasons

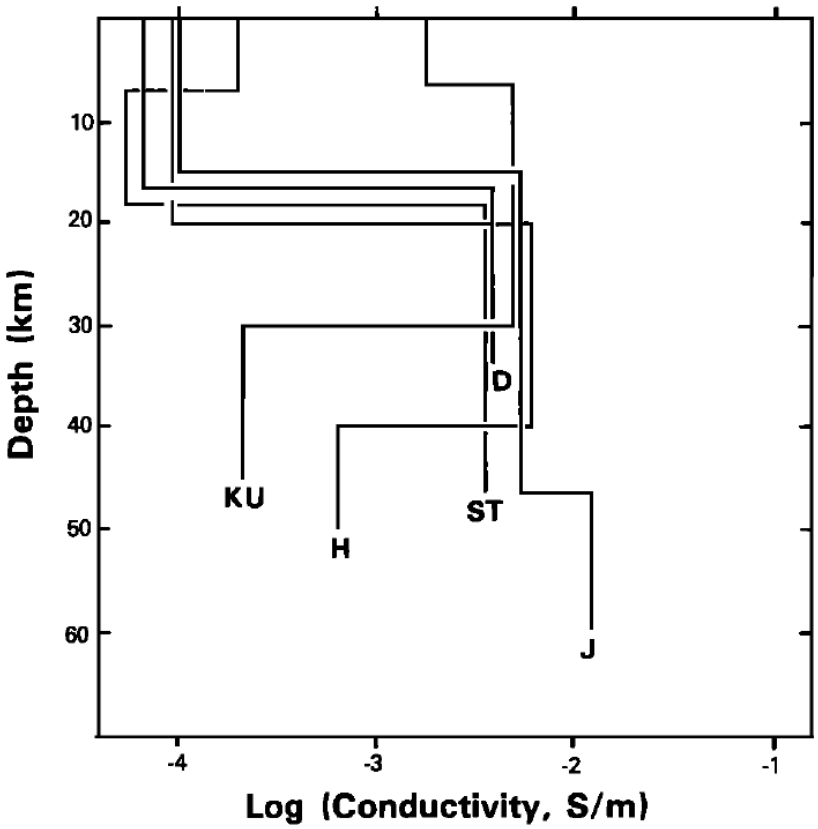


Figure 2.3: *The proposed three-layer model of the crust as measured over Precambrian terranes. The exception is Jones (1982) - J, where a resistive deeper layer was measured (KU - Kurtz and Garland, 1976; H - Hutton et al., 1981; ST - Sternberg, 1979; D - Duncan et al., 1980)(Shankland and Ander, 1983).*

are partial melts (Shankland and Ander, 1983) and the presence of interconnected brine or carbon film (Jones and Ferguson, 2001). A consequence of MT data error, inadequacy and insufficiency is an inability to resolve the depth to the base of a conductive layer (crustal base) when it is underlain by a resistive layer (resistive uppermost mantle)(Jones, 1993). Therefore, in contrast to seismological methods, where the Moho (crust-mantle boundary) is well resolved, with EM probing the depth to the conductivity jump at the Moho, if present, is almost invisible. However, in some cases the conductivity at the base of the crust is not high, but anomalously low. In parts of Scandinavia (Jones, 1982)(Figure 2.3) and also the Slave Craton (Jones and Ferguson, 2001) a resistive lowermost crust was observed and the Moho could, and was detected (Jones and Ferguson, 2001).

2.3 Conductivity of the mantle

The temperature-dependence of conductivity (semiconduction) persists into the Earth's mantle. However, anomalous regions or layers do exist, to a lesser extent than in the crust, and two areas of great interest to many geophysicists are the transition zone and the proposed electrical asthenosphere. The latter is defined as the weaker part of the upper mantle, underlying the more rigid lithosphere, where flow can occur by plastic deformation or creep (Ranalli, 1987, p. 67). It is an area of reduced seismic velocity (Ranalli, 1987, p. 138) and high conductivity and it is difficult to define beneath Archaean cratons (Eaton et al., 2009). The high conductivity can either be explained by the presence of partial melts or water and it is estimated to be around $0.05 - 0.2$ $\mathrm{S.m^{-1}}$ (Jones, 1999). While the conductivity of the electrical asthenosphere is relatively well defined, its depth is highly variable and has been shown to be as shallow as 15 km in certain areas and 500 km deep in others (Jones, 1999). The second anomalous region of interest, the transition zone, where olivine transforms to its higher pressure form called perovskite, is much less variable in depth than the asthenosphere, as it is a pressure boundary so is virtually uniform over the whole Earth. After its discovery several decades ago, using seismology, the zone has now been narrowed down to lie within the depths 410 and 660 km (Masters and Shearer, 1995, p. 94). The anomalous behaviour of seismic velocity, and more recently conductivities observed using MT, is now well understood to be caused by a $\alpha \rightarrow \beta \rightarrow \gamma$ phase change (olivine $\rightarrow$ wadsleyite $\rightarrow$ ringwoodite) of olivine under the high pressures and temperatures at mid-mantle depths.

The reason for the conductivity variations in the transition zone rocks relate to its semiconductive nature. Most materials found within the earth are effectively insulators at room temperature, but because of the high temperatures ($> 500\,℃$) at upper mantle depths and deeper down, materials become semiconductors and their point defects and impurities start to play a larger role in the conduction process. Phase changes in the transition zone lead to changes in point defect chemistry (Nover, 2005), which explains the sharp changes in conductivity observed at the 410, 520 (only observed in the laboratory) and 660 km discontinuities (Figure 2.4). The physics of semiconduction is more complex than explained, but the most recent understanding of what drives semiconduction in the mantle, is the high dependence of conductivity on the presence of small quantities of water and iron incorporated in the crystal

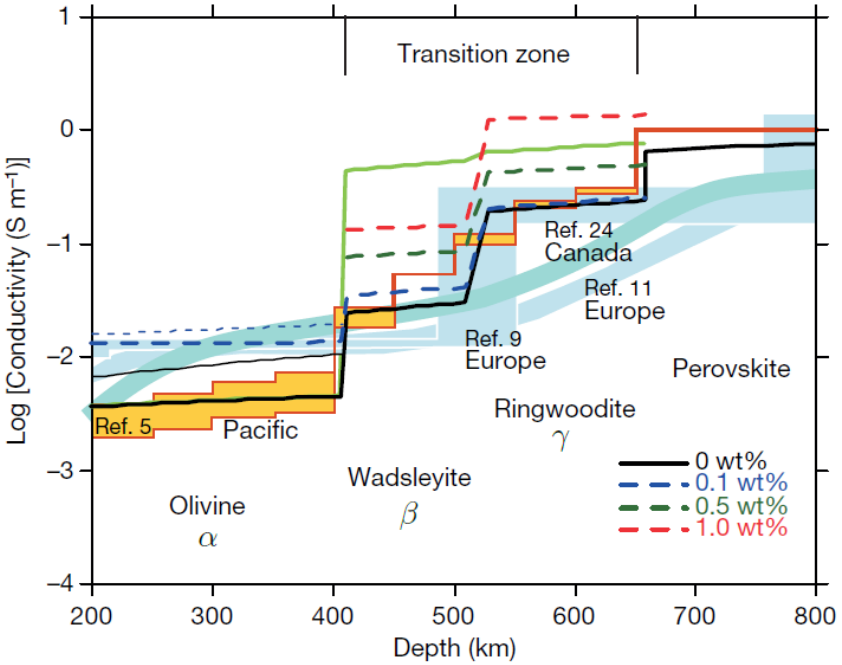


Figure 2.4: *Laboratory results obtained by Yoshino et al. (2008) on the α, β and γ phases of olivine, where the amount of water is varied for the β and γ phases. For comparison, results from EM studies by Olsen (1998) - Ref. 5, Kuvshinov et al. (2005) - Ref. 9 and Neal et al. (2000) - Ref. 24 are shown. Taken from Yoshino et al. (2008).*

structure of mantle minerals (Yoshino et al., 2008). Semiconduction in the mantle is therefore mainly by proton motion (H+, water present) and small polaron hopping (electron holes hopping by Fe2+ and Fe3+, iron present) and equation (2.2) can be modified to (Yoshino et al., 2008):

$$\sigma = \sigma_{0h} e^{\left(-\frac{H_h}{kT}\right)} + \sigma_{0p} e^{\left(-\frac{H_p}{kT}\right)}, \tag{2.3}$$

where H is the activation enthalpy, the subscripts h and p stand for polaron hopping and proton conduction, respectively, and k is the Boltzmann constant. Once again σ_0 is the limiting value of conductivity as the absolute temperature T approaches infinity.

The aim of the experiment by Yoshino et al. (2008) was to determine the dominance of either term on the right-hand side of equation (2.3). The fundamental result was that test samples containing little or no water compared much better to EM prospecting results than samples that contained water (Figure 2.4). Yoshino et al. (2008) concludes that the mantle transition zone must be dry or have less than 0.1 % water in it.

The temperature dependence of conductivity continues into the lower mantle, and, owing to high temperatures at lower mantle depths, the temperature according to equation (2.2) does not vary greatly (exponential term tends to 1). The conductivity is estimated to vary by less than a factor of 5 and reach a maximum of $3 - 10$ S.m^{-1} (Shankland et al., 1993).

2.4 Previous conductivity studies in the study regions

The first major investigation of the conductivity of northern Namibia and Botswana was a magnetovariational study in 1972 (de Beer et al., 1976). The study comprised 25 three-component magnetometers spanning across an area that included central and northern Namibia, Botswana and western Zimbabwe (Figure 2.5). The study, originally designed to examine possible conductivity contrasts of the crust and upper mantle between the Damara Orogen in Namibia and the seismically active Okavango Delta and central Kalahari region in Botswana (Hutchins and Reeves, 1980 and van Zijl and de Beer, 1983)(Figure 2.5), instead discovered a long east-west trending conductor crossing the survey area at depth (Figure 2.5).

The magnetovariational method is well suited to detect lateral conductivity variations but has poor depth resolution. Therefore, although the surface outline of the conductor was accurate within an error that depends on the station spacing ($50 - 150$ km), there was great uncertainty in its depth determination, and originally it was deduced that the conductor lies at approximately 50 km depth (de Beer and van Zijl, 1975). To obtain greater accuracy in the horizontal and vertical extent of the conductor, a second more dense magnetometer array covering only Namibia with a station spacing of approximately 60 km was installed in 1977 (de Beer et al., 1982)(Figure 2.6a). The greater spatial accuracy showed the conductor in Namibia to be curved rather than linear, following the trend of the Central Zone of the DMB. Its depth, or more accurately the anomalous induced currents flowing within it, was determined to be less than 45 km (de Beer et al., 1982).

In addition to the denser magnetometer array several Schlumberger soundings, sensing structure at crustal depths, were collected in the areas of anoma-

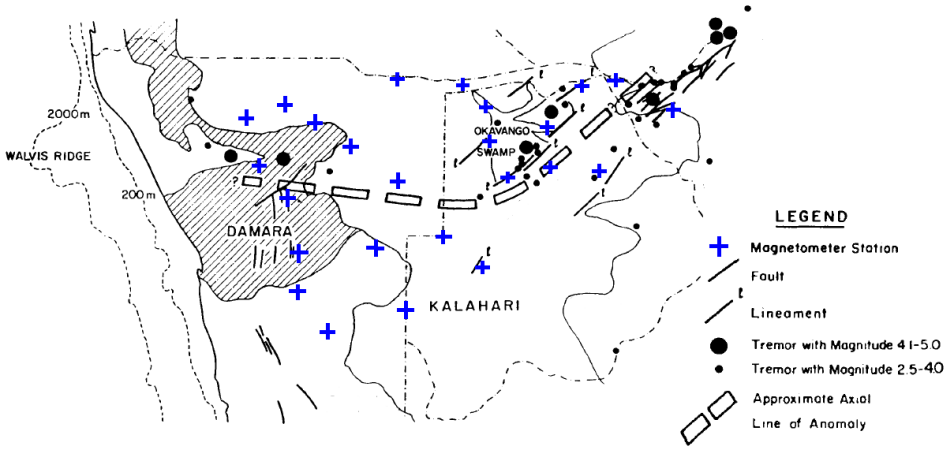


Figure 2.5: *The magnetometer stations of the 1972 array located in South West Africa (Namibia), Botswana and Zimbabwe (de Beer et al., 1976). Also indicated are the tectonic features in the study region and an approximate axial line of the conductive anomaly.*

lous current concentrations. A Schlumberger sounding has superior depth resolution, and the depth to the top of the conductor was found to vary from 3 to 10 km (de Beer et al., 1982). In addition, inversions of the Schlumberger sounding curves inferred that the resistivity of the conductor was less than 20 Ω.m and that of the surrounding upper crust ranged from 5000 to more than 20 000 Ω.m. An interesting geological fact is that 14 post-Karoo alkaline igneous complexes (the youngest in the DMB, Marsh, 1973)(Figure 2.7a) occur within the conductor in Namibia. De Beer et al. (1982) conclude that, because of its correlation with the young igneous complexes in Namibia and seismicity in Botswana, the conductor outlines a zone of weakness in the lithosphere that continues into Botswana (Figure 2.6b).

In a more recent study, a dense profile of MT stations were deployed across the western end of the conductor (Figure 2.7a). Similar to earlier studies, an anomalous highly conductive middle to lower crust (as high as 0.2 $S.m^{-1}$) and a resistive upper crust ($5000 - 15\,000$ Ω.m) were detected (Ritter et al., 2003)(Figure 2.7b). In addition, the highly dense station spacing of $4 - 12$ km led to the discovery of anisotropic conductivities within, and parallel to, the Waterberg Fault/Omaruru Lineament (Weckmann et al., 2003), which is one of the tectono-stratigraphic zone boundaries of the DMB (Figure 2.7b). Three-component magnetic data collected at geomagnetic observatories in central Namibia have also been analysed (Korte et al., 2007), and show regions of anomalous high conductivity at lithospheric depths between the

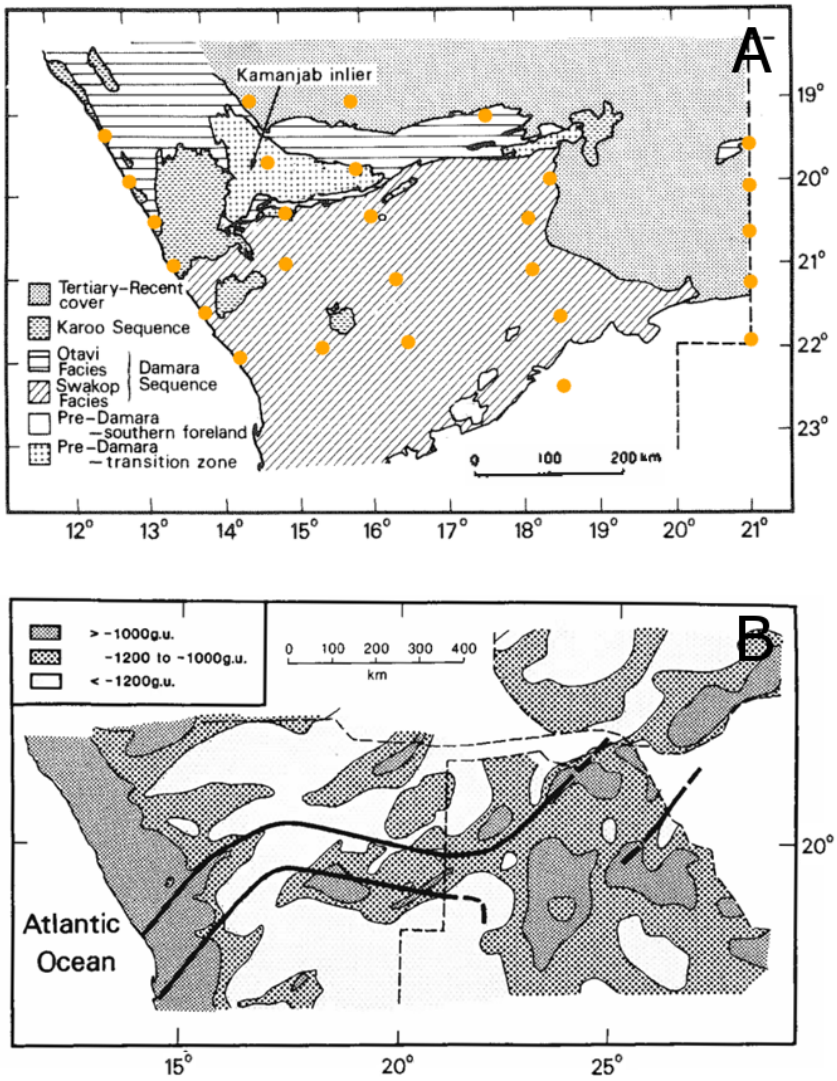


Figure 2.6: *The more dense 1977 magnetometer array (dots) relative to regional geology in Namibia (a), and the proposed conductor, determined with the 1972 and 1977 arrays and Schlumberger sounding data, crossing mainly Namibia and Botswana, in relation to a simplified Bouguer anomaly map (b)(van Zijl and de Beer, 1983).*

Tsumeb and Windhoek observatories.

When compared to the typical resistive mid-crustal regions observed around the Earth (see Section 2.2), it is clear why the conductor in the DMB is termed anomalous. Because the temperature is lower than 500 ℃ at mid-crustal depths and the DMB is far from any active volcanic zones or plate margins, it is impossible to explain the high conductivity of the conductor as being due to the semiconductive nature of the crystalline rocks or the presence of partial melt. Van Zijl and de Beer (1983) note that the most

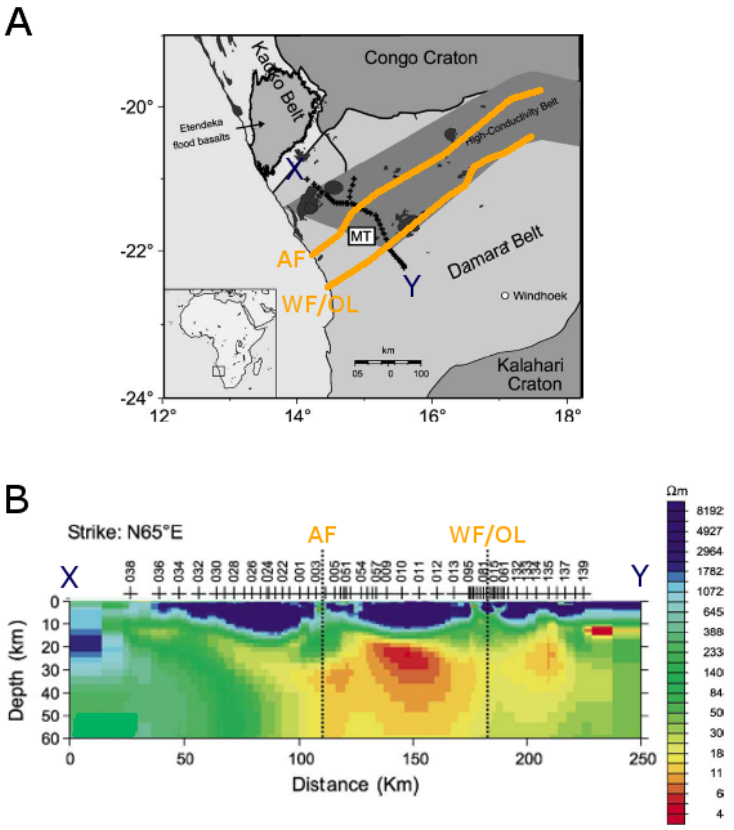


Figure 2.7: *a) The DMB sandwiched between the Kalahari and Congo Cratons in Namibia and the* $1998 - 99$ *MT profile (x-y) crossing the conductive belt. Post-Karoo alkaline igneous complexes are indicated in dark grey. b) 2D MT inversion results showing the highly conductive middle crust in the central part of the profile and the resistive upper crust. AF = Autseib Fault, WF/OL = Waterberg Fault/Omaruru Lineament (Ritter et al., 2003).*

plausible explanation for the high conductivity is the presence of serpentinite, the only rock that could develop the necessary high conductivity at mid-crustal temperatures. The highly conductive mineral associated with the process of serpentinization is magnetite, and if distributed appropriately on grain boundaries it can drastically increase the conductivity of a rock (Pakhomenko et al., 1973). The process of serpentinization requires a large amount of water and van Zijl and de Beer (1983) admit explaining the origin of it during DMB formation, either from the mantle or subduction, remains the only problem with the serpentinite model. Recent advances in understanding conductive anomalies at crustal depths point to the greater presence of fluids, fault gouge, sulfides or graphite in shear zones as a more plausible explanation for the conductor (Ritter et al., 1999). Graphite-bearing marble units are widespread in the stratigraphy forming part of the conductor and

Ritter et al. (2003) state that it is the most plausible cause of the high conductivity observed. Also, motion along shear planes is the ideal mechanism to ensure an interconnected network of conductive graphite over large distances.

The conductor in the DMB is not a unique example of an anomalous highly conductive belt in the Earth's crust. Other examples are the 140 km wide and 1000 km long Southern Cape Conductive Belt (SCCB) in South Africa (Weckmann et al., 2007), conductive belts in Ireland and Britain (Bailey and Edwards, 1976) and the 1500 km long North American Central Plains (NACP) anomaly (Jones et al., 1997). The SCCB consists of two conductive regions (2 Ω.m and lower) that are believed to be connected (Weckmann et al., 2007). The first is situated in the upper crust and is caused by carbonaceous shales and pyrite in the Karoo Basin. The second is a mid-crustal phenomenon reaching depths of 25 km, and, similar to the DMB, is associated with graphite-rich shear zones. Like both the SCCB and DMB conductive belts, the high conductivities (< 1 Ω.m) encountered at the southern extremity of the NACP conductive anomaly are linked to graphite located in local shear zones and fault systems. However, a different mechanism is possibly responsible for the remainder of the NACP anomaly. Jones et al. (1997) conclude, after years of studying the anomaly on scales ranging from $50-500$ km to 1 cm, that sulphides concentrated along fold hinges are the main cause of the high conductivities and anisotropy ($2-3$ orders of magnitude) observed. The NACP anomaly is mostly situated at mid- to lower crustal depths and its top is at approximately 10 km depth beneath the Willison Basin. Farther north, it is exposed at the surface (Jones et al., 1997). Similarly, the conductive belts stretching between Britain and Ireland are located at mid- to lower crustal depths and Banks et al. (1996) found them to correlate very well with structural features in the Iapetus suture zone that most probably contain graphite.

Chapter 3

The MT method

The MT method is used to investigate variations in electrical conductivity within the Earth, but unlike most EM methods it can be used for both high resolution shallow (uppermost few metres) and more regional crustal and mantle studies. The versatility of the method is attributed to the frequency-dependant diffusive manner in which EM energy dissipates into the Earth (Simpson and Bahr, 2005, p. 15). The instrumentation used during data acquisition varies depending on which frequencies are being acquired for investigation. The variability has led to the MT method branching out into a multitude of methods that more clearly characterizes the frequencies used, and subsequent depths of interest. The methods in order of decreasing frequency ranges are; Radio-magnetotellurics (RMT, $10 - 300$ kHz)(Turberg et al., 1994), AMT ($1-1000$ Hz)(Santos et al., 2006), BBMT ($0.001-100$ Hz) and Long-period Magnetotellurics (LMT, $0.00001 - 1$ Hz)(Unsworth et al., 2005). However, all of these are one-and-the-same, with the exception of RMT that sometimes considers electrical permittivity.

MT in general is a passive geophysical method, using natural variations in the Earth's magnetic field as a source. However, in cases where the natural signal is weak and/or a strong noise component is present, most often at AMT frequencies (Goldstein and Strangway, 1975), an artificial source is used.

3.1 Assumptions of the MT method

To reduce the complex process of EM induction within the Earth to a problem that is mathematically definable and thus enabling information to be

gathered about the Earth through analytical scrutiny of EM data, a few simplifying assumptions have to be made. The eight assumptions of the MT method are listed below and are elaborated on in the following sections (Simpson and Bahr, 2005, p. 16):

1. Maxwell's electromagnetic equations are obeyed.
2. Electromagnetic energy originates from outside the Earth only and propagates within it diffusively.
3. All electromagnetic fields may be treated as conservative and analytic away from their sources.
4. The MT source field is approximated as a uniform plane-polarized EM wave that approaches the Earth's surface at near vertical angles. In polar and equatorial regions this assumption may be violated, however, by considering a simplified Earth model, useful interpretations can still be made.
5. Due to the near-vertical propagation of the source field no accumulation of charge is expected to be present along conductivity discontinuities in a layered Earth. In a multi-dimensional Earth, charges can accumulate along discontinuities or along gradients in conductivity.
6. The Earth behaves as an ohmic conductor, that is $\vec{J} = \sigma\vec{E}$, and charge is conserved.
7. The electric displacement field is quasi-static for MT (not including RMT) frequencies, therefore, displacement currents are considered negligible compared to conduction currents.
8. Any variations in the electrical permittivities and magnetic permeabilities of rocks are assumed negligible compared to bulk rock conductivities that vary by orders of magnitude.

3.2 Electromagnetic induction within the Earth

3.2.1 Maxwell's equations and the quasi-static assumption

Maxwell's equations are a set of fundamental laws on which all advances in EM theory, including the theoretical basis of MT, are built. The four equations known as Maxwell's equations, in differential form and in time domain, are (Griffiths, 1999, p. 330):

$$\text{Gauss' law for electricity:} \quad \nabla \cdot \vec{D} = \rho_f, \tag{3.1}$$

$$\text{Gauss' law for magnetism:} \quad \nabla \cdot \vec{B} = 0, \tag{3.2}$$

$$\text{Faraday's law:} \quad \nabla \times \vec{E} = -\frac{\partial \vec{B}}{\partial t}, \tag{3.3}$$

$$\text{Ampere-Maxwell's law:} \quad \nabla \times \vec{H} = \vec{J}_f + \frac{\partial \vec{D}}{\partial t}, \tag{3.4}$$

where ρ_f, $\vec{D}$ and $\vec{E}$ are defined as the free charge per unit volume, the electrical displacement and electric field, respectively, and $\vec{J}_f$, $\vec{B}$ and $\vec{H}$ are called the conduction current, magnetic field strength and magnetic intensity, respectively. Gauss' law for electricity (3.1) states that a collection of static non-zero electrical charge will always have an associated divergent electric field (Griffiths, 1999, p. 69). Gauss' law for magnetism (3.2) in turn indicates that any resultant magnetic field is always non-divergent (Griffiths, 1999, p. 232), a fact attributed to the non-existence of magnetic point sources (no magnetic analog to electric charge).

The final two Maxwell equations, Faraday's law (3.3) and Ampere-Maxwell's law (3.4), are the ones central to the process of induction. Faraday's law states that a time-varying magnetic field will induce an electric field (Griffiths, 1999, p. 302). Ampere-Maxwell's law explains how a magnetic field is created by an existing electric field. It shows the contribution of freely moving (conduction current, $\vec{J}_f$) and bounded (displacement current, $\frac{\partial \vec{D}}{\partial t}$) charges, in the presence of an electric field, to the created magnetic field. The constitutive equations that relate the two terms to the applied electric field are, $\vec{J}_f = \sigma \vec{E}$ and $\vec{D} = \epsilon \vec{E}$ (Keller, 1988, p. 14), and substituting into

(3.4) together with $\vec{B} = \mu\vec{H}$ gives (Keller, 1988, p. 15):

$$\nabla \times \vec{B} = \mu\sigma\vec{E} + \mu\epsilon\frac{\partial\vec{E}}{\partial t}, \tag{3.5}$$

where σ, ϵ and μ characterize the electrical conductivity, permittivity and magnetic permeability of the material. Because of the similarity of terms in both Faraday's law (3.3) and (3.5), an explicit relationship can be found between the fields $\vec{E}$ and $\vec{B}$ and the parameters σ, ϵ and μ.

Assumption 4 (see page 30) states that the EM source field for MT can be considered planar. Therefore, the EM energy travels in a single direction z, positive downwards, varying sinusoidally in time and space and vectors $\vec{E}$ and $\vec{B}$ lie in the xy-plane (Simpson and Bahr, 2005, p. 17):

$$\vec{E} = \vec{E_0}e^{i\omega t - kz}, \tag{3.6}$$

$$\vec{B} = \vec{B_0}e^{i\omega t - kz}. \tag{3.7}$$

Equations (3.3) and (3.5) can now be written in the frequency domain as:

$$\nabla \times \vec{E} = -i\omega\vec{B}, \tag{3.8}$$

$$\nabla \times \vec{B} = \mu\sigma\vec{E} + i\omega\mu\epsilon\vec{E}. \tag{3.9}$$

The quasi-static approximation (assumption 7, page 30) indicates that, for frequencies utilized in the MT method (except for RMT), within the Earth time-varying conduction currents are much larger than time-varying displacement currents (Price, 1973). In terms of equation (3.9) it means that conductivity is much larger than the product of angular frequency and permittivity ($\sigma \gg \omega\epsilon$).

Justification of the quasi-static assumption can be demonstrated by means of a simple calculation. Considering the dielectric constants (ϵ_r, where $\epsilon = \epsilon_r\epsilon_0$, ϵ_0 is the permittivity of free space and equal to 8.85×10^{-12} F.m^{-1}) of minerals and rocks listed in Table 3.1, a relatively high dielectric constant is approximately 50. Using a frequency of 10 000 Hz (the highest frequency in

Table 3.1: *Dielectric constants and relative magnetic permeabilities of common rocks and minerals. Dielectric constants measured at 100 kHz and higher (modified from Telford et al., 1990, pp. 454-7).*

Dielectric constant (ϵ_r)		**Relative permeability (μ_r)**	
Norite	61	Magnetite	5
Granite	4.8 to 18.9	Pyrrhotite	2.55
Diorite	6	Ilmenite	1.55
Sandstone	4.7(dry) to 12(moist)	Hematite	1.05
Clays	7(dry) to 43(moist)	Calcite	0.99
Water(20℃)	80.36	Quartz	0.99

the current study) the product $\omega\epsilon$ is:

$$\begin{aligned}\omega\epsilon &= (2\pi f)(\epsilon_r\epsilon_0)\\ &= (2\pi \cdot 10\,000\,\text{Hz})(50 \cdot \epsilon_0)\\ &= 2.78 \times 10^{-5}\,\text{S.m}^{-1}.\end{aligned}$$

Therefore, for displacement currents to be comparable to conduction currents the conductivity of the very uppermost subsurface (see "skin depth", page 37) must be of the order of $10^{-4} - 10^{-5}$ S.m^{-1}. Very low conductivities of the order of $10^{-4} - 10^{-5}$ S.m^{-1} exist in the Earth, at mid-crustal depths (see Section 2.2) and Archaean cratonic regions (Jones et al., 2003), but are less common globally, especially at the uppermost surface. Thus, the quasi-static assumption is justified and the displacement term in equation (3.9) (second term on right-hand side) can be neglected. As the frequency of investigation is lowered, the assumption becomes even more valid.

In MT the magnetic permeability of rocks (μ) is taken as the value of free space (μ_0), where $\mu = \mu_r\mu_0$ and μ_r is the relative magnetic permeability of the material, because of its low variability when compared to conductivity variations (assumption 8, page 30). Table 3.1 shows relative permeability values (μ_r) of some minerals and it is clear that only for the most magnetic minerals the relative permeability is much greater than 1 (the difference between the magnetotelluric responses of a non-magnetic and magnetic conductive material increases as μ_r increases, Kao and Orr, 1982). Thus in equation (3.9) μ is now replaced by μ_0 and takes the form:

$$\nabla \times \vec{B} = \mu_0\sigma\vec{E}. \tag{3.10}$$

3.2.2 Diffusive EM energy propagation

With Maxwell's equations in the appropriate form for MT exploration, an attempt can be made at describing the interactions of EM fields with the conductive Earth. Firstly, we consider the source, above the Earth's surface, to be a time-varying magnetic field which in turn induces an electric field according to Faraday's law (3.1). While propagating in the space between the source and the surface, where $\sigma_{air} \to 0$ (Vozoff, 1991, p. 643), Ampere's law in the form of equation (3.10) is invalid; in fact it is the conduction term in equation (3.9) that becomes negligible. Therefore, similar to a vacuum (Griffiths, 1999, p. 375), the induced electric field will create a secondary magnetic field according to Ampere's law, that is in-phase with the original magnetic field. The process is explained sequentially, but in reality it is instantaneous and what is observed are $\vec{E}$ and $\vec{B}$ fields that are in phase and travelling unperturbed to the surface.

At the Earth's surface (the plane $z = 0$), and within it, the same process continues but now conduction currents rather than displacement currents dominate, and Ampere's law in the form of equation (3.10) is used. The conduction currents create a secondary magnetic field out of phase with the original magnetic field, and thus disturb the EM fields of the source (Schmucker and Weidelt, 1975). Because of the cycle of induction and subsequent disturbance of the original fields (Figure 3.1), the EM wave will decay into the Earth with $\vec{E}$ and $\vec{B}$ out of phase. The manner in which the $\vec{E}$ and $\vec{B}$ fields decay and their phase difference depends on the complexity of the conductive Earth (Weidelt, 1975).

It can be shown mathematically, that the behaviour of low frequency (that is, no displacement currents) EM fields within a uniform Earth is best described by the diffusion equation (a second-order partial differential equation)(Simpson and Bahr, 2005, p. 20). Firstly, apart from obeying Maxwell's equations the EM fields must also obey appropriate conditions applicable at the boundaries between homogeneous conductivity regions. The five bound-

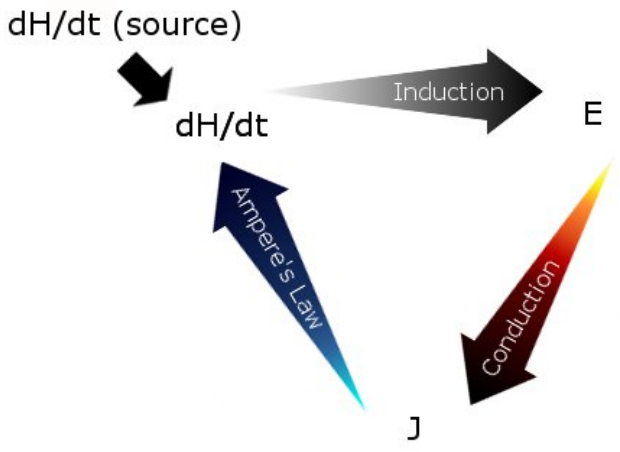


Figure 3.1: *EM induction cycle within the Earth (after Schmucker and Weidelt, 1975).*

ary conditions are (Ward and Hohmann, 1988, pp. 148-9):

$$\vec{B}_{n1} = \vec{B}_{n2}, \tag{3.11}$$

$$\vec{D}_{n2} - \vec{D}_{n1} = \sigma_f, \tag{3.12}$$

$$\vec{J}_{n1} = \vec{J}_{n2}, \tag{3.13}$$

$$\vec{H}_{t1} = \vec{H}_{t2}, \tag{3.14}$$

$$\vec{E}_{t1} = \vec{E}_{t2}. \tag{3.15}$$

The subscripts n and t refer to the normal and tangential directions relative to the boundary, respectively, σ_f is the free charge per unit area and the other symbols have their usual meaning. The numbers 1 and 2 refer to the two regions of homogeneous conductivity on either side of the boundary. The boundary conditions state that all the normal and tangential fields are continuous across the boundary, except the normal $\vec{D}$ field (equation 3.12). As ϵ on both sides of the boundary are equal (assumption 8, page 30), it can be deducted from equation (3.12) that the two normal electric fields are also discontinuous. The discontinuity is balanced by a charge build-up σ_f on the boundary surface (Price, 1973). Consequently, in a uniform and layered Earth with the source field vectors $\vec{E}$ and $\vec{B}$ both in the xy-plane, there can be no charge build-up on the horizontal boundaries (assumption 5, page 30).

The diffusion equation in terms of either $\vec{E}$ or $\vec{B}$ can now be derived by taking the curl of equations (3.8) or (3.10) and making use of the identity

(Griffiths, 1999):

$$\nabla \times (\nabla \times \vec{A}) = \nabla(\nabla \cdot \vec{A}) - \nabla^2 \vec{A}. \tag{3.16}$$

Taking the curl of equation (3.8) while utilizing the conclusion of zero charge build-up in a uniform and layered Earth (Simpson and Bahr, 2005, p. 20), therefore $\nabla \cdot \vec{E} = 0$, and substituting in equation (3.10) we find (Patra and Mallick, 1980, p. 232):

$$\begin{aligned} \nabla \times (\nabla \times \vec{E}) &= \nabla \times (-i\omega \vec{B}) \\ \nabla(\nabla \cdot \vec{E}) - \nabla^2 \vec{E} &= \nabla \times (-i\omega \vec{B}) \\ -\nabla^2 \vec{E} &= \nabla \times (-i\omega \vec{B}) \\ \nabla^2 \vec{E} &= i\omega\mu_0\sigma\vec{E}. \end{aligned} \tag{3.17}$$

Similarly, by taking the curl of equation (3.10) and using Gauss' law for magnetism (3.2), the same expression is obtained in terms of $\vec{B}$, namely:

$$\nabla^2 \vec{B} = i\omega\mu_0\sigma\vec{B}. \tag{3.18}$$

The following is a solution to the diffusion equation for $\vec{E}$ (equation 3.17)(Simpson and Bahr, 2005, p. 21):

$$\vec{E} = \vec{E}_1 e^{i\omega t - kz} + \vec{E}_2 e^{i\omega t + kz}, \tag{3.19}$$

where $\vec{E}_1 e^{i\omega t - kz}$ and $\vec{E}_2 e^{i\omega t + kz}$ represent parts of the total electric field that decrease $(-kz)$ and increase $(+kz)$ with increasing depth, respectively. In a uniform half-space Earth there are no horizontal layers that reflect EM energy (Patra and Mallick, 1980, p. 233) or any sources of EM energy (assumption 2, page 30), therefore $\vec{E}_2 = 0$ and equation (3.19) becomes:

$$\vec{E} = \vec{E}_1 e^{i\omega t - kz}. \tag{3.20}$$

As all points on an infinite source plane orientated perpendicular to the propagation direction have the same $\vec{E}$ value (also holds for $\vec{B}$)(Griffiths, 1999, p. 375) and the Earth is uniform, $\frac{\partial \vec{E}}{\partial x} = \frac{\partial \vec{E}}{\partial y} = 0$. Differentiating $\vec{E}$ twice with respect to z only, we obtain:

$$\frac{\partial^2 \vec{E}}{\partial z^2} = k^2 \vec{E} = i\omega\mu_0\sigma\vec{E}. \tag{3.21}$$

The propagation constant k can be split into real and imaginary parts, and

the inverse of the real part is termed the EM skin depth (Simpson and Bahr, 2005, p. 22):

$$k = \sqrt{\omega\mu_0\sigma/2} + i\sqrt{\omega\mu_0\sigma/2}, \tag{3.22}$$

$$\text{skin depth} = \sqrt{2/\omega\mu_0\sigma}. \tag{3.23}$$

The skin depth is the depth at which the amplitude of the EM field decreases to $1/e$ of its surface value. It is therefore an indication of the depth to which the EM field is sensitive. Equation (3.23) shows that the skin depth increases if either the conductivity σ of the uniform Earth and/or the frequency of investigation f are decreased (resistivity ρ and period T increased). The process of diffusion also ensures that EM field sensitivity increases in all lateral directions away from the observation point for the same decreased frequency and/or conductivity (Schmucker, 1973).

The skin depth effect and lateral sensitivities have important implications for how the Earth is interpreted from an observation point. Although the Earth is certainly a 3D conductive body (see Chapter 2), from a point, depending on the distance to the first boundary, the subsurface could be interpreted as uniform at sufficiently high frequency and higher dimensional at a lower frequency. The skin depth (equation 3.23) is accurate for uniform conductivity, but is only an approximate indication of depth and lateral sensitivities in a higher dimensional conductivity region (Spies, 1989), because here the electric and magnetic fields decay differently (Berdichevsky and Dmitriev, 2002, p. 80 and Jones, 2006).

3.2.3 The MT impedance tensor

In MT, information regarding the conductivity of the Earth is obtained by relating the electric and magnetic fields measured on the surface to each other. Mathematically, the terms that relate the horizontal components of the magnetic to electric field are the impedances Z_{ij} (Vozoff, 1991, p. 658):

$$E_x = Z_{xy}H_y + Z_{xx}H_x, \tag{3.24}$$

$$E_y = Z_{yx}H_x + Z_{yy}H_y, \tag{3.25}$$

where $\vec{H} = \vec{B}/\mu_0$, in units of Ω. In general the impedance is written in tensor form and has a value at each measured frequency (Berdichevsky, 1999):

$$\begin{pmatrix} E_x(\omega) \\ E_y(\omega) \end{pmatrix} = \begin{pmatrix} Z_{xx}(\omega) & Z_{xy}(\omega) \\ Z_{yx}(\omega) & Z_{yy}(\omega) \end{pmatrix} \begin{pmatrix} H_x(\omega) \\ H_y(\omega) \end{pmatrix}. \tag{3.26}$$

The impedance tensor has characteristic entries depending on the dimensionality of the region of interest.

3.2.3.1 The uniform and one-dimensional (1D) impedance tensor

If the conductive subsurface is uniform the only non-zero terms in Faraday's law (3.8) are $\frac{\partial E_x}{\partial z}$ and $\frac{\partial E_y}{\partial z}$ then differentiating equation (3.20) with respect to z once yields (Patra and Mallick, 1980, p. 233):

$$\frac{\partial E_x}{\partial z} = -i\omega\mu_0 H_y = -kE_x, \tag{3.27}$$

$$\frac{\partial E_y}{\partial z} = i\omega\mu_0 H_x = -kE_y. \tag{3.28}$$

For a 1D Earth, there is no coherence between electric and magnetic fields in the same direction ($Z_{xx} = Z_{yy} = 0$), hence the only non-zero elements of the characteristic impedance tensor of a uniform region ($\boldsymbol{Z_{uni}}$) are $Z_{xy} = E_x/H_y$ and $Z_{yx} = E_y/H_x$, consequently:

$$\boldsymbol{Z_{uni}} = \begin{pmatrix} 0 & i\omega\mu_0/k \\ -i\omega\mu_0/k & 0 \end{pmatrix}. \tag{3.29}$$

If the regional conductivity varies only in the z-direction (in either a continuous or discontinuous manner, 1D Earth), $\frac{\partial \vec{E}}{\partial x} = \frac{\partial \vec{E}}{\partial y} = 0$ still holds, and because no charge accumulates on vertical boundaries or conductivity gradients and no anomalous currents exist, there is again no coherence between fields in the same direction (Simpson and Bahr, 2005, p. 35). The only non-zero elements of a 1D impedance tensor ($\boldsymbol{Z_{1D}}$) are $Z_{xy} = E_x/H_y$ and $Z_{yx} = E_y/H_x$, and they are equal in magnitude because conductivity is uniform on any horizontal plane (Cagniard, 1953):

$$\boldsymbol{Z_{1D}} = \begin{pmatrix} 0 & Z_{xy}(\omega) \\ -Z_{xy}(\omega) & 0 \end{pmatrix}. \tag{3.30}$$

The negative sign is introduced because the cross-product of E_y and H_x points in the negative z-direction (upwards) and needs to point in the direc-

tion of the EM wave propagation (downwards into the Earth). In a layered 1D Earth, the impedance Z_{xy} has an analytical solution. As the EM energy is reflected at the boundaries between layers, every layer has a downward moving transmitted and upward moving reflected EM wave (Patra and Mallick, 1980, p. 234) that is a function of the propagation constant k_n:

$$E_{xn} = E_{1n}e^{i\omega t - k_n z} + E_{2n}e^{i\omega t + k_n z}, \tag{3.31}$$

$$H_{yn} = -\tfrac{k_n}{i\omega\mu_0}(-E_{1n}e^{i\omega t - k_n z} + E_{2n}e^{i\omega t + k_n z}). \tag{3.32}$$

By taking the ratio of equations (3.31) and (3.32) and replacing E_{1n} and E_{2n} with their appropriate values at the boundaries, with all values being dependant on the magnitude of the surface electric field, the general expression for a n-layered 1D Earth impedance is (Patra and Mallick, 1980, p. 237):

$$Z_{xy} = \frac{i\omega\mu_0}{k_1}\coth\left[k_1h_1 + \coth^{-1}\left\{\frac{k_1}{k_2}\coth\left(k_2h_2 + \coth^{-1}\left(\frac{k_2}{k_3}\ldots\right.\right.\right.\right.$$
$$\left.\left.\left.\left. + \coth^{-1}\left(\frac{k_{n-2}}{k_{n-1}}\coth\left(k_{n-1}h_{n-1} + \coth^{-1}\frac{k_{n-1}}{k_n}\right)\right)\right)\right)\right\}\right], \tag{3.33}$$

where h_n is the thickness of layer n. In view of the fact that the electric field in a uniform and 1D Earth is constant in any horizontal plane there is no induced H_z (Cagniard, 1953).

3.2.3.2 The 2D impedance tensor

If a region of conductivity is termed 2D, the conductivity, within the sensitivity region of the EM fields, varies in the z-direction and one horizontal direction, usually taken as the y-direction. An ideal 2D case (2D Earth), consisting of a vertical contact forming the plane $y = 0$ between two homogeneous conductivity regions (Figure 3.2), is used to derive the EM fields predicted by Maxwell's equations. An example of an ideal case is a simple vertical fault (d'Erceville and Kunetz, 1962) or vertical dyke (thickness of dyke is comparable to its depth, Rankin, 1962).

An evaluation of Faraday's law (3.8) and Ampere's law (3.10) shows that, for a 2D Earth, electric and magnetic fields remain mutually orthogonal. In addition, decoupling of each field component occurs in response to the 2D structure and hence two separate cases of induction exist, namely: a) an electric field component and b) a magnetic field component each polarized

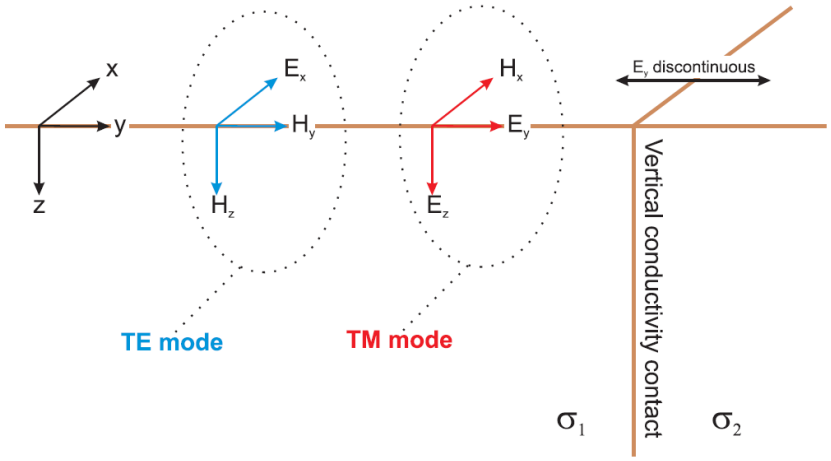


Figure 3.2: *The fault model and decoupling of the EM wave into TE and TM modes (Hamilton, 2008).*

parallel to the vertical contact (Simpson and Bahr, 2005, pp. 28-29)(Figure 3.2). The mode in which E_x is polarized, and thus the current flows, parallel to the contact is called the transverse electric (TE) mode (also called the E-parallel or E-polarization mode), and the induced fields coupled to E_x are (Jones and Price, 1970):

$$\frac{\partial E_x}{\partial y} = i\omega\mu_0 H_z, \tag{3.34}$$

$$\frac{\partial E_x}{\partial z} = -i\omega\mu_0 H_y, \tag{3.35}$$

$$\frac{\partial H_z}{\partial y} - \frac{\partial H_y}{\partial z} = \sigma E_x. \tag{3.36}$$

The mode where H_x is polarized parallel to the contact and thus current flows across it is called the transverse magnetic (TM) mode (also called the H-parallel or B-parallel or H-polarization or B-polarization or E-perpendicular mode), and the induced fields coupled to H_x are (Jones and Price, 1970):

$$\frac{\partial H_x}{\partial y} = \sigma E_z, \tag{3.37}$$

$$-\frac{\partial H_x}{\partial z} = \sigma E_y, \tag{3.38}$$

$$\frac{\partial E_z}{\partial y} - \frac{\partial E_y}{\partial z} = i\omega\mu_0 H_x. \tag{3.39}$$

The measured TE and TM modes together provide all the information needed to describe a 2D Earth. The 2D impedance tensor, when one measurement axis is parallel and the other perpendicular to strike, therefore has two non-

zero elements, namely:

$$\boldsymbol{Z_{2D}} = \begin{pmatrix} 0 & Z_{xy}(\omega) \\ Z_{yx}(\omega) & 0 \end{pmatrix} = \begin{pmatrix} 0 & Z_{TE}(\omega) \\ Z_{TM}(\omega) & 0 \end{pmatrix}. \tag{3.40}$$

The behaviour of the EM fields at and around the vertical conductivity contact is governed by the conservation of current. Boundary condition 3 (equation 3.13) states that the component of current density normal to a boundary J_n must always be continuous across it. Therefore, because just above the surface, $J_{z-} \to 0$, as $\sigma_{air} \to 0$, so also just below the surface $J_{z+} \to 0$ and thus $E_{z+} \to 0$ because the conductivity in the Earth is always greater than zero (Price, 1973). Another consequence of boundary condition 3 is that for the TM mode the current J_y must flow continuously across the boundary and because $\sigma_1 \neq \sigma_2$ (Figure 3.2) the electric field E_y has to be discontinuous across it. Therefore, by boundary condition 2 (equation 3.12), there will be a surface charge distribution on the contact plane.

3.2.3.3 The 3D impedance tensor

A region is considered 3D when the conductivity varies in all three orthogonal directions; x, y and z (3D Earth). The added dimension means that there are more conductivity boundaries and thus more charge build-up. In addition, the current flow is more anomalous and complicated than in the 1D and 2D Earth (Weidelt, 1975) and the impedance tensor elements are all non-zero:

$$\boldsymbol{Z_{3D}} = \begin{pmatrix} Z_{xx}(\omega) & Z_{xy}(\omega) \\ Z_{yx}(\omega) & Z_{yy}(\omega) \end{pmatrix}. \tag{3.41}$$

In reality, all regions explored with MT are 3D and, although some can be very closely approximated to be uniform, 1D or 2D, the recorded impedance tensor may appear 3D because of noisy measurements and also a phenomenon called distortion (see Section 3.6).

3.2.3.4 Apparent resistivity and phase

The electric impedance is a complex number and can be separated into amplitude and phase. The amplitude of an impedance tensor component (Z_{ij}) is related to apparent resistivity $\rho_{a,ij}$ by (Simpson and Bahr, 2005, p. 34):

$$\rho_{a,ij} = \frac{1}{\mu_0 \omega} |Z_{ij}(\omega)|^2 = 0.2T |Z_{ij}(\omega)|^2 \quad (\Omega.\mathrm{m}), \tag{3.42}$$

and the phase ϕ_{ij} of the impedance (not the complex resistivity) can be calculated by:

$$\phi_{ij} = \tan^{-1}\left(\frac{Im\{Z_{ij}\}}{Re\{Z_{ij}\}}\right). \tag{3.43}$$

The apparent resistivity of a region is the sum of the resistivities of all structures that the EM energy is sensitive to at a given frequency. As the frequency decreases, EM energy becomes sensitive to a greater volume, and more structures are averaged to obtain ρ_a. Therefore, as the frequency decreases the ability of MT to resolve individual structures and boundaries becomes weaker. For a uniform region the apparent resistivity is equal to the uniform resistivity.

The impedance phase is the angle that the recorded magnetic field lags behind the electric field. In a uniform region the imaginary and real parts of the impedance are equal at all frequencies, therefore the phase difference between magnetic and electric field is 45°. Physically, the 45° difference relates to the primary (source) and secondary magnetic fields being equal, independent of the uniform conductivity (also holds in 1D Earth)(Berdichevsky and Dmitriev, 2002, p. 55), and 90° out of phase. Thus, when combined, the total magnetic field is 45° out of phase with the induced electric field. In all other cases the phase difference varies between 0° ($\phi \to 0$ as $\sigma \to 0$) and 90° ($\phi \to 90$ as $\sigma \to \infty$)(Schmucker, 1985, p. 115 and Berdichevsky and Dmitriev, 2002, p. 65).

The skin depth for period T (inverse of frequency) in a 1D, 2D and 3D Earth is calculated by replacing ρ in equation (3.23) by ρ_a. Two other commonly used depth estimators, indicated by Jones (1983) to be exactly equivalent, are the Niblett transformation (Niblett and Sayn-Wittgenstein, 1960) and Bostick approximation (Bostick, 1977). The Niblett-Bostick (NB) depth estimate for an apparent resistivity value at a period T, $\rho_a(T)$, is calculated by:

$$d_{NB} = \sqrt{\frac{\rho_a(T)T}{2\pi\mu_0}} = 356\sqrt{\rho_a(T)T} \quad \text{(m)}. \tag{3.44}$$

Although the NB-depth estimate was created to calculate the maximum depth to which the EM energy is sensitive to in a 1D Earth, depths obtained using the same equation, while substituting the apparent resistivity components $\rho_{a,ij}$ for ρ_a, are used as a rough indicator of vertical and lateral

penetration in a 2D and 3D Earth.

3.2.4 The tipper

It is clear from Faraday's law (3.8) that $\vec{H}$ only has an induced vertical component when $\nabla \times \vec{E}$ has a vertical component, that is, when $\frac{\partial E_x}{\partial y} - \frac{\partial E_y}{\partial x} \neq 0$. In any scenario where there are lateral changes in conductivity, there will also be lateral changes in horizontal current flow, $\frac{\partial J_x}{\partial y}$ and $\frac{\partial J_y}{\partial x}$ (that is, $\frac{\partial E_x}{\partial y}$ and $\frac{\partial E_y}{\partial x}$), and thus $\nabla \times \vec{E}$ will have a vertical component. The measured vertical magnetic field, H_z, is normalized by the horizontal magnetic fields to obtain the tipper (modified from Berdichevsky, 1999):

$$H_z = T_{zx} H_x + T_{zy} H_y. \tag{3.45}$$

The tipper components, T_{zx} and T_{zy}, quantify the tipping of the H_x and H_y fields out of the horizontal plane and are complex since they may include phase shifts (Vozoff, 1991, p. 661). Also, although the components are dependent on the measurement axis, the magnitude and direction of the tipper are rotationally invariant functions of subsurface conductivity (Labson et al., 1985).

In regions of the Earth where the source field has no H_z, the tipper provides invaluable information about lateral conductivity changes in a 2D and 3D Earth. Even in cases where the source field has a non-zero H_z, the tipper is still useful, provided the non-uniform source is compensated for. The tipper can be used to determine which side of a contact is more conductive, and depending on the convention used, when portrayed as vectors, the real vector is calculated to either point towards (Parkinson, 1959)(used in current study) or away from (Wiese, 1962) the more conductive side. It is also used to remove the 90° ambiguity inherent to any measured 2D impedance tensor. Equations (3.34) to (3.39) show that the only 2D mode where a non-zero H_z is induced is the TE mode. Therefore in a 2D Earth, with the measurement x-axis parallel to strike, $T_{zx} = 0$ and the tipper is directed perpendicular to strike.

3.3 The MT source fields

The Earth's magnetic field consists of external and internal parts (Gauss, 1839). As pointed out, variations in the external field act as a source for MT, and are responsible for the induced currents flowing within the Earth which in turn have their own associated magnetic fields forming part of the internal field. To the MT practitioner it is of paramount importance to understand the spatial and temporal variations of the external field and to see how far it deviates from a uniform plane-wave source.

3.3.1 Causes and characteristics of the external magnetic field variations

At high frequencies ($8-100\,000$ Hz) the external field variations are generated by interactions in the Earth-ionosphere waveguide (Simpson and Bahr, 2005, p. 3), with the source of EM energy being lightning (Vozoff, 1991, p. 645). Low frequency variations (11 years to 8 Hz) are mostly owing to interactions between the solar wind from the Sun and the Earth's magnetosphere (Simpson and Bahr, 2005, p. 3). Variations in the solar wind inevitably lead to low-frequency variations in the external magnetic field. However, even if the solar wind was time-invariant, there would still be variations in the external magnetic field as a result of the Sun's and Moon's tidal effects on the magnetosphere as the Earth rotates (Merrill and McElhinny, 1983, p. 53). Regular and irregular variations in the magnetic field, the names they are given, their amplitudes and equivalent current sources in the ionosphere and magnetosphere are listed in Table 3.2.

The power spectrum of the magnetic field decreases monotonically with increasing frequency (Vozoff, 1991, p. 644) and the spectrum contains two regions of anomalous low energy, namely, the MT dead band roughly around 1 Hz (Simpson and Bahr, 2005, p. 3) and the AMT dead band at $1-5$ kHz (Garcia and Jones, 2002)(Figure 3.3). The cause of the low signal strength in the MT and AMT dead bands is a change in the EM source. The change in source for the MT dead-band is from ionospheric-induced to lightning-induced EM energy while the source across the AMT dead band changes from lightning storms originating from the cloud-to-stratosphere (up to 1 kHz) to storms originating from the stratosphere-to-ground (5 kHz and higher)(Jones, 2002b).

Table 3.2: *Classification of regular and irregular geomagnetic variations (modified from Schmucker, 1985, p. 36). t = Fundamental period for regular variations, period range for irregular variations; a = auroral zones; m = mid-latitudes; l = low latitudes; dd = dip equator on day-side.*

Type	Symbol	Period (t)	Amplitude (nT)	Source
Solar cycle variations	-	11 yrs	20	Equatorial ring current (ERC) modulation by sunspot cycle
Annual variations	-	1 year	5	Ionospheric sources
Semi-annual variations	-	6 months	5	ERC modulation within the Earth's orbit around the Sun
Smoothed storm-time variations	-	-	-	Enhanced ERC after magnetic storms
- storm-time dependant part	Dst	2-27 days	100	
- disturbance local time inequality	DS	12-24 hrs	100	
Solar daily variations	S	1 day	-	Ionospheric current loops on day-side sectors of both hemispheres
- on quiet days	Sq	1 day	30-60 (m,l); 60-120 (dd)	
- enhanced on disturbed days	SD	1 day	10-20	
Lunar daily variations	L	25 hrs[a]	1-3	Dual ionospheric current loops on both hemispheres
Polar magnetic storms and short-lived substorms	DP	10 min-2 hrs	-	Auroral Electrojet in the ionosphere with connecting field-aligned currents to plasma regions of the magnetosphere
- centre of disturbance in the night-time auroral zone	DP1	-	1000 (a); 100 (m,l)	
- correlated irregular variations in low latitudes	DP2	-	100 (a); 10 (m,l); 100 (dd)	
Substorms as observed in mid-latitudes (bays)	b	30 min-2 hrs	20-100 (a,m); 5-25 (l)	Special effect in connection to polar magnetic storms
Sudden storm commencement	ssc	2-5 min	10-100	Impact of intense solar particle stream on magnetopause
Solar flare effect	sfc	10-20 min	10	Short-lived enhancement of Sq currents in the ionosphere
Ultra low frequency (ULF) pulsations	p	0.2-600 s	-	Standing and propagating hydromagnetic waves in the magnetosphere
- regular continuous pulsations	pc	150-600 s (pc5)	100 (a); 10 (m)	
		45-150 s (pc4)	2	
		5-45 s (pc2,3)	0.5	
		0.2-5 s (pc1)	0.1	
- irregular transient pulsations	pi	1-150 s[b]	1	
Schumann resonance oscillations	-	1/7.8 s	<0.1	Cavity resonance Earth-ionosphere for EM waves
Extra low frequency emissions, including atmospherics	ELF	0.001-0.2 s	<0.1	Propagating EM waves in the Earth-ionosphere waveguide (ELF) and propagating hydromagnetic waves in the magnetosphere (VLF and ELF)
Very low frequency emissions, including whistlers	VLF	0.00001-0.001 s	-	

[a] Changed from original 1 day to 25 hrs (Merrill and McElhinny, 1983)

[b] Upper limit changed from original 100 s to 150 s (McPherron, 2005)

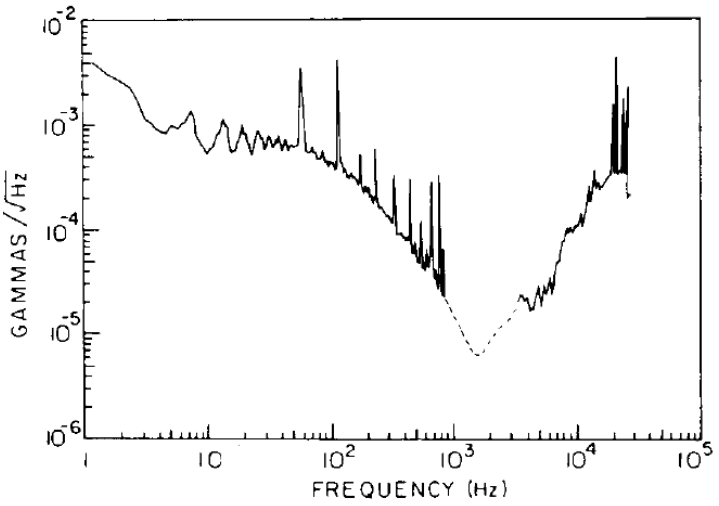


Figure 3.3: *An observed high frequency spectrum at California, 14 July 1980 (Labson et al., 1985), showing the region of low signal strength in between 1 and 5 kHz known as the AMT dead band.*

3.3.2 Effects of non-uniform sources on MT data

In most cases the plane-wave assumption is valid, because the spatial extent over which the source field can be considered uniform is much larger than the depth of interest. In some regions on Earth, for example the Auroral Electrojet (AEJ, between 58° and 75° geomagnetic latitude) and Equatorial Electrojet (EEJ, within 3° on either side of magnetic dip equator), the source field is highly variable spatially. In such cases the length scales defining the overhead source (L1), the lateral non-uniformity of the subsurface conductivity (L2) and the depth of penetration (L3) become comparable (Schmucker, 1973). The first attempt in trying to understand what affect a non-uniform source would have on MT responses was made by Price (1962), and later a correction for the source field effect was proposed by Srivastava (Srivastava, 1965). Price (1962) pointed out that a decrease in the spatial wavelength of the source is accompanied with an underestimation in apparent resistivity and an overestimation in phase, for cases where the source geometry can be adequately characterized as sinusoidal in space, and expectedly the effect becomes greater with increasing period because of the increase in L3 (Figure 3.4).

In practice, no MT source field is repetitive in the space domain, and after realizing this, a departure was made from what Price (1962) suggested and a number of different source models were proposed. A line current model

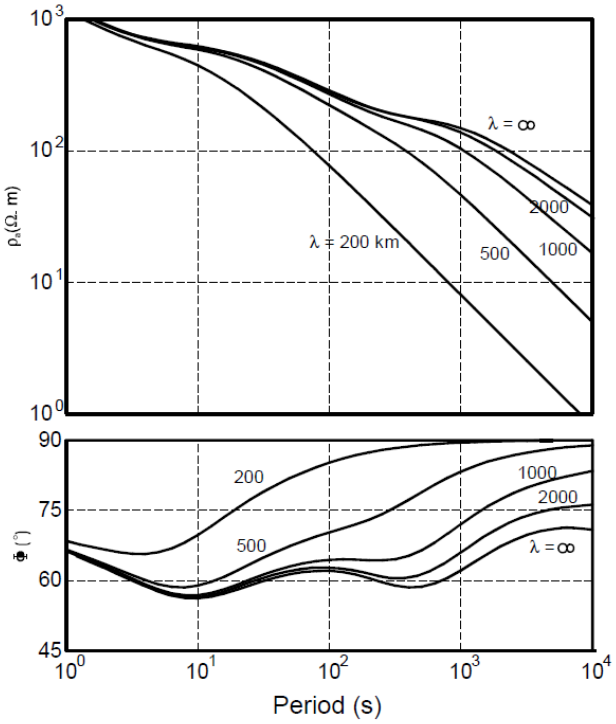


Figure 3.4: *The effect of decreasing the spatial wavelength of the overhead source from $\lambda = \infty$ (plane-wave) to $\lambda = 200$ km on 1D MT apparent resistivity and phase values (Jones and Spratt, 2002).*

(Hermance and Peltier, 1970), and later a line current model varying in intensity according to a Gaussian distribution (Peltier and Hermance, 1971), was created to describe the source field effects due to the AEJ and EEJ. The line current has infinite length and can best be used to describe the expected source field effects owing to the EEJ. The modelling results indicate that the Gaussian line current only affects the response curves at very low frequencies and the effect is greater for a more resistive subsurface (L3 is larger for a resistor than a conductor at a specific period). Hutton (1972) models the EEJ more realistically, the system has both latitudinal and longitudinal gradients, and shows that response curves are affected at BBMT frequencies and care should certainly be taken when interpreting MT results obtained in the equatorial regions (Mareschal, 1986).

Three-dimensional models created to imitate quasi-static current systems in the AEJ have also been proposed (Pirjola, 1992; Pirjola, 1998; Viljanen et al., 1999). Viljanen et al. (1999) admit that despite all the complexities taken into account in their 3D model, source field effects are still very unpredictable. Viljanen et al. (1999) state that, depending on the 3D model used,

apparent resistivities can be obtained that are larger than, smaller than, and very nearly equal to the response curves obtained when a plane wave source is considered, a result shown previously by other authors, for example, Jones (1982).

A simple proposed solution to the non-uniform source problem is to estimate intervals when the source field is most uniform and not contaminated with source field effects, rather than trying to extract useful information from field recordings that contain source effects (Jones and Spratt, 2002). Vertical magnetic fields are more sensitive to non-uniform source fields than MT responses, and this fact forms the cornerstone of the proposed method of Jones and Spratt (2002). Vertical magnetic and electric fields do not penetrate the ionosphere (Vozoff, 1991, p. 643); therefore the only vertical fields not related to induction in higher dimensional regions must be due to source field effects (observed mostly in EEJ and AEJ). Thus, by observing vertical field variations and identifying periods of large amplitude variations (uncorrelated with large horizontal field amplitudes), disregarding these contaminated periods, and processing only the unaffected data, very encouraging results can be obtained (Jones and Spratt, 2002). This method was applied in a region where the conductivity distribution is 1D (Jones and Spratt, 2002) and, to further test its robustness, it should be applied in a higher dimensional environment where a non-uniform source is present.

3.4 MT data acquisition

MT data acquisition involves the recording of time-varying magnetic and electric field components on the Earth's surface. The horizontal electric field is obtained by measuring the potential difference between two distant electrodes and dividing that difference by their separation distance. In all, a complete MT site needs five working electrodes, two pairs are used to measure the electric field in two orthogonal horizontal directions, the fifth is the ground electrode, installed close to the point where the two orthogonal electrode lines cross. The magnetic field is recorded by three magnetometers, one for each of the three orthogonal directions. The vertical magnetometer is only installed when logistically possible. The vertical electric field is not measured at the surface because it is too small (see page 41). In addition to providing the geographical location of the MT site, a Global Positioning

System (GPS) is installed to provide very accurate timing for the recorded electric and magnetic field variations. All the instruments are connected to a central recording unit which is battery powered (Figure 3.5).

In the current study, data were acquired over both the AMT and BBMT frequency ranges. The layout strategy is the same for both AMT and BBMT, the only difference being that for AMT the two electrodes in each pairs are closer spaced, and the magnetometer coils are shorter. In general, for AMT the two electrodes are 50 m apart and for BBMT 100 m, although there are no hard-and-fast rules. Before acquisition could begin the magnetometer coils, the GPS and recording unit (all from Phoenix Geophysics™) were calibrated to derive the appropriate calibrations for the frequency range of data acquisition. Some MT practitioners prefer the MT site layout to be such that one of the horizontal orthogonal directions is parallel to the locally dominant geological strike. In the current study the orthogonal directions were always chosen to align with magnetic north-south and east-west (measured with a compass)(Figure 3.5). During installation of a site all electrodes and magnetometers are placed underground to shield the instruments as much as possible from the effects of diurnal temperature variations. Lead, lead-chloride ($Pb - PbCl_2$) electrodes were used and placed within a bucket containing a mixture of salt and mud before buried in the ground (Petiau and Dupis, 1980). The salt bucket is used to decrease the contact resistance between electrode and ground.

A location for an MT site must be chosen in such a way as to avoid or minimize the effects of man-made and natural noise. Examples of man-made noise are: DC railway lines, powerlines and electric fences and examples of natural noise are wind, lightning (if within a few kilometres of the survey area), animals and people. There are filters available that remove noise from AC current sources, but great care must be taken in avoiding all forms of DC noise because it contaminates all frequencies and is extremely difficult, and sometimes impossible, to remove. The recording unit, GPS and all wires must remain hidden from sight as best possible as to avoid attracting attention from curious animals and people. Apart from covering the wires to avoid man-made noise they must also be covered to guard against the effects of wind noise. Wires being displaced by wind through the Earth's magnetic field will create an additional electric field that contaminates recorded data

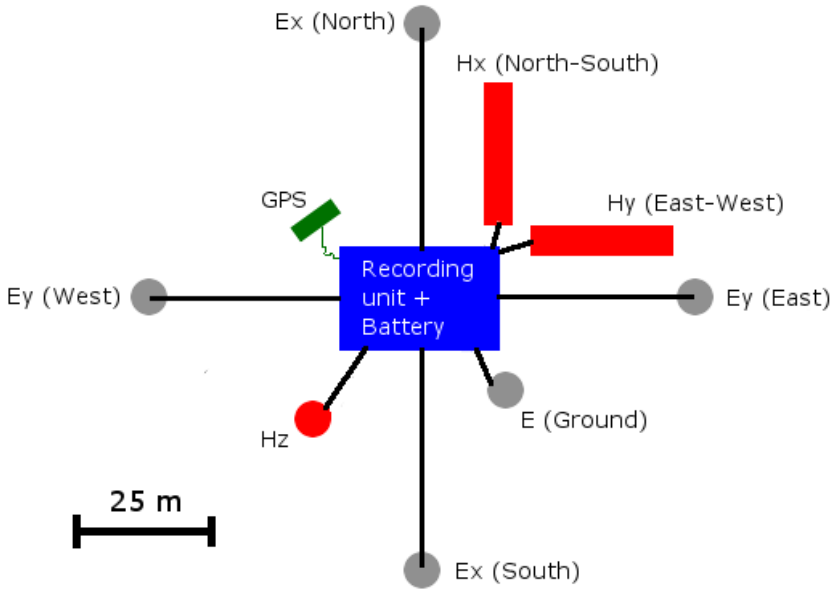


Figure 3.5: *A '+'-shaped BBMT site layout with magnetometers (H) and electrode lines (E) aligned with magnetic north-south and east-west.*

(Vozoff, 1991, p. 669). All wires must also be as straight as possible, because loops and curves in the wires will lead to inductive coupling (Swift, 1967).

A few MT sites are normally installed concurrently in both AMT (in array fashion) and BBMT (along a profile), so that there is considerable overlap in the recorded time windows to allow for remote referencing. An AMT site is left to record data for only a few hours while a BBMT site will record data for $2-3$ days. Some of the AMT sites in the current study had co-located BBMT sites, and in such cases the BBMT recordings only took half a day.

The researcher was one of four field participants taking part in all of Phase 4 of SAMTEX. Phase 4 started in February 2008 and ended in June of the same year and MT stations were installed in Namibia, Botswana and South Africa. In total 22 AMT, 140 BBMT and 29 LMT sites were installed during this period. The four participants were accompanied in the field by various other participants that aided in the acquisition of field data.

3.5 MT data processing

The aim of MT data processing is to obtain reliable and unbiased impedance tensor elements (apparent resistivity and phase responses) and tipper vectors from the recorded time-varying electric and magnetic field components

(Figure 3.6).

3.5.1 Data pre-conditioning

Before the data can be transferred from the time to the frequency domain it has to be pre-conditioned. Pre-conditioning includes splitting the time-series into smaller sections that are equal in size and using a windowing function (Hamming, Hanning, Parzen, etc.) on the time-sections to reduce the effect of finite observation length end trends. Several time-sections are needed to allow for statistical analysis of the data, and the size of the section depends on the frequency band being evaluated (the larger the frequency the smaller the time-section). Pre-conditioning also includes the removal of severe noise from the data, such as the spikes caused by close proximity lightning strikes.

3.5.2 Time domain to frequency domain

Transformation of the recorded time-varying fields from the time domain to the frequency domain is usually done with some form of Fast Fourier Transform (FFT) base-2 algorithm, meaning the number of data points in each time-section must be 2^N. The time-sections are evaluated using all the standard methods of spectral analysis (Bendat and Piersol, 1971) and a few new approaches are also in use, such as cascade decimation (Wight and Bostick, 1980). Recently, some authors have suggested using wavelet methods for the transformation into the frequency domain of very noisy sections of data (Garcia and Jones, 2008), but, owing to the lack of in-depth research and experience in using wavelet transforms on MT data, wavelet methods are not yet commonly used.

The choice of which frequencies to evaluate is somewhat arbitrary, but two conditions apply (Simpson and Bahr, 2005, p. 62):

- The evaluated frequencies (or periods) should be equally spaced on a logarithmic scale.
- The FFT can provide a large number of frequencies per decade (especially high frequencies) but $6 - 10$ frequencies should only be used for evaluation.

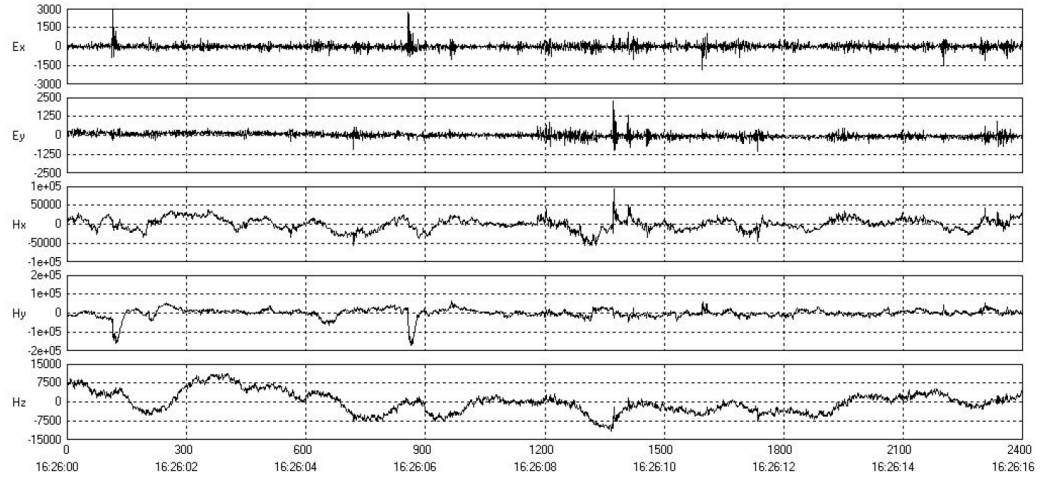


Figure 3.6: *The recorded electric and magnetic field components for BBMT site ELZ291 in northern Namibia over 16 seconds. Data are sampled at 150 samples/second and the magnetic scales are in nT and the electric scales in mV/km.*

3.5.3 Estimation of impedance tensor and tipper

The MT impedance tensor elements are typically estimated from recorded data by the use of auto-power and cross-power density spectral averages (Sims et al., 1971), where the averages can be over neighbouring frequencies, can be over different events at the same frequency, or a combination of both, which is the usual case. For example, the impedance Z_{xy} is calculated by multiplying equation (3.24) with the complex conjugates of all four of the horizontal recorded fields $(\overline{E}_x^*, \overline{E}_y^*, \overline{H}_x^*, \overline{H}_y^*)$ (frequency-dependence from here on assumed):

$$\overline{E_x E_x^*} = Z_{xx}\overline{H_x E_x^*} + Z_{xy}\overline{H_y E_x^*}, \tag{3.46}$$

$$\overline{E_x E_y^*} = Z_{xx}\overline{H_x E_y^*} + Z_{xy}\overline{H_y E_y^*}, \tag{3.47}$$

$$\overline{E_x H_x^*} = Z_{xx}\overline{H_x H_x^*} + Z_{xy}\overline{H_y H_x^*}, \tag{3.48}$$

$$\overline{E_x H_y^*} = Z_{xx}\overline{H_x H_y^*} + Z_{xy}\overline{H_y H_y^*}. \tag{3.49}$$

When considering a plane wave source, equations (3.46) to (3.49) are all independent of each other and only two are therefore needed to solve for Z_{xy}. There are six possible ways in which a pair can be formed from the four

independent equations (Sims et al., 1971);

$$\overline{Z}_{xy} = \frac{(\overline{H_x E_x^*})(\overline{E_x E_y^*}) - (\overline{H_x E_y^*})(\overline{E_x E_x^*})}{(\overline{H_x E_x^*})(\overline{H_y E_y^*}) - (\overline{H_x E_y^*})(\overline{H_y E_x^*})}, \tag{3.50}$$

$$\overline{Z}_{xy} = \frac{(\overline{H_x E_x^*})(\overline{E_x H_x^*}) - (\overline{H_x H_x^*})(\overline{E_x E_x^*})}{(\overline{H_x E_x^*})(\overline{H_y H_x^*}) - (\overline{H_x H_x^*})(\overline{H_y E_x^*})}, \tag{3.51}$$

$$\overline{Z}_{xy} = \frac{(\overline{H_x E_x^*})(\overline{E_x H_y^*}) - (\overline{H_x H_y^*})(\overline{E_x E_x^*})}{(\overline{H_x E_x^*})(\overline{H_y H_y^*}) - (\overline{H_x H_y^*})(\overline{H_y E_x^*})}, \tag{3.52}$$

$$\overline{Z}_{xy} = \frac{(\overline{H_x E_y^*})(\overline{E_x H_x^*}) - (\overline{H_x H_x^*})(\overline{E_x E_y^*})}{(\overline{H_x E_y^*})(\overline{H_y H_x^*}) - (\overline{H_x H_x^*})(\overline{H_y E_y^*})}, \tag{3.53}$$

$$\overline{Z}_{xy} = \frac{(\overline{H_x E_y^*})(\overline{E_x H_y^*}) - (\overline{H_x H_y^*})(\overline{E_x E_y^*})}{(\overline{H_x E_y^*})(\overline{H_y H_y^*}) - (\overline{H_x H_y^*})(\overline{H_y E_y^*})}, \tag{3.54}$$

$$\overline{Z}_{xy} = \frac{(\overline{H_x H_x^*})(\overline{E_x H_y^*}) - (\overline{H_x H_y^*})(\overline{E_x H_x^*})}{(\overline{H_x H_x^*})(\overline{H_y H_y^*}) - (\overline{H_x H_y^*})(\overline{H_y H_x^*})}, \tag{3.55}$$

where the overlined letters refer to the estimated spectral averaged quantities. Six equations are obtained in similar fashion for the other three impedance tensor elements. All spectral estimates contain some form of noise, be it instrumental or the effects of a non-plane-wave source. If we assume the noise to be uncorrelated with any naturally induced field and with the noise in all other recorded components, then the only terms where noise will have an effect is in the auto-power spectra of each component, as the noise correlates with itself. For example, consider the auto-power spectra of one recorded component of the electric field $\overline{E}_x$, which consists of a noise-free induced field E_x plus some noise E_{xn} (Simpson and Bahr, 2005, p. 72):

$$\begin{aligned}(\overline{E_x E_x^*}) &= \langle E_x + E_{xn} \rangle \langle E_x^* + E_{xn}^* \rangle \\ &= \langle E_x E_x^* \rangle + 2\langle E_x E_{xn} \rangle + \langle E_{xn} E_{xn}^* \rangle \\ &= \langle E_x E_x^* \rangle + \langle E_{xn} E_{xn}^* \rangle, \end{aligned} \tag{3.56}$$

given that $\langle E_x E_{xn} \rangle = 0$ for uncorrelated noise and signal. The same expression (equation 3.56) is obtained for the three other auto-powers, $\overline{E_y E_y^*}$, $\overline{H_x H_x^*}$ and $\overline{H_y H_y^*}$. Meanwhile, the cross-power spectral densities contain no noise term. To understand the effects of noise on calculated impedances, consider the simple model of a 1D Earth. Equations (3.52) and (3.53) become indeterminant for a 1D Earth with unpolarized incident fields, because the expectation values of the terms $\overline{E_x E_y^*}$, $\overline{E_x H_x^*}$, $\overline{E_y H_y^*}$ and $\overline{H_x H_y^*}$ are zero (Sims et al., 1971). Of the other four stable terms, Swift (1967) originally showed that equation (3.55) is downward biased by random noise in the magnetic field, whilst unaffected by random noise in the electric field. In the same way equation (3.54) is also downward biased by noise in H_y, and with a decou-

pled source field incident on a 1D Earth, equations (3.54) and (3.55) can be simplified to (Sims et al., 1971):

$$\overline{Z}_{xy} = \frac{\langle E_x H_y^* \rangle}{\langle H_y H_y^* \rangle + \langle H_{yn} H_{yn}^* \rangle} = Z_{xy} / \left(1 + \frac{H \text{ noise power}}{H \text{ signal power}} \right). \tag{3.57}$$

Under the same conditions the other two stable terms, equations (3.50) and (3.51), are shown to be upward biased by random noise in E_x (Sims et al., 1971):

$$\overline{Z}_{xy} = \frac{\langle E_x E_x^* \rangle + \langle E_{xn} E_{xn}^* \rangle}{\langle H_y E_x^* \rangle} = Z_{xy} \left(1 + \frac{E \text{ noise power}}{E \text{ signal power}} \right). \tag{3.58}$$

In 2D and 3D conductivity regions equations (3.50), (3.51), (3.54) and (3.55) are also the most stable, provided the source field is not highly polarized (Sims et al., 1971). In MT the recorded electric field is typically noisier than the recorded magnetic field (Figure 3.6), therefore the estimation of $\overline{Z}_{xy}$ through equation (3.55) is both the least-biased and statistically the best (Jones, 2002a). This is not true however in the AMT dead-band, $1 - 5$ kHz, where the magnetic field is noisiest and so using the electric field to derive cross-spectra will be more stable.

One method of removing the bias in MT data caused by random errors is the remote-reference method (Gamble et al., 1979; Clarke et al., 1983; Goubau et al., 1979). This method involves recording data simultaneously at two different sites and utilizing the recorded magnetic field of the remote site in computing the auto- and cross-powers of the local site, to give an unbiased estimate of equation (3.55):

$$Z_{xy} = \frac{(\overline{H_x H_{xr}^*})(\overline{E_x H_{yr}^*}) - (\overline{H_x H_{yr}^*})(\overline{E_x H_{xr}^*})}{(\overline{H_x H_{xr}^*})(\overline{H_y H_{yr}^*}) - (\overline{H_x H_{yr}^*})(\overline{H_y H_{xr}^*})}, \tag{3.59}$$

where H_{xr}^* and H_{yr}^* are the magnetic components of the remote site. The recorded electric field of a remote site can also be used in remote reference processing, but in general the magnetic field is used. The magnetic field is preferred as it is less noisy and the horizontal magnetic field is more homogeneous in a higher dimensional region and is less susceptible to being polarized (Simpson and Bahr, 2005, p. 67). The homogeneous magnetic field is ideal for remote reference processing because it means the induced magnetic fields at two remote sites are highly coherent. Successful remote processing also

requires the remote and local sites to be a distance apart (generally 20 km or more) that ensures the noise components in their respective recorded fields to be uncorrelated. Sometimes correlated noise is unavoidable, for example DC railway noise, and then remote reference processing is no better when compared to local processing (Pádua et al., 2002). Recently Pomposiello et al. (2009) proposed using an algorithm that predicts apparent resistivity from phase to extract unbiased estimates from remote referencing of two sites with correlated noise.

The processing steps applied thus far need to be repeated for all frequencies and Fourier transformed time-sections. Apart from the original weighting and stacking done to form spectral estimates, weighting and stacking can again be applied to the impedance estimates for every time-section at a specific frequency to ensure the impedance tensor elements are unbiased. There are some robust processing techniques available that compute reliable impedance tensor elements by removing outliers (Egbert and Booker, 1986; Egbert, 1997; Chave and Thomson, 2004; Jones and Jödicke, 1984). The Jones and Jödicke (1984) technique is incorporated into Phoenix Geophysics™ software and is also the technique used in the current study. Jones et al. (1989) compare some robust and non-robust techniques that were available in the 1980s and point out the importance of using robust processing and using a remote reference.

The same procedure is followed in the calculation of the tipper elements, where typically no electric field components are involved. Equation (3.45) is multiplied with the complex conjugates of the two horizontal magnetic fields $(\overline{H}_x^*, \overline{H}_y^*)$ to form the only pair of simultaneous equations used to calculate T_{xz} and T_{yz} as follows (Simpson and Bahr, 2005, p. 68):

$$T_{xz} = \frac{(\overline{H_z H_{xr}^*})(\overline{H_y H_{yr}^*}) - (\overline{H_z H_{yr}^*})(\overline{H_y H_{xr}^*})}{(\overline{H_x H_{xr}^*})(\overline{H_y H_{yr}^*}) - (\overline{H_x H_{yr}^*})(\overline{H_y H_{xr}^*})}, \tag{3.60}$$

$$T_{yz} = \frac{(\overline{H_z H_{yr}^*})(\overline{H_x H_{xr}^*}) - (\overline{H_z H_{xr}^*})(\overline{H_x H_{yr}^*})}{(\overline{H_x H_{xr}^*})(\overline{H_y H_{yr}^*}) - (\overline{H_x H_{yr}^*})(\overline{H_y H_{xr}^*})}, \tag{3.61}$$

where H_{xr}^* and H_{yr}^* are the magnetic components of the remote site. Magnetic components recorded locally can also be used in the calculation of the tipper but then the risk of obtaining biased tipper estimates is high.

3.6 Distortion

Distortion is defined (Groom and Bahr, 1992 and Utada and Munekane, 2000) as all the effects that a relatively small 3D conductive body, normally located close to the surface, has on the EM fields induced in a larger background structure. Therefore, distortion effects are a source of noise in MT data and need to be removed from the measured impedance tensor to obtain reliable and accurate estimates of the conductivity of the regional background structure. The distorting effects can be both inductive (currents form closed loops within the heterogeneity) and galvanic (charges on the surface of the heterogeneity) depending on the size of the distorting heterogeneity relative to the skin depth of EM fields in the regional background (Utada and Munekane, 2000). Galvanic distortion effects associated with changing topography are also common and manifests itself in measured apparent resistivity curves as the well known static shift phenomenon (Jiracek, 1990). In some cases distortion is so severe that phase differences between the off-diagonal pairs (when Z_{yx} is computed in the first quadrant) of greater than 90° are observed.

3.6.1 Distortion effects on the impedance tensor and tipper

Where considering a 3D distorting body within a 2D regional background, the recorded horizontal electric $\vec{E}^m$ and magnetic fields $\vec{H}^m$, and vertical magnetic field H_z^m, are all related to the regional horizontal electric field $\vec{E}^r$ by distorting terms $\boldsymbol{C}, \boldsymbol{D}$ and $\vec{Q}$ (Chave and Smith, 1994):

$$\vec{E}^m = \boldsymbol{C}\vec{E}^r, \tag{3.62}$$

$$\vec{H}^m = \vec{H}^r + \boldsymbol{D}\vec{E}^r, \tag{3.63}$$

$$H_z^m = H_z^r + \vec{Q}\vec{E}^r, \tag{3.64}$$

where $\vec{H}^r$ and H_z^r are the regional horizontal and vertical magnetic fields, respectively. Equations (3.62) to (3.64) can be combined to relate the measured impedance tensor $\boldsymbol{Z^m}$ (measurement and strike axes coincide) and tipper $\vec{T}^m$ to the regional impedance tensor $\boldsymbol{Z^r_{2D}}$ and tipper $\vec{T}^r$, respectively (Chave and Smith, 1994):

$$\boldsymbol{Z^m} = \boldsymbol{C} \cdot \boldsymbol{Z^r_{2D}} \cdot (\boldsymbol{I} + \boldsymbol{D}\boldsymbol{Z^r_{2D}})^{-1}, \tag{3.65}$$

$$(\vec{T}^m)^T = ((\vec{T}^r)^T + \vec{Q}^T \boldsymbol{Z^r_{2D}}) \cdot (\boldsymbol{I} + \boldsymbol{D}\boldsymbol{Z^r_{2D}})^{-1}, \tag{3.66}$$

where $\boldsymbol{C}$ and $\boldsymbol{D}$ are 2×2 matrices, $\boldsymbol{I}$ is the identity matrix, $\vec{Q}$ is a column vector and superscript T denotes the transpose of a matrix or vector.

If the size of the distorting body is comparable to the skin depth (or inductive scale length) in the 2D region the terms $\boldsymbol{C}, \boldsymbol{D}$ and $\vec{Q}$ are complex and frequency-dependent, because both inductive and galvanic distortion of the regional EM fields are present (Chave and Smith, 1994). If the skin depth in the 2D region is much larger than the largest dimension of the distorting body the regional EM fields are only affected by galvanic distortion and the terms $\boldsymbol{C}, \boldsymbol{D}$ and $\vec{Q}$ are real and frequency-independent (Chave and Smith, 1994).

In the case of galvanic distortion the boundary charges and anomalous electric field caused by the charges are proportional and in phase with the regional electric field (Smith, 1995). Consequently, galvanic distortion of the regional electric field persists at all frequencies (Smith, 1995)(Figure 3.7) and the recorded and regional electric fields are proportional by the constant $\boldsymbol{C}$ (equation 3.62). If the distorting body is conductive the anomalous electric field will cause currents to channel into it, and if it is resistive currents will be deflected around it (Jiracek, 1990). The anomalous current flow leads to galvanic distortion of the regional magnetic field. However, galvanic distortion of the magnetic field decreases with decreasing frequency (Figure 3.7), because the anomalous currents that are proportional to the regional electric field become negligible at low frequencies compared to the regional deeper currents induced by the regional magnetic field (equations 3.63 and 3.64)(Smith, 1997). The effects of galvanic distortion on the magnetic field will decay with frequency in accordance with the impedance tensor decay, which is approximately as $\sqrt{\omega}$ (Chave and Smith, 1994).

Due to the negligible effects of galvanic distortion on the regional magnetic field at low frequencies, and the difficulty in removing it from a measured impedance tensor, most MT practitioners only consider the regional impedance to be affected by frequency-independent galvanic distortion of the electric field. Therefore equations (3.65) and (3.66) are reduced to:

$$\boldsymbol{Z^m} = \boldsymbol{C} \cdot \boldsymbol{Z^r_{2D}}, \tag{3.67}$$

$$\vec{T}^m = \vec{T}^r. \tag{3.68}$$

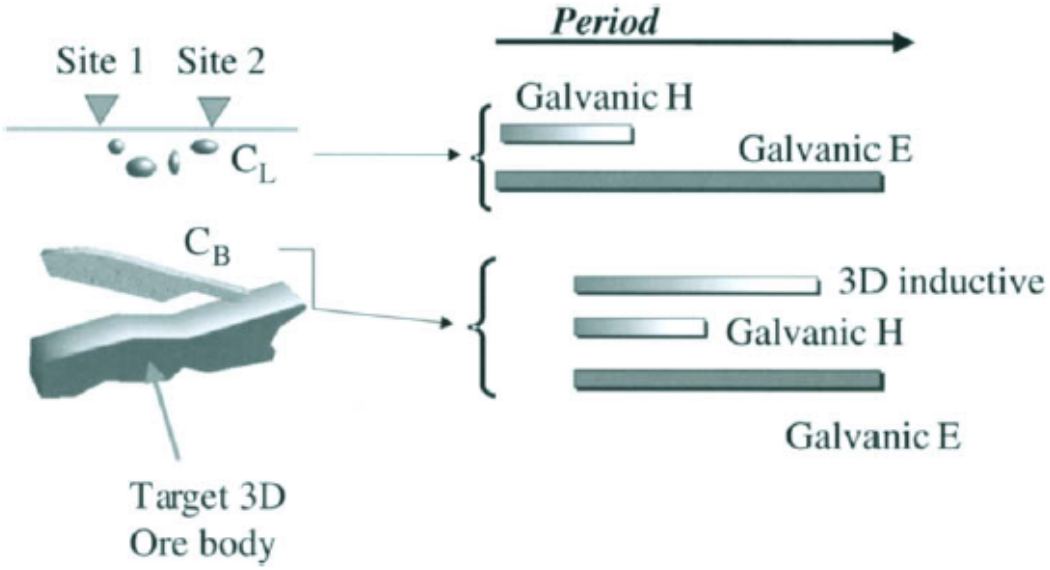


Figure 3.7: *The frequency dependence of the galvanic and inductive effects of distorting bodies C_L and C_B (Garcia and Jones, 2001).*

There have been attempts by some researchers to remove galvanic distortion of the magnetic field from synthetic and recorded data (Zhang et al., 1993; Chave and Jones, 1997; Smith, 1997). The authors stress the importance of removing it from recorded data, especially at high frequencies, in an attempt to obtain accurate impedance tensors and tippers.

3.6.2 Decomposition of the MT impedance tensor

The assumption of zero galvanic distortion of the magnetic field means the process of MT impedance tensor decomposition only involves the removal of the distorting term $\boldsymbol{C}$ from the measured impedance tensor $\boldsymbol{Z^m}$. The effect of the real frequency-independent term $\boldsymbol{C}$ on the regional impedance is two-fold. First, it causes static shifting of apparent resistivity curves, and second, it produces a measured impedance tensor with four non-zero elements that are mixtures of the two non-zero elements in the regional impedance tensor $\boldsymbol{Z^r_{2D}}$ (Groom and Bahr, 1992). Smith (1995) parameterizes the term $\boldsymbol{C}$ in such a way that it intuitively indicates its two-fold effect on a regional impedance tensor:

$$\boldsymbol{C} = \begin{pmatrix} g_x \cos(\beta_x) & -g_y \sin(\beta_y) \\ g_x \sin(\beta_x) & g_y \cos(\beta_y) \end{pmatrix}, \tag{3.69}$$

where g_x is the static shift in the x-orientated regional electric field (E_x) and β_x is the clockwise rotation angle of E_x. Similarly, g_y is the static

shift in E_y and β_y is the clockwise rotation angle of E_y. Equation (3.69) is in essence also the parameterization of $\boldsymbol{C}$ given by (Bahr, 1988). Another widely used parameterization of $\boldsymbol{C}$ is the one introduced by Groom and Bailey (1989)(GB-decomposition):

$$\boldsymbol{C_{GB}} = g\boldsymbol{T}\cdot\boldsymbol{S}\cdot\boldsymbol{A} = \frac{g}{N_1N_2N_3}\begin{bmatrix} 1 & -t \\ t & 1 \end{bmatrix}\begin{bmatrix} 1 & e \\ e & 1 \end{bmatrix}\begin{bmatrix} 1+s & 0 \\ 0 & 1-s \end{bmatrix}, \quad (3.70)$$

where g is a scaling factor, $N_1 = 1/\sqrt{1+t^2}$, $N_2 = 1/\sqrt{1+e^2}$, $N_3 = 1/\sqrt{1+s^2}$ and the matrices $\boldsymbol{T}, \boldsymbol{S}$ and $\boldsymbol{A}$ are called the twist, shear and anisotropy tensors, respectively. The scalars t, e and s vary between -1 and 1 and quantify the amount of twist, shear and anisotropy caused by the distorting body(ies). The four unknown scalars t, e, s and g, plus the four unknowns of the impedance tensor defining the regional 2D Earth (Re(Z_{xy}), Im(Z_{xy}), Re(Z_{yx}) and Im(Z_{yx})), plus the rotation angle used to transform the measured impedance tensor ($\boldsymbol{Z^m}$) to the regional 2D impedance tensor ($\boldsymbol{Z^r_{2D}}$) when measurement and strike coordinates do not coincide;

$$\boldsymbol{Z^m} = \boldsymbol{R(\theta)}\cdot\boldsymbol{C_{GB}}\cdot\boldsymbol{Z^r_{2D}}\cdot\boldsymbol{R(\theta)}^T, \quad (3.71)$$

where $\boldsymbol{R(\theta)}$ is the rotation matrix, equals nine unknowns per frequency. As there are only eight knowns, given by the four complex impedance tensor elements of the measured impedance, the problem of complete distortion decomposition is underdetermined. The strength of the GB-decomposition is that it separates the determinable and indeterminable parts of $\boldsymbol{C_{GB}}$ (Groom and Bailey, 1989). The terms g and $\boldsymbol{A}$ in equation (3.70) together form the indeterminable part and are related to an amplification or static shift in the magnitude of the impedance tensor (apparent resistivity). The static shift effect can never be mathematically removed from MT data without the use of a priori knowledge such as conductivity information of the uppermost subsurface obtained from a collocated time-domain EM survey (Sternberg et al., 1988). The distortion problem is now reduced to the determination of only seven unknowns of which the rotation angle has been shown to be least stable (Jones and Groom, 1993). In the current study an extended form of the GB-decomposition is used, as developed by McNeice and Jones (2001), that is suited for multisite, multifrequency analysis. With the extended GB-decomposition a global minimum is sought to determine the most appropriate geoelectric strike direction and twist and shear distortion parameters for a

range of frequencies and set of sites. Consequently, the ratio of unknowns to knowns is less compared to the conventional single-site single-frequency GB method and is greatly reduced when more frequencies and/or sites are added during computation.

The removal of galvanic distortion of the electric field from 3D regional data is more difficult, because from the measured eight knowns (real and imaginary components of the four measured impedances), eight unknowns (complex impedance tensor defining the regional 3D Earth, equation 3.41) plus the distortion terms need to be extracted. There have been attempts by some researchers to extract a 3D regional impedance tensor from distorted data with only limited success (Utada and Munekane, 2000; Garcia and Jones, 2001; Caldwell et al., 2004). The MT phase tensor (Caldwell et al., 2004) is a tool often used to extract phase information only of the 3D regional impedance from distorted data. The tool is successful because although the phases of the impedance tensor will be mixed by galvanic distortion it remains unaffected by static shifts. The tool is also useful in determining the dimensionality of the regional background structure in the presence of galvanic distortion of the electric field (Caldwell et al., 2004).

3.7 Inversion of MT data

The process of inversion is the opposite of forward modelling. It involves taking a set of recorded data $\vec{d}$ and obtaining a mathematical Earth model $\vec{m}$ that is related to the data by some function $G(\vec{m})$ (Aster et al., 2005):

$$\vec{d} = G(\vec{m}) + \vec{e}, \tag{3.72}$$

where $\vec{e}$ is the error vector involved in the calculation. The error $\vec{e}$ includes recording errors and also errors because of the researchers' inability to mathematically model the Earth at all levels (model errors). The aim of any inversion is to minimize the model errors as much as possible, because the recording errors cannot be minimized or removed during the inversion process. Some geophysical inverse problems are linear, in such cases equation (3.72) can be modified to (Aster et al., 2005):

$$\vec{d} = G\vec{m} + \vec{e}. \tag{3.73}$$

The diffusive manner of EM energy propagation in the Earth makes the MT inverse problem non-linear. If the conductivity of some layer in a 1D Earth model is doubled, the same doubling in the measured impedance over a certain frequency range is not observed, because although EM energy (over that specific frequency range) primarily senses the said layer it is also sensitive to the layers above and below it. To ensure that solutions can easily be found for non-linear inverse problems, and that the process is not time consuming, non-linear problems are linearized, meaning small model changes are assumed to have linear relationships to small data changes.

In addition to being non-linear, because the data consist of a finite set of imprecise observations, solutions to MT inversions are also non-unique. The non-uniqueness or instability of MT inversions increases as the number of allowed parameters (roughness) increases, while the misfit between data and model decreases. Therefore, MT inversion is always a trade-off between the smoothness or simplicity of a model and its misfit to data. In order to stabilize the inversion process and improve its uniqueness, supplementary a priori information, such as known conductivity discontinuities, is needed and also implementing the method of regularization (Berdichevsky and Dmitriev, 2002, p. 9) by applying, for example, a smoothness constraint.

3.7.1 1D Inversion

A thorough review of the 1D inverse problem is given by Parker (1983). Theoretical examination (Bailey, 1970) shows that if data recorded over a perfect 1D region at all frequencies is uncontaminated by noise, the 1D inversion result would be unique.

The first attempt at deriving from an apparent resistivity-period $\rho_a(T)$ response curve a smoothly varying resistivity - depth profile $\rho(h)$ was formulated by Niblett and Sayn-Wittgenstein (1960):

$$\rho(h) = \rho_a(T)\frac{1+m(T)}{1-m(T)}, \tag{3.74}$$

where h is the Niblett-Bostick depth (equation 3.44) and $m(T)$ is the slope

of the $\log(\rho_a)$-$\log(T)$ response curve:

$$m(T) = \frac{d[\log \rho_a(T)]}{d[\log(T)]}. \tag{3.75}$$

Since then various researchers have produced 1D inversion schemes that produce models that range from rough and well-fit to smooth and simplistic. Parker (1980) pointed out that the model with the best possible fit to noisy data from a 1D impedance is a series of conductance spikes embedded in a infinitely resistive background (D^+ model). The D^+ model was later formulated to test, in a self-consistent way, which apparent resistivity and phase estimates are outliers and need to be removed to give better inversion results (Parker and Booker, 1996). At the other extreme of 1D MT inversion schemes, least-structure (smooth) inversions provide results with larger misfits but the risk of overinterpreting results (containing extraneous structure) is reduced (Constable et al., 1987 and Smith and Booker, 1988). Occam's inversion (Constable et al., 1987) is one approach to give the smoothest possible model within a user-defined misfit, where "smoothness" must be carefully defined. Layered inversions form the set of inversion schemes in between the two extremes (Fischer et al., 1981).

3.7.2 2D Inversion

A 2D inversion is an iterative process (as are all MT inversion problems) that assigns every cell in a user-defined 2D vertical grid a uniform resistivity value. Most 2D inversion algorithms available operate on the philosophy of least structure (de Groot-Hedlin and Constable, 1990; Smith and Booker, 1991; Siripunvaraporn and Egbert, 2000; Rodi and Mackie, 2001), and involve the minimization of both a data-model misfit and model roughness. It is normally possible to minimize conductivity gradients (adjust the smoothness) in both horizontal and vertical directions (regularization). The algorithm by Rodi and Mackie (2001), incorporated into the WinGLink™ software package (Geosystems™) and also used in the current study, attempts to minimize the function $\psi(\vec{m})$, which is defined as:

$$\psi(\vec{m}) = (\vec{d} - G(\vec{m}))^T \boldsymbol{V}^{-1} (\vec{d} - G(\vec{m})) + \lambda \vec{m}^T \boldsymbol{L}^T \boldsymbol{L} \vec{m}, \tag{3.76}$$

where the first term on the right-hand side is the model misfit and the second is the regularization term. The matrix $\boldsymbol{V}$ plays the role of the variance of

the error vector $\vec{e}$ (equation 3.72), λ is the regularization parameter and the matrix $\boldsymbol{L}$ is chosen such that when the grid cells are uniform, $\boldsymbol{L}\vec{m}$ approximates the Laplacian of $\log(\rho)$ (allowing order of magnitude variations in ρ, as is realistically expected)(Rodi and Mackie, 2001).

In addition to adjusting the regularization parameters it is also possible to weight the contributions of the TE and TM modes in a 2D inversion. It is important to weight the two modes differently if necessary, because they provide different information about a 2D Earth (Swift, 1971) and are also affected differently by 3D effects (Ledo, 2006 and Wannamaker et al., 1984).

3.7.3 3D Inversion

3D inversion of MT data (Siripunvaraporn, 2010) and also joint inversion of MT data and other geophysical datasets such as seismic data (Moorkamp et al., 2007) are, at present, the most active areas of research. However, because of the limited availability of free 3D inversion codes and software and the longer computational time of 3D inversions, 2D inversion schemes still remain the more popular option amongst most in the MT community. Also, the acquisition of MT data in a manner suitable for 3D inversion (in array format) are, in most cases, logistically more difficult than acquiring data along a profile (coinciding with a road for example) that suit 2D inversion methods more. At present the only freely available 3D inversion code is the one based on the algorithm by Siripunvaraporn et al. (2005). In addition to continual development and testing of new algorithms and codes (Han et al., 2008; Avdeev and Avdeeva, 2009; Farquharson and Craven, 2009; Lin et al., 2011), recent times have seen the application of 3D inversion tools to a wide range of scientific problems, including the exploration of ore bodies (Xiao et al., 2010) and hydrocarbons (He et al., 2010), geothermal and volcano studies (Árnason et al., 2010 and Heise et al., 2010) and tectonics (Patro and Egbert, 2008).

Chapter 4

Data processing and strike analysis

Section 3.5 shows the general data processing steps that are taken to obtain interpretable impedance tensor elements from recorded MT data. In chapter four a short summary is given of the specific processing steps applied to the Otjiwarongo and Katima Mulilo data. The results from strike analysis (following procedures in Section 3.6.2) of the obtained impedance tensors are shown in Section 4.2. The purpose of strike analysis is two-fold: 1) it provides a geoelectric strike angle to which the impedance tensor is rotated with the purpose of decoupling the TE and TM modes (equation 3.40); and 2) it removes the determinable parts of galvanic distortion of the electric field from the impedance tensor (equation 3.71).

4.1 Data processing

Programs included in the Phoenix Geophysics™ software package were used for most of the data processing in the current study. Many of the steps discussed in Section 3.5 are automated in the programs used, making the processing of MT data user friendly and time saving. Because data processing was quick, most of it was completed as soon as possible after data acquisition during field work. Rapid processing and subsequent investigation of calculated response functions soon after acquisition ensured that recorded data were not taken away from the field work area whilst contaminated by a temporary noise source. If the data are contaminated by a permanent noise source or the source field strength is low for long periods, re-installation is of no use and robust processing techniques need to be attempted on the con-

taminated data.

The program SSMT2000 was used to pre-condition the time-series data (Section 3.5.1), convert it from the time domain to frequency domain and calculate impedance estimates. Impedances were estimated using the stacking cascade decimation scheme incorporated into SSMT2000, which is identical to method 4 in Jones et al. (1989). The inputs needed for the processing of a single site with SSMT2000 are the table file (containing time, date and location information as well as the lengths of the electrode lines and magnetometer coil identification numbers), the time-series files documenting electric and magnetic field variations over several frequency bands, and the calibration files of the magnetometer coils and recording unit used. In most cases recording took place at a local site with at least one remote reference site recording simultaneously. In the case of remote reference processing, the time-series, table and calibration files from both local and remote sites are needed. In all cases where data from a remote site were available the remote magnetic fields were used in the impedance estimation of the local site, and where more than one remote site recorded simultaneously, multiple impedance estimates were obtained using data from each remote site. For logistical reasons, two AMT sites in the Otjiwarongo region, ELG002A and ELG004B, had no remote site and were subsequently processed locally using their respective local magnetic fields (equation 3.55). Appendix A shows the locations of the Otjiwarongo and Katima Mulilo sites and their respective remote references used during processing.

The program MTeditor was used to evaluate the calculated impedances and response curves, select the remote-reference impedance estimate that was smoothest and contains the least amount of noise (if more than one estimate is available), and remove outliers from the set of impedance estimates (calculated from the set of time-sections) at each frequency. The primary removal of outliers is based on a jacknife approach (Jones and Jödicke, 1984) that is incorporated into MTeditor (hereinafter called automatic edit). The jacknife operation identifies impedance estimates as outliers by sequentially removing each one before calculating a variance and determining which estimate, when omitted, produces the minimum variance. This process is repeated until the variances cannot be further reduced. Automatic editing is followed by a secondary user-defined selection and removal of outliers (manual edit) at each

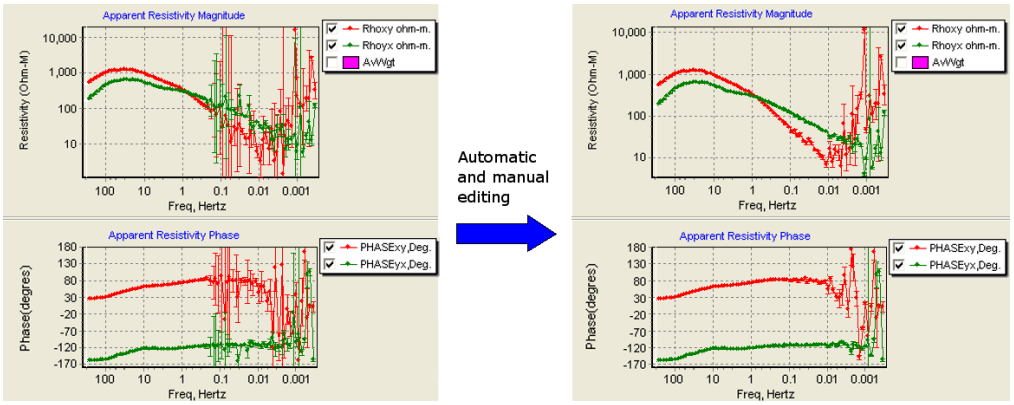


Figure 4.1: *Apparent resistivity and phase response curves calculated from the off-diagonal impedance tensor elements (xy and yx) of BBMT site ELG091A (Otjiwarongo region) before and after automatic and manual editing.*

frequency. At all sites, automatic and manual editing produced smoother, less noisy and thus more reliable response curves (Figure 4.1). The one consistent poorly estimated frequency range that could also not be improved with editing, is the AMT dead-band (Figure 4.2). At low frequencies, < 1 Hz in AMT (Figure 4.2) and $< 0.01 - 0.001$ Hz in BBMT (Figure 4.1), the removal of outliers was more difficult, because the set of impedance estimates per frequency becomes smaller as frequency is lowered.

After satisfactory response curves were obtained from all the data, the AMT responses with collocated BBMT data were merged and, together with the sites where either only AMT or BBMT data were acquired, rotated from magnetic to true north (Appendix B). The code (pers. comm. Prof. Alan G. Jones) used to merge the data, computes an average scaling factor for each of the two datasets across an overlapping frequency range where the separate response curves are approximately parallel, and subsequently combines the datasets after each has been multiplied by its computed scaling factor. The scaling factors computed in all the merging operations in the current study were approximately 1 for both the AMT and collocated BBMT datasets, as they should be. The proximity to unity was anticipated prior to merging, because during data acquisition the same electrodes, electrode layout and recording unit were used for both AMT and collocated BBMT methods. If different electrode layouts were used, it is probable that the AMT and BBMT data would be affected differently by galvanic distortion, whilst using different electrodes and recording units would lead to dissimilar amplifications of the

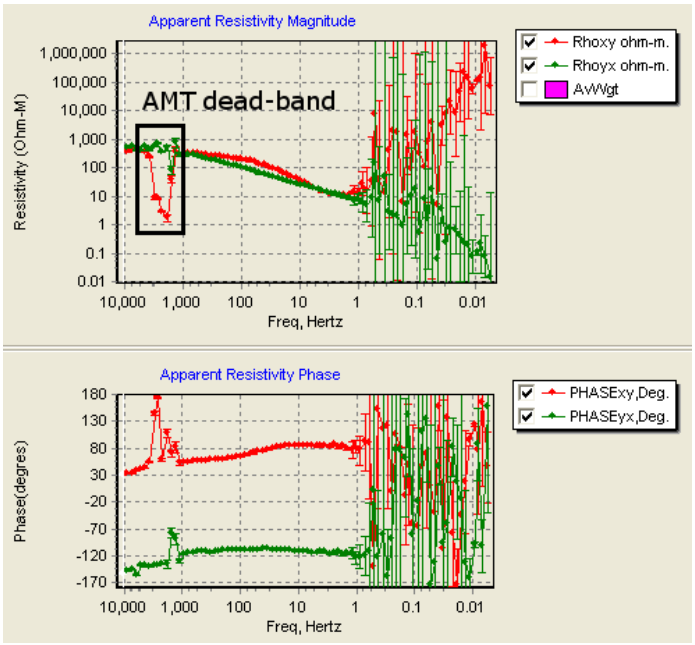


Figure 4.2: *Apparent resistivity and phase response curves calculated from the off-diagonal impedance tensor elements (xy and yx) of AMT site ELG014A (Otjiwarongo region) showing poor response estimates post-editing in the* $1 - 5$ *kHz frequency range, known as the AMT dead-band.*

datasets.

Any rotation of an estimated impedance tensor leads to mixing of the original impedance tensor elements. Editing of impedance estimates in MTeditor was completed on only the off-diagonal impedance tensor elements at each frequency and site. Therefore, any noise present only in the diagonal impedance tensor elements (xx and yy), that is not present in a time-section and related impedance estimate removed during editing of xy and yx, will, during rotation to true north and later rotation into strike coordinates, contaminate the original edited off-diagonal impedance tensor elements. Consequently, a final step of editing is completed in WinGLink™ prior to 2D inversion of the TE and TM modes (xy and yx in strike coordinates). Rotation of an impedance tensor to strike coordinates before editing is rarely applied in practice, because the angle of rotation (strike) is calculated from the unrotated tensor and for that calculation to be accurate smooth and low noise (that is, edited) response curves are needed.

4.2 Strike analysis

After rotation to true north and before inversion the data still need to be evaluated for source field effects and galvanic distortion needs to be removed. In the AMT frequency range source field effects need not be considered, because the spatial extent of the distant lightning source is much larger than the shallow depths of investigation. Similarly, in the BBMT frequency range source field effects are also negligible, because both the Otjiwarongo and Katima Mulilo array locations are at mid-latitudes, and a sufficient distance away from the EEJ and AEJ (Section 3.3.2) for the source field to be considered uniform and planar. The analysis of geoelectric strike and removal of galvanic distortion is done with a multisite, multifrequency expansion of the GB-decomposition (McNeice and Jones, 2001) and the code used for strike analysis (pers. comm. Prof. Alan G. Jones) is hereinafter referred to as 'Strike'.

4.2.1 Single site strike analysis

To obtain an understanding of the dimensionality of subsurface conductivity structure in the Otjiwarongo and Katima Mulilo regions the program Strike was used to calculate a geoelectric strike angle for each site over all available frequencies (Figures 4.3 and 4.4). Strike provides a strike angle that, together with the calculated distortion parameters (equation 3.70), form part of a GB-model that has the lowest possible misfit with the data. The GB-errors, in combination with the average phase difference between the TE and TM modes (in the calculated strike coordinate frame), provide information about the dimensionality of the subsurface and the severity of galvanic distortion.

In all instances where Strike was used an error floor of 3.5 % was assigned to the calculated impedances, which corresponds to approximately 2° in phase and 7 % in apparent resistivity. Given the assigned error floor, a GB-error of 2 or lower is defined as adequate for a calculated GB-model to describe a measured dataset. If a GB-error of greater than 2 is obtained, the GB-model is inadequate at explaining the observed data. Stated differently, a high GB-error indicates (apart from noisy data) that distortion is severe and/or the regional conductivity structure is 3D. The majority of GB-errors associated with the single site strike analysis in the Otjiwarongo region are at or below 2, therefore the assumption of a 2D regional structure for each individual site

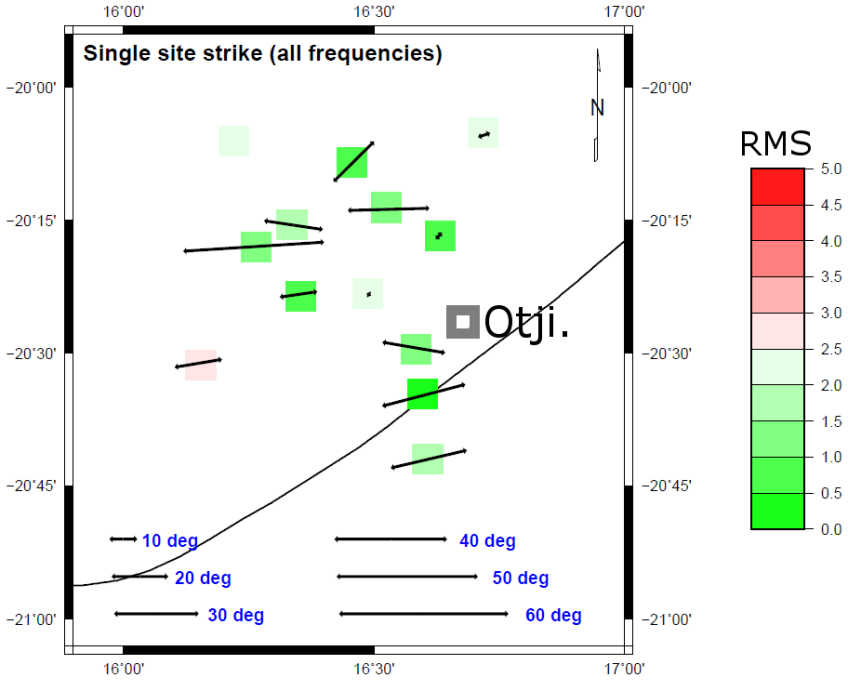


Figure 4.3: *Strike angles computed for each individual MT site in the Otjiwarongo region (Otji. = Otjiwarongo) over all the available frequencies. The colours of the boxes indicate the GB-errors (RMS - root mean square, see text) for each calculation of strike and the arrow lengths depict the phase differences between TE and TM modes at each site. The NE-trending line is a prominent intra-DMB magnetic feature and represents the dominant structural trend in the area (see Figure 1.2).*

is valid (Figure 4.3). In the Katima Mulilo region the 2D assumption is also valid as all the GB-errors associated with the single site strike analysis are below 2 (Figure 4.4).

Inherent to the MT method is a 90° ambiguity in the determination of strike. The ambiguity is overcome with the use of geological information, tipper (see Section 3.2.4) and other geophysical data, such as magnetics. In the Otjiwarongo region the calculated strike angles were rotated, if needed, by 90° to align as best possible with structural trends in geology (Figure 1.8) and regional magnetic data (Figure 4.3). Due to thick sedimentary cover in the Katima Mulilo region no structural information was available and only regional magnetic data was used to remove the ambiguity in strike determination (Figure 4.4).

If the phase difference between TE and TM modes is close to zero, and pro-

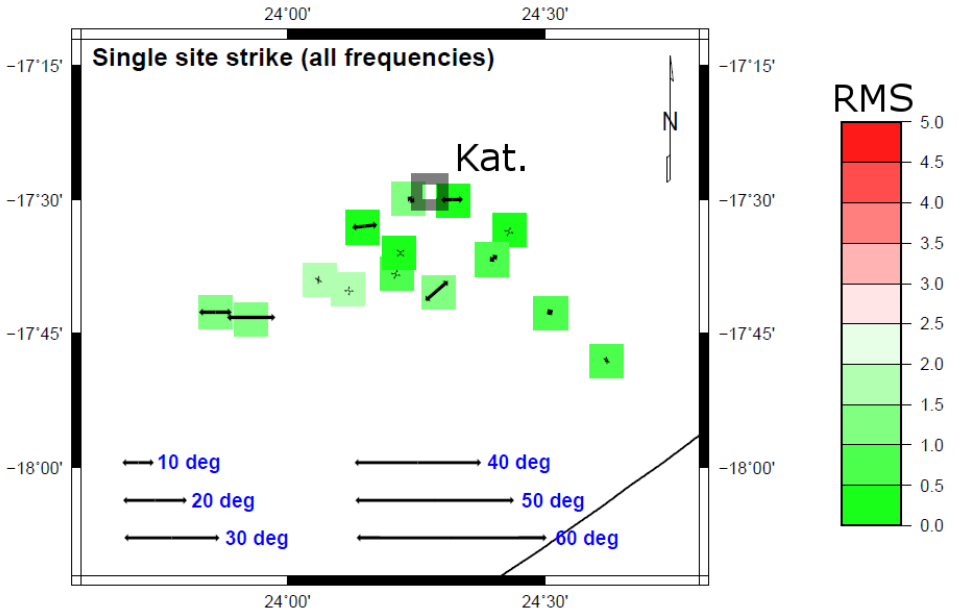


Figure 4.4: *Strike angles computed for each individual MT site in the Katima Mulilo region (Kat. = Katima Mulilo) over all the available frequencies. The colours of the boxes indicate the GB-errors (RMS - root mean square) for each calculation of strike and the arrow lengths depict the phase differences between TE and TM modes at each site. The NE-trending line is a prominent intra-DMB magnetic feature and represents the dominant structural trend in the area (see Figure 1.3).*

vided the GB-error is below the tolerance level of 2, the dimensionality of the subsurface is approximately 1D (1D off-diagonal impedance tensor elements are equal at all frequencies, equation 3.30). If the phase difference is large and the GB-error is below 2 the subsurface structure (within the frequency-dependent sensitivity region) is in part, if not totally, 2D. The phase differences combined with the errors in the Otjiwarongo region indicate that a 2D inversion of data will be appropriate (Figure 4.3). In the Katima Mulilo region the results show that a 2D inversion of data will also be appropriate and, because many sites have small phase differences, a 1D inversion can provide a good approximation of the regional conductivity structure (Figure 4.4). Before the 2D inversions may commence, a single strike angle must be obtained for each region, and each angle must have an associated GB-error that is acceptable when averaged over all sites in the region.

4.2.2 Multisite strike analysis

4.2.2.1 Otjiwarongo region

In the process of finding a single strike angle that fits the Otjiwarongo data, the data were rotated to user-defined strike directions in increments of 10°, with the aim of observing changes in GB-errors (which Strike tries to minimize during strike angle determination) with rotation. If the subsurface in the region is characterized by a dominant strike direction, the average GB-error for the Otjiwarongo data will be lowest within an angle range centred on the dominant strike direction. The interesting result was that for all rotations the GB-errors at each individual site remained approximately equal (Figure 4.5). GB-errors calculated for the rotation of site ELG005s data from 0° to 90° showed the largest variation, with a standard deviation of 0.43. At all the other sites a standard deviation of 0.26 or lower was computed. The fact that the GB-errors remain approximately constant with rotation could indicate a 1D environment, but the large phase differences suggest otherwise. Subsequently, it was concluded that the small change in errors indicate that each site contains, for most of the available frequencies, data with associated GB-errors that remain largely unchanged by rotation (approximately 1D). Therefore, although there are one or two frequency decades containing higher dimensional data, with rotation-dependent GB-errors, during rotation the GB-error at each site remains relatively unchanged, because it is averaged over the entire available frequency range.

The problem of finding a strike angle for the Otjiwarongo region is now reduced to identifying the frequencies at each site that have higher dimensional characteristics and calculating an average strike angle using only the identified higher dimensional data. In the Otjiwarongo region, data from each site were analysed decade-by-decade, by assigning strike angles from 0° to 90° to each decade independently and observing the associated change in GB-errors (Figure 4.6). Only the decades characterized by relatively large GB-error versus angle changes, where the GB-errors drops below the tolerance level of 2 within some angle range, were selected for further strike analysis (Figure 4.6). Of the 13 Otjiwarongo sites only 8 had decades that passed the criterion for higher dimensionality (Figure 4.6). Due to the consistently poor impedance estimates in the AMT dead-band, the decade 10 000 − 1000 Hz was not considered for further analysis, even if it appeared

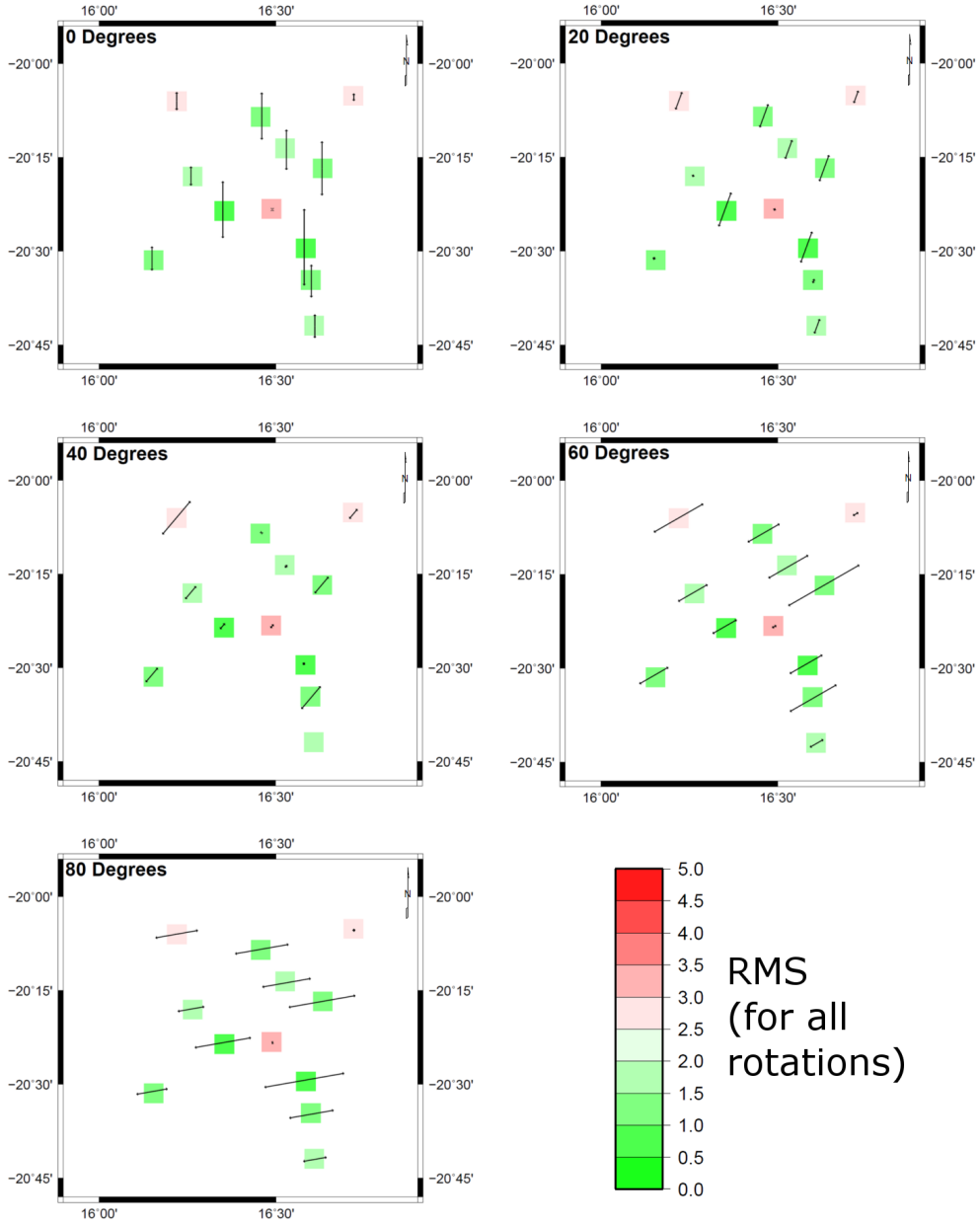


Figure 4.5: *GB-errors (RMS) and phase differences computed after assigning strike angles of 0°, 20°, 40°, 60° and 80° to data from the Otjiwarongo region.*

to have 2D characteristics. The 8 sites, their frequency decades that were determined to be higher dimensional, and the strike angles computed using Strike are listed in Table 4.1 and depicted graphically in Figure 4.7.

After examining the 8 groups of frequencies it was concluded that there is no common frequency or NB-depth range that can contain frequencies from all the groups and subsequently used in Strike, in multisite mode, to compute

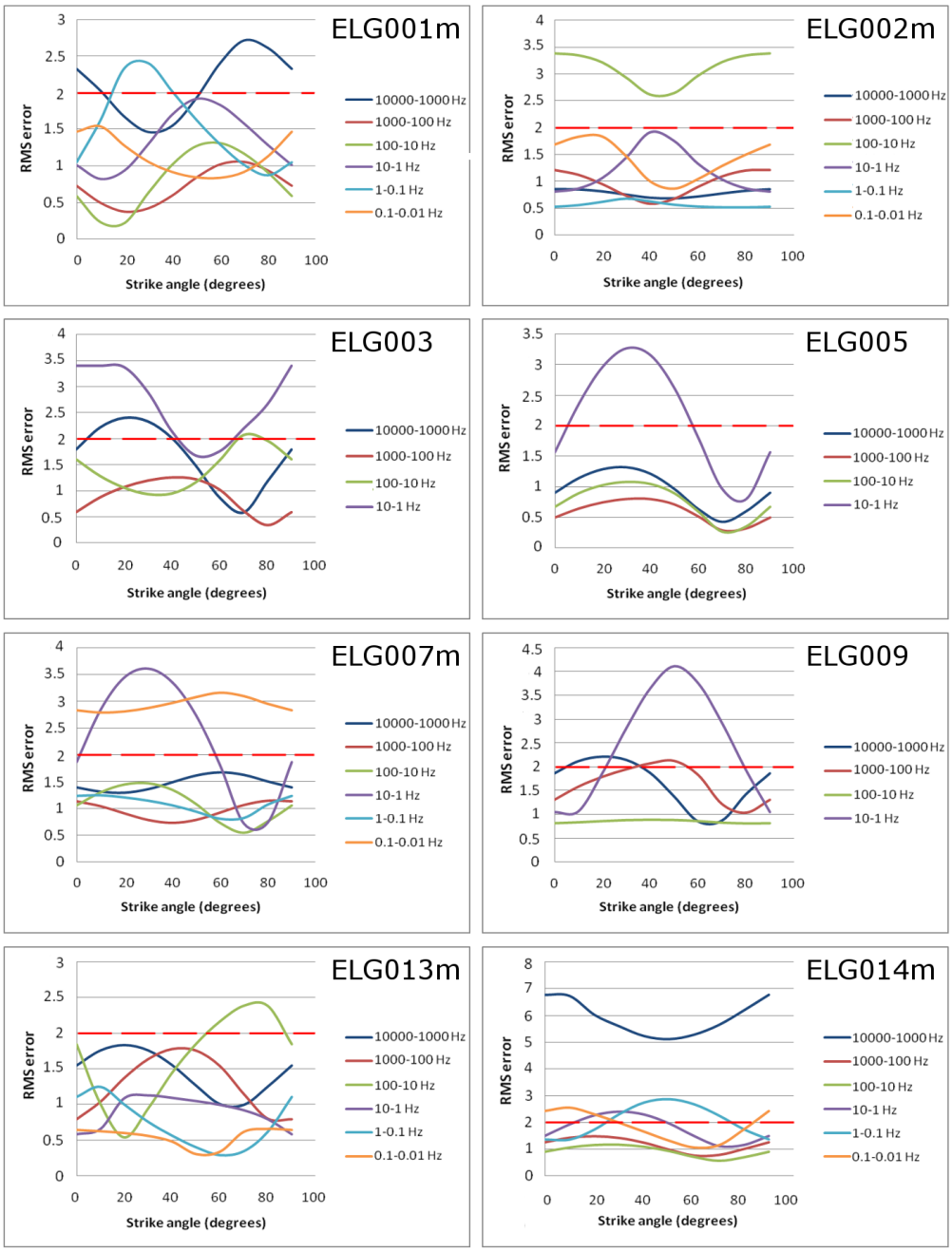


Figure 4.6: *Plots of GB-error (RMS error) versus strike angle for the available decades of 8 Otjiwarongo sites that have decades with higher dimensional characteristics. Sites where AMT and BBMT data were merged are indicated with an 'm'. Note the high GB-errors in the decade* $10\,000 - 1000$ *Hz of site ELG014m and compare with the poor apparent resistivity and phase estimates in the AMT dead-band contained in the same decade in Figure 4.2.*

a single strike angle for the 8 sites. Consequently, a single strike angle was obtained by calculating a simple arithmetic average of the 8 strike estimates. The resultant average was 82° and the corresponding average GB-error for

Table 4.1: *The 8 selected Otjiwarongo (Otji) and 7 selected Katima Mulilo (KM) sites (see text), their frequency decades determined to be higher dimensional, the strike angles computed for the identified decades and the GB-errors (RMS) associated with each computation.*

Otji sites	**Frequencies (Hz)**	**Strike (degrees)**	**GB-error**
ELG001m	$1 - 0.1$	80.02	0.89
ELG002m	$100 - 10$	43.66	2.57
ELG003	$10 - 1$	53.14	1.64
ELG005	$10 - 1$	75.77	0.71
ELG007m	$10 - 1$	73.49	0.44
ELG009	$10 - 1$	94.77	0.88
ELG013m	$100 - 10$	109.42	0.54
ELG014m	$10 - 0.1$	93.32	1.44
KM sites	**Frequencies (Hz)**	**Strike (degrees)**	**GB-error**
CPV028	$1 - 0.001$	57.51	1.92
ELZ101m	$1 - 0.1$	54.87	1.50
ELZ102m	$1 - 0.01$	48.69	2.53
ELZ201m	$1 - 0.1$	92.57	1.10
ELZ294	$0.1 - 0.01$	57.81	0.34
RAK053	$0.1 - 0.001$	51.45	1.47
RAK054	$1 - 0.01$	54.72	0.35

all 13 Otjiwarongo sites in the resultant strike direction was 1.86.

4.2.2.2 Katima Mulilo region

The single site strike analysis of the Katima Mulilo data demonstrated that there is a high degree of one-dimensionality in the region. Therefore, upon rotation of the data, the consistency in GB-errors, similar to the Otjiwarongo data, was expected. Subsequently, the same decade-for-decade analysis applied in the Otjiwarongo region was used to analyse the Katima Mulilo data to extract minor parts of higher dimensional data from the predominantly 1D data (Figure 4.8). Of the 14 Katima Mulilo sites, only 7 had decades that passed the criterion for higher dimensionality (Figure 4.8). The 7 sites, their frequency decades that were determined to be higher dimensional, and the strike angles computed using Strike, are listed in Table 4.1 and depicted graphically in Figure 4.9. After examination there was no overlapping frequency or NB-depth range found for the higher dimensional frequencies of the 7 sites, and once again an arithmetic average was calculated to obtain a representative strike angle for the Katima Mulilo region. The resultant average was 54° and the corresponding average GB-error for all 14 Katima

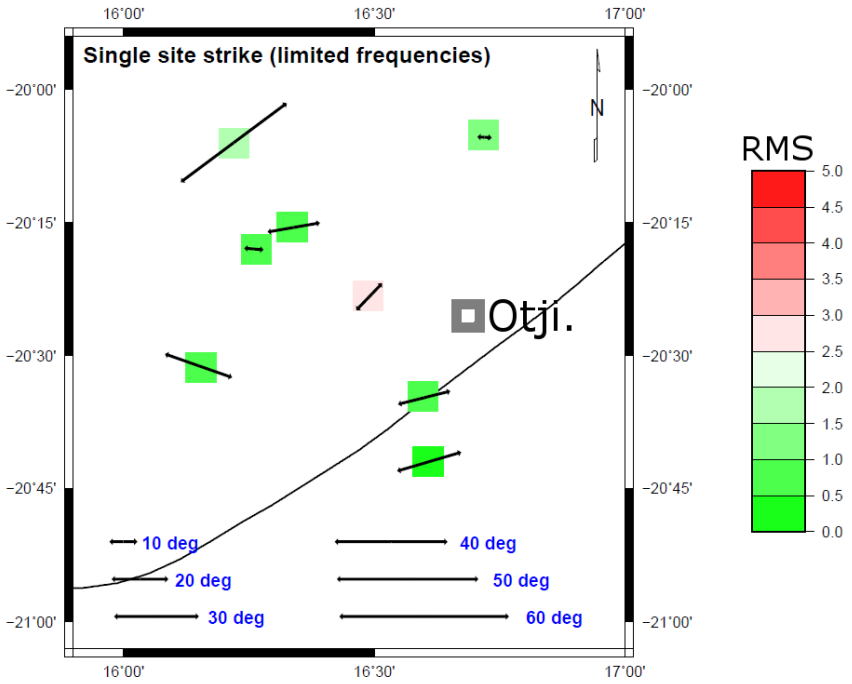


Figure 4.7: *Strike angles (arrow directions), GB-errors (RMS, box colours) and phase differences (arrow lengths) for the 8 Otjiwarongo sites, which passed the higher dimensional criterion, computed over the limited number of frequencies that have higher dimensional characteristics.*

Mulilo sites in the resultant strike direction was 1.12.

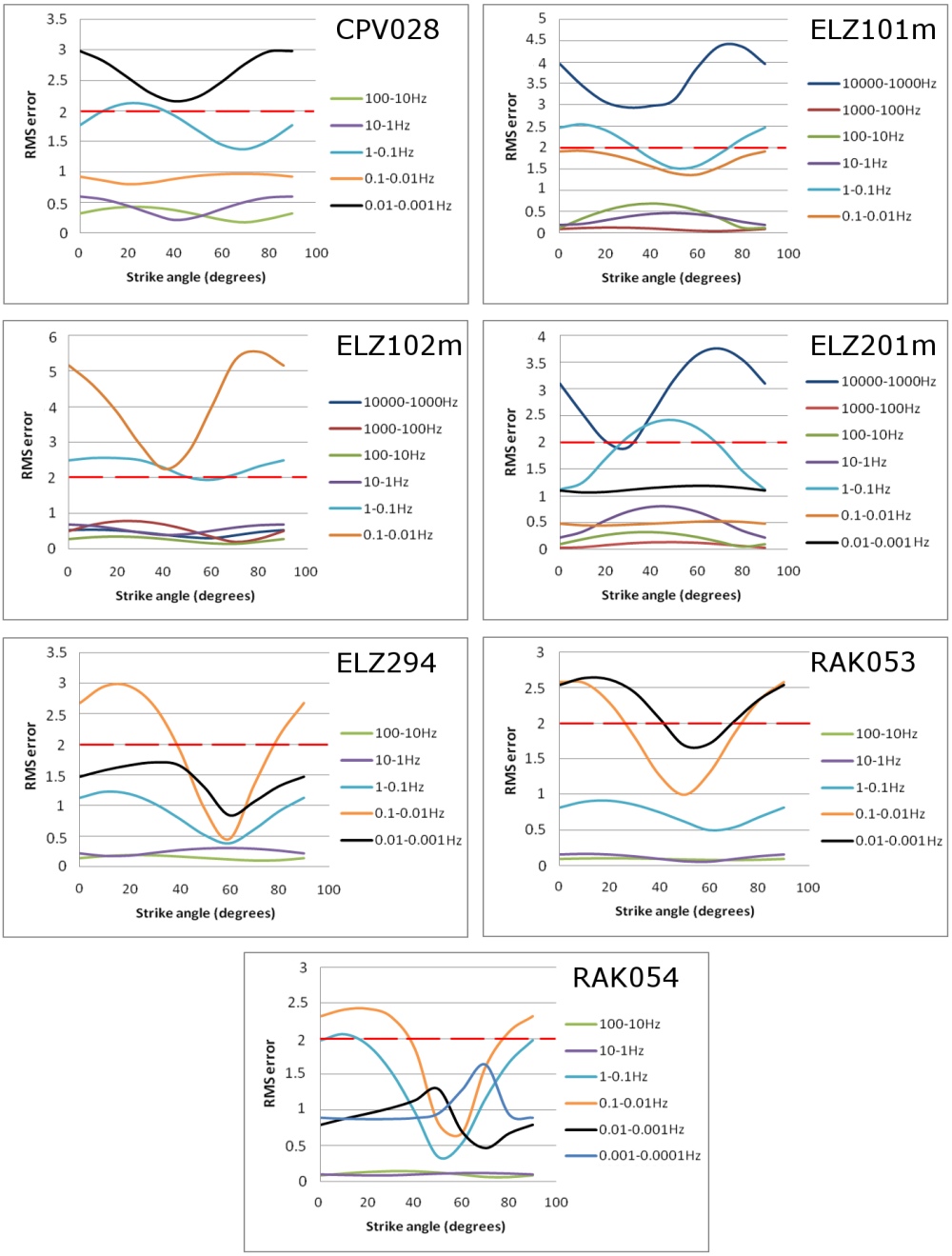


Figure 4.8: *Plots of GB-error (RMS error) versus strike angle for the 7 Katima Mulilo sites that have decades with higher dimensional characteristics. Sites where AMT and BBMT data were merged are indicated with an 'm'.*

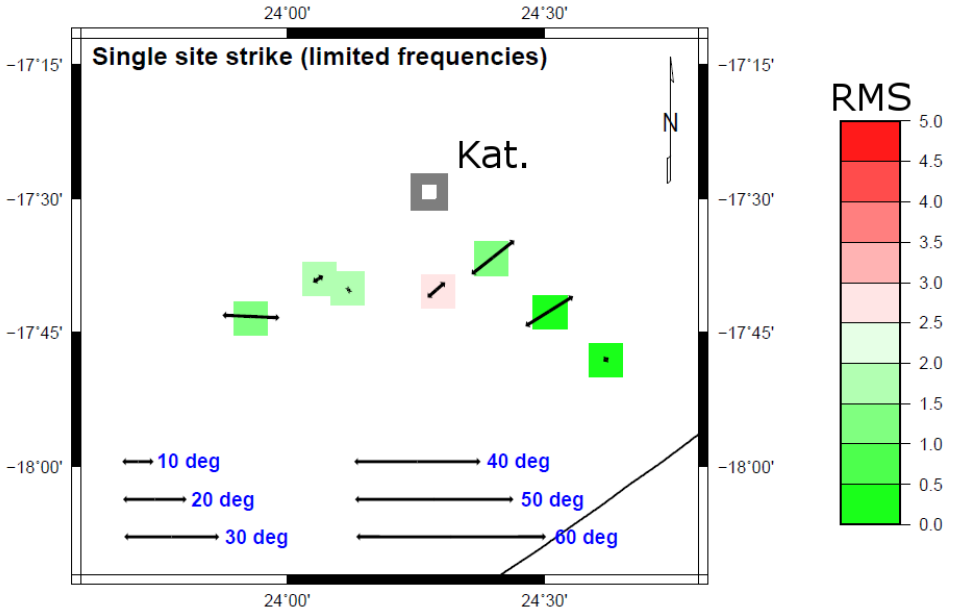


Figure 4.9: *Strike angles (arrow directions), GB-errors (RMS, box colours) and phase differences (arrow lengths) for the 7 Katima Mulilo sites, which passed the higher dimensional criterion, computed over the limited number of frequencies that have higher dimensional characteristics.*

Chapter 5

2D inversion of MT data

The determination of Otjiwarongo data in 82° and Katima Mulilo data in 54°, and simultaneous removal of galvanic distortion from each site, were iteratively repeated 101 times. The iterative process ensured that statistical analysis of data, and subsequent calculation of an error for each impedance estimate (and apparent resistivity and phase estimate), were possible. The errors, calculated in strike-coordinates, are the post-rotation counterparts of the uncertainties in the original impedance measurements.

Following error estimation, the data were imported into the program WinGLink™. In WinGLink™, after import and prior to 2D inversion, a 2D profile, which serves as the surface expression of a hypothetical plane on which a mesh for inversion is created, needed to be constructed for each region. A 2D profile is orientated 90° to strike so that when data from MT sites, situated off profile, are projected onto profile the projection is accomplished parallel to strike. If the conductivity subsurface structure beneath an arrangement of MT sites is perfectly 2D, the 2D profile can be placed anywhere, resulting in varying projection distances of sites, if the profile is orientated perpendicular to strike the same 2D inversion model will be obtained. In practice no subsurface region and MT data sampling the region, are ever perfectly 2D and therefore a 2D profile is placed in a location that minimizes the projection distances of sites. In the Otjiwarongo and Katima Mulilo regions the acquisition of data in array format lead to profiles being placed in regions where the site density was highest; stated differently, where the highest number of sites with the smallest possible projection distances could be included in the profile. The Otjiwarongo sites nearest to the chosen profile, and included in the inversion process, were ELG007m, ELG005, ELG004, ELG002m, ELG012,

ELG009, ELG001m and ELG008 (Figure 5.1a). The Katima Mulilo sites included in its 2D inversion were RAK054, ELZ294, RAK053, ELZ102m, CPV029, ELZ002, ELZ555 and ELZ001 (Figure 5.1b).

After selecting the sites that would be included in the 2D inversions, the sites' apparent resistivity and phase responses were edited again before being inverted. The editing consisted of removal of poor apparent resistivity and phase estimates (for individual, or both, TE and TM modes) and manual shifting of the TE and TM apparent resistivity curves to attempt to correct for static shifts. In contrast to the editing during data processing, where outliers are removed from a set of impedance estimates to obtain a better average estimate at a given frequency, here outliers are removed from the response curves leaving some frequencies without estimates. The outliers were identified by calculating a D^+ model (in WinGLink™) for each of the TE and TM curves and plotting the forward responses of the D^+ models on top of the measured data and observing which estimates conformed least to the smooth D^+ curves. In general the data points removed by editing in the current study were estimates in the AMT dead-band. If a number of data points at successive frequencies were identified as outliers, and subsequently removed, the smooth D^+ curve, representative of the data, instead of the data was used in the inversion process.

Sites which require static shift corrections are characterized by a parallel offset between the TE and TM apparent resistivity curves (most discernable at the highest frequencies) that is not accompanied by a phase difference between the TE and TM phase curves over the same frequency range. The true resistivity value of the shallow subsurface, which both TE and TM apparent resistivity curves should approach at high frequencies in the absence of static shifting, remains unknown without a priori information. In the current study, for sites where clear frequency-independent static shifts were encountered, the correct resistivity levels were assumed to be in the geometric centre between the TE and TM curves and the appropriate parallel shifts in the curves were applied. If the assumption is incorrect, the consequences would not be detrimental, because the 2D inversion algorithm used, in addition to resistivity, also inverts for static shifts in the process of obtaining the smoothest possible model.

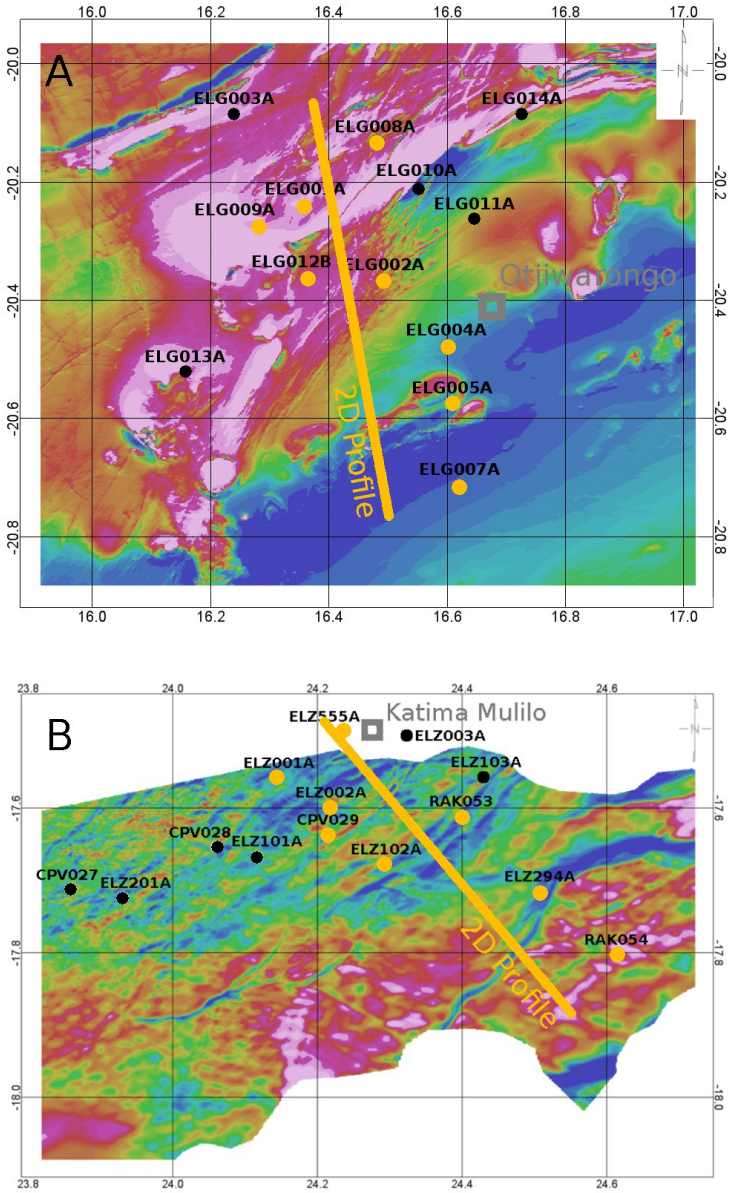


Figure 5.1: *2D inversion profiles created perpendicular to the 82˚ and 54˚ average strike directions in the Otjiwarongo (a) and Katima Mulilo (b) regions, respectively. The 8 sites included in the 2D inversion of each region are indicated.*

5.1 Creating a mesh

Creating a mesh (grid) for a 2D MT inversion involves dividing a flat plane, by means of vertical and horizontal gridlines, into rectangular cells that are each assigned a uniform resistivity value during inversion Simpson and Bahr (2005, p. 122). Mesh construction was found to be an exercise in generating an arrangement of cells that is in accordance with the physics of EM induction

whilst still achieving both efficient and rapid convergence of the inversion algorithm. The following general guidelines were followed whilst creating a mesh for the two inversions:

1. The first horizontal gridline was placed approximately half the smallest skin depth of all the sites (at the highest available frequencies) from the surface. The surface was represented by a horizontal line because no significant elevation changes were observed between sites within the two arrays.

2. In accordance with the loss in resolution with increasing depth as EM energy diffuses into the Earth, each successive horizontal gridline was separated from the previous one by a distance that gradually increased with depth.

3. Because sites were arranged in array format, the inter-site spacing was irregular after projecting them onto a profile. Subsequently, the density of vertical gridlines were made highest around site locations (on the profile) and less dense in between, and away from, sites, in accordance with the fact that resolution decreases laterally away from an observation point with decreasing frequency. If data were collected along a linear profile, the inter-site spacing would be approximately constant and hence the vertical gridline spacing could be made regular.

4. All horizontal and vertical gridlines assigned to a 2D plane were done such that the aspect ratios (length-to-width ratio) of the rectangular cells remained reasonable. A reasonable aspect ratio, in this case, is one which is not less than 0.025 and not greater than 40.

WinGLink™ automatically generates an inversion plane wide and deep enough so that the inversion results beneath the sites are not influenced by edge effects.

Each completed mesh was tested by computing a forward model with a uniform resistivity of 100 Ω.m assigned to all cells. If the forward responses showed a resistivity of 100 Ω.m at all frequencies, as it should without any numerical errors related to an inappropriate mesh, the mesh was considered appropriate for inversion; if not, the mesh was adjusted until the correct forward responses were obtained. The uniform 100 Ω.m meshes were used as starting models for the 2D inversions.

5.2 L-curve

The amount of regularization (smoothing) in an inversion (weight of the second term in equation 3.76) is controlled by a smoothing operator. In inverse theory the optimal trade-off between a smooth poorly fit and rough well fit model (that is, optimal smoothing operator value) is determined with the L-curve (Hansen, 1992). The L-curve has been used in both seismology (Boschi et al., 2006) and MT (Schwalenberg et al., 2002) to great effect. As the title suggests, the L-curve is a plot, of data misfit versus roughness, that takes an L-shape and the smoothing operator value associated with the 'elbow' of the L-shape is chosen as the optimal value for the inversion. The 'elbow' is the point after which an increase in roughness leads to a minimal decrease in misfit, and such an increase is deemed unnecessary.

In WinGLink™ the main user-defined smoothing operator, denoted by the Greek letter tau, τ, was determined prior to each inversion using an L-curve. L-curves were constructed for the Otjiwarongo and Katima Mulilo data by gradually decreasing τ from 100 to 1, running a smooth 2D inversion for each of the τ values, and plotting the resultant root mean square (RMS) errors versus τ values (Figure 5.2). Both TE and TM modes were inverted for, and, by assigning much larger error floors to the apparent resistivities than the phases, emphasis on fit was placed predominantly on phase. A maximum of six decades of TE and TM mode data and minimum frequencies of 0.01 Hz and 0.001 Hz were allowed in all the Otjiwarongo and Katima Mulilo inversions, respectively. L-curves were generated using both uniform and standard grid Laplacian regularization (Figure 5.2) with the default α and β values, and accompanying minimum cell dimensions above which β takes effect, selected (see Section 5.3 for a discussion on regularization settings). Of the four L-curves calculated the only two that had identifiable L-shapes were the uniform grip Laplacian inversion of the Otjiwarongo data and the standard grid Laplacian inversion of the Katima Mulilo data (Figure 5.2). The τ values selected from the two comprehensible L-curves, and used in the smooth inversions that follow, were 20 and 10 for the Otjiwarongo and Katima Mulilo data, respectively. After further analysis of the other two L-curves, τ values of 7 and 10 were selected for the standard grid Laplacian inversions of the Otjiwarongo data and the uniform grid Laplacian inversions of Katima Mulilo data, respectively.

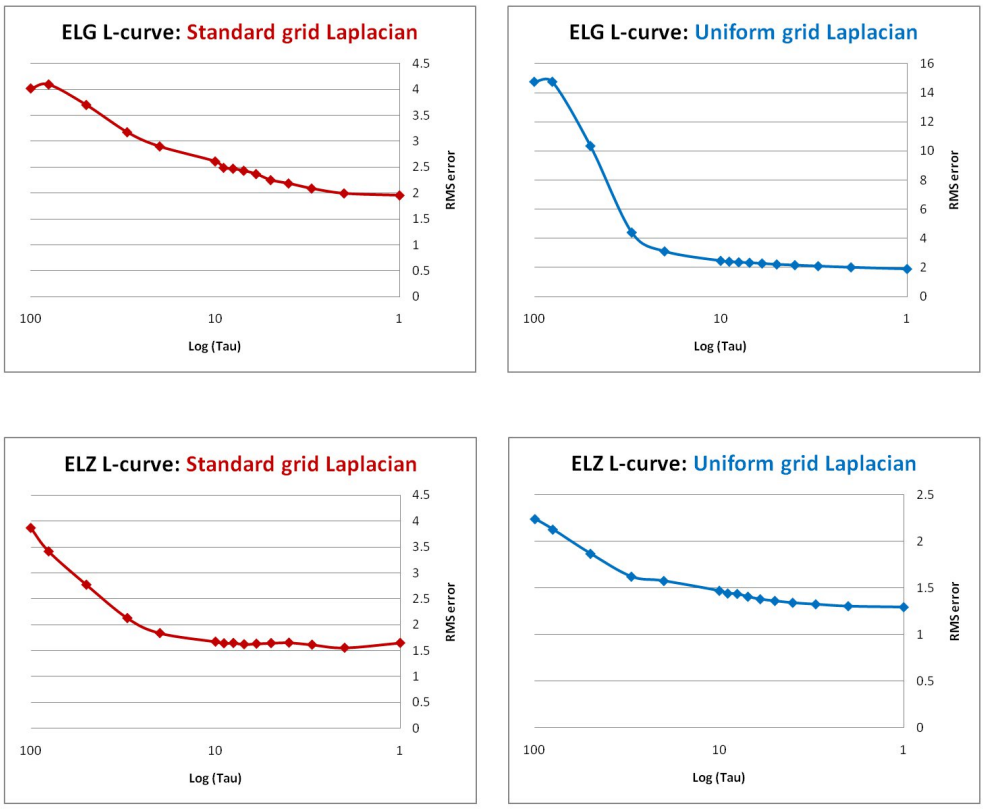


Figure 5.2: *L-curves generated for the Otjiwarongo (top) and Katima Mulilo (bottom) data by plotting τ versus RMS error. For comparison, inversions were run with both standard grid and uniform grid Laplacian regularization selected. 100 iterations were needed for the inversions of Otjiwarongo data to converge to an acceptable RMS level, whilst only 20 iterations were needed for inversions of the Katima Mulilo data. A more regular mesh was created for the uniform grid Laplacian inversion of the Katima Mulilo, because there was no convergence of the inversion algorithm while using the original mesh.*

5.3 Regularization settings

In addition to τ there are also other parameters in WinGLink™ that can be varied to control the amount and degree of regularization applied in an inversion. Firstly, the regularization order can be alternated between minimization of the Laplacian and minimization of the gradient of a model. Minimization of the Laplacian (default option) was selected, because, although minimizing the gradient produces a smoother model, the same smoothness can be obtained by selecting the default option and varying the other regularization parameters, such as τ. Secondly, it is possible to specify either a uniform grid or standard grid Laplacian regularization to be applied on the created meshes. Selecting standard grid Laplacian regularization ensures

that emphasis on fit is placed on regions where the mesh density is highest (that is, at shallow depths and close to sites where MT resolution is highest), while selecting uniform grid Laplacian regularization leads to equal emphasis on fit being placed on all cells. Hence, using uniform grid Laplacian regularization during inversion will produce smoother models than when standard grid Laplacian regularization is used. Both uniform grid and standard grid Laplacian options were used in the inversions of the Otjiwarongo and Katima Mulilo data. Thirdly, by enabling weighting parameters α and β further constraints can be placed on the amount of smoothing. The parameter α multiplies the horizontal derivatives of the Laplacian and therefore produces greater smoothing in the horizontal direction. The parameter β places greater weight on resolving cells which exceed certain dimensions (H and V) and is especially needed when using standard grid Laplacian regularization, in which case minimal emphasis is placed on the resistivities of large cells.

The optimal α and β values to use in the standard grid Laplacian inversions of the two datasets were selected by noting how the RMS errors of inversions varied as different pairs of weighting parameters were used, and selecting the pair which gave the smallest RMS error (Table 5.1). Both TE and TM modes (with equal error floors) and both apparent resistivities and phases were inverted for and the option to invert for static shifts was selected. Static shift inversion in WinGLink™ is based on the assumption that for a number of sparsely distributed MT sites the sum of the natural logarithm of the static shifts should sum to zero (de Groot-Hedlin, 1991). For both standard grid Laplacian inversions of the Otjiwarongo and Katima Mulilo data α and β values of 1 and 3, respectively, produced the lowest RMS errors and were subsequently used in all further standard grid Laplacian inversions (Table 5.1). Because of the equal weighting assigned to all cells when using uniform grid Laplacian regularization, α and β values were kept at the default values of 1 and 1, respectively, and H and V remained 0 m and 0 m, respectively[1].

5.4 TE and TM mode inversion

Generally the TM mode is more sensitive to boundaries between different conductivity regions (owing to the galvanic effects of charges on boundaries)

[1]The general reference for Section 5.3 is the WinGLink™ user manual, see `http://www.geosystem.net`

Table 5.1: *RMS errors for inversions of the Otjiwarongo and Katima Mulilo data using standard grid Laplacian regularization and varying weighting parameters α and β. H and V were kept at the default values of 500 m and 500 m, respectively. The absence of entries for some Katima Mulilo inversions indicates that there was no convergence of the inversion algorithm for the α and β values shown (see Appendix C for models).*

	$\beta = 1$	$\beta = 2$	$\beta = 3$	
Otjiwarongo	4.10	3.39	2.96	$\alpha = 1$
	4.36	3.69	3.55	$\alpha = 2$
	4.81	3.84	3.73	$\alpha = 3$
Katima Mulilo	4.99	3.76	2.52	$\alpha = 1$
	4.74	-	-	$\alpha = 2$
	-	-	-	$\alpha = 3$

while the TE mode is more sensitive to currents flowing within the different regions (see Section 3.2.3.2). Consequently, and because of diffusion, the TM mode is more sensitive to shallow resistive structures and the TE mode is more sensitive to deep conductive structures (assuming isotropic conductivities, Berdichevsky, 1999). To observe the unique information given by each mode in the Otjiwarongo and Katima Mulilo regions, the two modes were independently inverted (Figures 5.3 and 5.4). In each case, the error floors assigned to the apparent resistivities and phases of the two modes were 8% and 3%, respectively, and static shifts were inverted for.

Earlier studies indicated that the TM mode is more robust to 3D effects than the TE mode (Wannamaker et al., 1984). More recent studies show that the greater robustness of the TM mode mostly applies to conductive 3D features (Berdichevsky, 1999). In addition, Berdichevsky (1999) also pointed out that for resistive 3D features both modes are equally robust, while in some geological models, such as a 3D resistive horst, it is even possible that the TE mode is the more robust component. In light of the findings by Wannamaker et al. (1984) and Berdichevsky (1999), an attempt can be made at explaining the RMS errors of the inversions of each of the modes.

The standard grid Laplacian inversions of the Otjiwarongo data gave much larger RMS errors for the TE than the TM mode (Figure 5.3). It is therefore concluded that the TE mode is more affected by 3D features, and in particular conductive 3D features. In contrast, the uniform grid Laplacian inversion of the TM mode gives a larger RMS error than the TE mode inversion (Figure

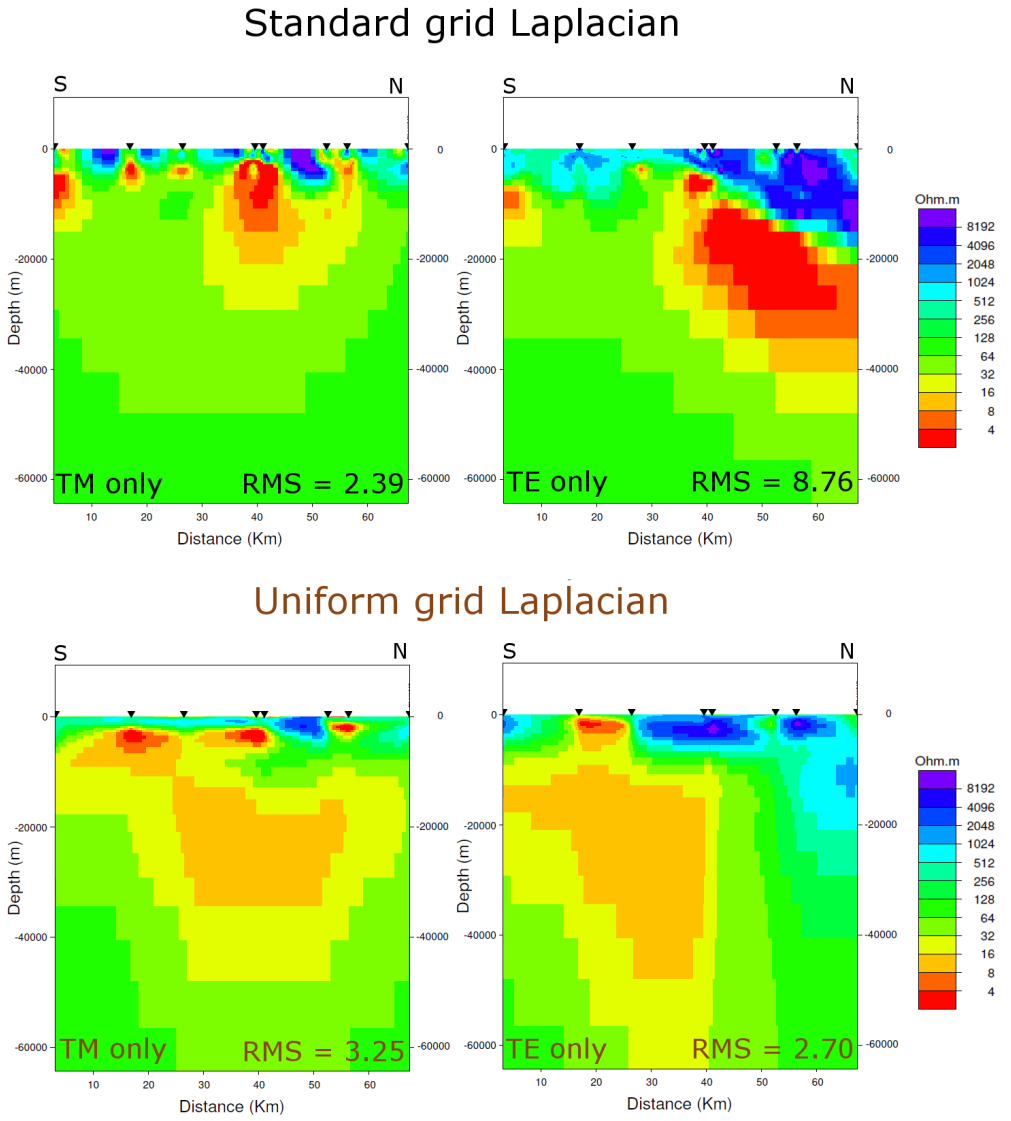


Figure 5.3: *Standard grid (top) and uniform grid (bottom) Laplacian inversions for the individual TM (left) and TE (right) modes of the Otjiwarongo data. The standard grid Laplacian weighting factors were;* $\alpha = 1$, $\beta = 3$, $H = 500\ m$ *and* $V = 500\ m$ *and the uniform grid Laplacian weighting factors were;* $\alpha = 1$, $\beta = 1$, $H = 0\ m$ *and* $V = 0\ m$.

5.3). The smoothness constraints placed on the inversion by using uniform grid Laplacian regularization counteracts the unique information provided by the TM mode, thus the higher TM RMS error is ascribed to regularization rather than effects of 3D features. The equal TE and TM RMS errors of the standard grid Laplacian inversions of the Katima Mulilo data (Figure 5.4) show that either the modes are unaffected by 3D features or both are affected by, and are equally robust to, resistive 3D features present. Again selecting uniform grid Laplacian regularization resulted in the TM mode inversion

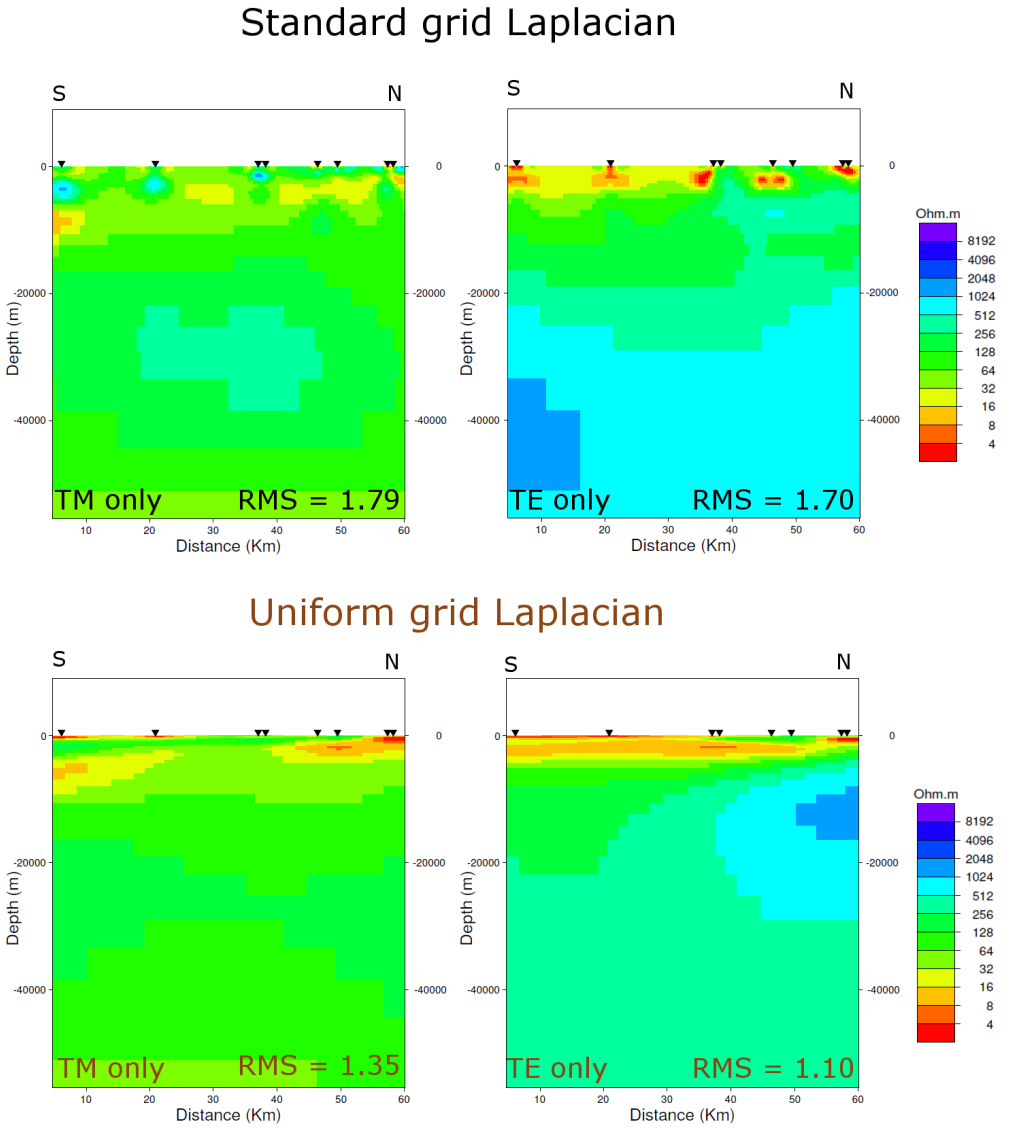


Figure 5.4: *Standard grid (top) and uniform grid (bottom) Laplacian inversions for the individual TM (left) and TE (right) modes of the Katima Mulilo data. The standard grid Laplacian weighting factors were;* $\alpha = 1$, $\beta = 3$, $H = 500\ m$ *and* $V = 500\ m$ *and the uniform grid Laplacian weighting factors were;* $\alpha = 1$, $\beta = 1$, $H = 0\ m$ *and* $V = 0\ m$.

of the Katima Mulilo data having a higher RMS error than the TE mode inversion (Figure 5.4).

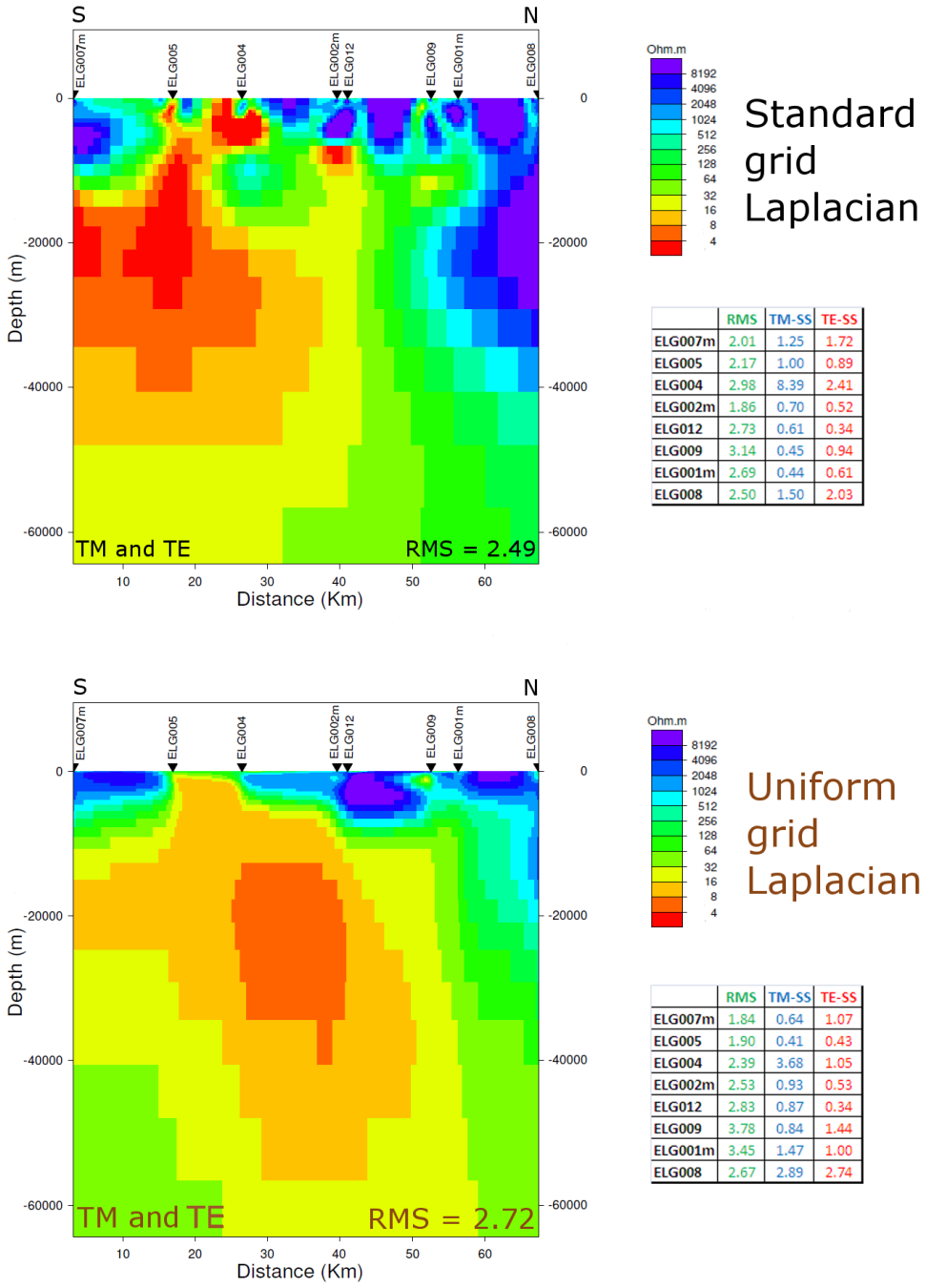
5.5 Joint TE and TM mode inversion

During joint inversion of the TE and TM modes of the Otjiwarongo data, and using standard grid Laplacian regularization, the influence of conductive

3D features were minimized by assigning error floors of 10% and 5%, and 8% and 3% to the TE and TM apparent resistivities and phases, respectively. To improve the RMS error of the joint TE and TM mode inversion while using uniform grid Laplacian regularization error floors of 8% and 3%, and 10% and 5% were assigned to the TE and TM apparent resistivities and phases, respectively. The equal RMS errors of the individual TE and TM mode standard grid Laplacian inversions (Figure 5.4) of the Katima Mulilo data resulted in the apparent resistivities and phases of both the modes being assigned equal error floors of 8% and 3%, respectively, during joint inversion. Error floors of 8% and 3%, and 10% and 5% were assigned to the TE and TM apparent resistivities and phases, respectively, of the Katima Mulilo data during joint uniform grid Laplacian inversion. The τ values and α, β, H and V values used during joint TE and TM mode inversions of the Otjiwarongo and Katima Mulilo data were discussed in Sections 5.2 and 5.3, respectively. For all inversions the option to invert for static shifts was selected.

Assigning error floors to the TE and TM apparent resistivities and phases can be performed in two ways. Either all the TE and TM components are given their appropriate error floors at once, and the inversion is completed, or one component is assigned its error floor, the inversion is started, then another component is assigned its error floor and the inversion continued, and so forth, until all the components are added. The latter option makes it possible for the components to be added to the inversion in different orders. By assigning appropriate error floors to components that were inverted first and much higher error floors to components not immediately required in the inversion, the order of Otjiwarongo and Katima Mulilo inversions were alternated between inverting for phase first and inverting for apparent resistivity first (Table 5.2).

The results showed that by varying the order in which the TE and TM components were added to the inversion, relatively large differences in RMS error, especially for the standard grid Laplacian inversions, could be obtained (Table 5.2). The joint inversion models with the lowest RMS errors in Table 5.2 are shown in Figure 5.5 for the Otjiwarongo data and in Figure 5.6 for the Katima Mulilo data.



	RMS	TM-SS	TE-SS
ELG007m	2.01	1.25	1.72
ELG005	2.17	1.00	0.89
ELG004	2.98	8.39	2.41
ELG002m	1.86	0.70	0.52
ELG012	2.73	0.61	0.34
ELG009	3.14	0.45	0.94
ELG001m	2.69	0.44	0.61
ELG008	2.50	1.50	2.03

	RMS	TM-SS	TE-SS
ELG007m	1.84	0.64	1.07
ELG005	1.90	0.41	0.43
ELG004	2.39	3.68	1.05
ELG002m	2.53	0.93	0.53
ELG012	2.83	0.87	0.34
ELG009	3.78	0.84	1.44
ELG001m	3.45	1.47	1.00
ELG008	2.67	2.89	2.74

Figure 5.5: *Standard grid (top) and uniform grid (bottom) Laplacian joint inversions of the TM and TE modes of the Otjiwarongo data. The standard grid Laplacian weighting factors were;* $\alpha = 1$, $\beta = 3$, $H = 500\ m$ *and* $V = 500\ m$ *and* $\tau = 7$. *The uniform grid Laplacian weighting factors were;* $\alpha = 1$, $\beta = 1$, $H = 0\ m$ *and* $V = 0\ m$ *and* $\tau = 20$. *Static shift inversion results for the TE (TE-SS) and TM (TM-SS) modes and individual RMS errors for each of the 8 sites are shown.*

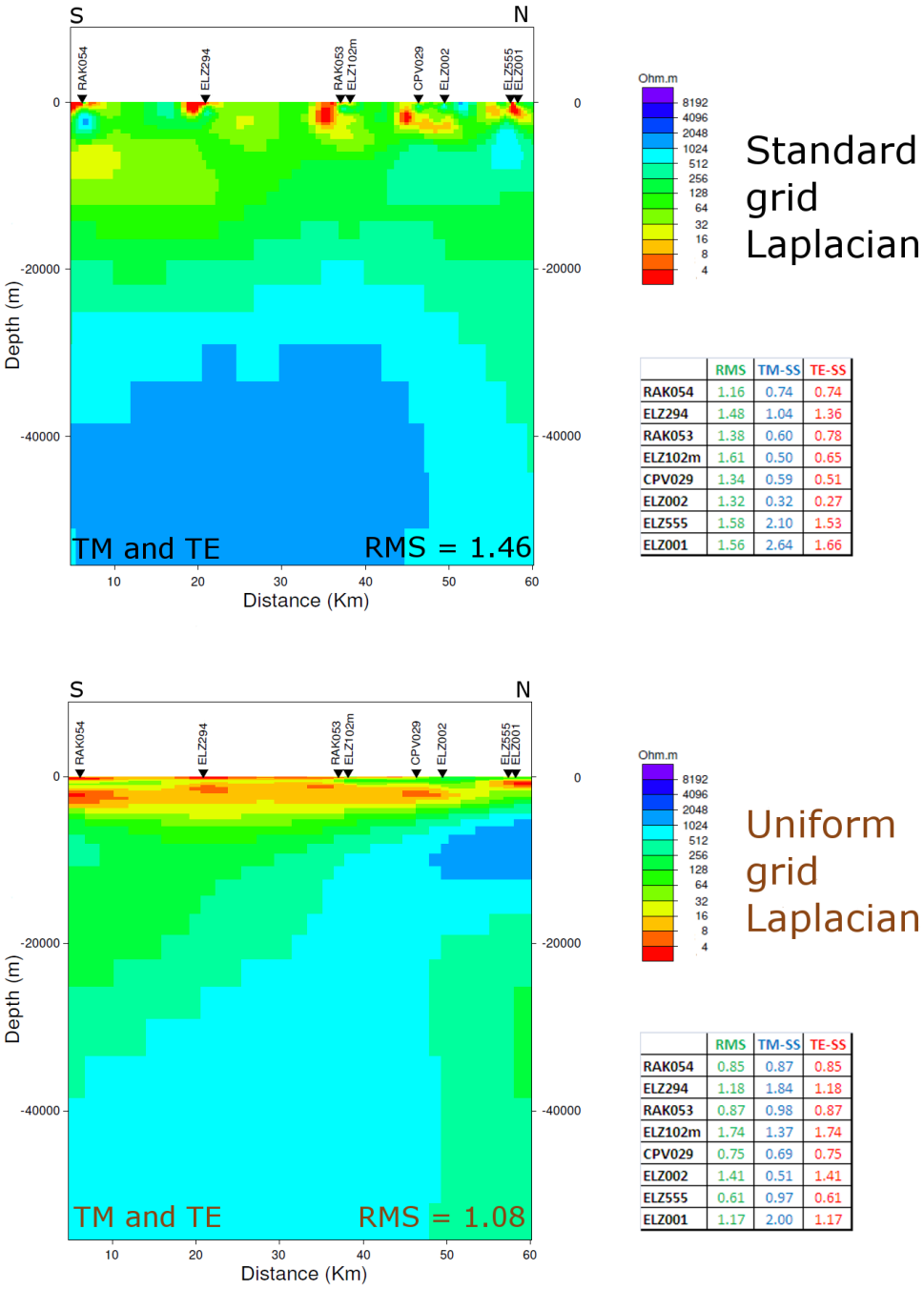


Figure 5.6: *Standard grid (top) and uniform grid (bottom) Laplacian joint inversions of the TM and TE modes of the Katima Mulilo data. The standard grid Laplacian weighting factors were;* $\alpha = 1$, $\beta = 3$, $H = 500\,m$ *and* $V = 500\,m$ *and* $\tau = 10$. *The uniform grid Laplacian weighting factors were;* $\alpha = 1$, $\beta = 1$, $H = 0\,m$ *and* $V = 0\,m$ *and* $\tau = 10$. *Static shift inversion results for the TE (TE-SS) and TM (TM-SS) modes and individual RMS errors for each of the 8 sites are indicated.*

Table 5.2: *RMS errors of joint inversions of TE and TM modes of the Otjiwarongo and Katima Mulilo data, where the order in which the apparent resistivities (ar) and phases (p) of the two modes were added to the inversions, was varied.*

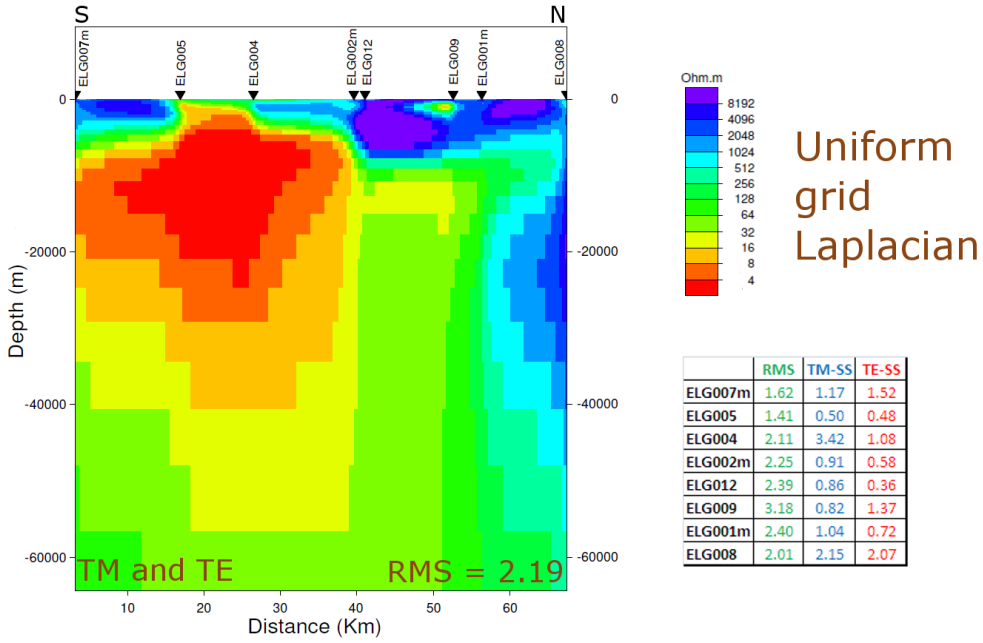
	Otjiwarongo		Katima Mulilo	
Component order	Standard	Uniform	Standard	Uniform
TMp,TEp,TEar,TMar	2.5225	2.7693	1.4576	1.0829
TMp,TEp,TMar,TEar	2.5767	2.8761	1.4637	1.0838
TEp,TMp,TMar,TEar	2.8857	2.7247	1.4622	1.0794
TEp,TMp,TEar,TMar	2.4924	2.7231	1.4614	1.0786
TMar,TEar,TEp,TMp	3.0690	2.8765	1.7782	1.0951
TMar,TEar,TMp,TEp	2.7664	2.8566	1.7715	1.0902
TEar,TMar,TMp,TEp	2.5613	2.8025	1.5557	1.0948
TEar,TMar,TEp,TMp	2.6111	2.8793	1.5689	1.0924

5.6 Sensitivity testing

Sensitivity testing in the current study encompasses determining which structures in the inversion models are robust and required by the data and which structures are artifacts of inversion (for example, artifacts of regularization).

5.6.1 Otjiwarongo inversion

With different τ values used for the standard grid and uniform grid Laplacian inversions of the Otjiwarongo data it was difficult to decide which model to use for further analysis and interpretation. Therefore, a second uniform grid Laplacian inversion was completed with τ set to 7. The order in which the TE and TM components were added to the inversion that resulted in the lowest possible RMS error was again TE phase, TM phase, TE apparent resistivity and TM apparent resistivity. A comparison of the two uniform grid Laplacian inversions with $\tau = 20$ (Figure 5.5) and $\tau = 7$ (Figure 5.7) shows that in general the same conductive and resistive structures are present, but that the resistivities of the structures differ between models. In addition, the standard grid and uniform grid Laplacian inversions, both with $\tau = 7$ (Figures 5.5 and 5.7), show greater similarity than in the case where $\tau = 7$ for the one and $\tau = 20$ for the other (Figure 5.5). A site-for-site misfit comparison between Figures 5.5 (top) and 5.7 shows that sites ELG012, ELG009 and ELG001m have large misfits (probably due to 3D effects), where large in this instance is defined as a misfit that is greater than the average RMS error of the entire model, for both the standard grid and uniform grid Laplacian



	RMS	TM-SS	TE-SS
ELG007m	1.62	1.17	1.52
ELG005	1.41	0.50	0.48
ELG004	2.11	3.42	1.08
ELG002m	2.25	0.91	0.58
ELG012	2.39	0.86	0.36
ELG009	3.18	0.82	1.37
ELG001m	2.40	1.04	0.72
ELG008	2.01	2.15	2.07

Figure 5.7: *Uniform grid Laplacian joint inversion of the TM and TE modes of the Otjiwarongo data with $\tau = 7$. Static shift inversion results for the TE (TE-SS) and TM (TM-SS) modes and individual RMS errors for each of the 8 sites are indicated.*

inversions. Interestingly, the two models differ the most around sites ELG004 and ELG002m, which correlates well with site ELG004 having a large RMS error in Figure 5.5 (top) and a small error in Figure 5.7 while the vice versa applies for site ELG002m. Because it is both smoother (minimizing the risk of over interpreting a model) and fits the data better (RMS of 2.19 compared to 2.49), the uniform grid Laplacian inversion model with $\tau = 7$ (Figure 5.7) was selected for further analysis instead of the standard grid Laplacian inversion model (Figure 5.5).

The chosen Otjiwarongo model has several features but there are two prominent ones. The first is a highly resistive shallow subsurface reaching a maximum depth of roughly 8 km between sites ELG012 and ELG009 that is interrupted by more conductive material beneath sites ELG005 and ELG004 (Figure 5.7). The second is a highly conductive mid-crustal conductor that appears to be connected with the conductive material interrupting the shallow resistive layer (Figure 5.7).

The robustness of the mid-crustal conductor was firstly tested by replacing

all resistivities included in the conductive region with 100 Ω.m, running the inversion again (with the same regularization settings), and noting whether the conductor reappeared. The conductor did reappear and was similar in location and appearance to the original one and the inversion produced the same RMS error (Figure 5.8). Secondly, the robustness of the conductor was tested by replacing all resistivities included in the conductive region by 100 Ω.m, locking the altered cells, running the inversion again and forcing other parts of the model to change to produce the same RMS error. The resultant inversion showed that there were no changes that could be made to the variable parts of the model to produce the previous RMS error of 2.19, and instead a larger RMS error of 4.55 was obtained (Figure 5.8). The same two robustness tests were applied on the shallow resistive layer with similar results. When the resistor was removed it reappeared unaltered after inversion (RMS error of 2.24), and when it was removed and the altered cells locked, no major changes were observed after inversion for the rest of the model while the RMS error increased to 14.71.

To obtain an indication of the lateral and vertical sensitivities of data at each site, the NB-depths for the various TE and TM modes were calculated and compared with the inversion model (Figure 5.9). With the comparison the effects of regularization can be appreciated. The comparison showed that much structure has been added by regularization that is not required by the data (Figure 5.9). To emphasize the role of regularization, most of the mid-crustal conductor was removed and still, after forward modelling, the RMS error of the altered model remained 2.19 (Figure 5.9). In view of the fact that with MT the base of a conductor is not well resolved, and because of regularization, an attempt was made to constrain the depth to the base of the Otjiwarongo conductor by locking parts of the conductor that the data are sensitive to, and running the inversion again (Figure 5.10). The resultant inversion model (Figure 5.10) shows that the depth to the base of the conductor is more constrained than in the original model (Figure 5.7) and was subsequently used in further analysis.

5.6.2 Katima Mulilo inversion

The uniform grid Laplacian inversion of the Katima Mulilo data is smoother and has a smaller RMS error than the standard grid Laplacian inversion (Fig-

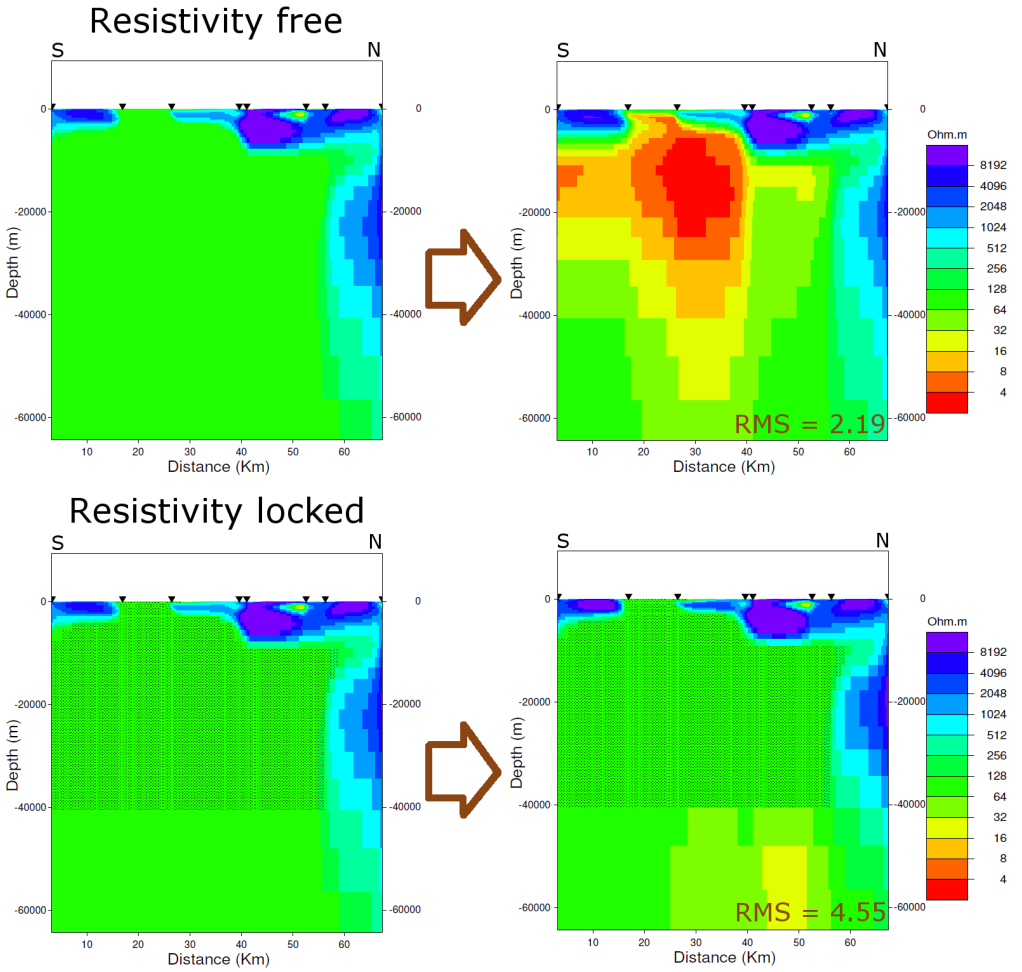


Figure 5.8: *Sensitivity tests done on the Otjiwarongo inversion by firstly removing the mid-crustal conductor, leaving all cells free to vary, and inverting again (top); and secondly, removing the conductor, leaving only cells outside the conductive region free, and inverting again (bottom).*

ure 5.6), and was therefore selected for further analysis. The most prominent feature in the chosen model is a shallow conductive layer that is detected by all sites and reaches a maximum depth of approximately 6 km (Figure 5.6). The robustness of the shallow conductive layer was tested, in a similar manner to the Otjiwarongo conductor, by firstly replacing all resistivities in the shallow subsurface with 100 Ω.m, running the inversion again (with the same regularization settings) and seeing if the conductive layer reappeared. The conductive layer did reappear and was identical to the original and the RMS error remained the same (Figure 5.11). Secondly, the shallow subsurface was given a value of 100 Ω.m, the altered cells were locked and the inversion was restarted. The second test result shows that although subtle changes were made to the rest of the model, the original RMS error of 1.08 could not be

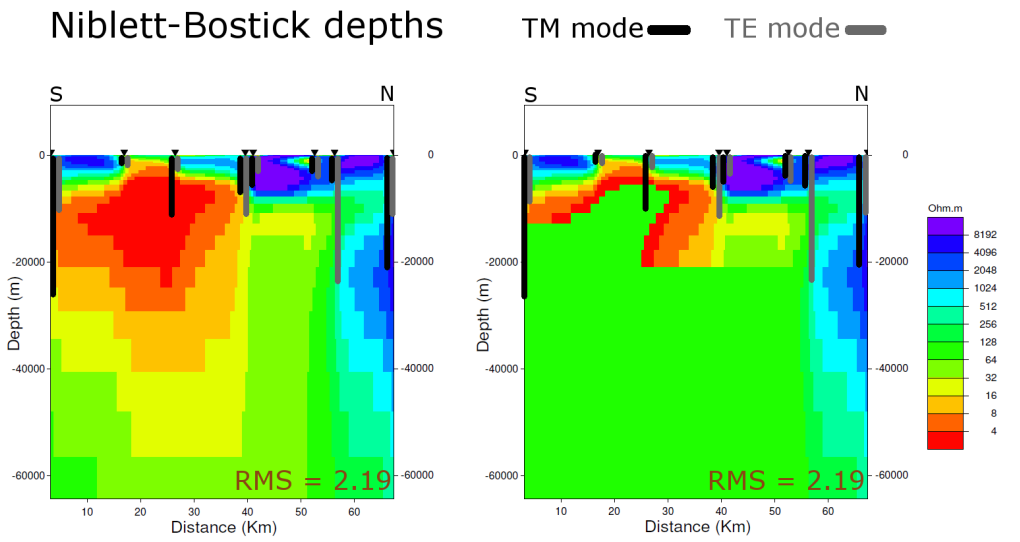


Figure 5.9: *NB-depths for the TE and TM modes of the 8 Otjiwarongo sites pointing out parts of the inversion model that the data are sensitive to, and removing parts of the conductor that the data are insensitive to (right).*

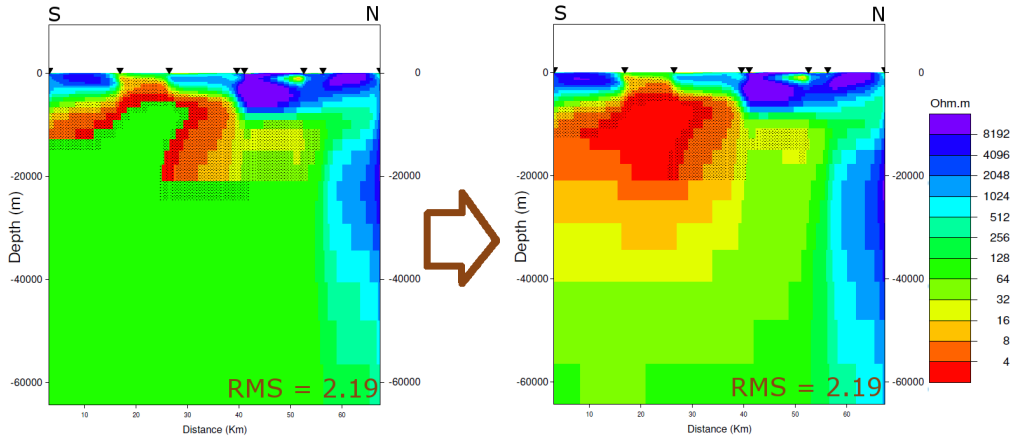


Figure 5.10: *Locking only the parts of the mid-crustal conductor that the Otjiwarongo data are sensitive to, and the inversion result with the appropriate cells locked (right).*

achieved, and instead the RMS error increase to 15.03 (Figure 5.11).

The NB-depths of the TE and TM modes of the Katima Mulilo data (Figure 5.12) indicate that there is much greater depth sensitivity when compared to the Otjiwarongo data (Figure 5.9). However, because the spacing between some sites is large compared with the depth of the conductive layer, parts of the layer can still be removed keeping the RMS error the same (Figure 5.9). To constrain the thickness and depth of the layer, only the parts of the model that the data are sensitive to were locked, similar to the Otjiwarongo

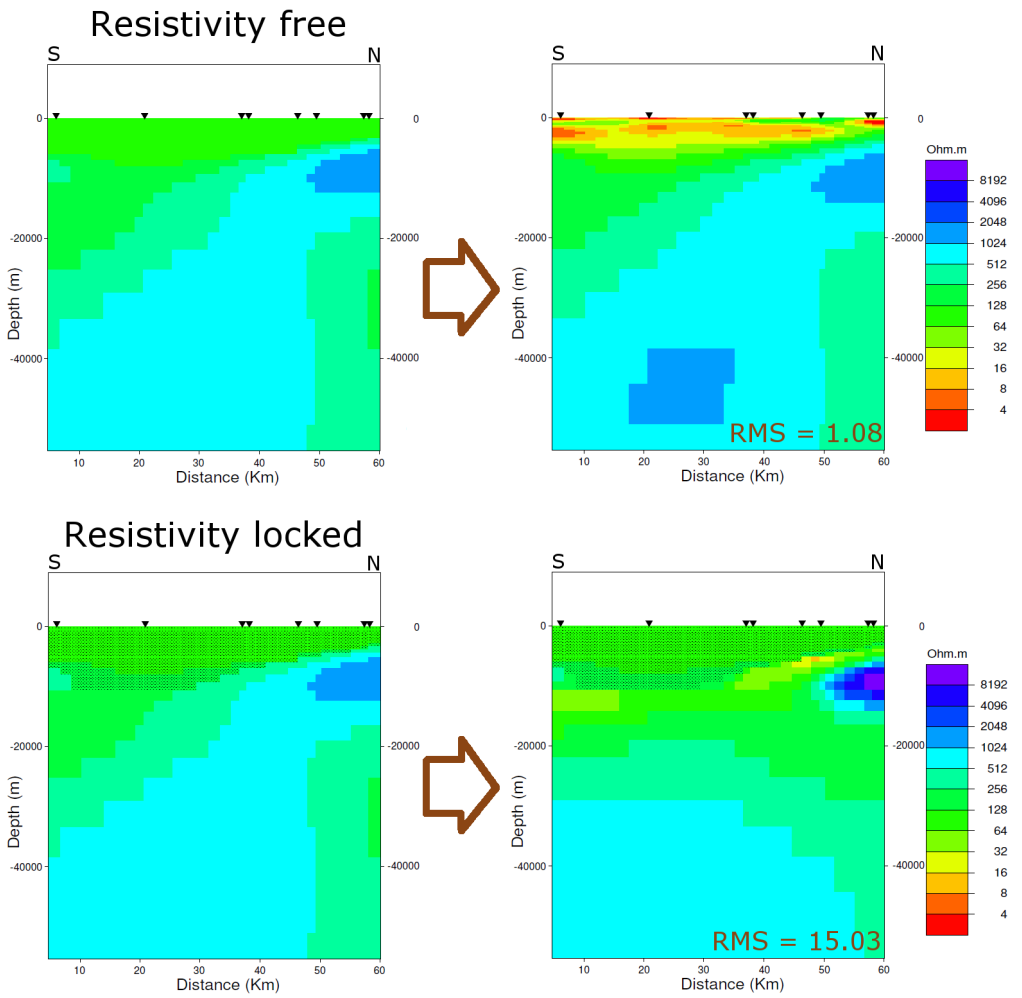


Figure 5.11: *Sensitivity tests done on the Katima Mulilo inversion by firstly removing the shallow conductive layer, leaving all cells free to vary, and inverting again (top); and secondly, removing the conductive layer, leaving only cells below the layer free to vary, and inverting again (bottom).*

conductor, and the inversion was run again (Figure 5.13). Unlike the Otjiwarongo inversion, the inversion result after locking the appropriate parts of the Katima Mulilo conductive layer was not different to the original inversion (compare Figures 5.6 and 5.13).

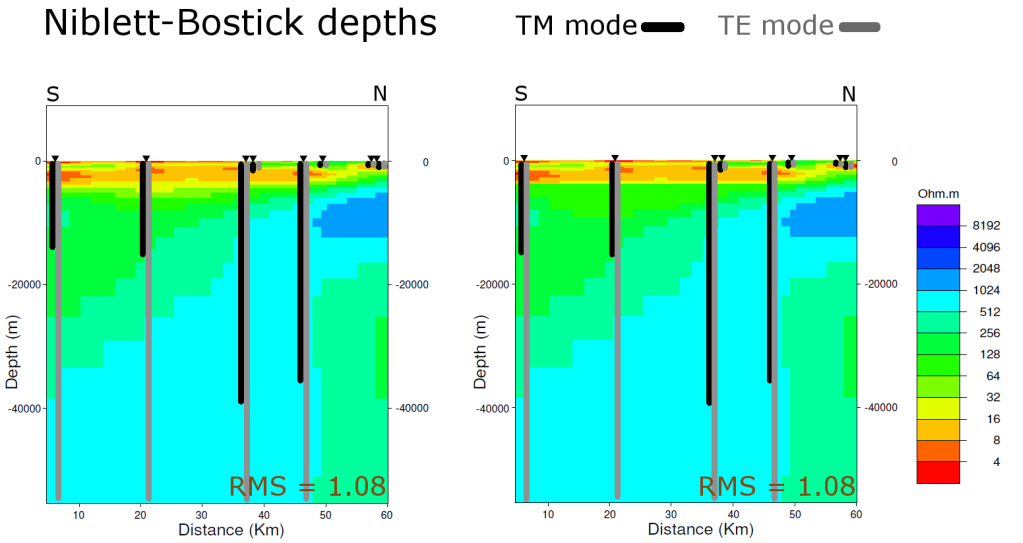


Figure 5.12: *NB-depths for the TE and TM modes of the 8 Katima Mulilo sites showing the great depth sensitivity obtained with the BBMT data, and the parts of the conductive layer that the data are sensitive to (right).*

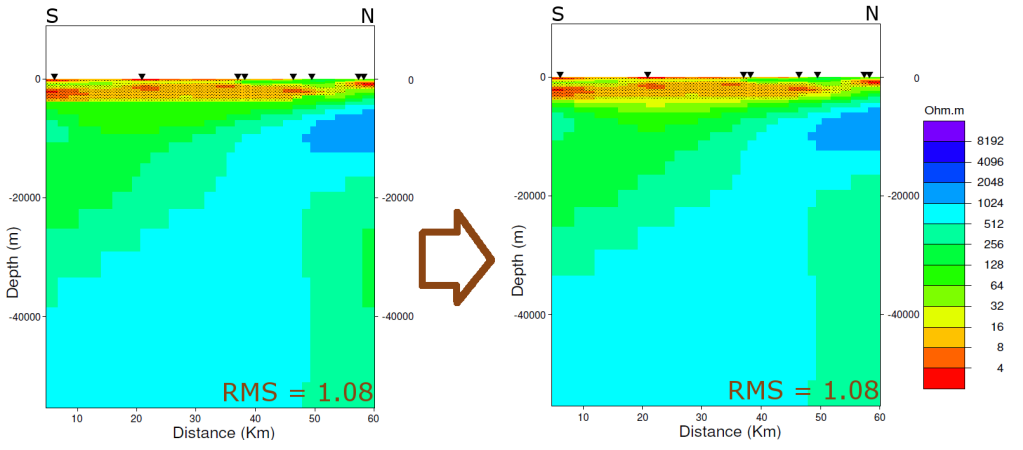


Figure 5.13: *Locking only the parts of the conductive layer that the Katima Mulilo data are sensitive to, and the inversion result with the appropriate cells locked (right).*

Chapter 6

3D interpolation of inversion results

In most cases MT data are acquired in a manner to make either 2D inversion or 3D inversion of data possible. There are only a few contrary examples, including one where data were recorded in array format and a 3D resistivity model was obtained by 2D inversion of data profiles and subsequent interpolation of the 2D inversion results (Garcia et al., 1999). Similar to the latter example, a 3D resistivity model must be obtained for central and northern Namibia and Botswana, by interpolation of 2D inversion results of SAMTEX data, including the newly inverted AMT models, acquired in the region (Figure 6.1).

The 2D inversion profiles in Namibia and Botswana are significantly separated and, in some cases, the distance between two adjacent profiles is as large as the profiles' lengths (Figure 6.1). If an interpolation was attempted on the profiles as is, the interpolation kernel would have to be large and the interpolation result would be highly detailed in narrow regions centred on profile locations and smooth in between. The only manner in which to introduce greater detail to regions in between the profiles is to provide the interpolation process with greater input.

Tectonostratigraphic, geological and geophysical evidence suggests that within the DMB and surrounding mobile belts there exist high degrees of structural linearity (see Sections 1.4 and 2.4). The continuity in structure over large distances lead to the hypothesis that resistivity also remains approximately constant over significant distances in the direction of regional strike. In ac-

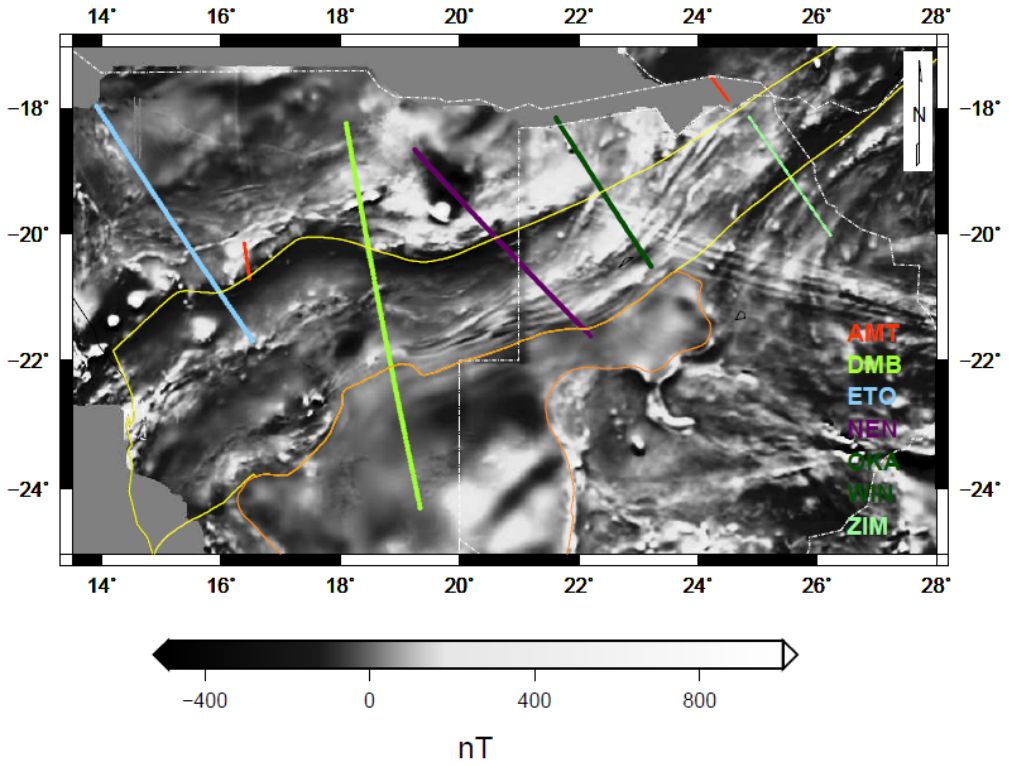


Figure 6.1: *2D inversion profiles of SAMTEX data acquired in central and northern Namibia and Botswana plotted on an aeromagnetic map of the region. 2D inversion results of profiles ETO, DMB, NEN and OKAWIN were provided by Mr. David Khoza and the result of profile ZIM was provide by Dr. Marion Miensopust.*

cordance with the hypothesis and to provide the interpolation with greater input, each profile was divided (if necessary) and projected, as far as possible, along appropriate strike directions.

Prior to interpolation of real projected data, a few scenarios were tested to determine how efficient the interpolation strategy would be in reproducing continuity in structure when 2D profiles are projected in specific directions.

6.1 Interpolation strategy

The interpolation strategy used in the current study is linear. Each interpolated resistivity value is the sum of all resistivity values contained in a cubic kernel (centred on the coordinates of the value being computed), that are weighted according to their distances away from the centre of the kernel

(weight decreases with increasing distance):

$$\log \rho(x, y, z)_{interp} = \frac{\sum_{i=1}^{n} \frac{\log \rho_i}{(1+d_i)^a}}{\sum_{i=1}^{n} \frac{1}{(1+d_i)^a}}, \tag{6.1}$$

where x, y and z are the coordinates of the value being calculated and the centre of the kernel, n is the number of available resistivity values within the confinements of the interpolation kernel, ρ_i is the resistivity value used in the calculation, d_i is the distance to that value and a is a positive integer. Log(ρ) rather than ρ is used in the interpolation, because the typical distribution for apparent resistivity, calculated from acquired data, based on statistical theory is non central chi-squared with 2 degrees of freedom (Chave and Lezaeta, 2007).

6.2 Interpolation testing

The first interpolation test was designed to determine how capable the algorithm is in replicating a bend in a conductive belt at crustal depths (akin to a bend in the DMB conductive belt only sampled by two 2D profiles). To imitate how data from a 2D profile, orientated perpendicular to strike, would sample a conductive belt, a conductive box (100 km by 40 km) of 5 Ω.m was embedded in a homogeneous 100 Ω.m half-space, the mesh was forward modelled and the forward responses inverted (Figure 6.2). The profile, and associated inversion result, was placed on either side of an imaginary bend, orientated perpendicular to the belt's strike (80° and -80° left and right of the bend, respectively), and then projected as far possible, in the direction of strike, towards the bend (Figure 6.3a). The grid onto which the profiles were imported had cell dimensions 5 km by 5 km by 1 km (same cell dimensions used in all other tests) and parallel profiles were 50 km apart (Figure 6.3a). The integer a in equation (6.1) was varied from 1 (Figure 6.3b) to 9 (Figure 6.3c) and the size of the interpolation kernel was $41 \times 41 \times 41$ cells. For the kernel to span the same distance horizontally and vertically, only every fifth resistivity value in the vertical direction was used in calculation.

The greater amount of smoothness introduced by using a small value for a produced a bend in which strike gradually changes from 80° to -80°, but a

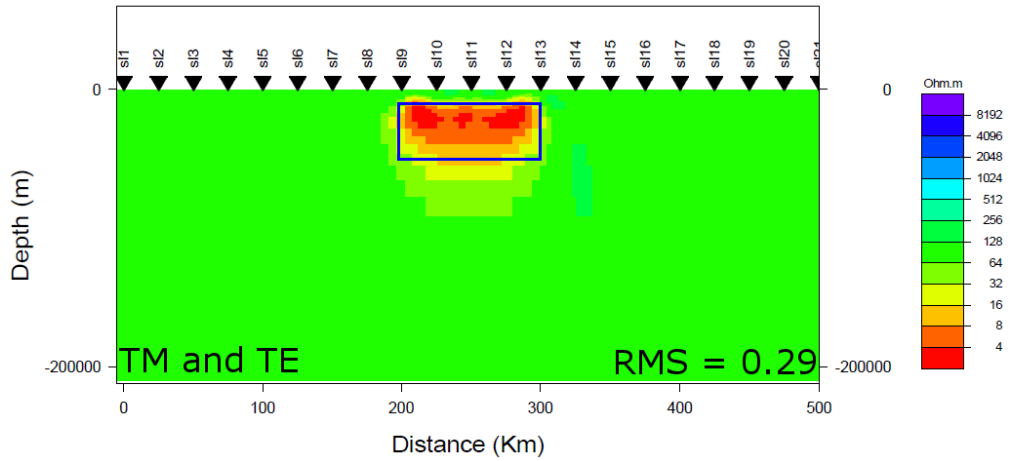


Figure 6.2: *Resistivity model obtained by inversion of MT responses calculated with forward modelling, where the forward model consisted of a conductive 5 Ω.m box (outline shown) embedded in a homogeneous 100 Ω.m half-space. WinGLink™ was used for the forward and inverse modelling. Standard grid Laplacian regularization was selected and the weighting factors were;* $\alpha = 1$, $\beta = 1.5$, $H = 500\ m$ *and* $V = 500\ m$ *and* $\tau = 3$.

conductive belt with inconsistent thickness and a resistivity that is too large (compare a and b in Figure 6.3). A large value for a produced a belt with correct thickness and resistivity but a sharper bend (compare a and c in Figure 6.3).

Further constraints were placed on the interpolation by adding an angle term to equation (6.1). The angle term weighs down resistivity values - which occupy cells that make angles relative to the interpolated cell - that are not parallel to strike in the region containing the resistivity values:

$$\log \rho(x,y,z)_{interp} = \frac{\sum_{i=1}^{n} \frac{\log \rho_i}{(1+d_i)^a} \cdot \cos^b \theta_i}{\sum_{i=1}^{n} \frac{1}{(1+d_i)^a} \cdot \cos^b \theta_i}, \tag{6.2}$$

where θ_i is the difference between the regional strike angle and the horizontal angle made by the cell occupying ρ_i and the cell located at the centre of the kernel (x, y, z), b is a positive integer and the other variables have the same meaning as in equation (6.1). The effects of the new term on interpolation were calculated by assigning strike angles of 80° and -80° to parallel profiles left and right of the imaginary bend, respectively, and varying b from 1 to 9 while still varying a from 1 to 9 (Figures 6.4, D.1 and D.2).

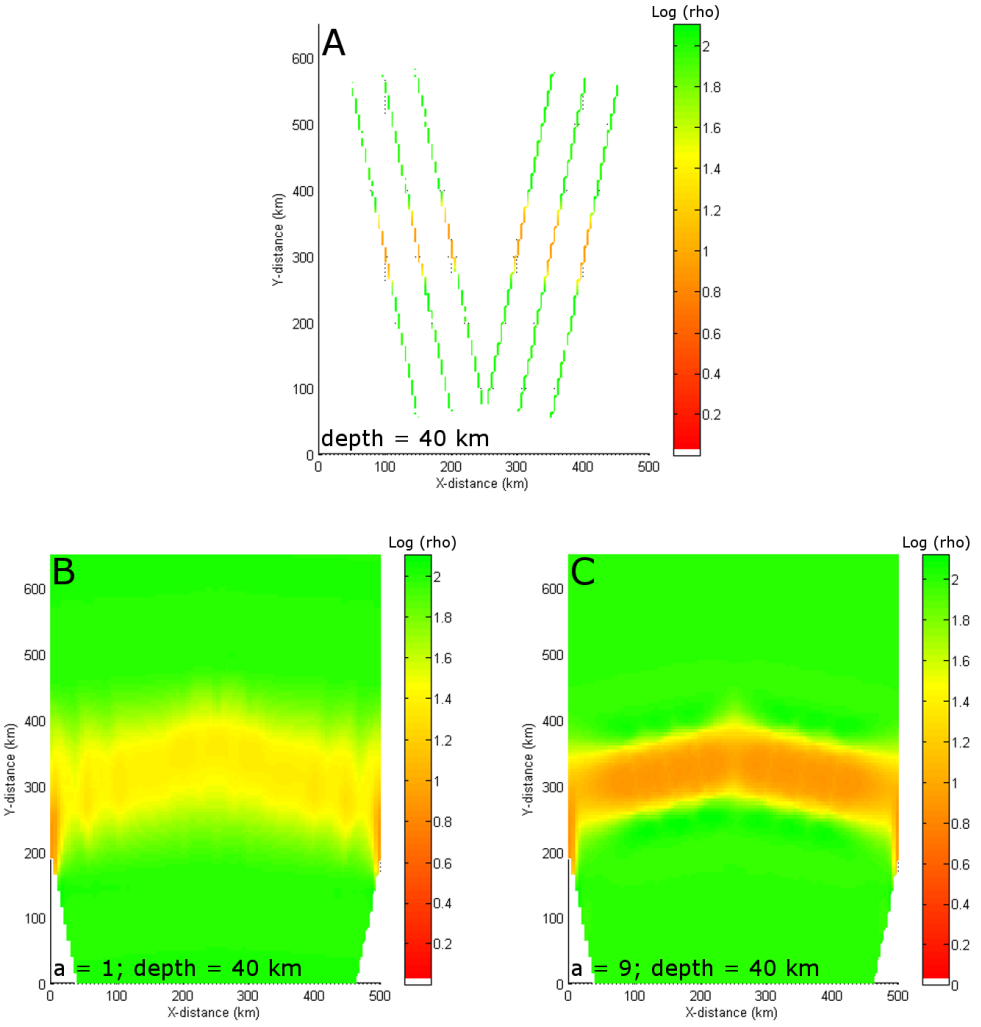


Figure 6.3: *Sections at 40 km depth of the original (leftmost and rightmost) and projected profiles (a) used as input in the first interpolation test and subsequent interpolation results with integer a set equal to 1 (b) and 9 (c).*

Problems encountered with the interpolation when resistivity values were weighted downwards according to distance only were partially corrected with the addition of the angle term in equation (6.2) (Figure 6.4). The effects of the new term were more visible with $a = 1$ than $a = 9$ (compare a and c with b and d in Figure 6.4). Also, a larger value for b lead to greater improvement in the initial interpolation problems than when a smaller value was used (compare a and b with c and d in Figure 6.4).

Following the first interpolation test, a second test was designed to investigate what results the interpolation algorithm would give when encountering vertical rather than lateral (that is, the first test) changes in resistivity. Two

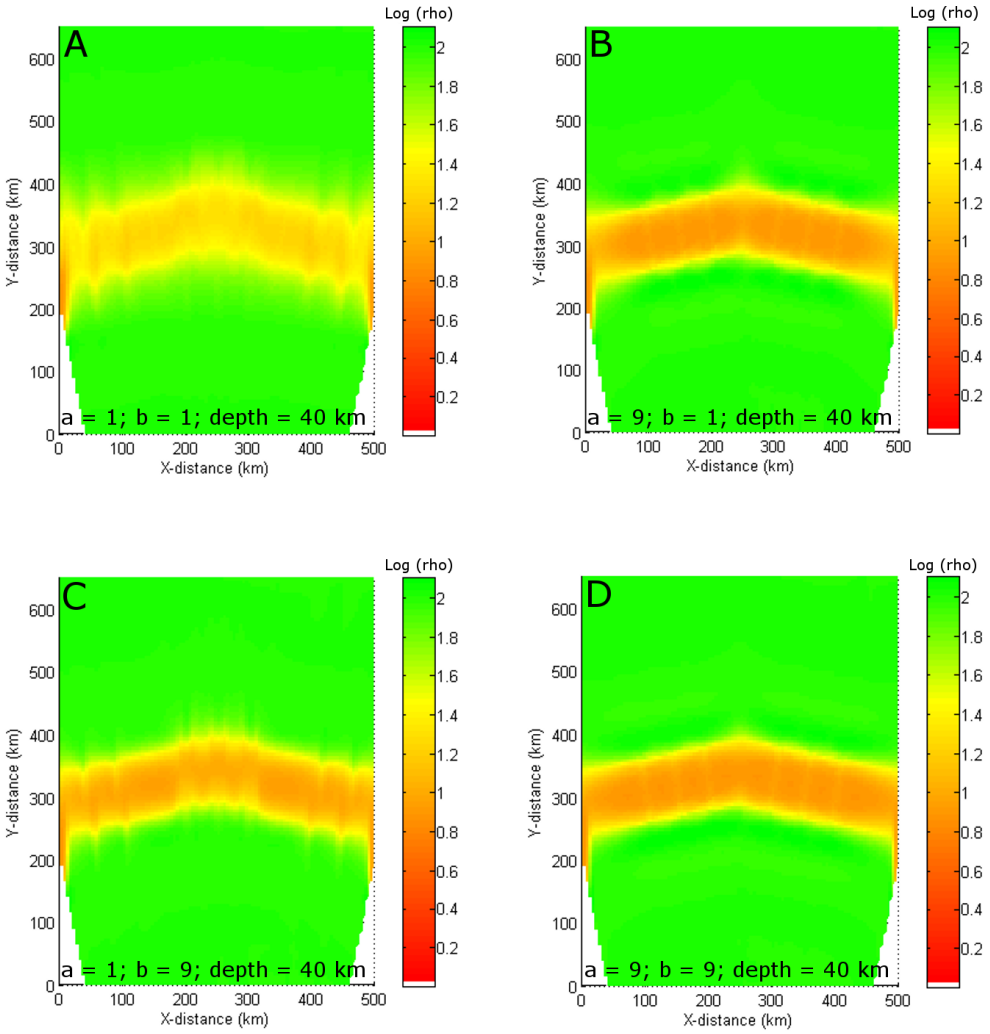


Figure 6.4: *Interpolation results at 40 km depth using the profile arrangement in Figure 6.3a as input and setting $a = 1$ and $b = 1$ (a), $a = 9$ and $b = 1$ (b), $a = 1$ and $b = 9$ (c) and $a = 9$ and $b = 9$ (d).*

forward models were created to imitate how a 2D profile would sample a conductive belt varying in depth. The first was a conductive 5 Ω.m box (150 km by 40 km) embedded in a 100 Ω.m homogeneous half-space where the top margin was 10 km from the surface, and the second contained the same conductive box and half-space but the box's top margin was 35 km from the surface (Figure 6.5). Using WinGLink™, MT responses were obtained through forward modelling of the two models, and the forward responses were inverted to obtain resistivity models representing the shallow and deep conductors (Figure 6.5).

The two 2D profiles, and associated inversion results (one shallow and one

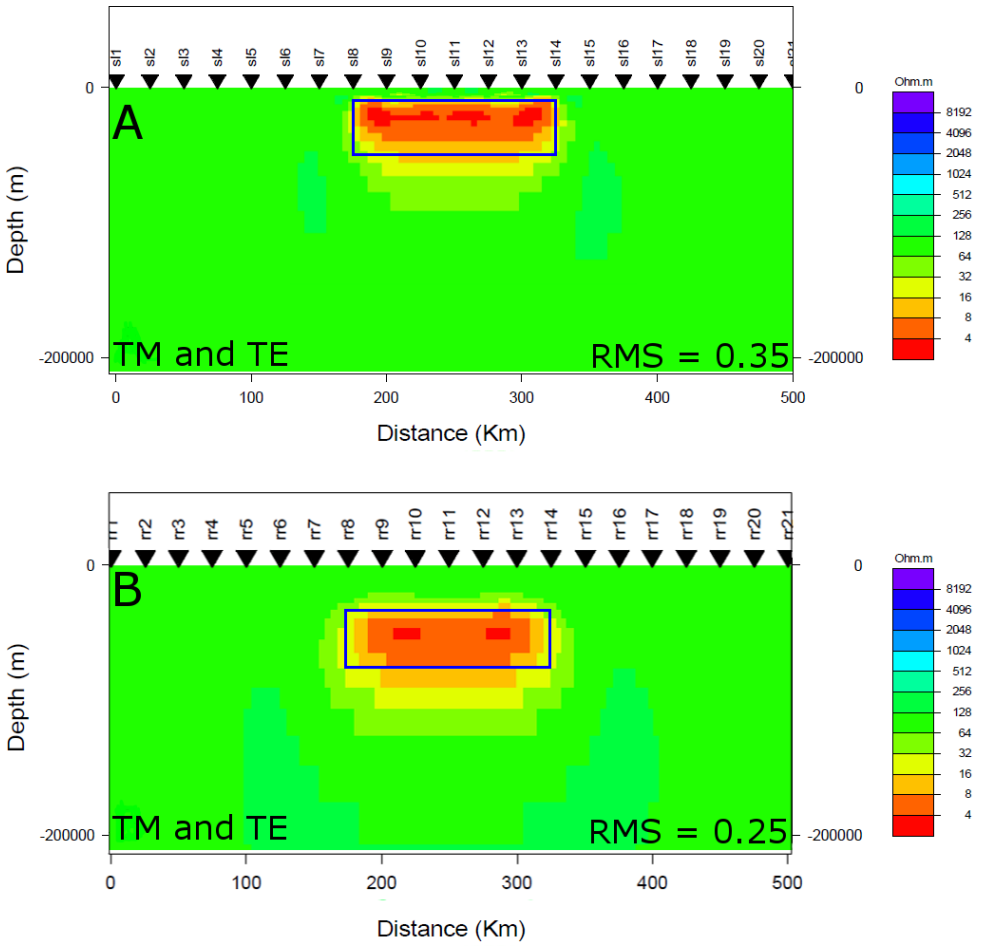


Figure 6.5: *Resistivity models obtained by inversion of MT responses calculated with forward modelling, where the forward models consisted of conductive 5 Ω.m boxes (outline shown), one with its top margin at 10 km depth (a) and the other 35 km depth (b), embedded in a homogeneous 100 Ω.m half-space. Standard grid Laplacian regularization was selected for both inversions and the same weighting factors of;* $\alpha = 1$, $\beta = 1.5$, $H = 500\ m$ *and* $V = 500\ m$ *and* $\tau = 3$, *were used.*

deep conductor), were placed parallel to each other, 300 km apart, and then each one was projected twice in increments of 50 km in the direction of the other (Figure 6.6a). Strike angles of 90° were given to all profiles, and interpolations were subsequently done with $a = 1$ (Figure 6.6b), $a = 9$ (Figure 6.6c) and a varied between 1 at 80 km depth and 9 at the surface (Figure 6.6d), with $b = 9$ for all three interpolations. The size of the interpolation kernel was $41 \times 41 \times 41$ cells. Because θ_i (equation 6.2) refers to an angle on a horizontal plane, varying the value of b would not lead to changes in structures observed on a vertical plane but only in the resistivity values of the structures themselves.

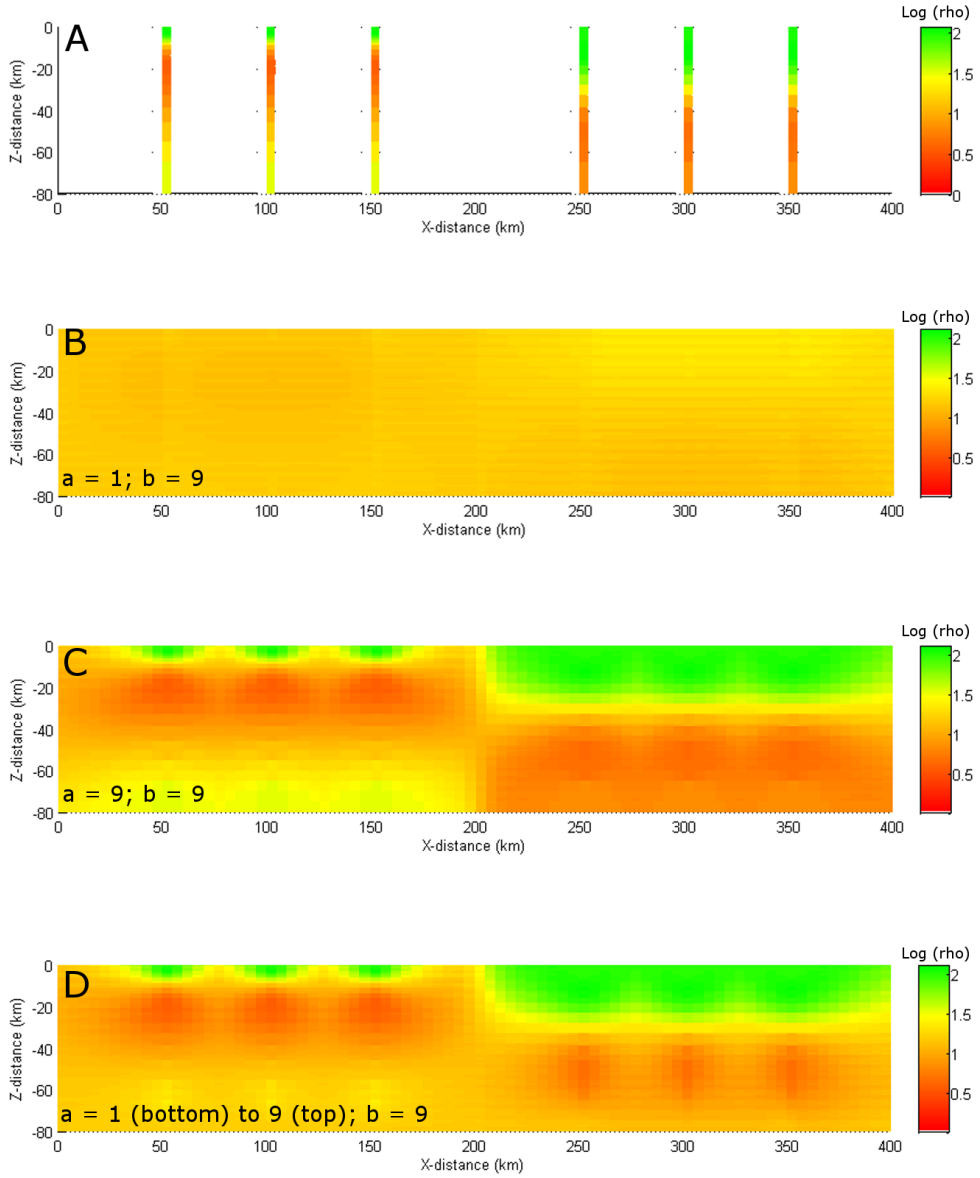


Figure 6.6: *A cross section through the centre of the profiles in Figure 6.5a (left three profiles) and 6.5b (right three profiles) after the profiles were placed parallel and 300 km apart and projected in the X-direction (a). Results for the second interpolation test, on the same vertical plane, where $a = 1$ and $b = 9$ (b), $a = 9$ and $b = 9$ (c) and a is varied from 1 at the bottom to 9 at the top while b is kept constant at 9 (d).*

In contrast to producing a satisfactory result in the first interpolation test (Figure 6.4c), a combination of $a = 1$ and $b = 9$ produced a result, in the second test, that was poor and excessively smooth in the vertical direction (Figure 6.6b). The poor result could be improved by introducing a second angle term in equation (6.2) that operates on angle differences in the verti-

cal direction. However, such a consideration is not pragmatic, because there exists few constraints on vertical strike variations when compared to lateral strike variations in resistivity. Using a value for a larger than 1 produced an interpolation result with better and more distinct continuity between the shallow and deep conductors, and the larger a was made, the steeper and narrower the connecting conductivity region became (Figure 6.6c and d).

The first interpolation test indicated that using a large value for b produces better interpolation results than when using a smaller value and that the optimal value for a should be greater than 1 but smaller than 9 (Figure 6.4). The second test showed that resistivity variations with depth, changes from excessively smooth to sharp when a is varied from 1 to 9 (while $b = 9$), therefore an optimal model should also be obtained when a is in between 1 and 9 (Figure 6.6). The aim of the third interpolation test was to determine the optimal value of a when $b = 9$.

The 2D profile containing a shallow conductor also used in the first test (Figure 6.2) was utilized in the third interpolation test. It was projected in the direction of strike on both sides of an imaginary bend in a conductive belt with strike on the left side remaining 90° and on the right side varied from 60° (Figure 6.7a) to 30° (Figure 6.7b), while all projected profiles remained parallel to 0°. Profiles left of the bend were assigned a 90° strike angle and profiles right of the bend were assigned strike angles of 60° and 30°, respectively. The size of the interpolation kernel used in the third test was $41 \times 41 \times 41$ cells and tests were done, for both profiles arrangements (Figure 6.7a and b), with $b = 9$ and a increased, incrementally by 1, from 1 to 9 (Figures 6.8 and 6.9).

In both scenarios tested, the value of a that produced the most satisfactory conductive belt, with no side-effects related to profiles not orientated perpendicular to strike and the projection direction, was 4 (Figures 6.8 and 6.9). Similarly, the interpolation result when using the profile arrangement in the second test (Figure 6.6a) and setting $a = 4$ and $b = 9$ produced a good connection between the shallow and deep conductors, which was not to smooth or to sharp (Figure 6.10).

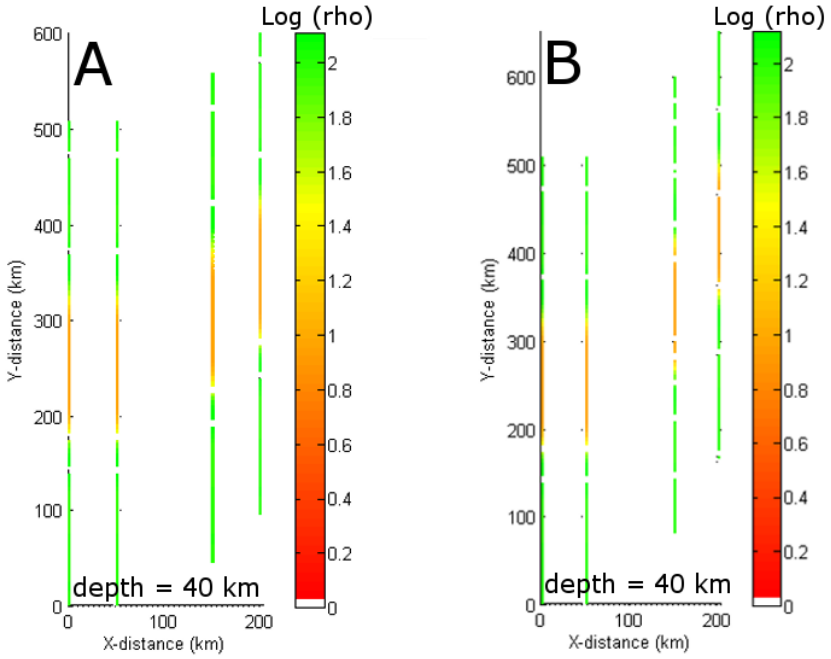


Figure 6.7: *Sections at 40 km depth of original and projected profiles used as input in the third interpolation test where strike on the right side of the bend in the conductive belt was varied between 60° (a) and 30° (b).*

6.3 Profile projections

Prior to interpolation the profiles were projected in specific directions and given strike values. Each profile was divided and projected differently for crustal ($0 - 50$ km) and lithospheric mantle ($50 - 200$ km) depths.

6.3.1 Crustal depths

Because regional magnetic data are reasonable indicators of tectonic fabric at crustal depths down to the Curie isotherm (Sutherland, 1999 and Hildenbrand et al., 2000), profiles were projected and given strike angles according to trends in large scale linear features in the regional magnetic data in Namibia and Botswana (Figure 6.11). Profiles were divided at points of intersection with the boundaries separating major geological provinces in southern Africa (Figure 1.1). Profile ETO was divided in a northern and southern part, correlating with locations of the Koaka Belt (Figure 1.6) and DMB, respectively, and projected and given strike angles accordingly. Profile DMB was separated in a northern, central and southern part and the parts were projected and given strike angles according to trends in the Congo Craton (southern margin according to geological map by Miller, 2008), DMB

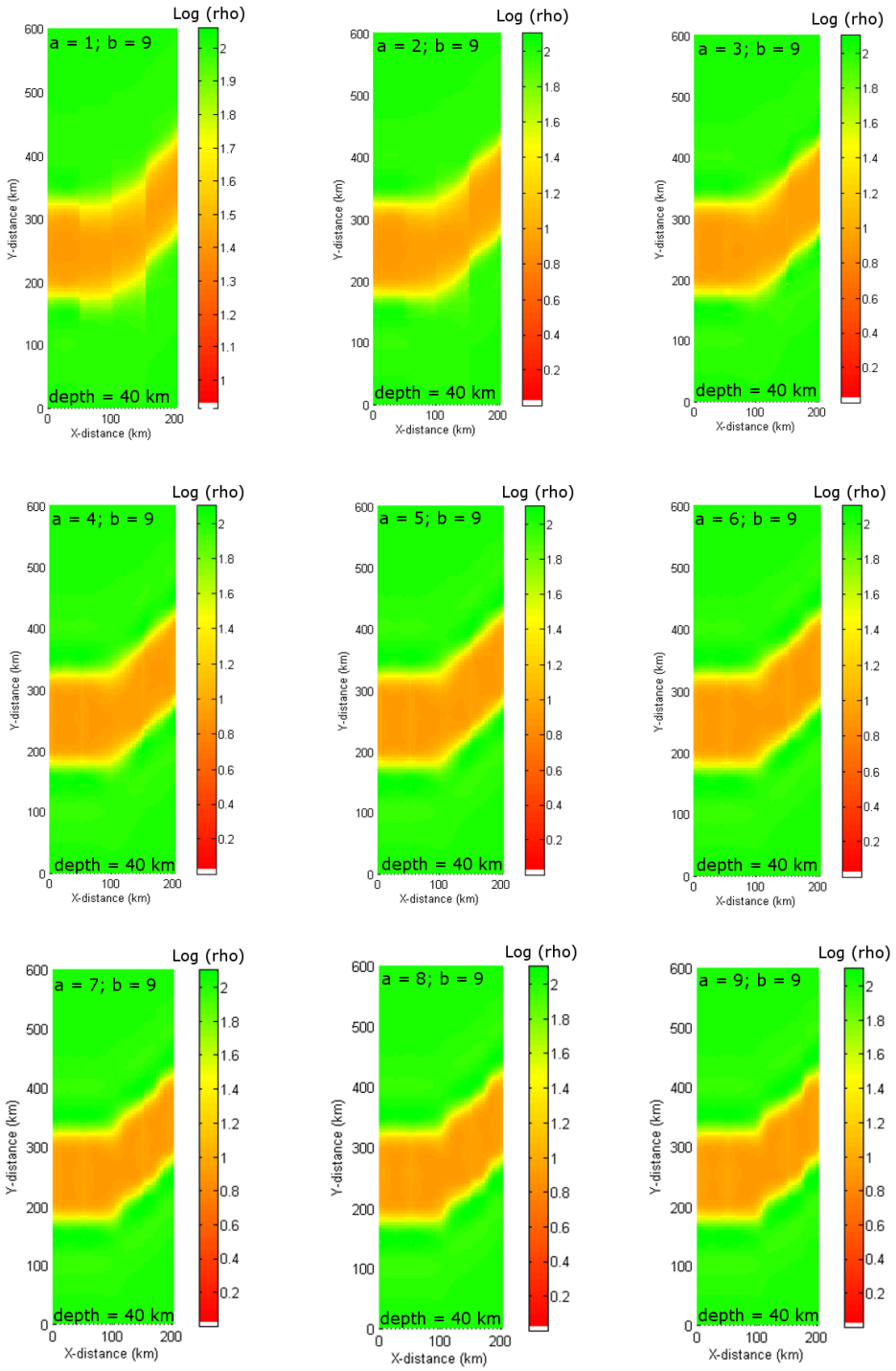


Figure 6.8: *Sections at 40 km depth showing interpolation results when using Figure 6.7a as input and varying a from 1 to 9 while keeping* $b = 9$.

and Rehoboth Terrane, respectively. Most of profile NEN and all of profile OKAWIN were projected in the direction of the DMB. The northern part of profile NEN, not projected according to trends in the DMB, was given strike angles according to trends in the Congo Craton and Daneib intrusion

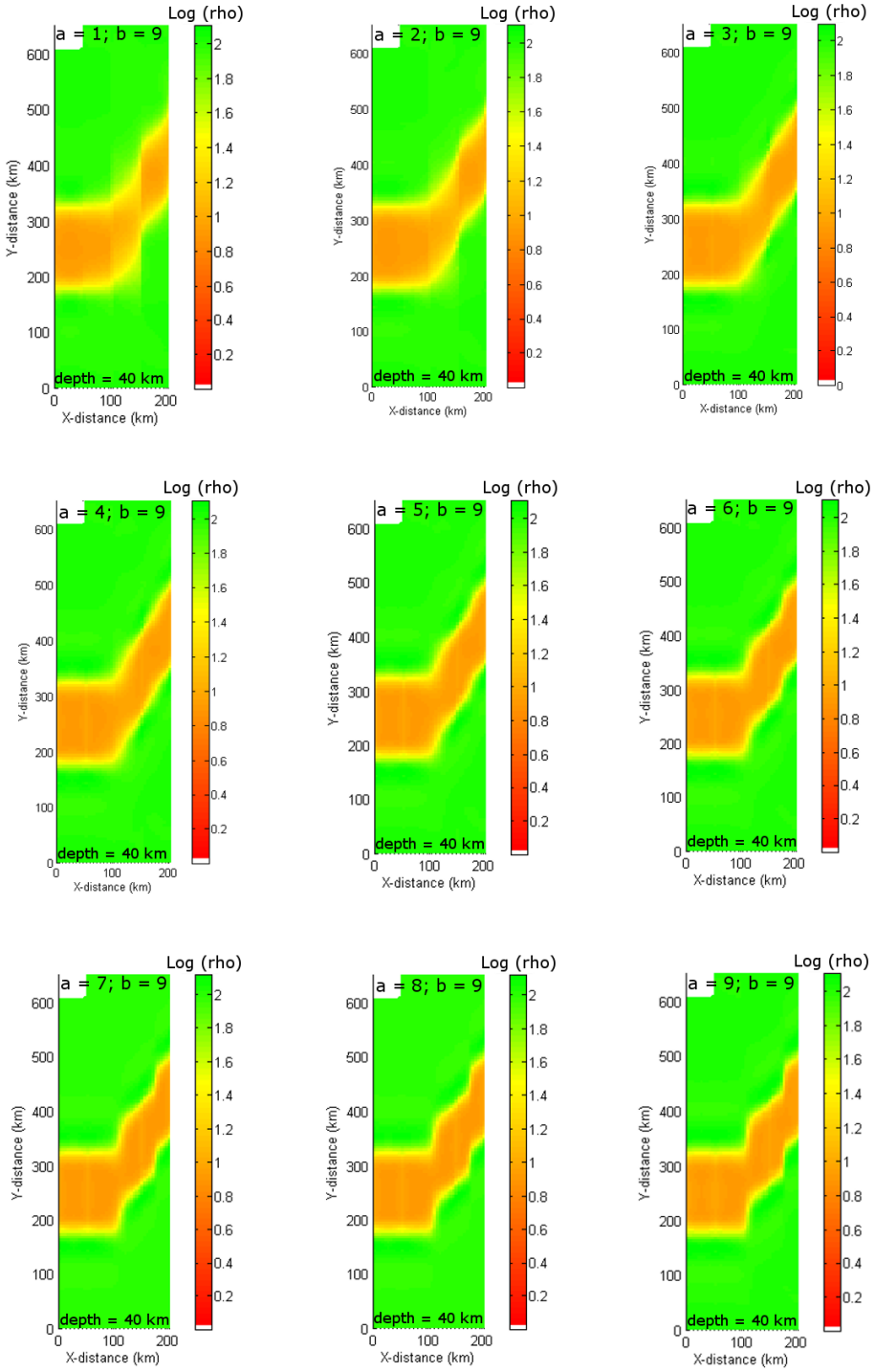


Figure 6.9: *Sections at 40 km depth indicating interpolation results when using Figure 6.7b as input and varying a from 1 to 9 while keeping* $b = 9$.

(see geological map by Miller, 2008), respectively. Profile ZIM was projected and given angle values according to trends in the Magondi Belt while the two AMT profiles were not projected but given respective strike values of 82° and 54°, which were the angles calculated using Strike in Chapter 4.

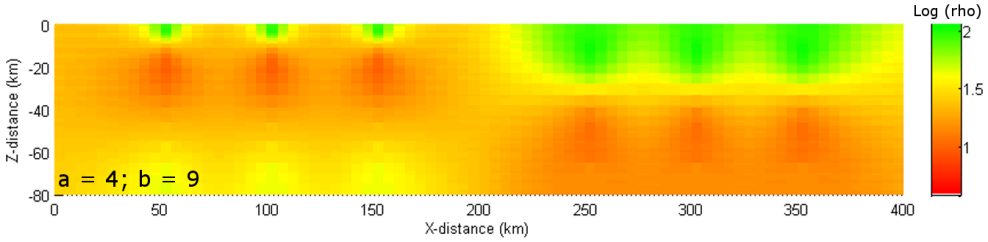


Figure 6.10: *Interpolation results using the profile arrangement in Figure 6.6a and setting $a = 4$ and $b = 9$.*

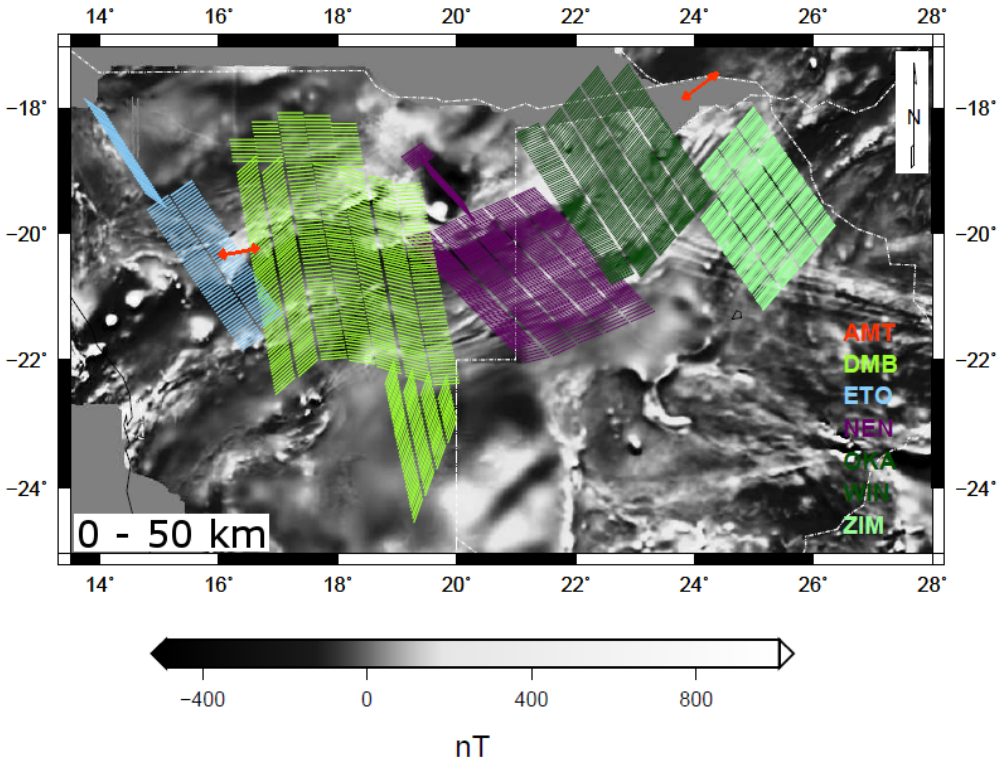


Figure 6.11: *Strike angles assigned to, and projection directions of, profiles ETO, DMB, NEN, OKAWIN, ZIM and the Otjiwarongo and Katima Mulilo AMT profiles for crustal depths, plotted on regional aeromagnetic data used as direction indicators for the projections.*

6.3.2 Lithospheric mantle depths

Features in regional magnetic data mostly give information about structure at crustal depths above the Curie Temperature and not lithospheric mantle depths. Therefore, information about lithospheric mantle strike can only be obtained with deep probing geophysical tools such as MT. Strike information in the depth range $50 - 200$ km for northern Namibia and Botswana was obtained by analyses of tippers computed in WinGLink™ and impedance strike angles computed with Strike.

Using WinGLink™, strike information was obtained by calculating tipper strike angles from the tipper components (equation 3.45) of each site. Tipper strike angles are, in an ideal 2D Earth, perpendicular to both real ($\vec{T}_{re}$) and imaginary ($\vec{T}_{im}$) induction arrows, given by equations (Berdichevsky and Dmitriev, 2002, p. 138):

$$\vec{T}_{re} = Re(T_{zx})\vec{x} + Re(T_{zy})\vec{y}, \tag{6.3}$$

$$\vec{T}_{im} = Im(T_{zx})\vec{x} + Im(T_{zy})\vec{y}. \tag{6.4}$$

In reality, no MT data are perfectly 2D and consequently the angle chosen to represent tipper strike in the current study was the one which minimized $\mid T_{zx} \mid^2$ (see Section 3.2.4, Gamble et al., 1982). Tipper strike angles were calculated for all sites in northern Namibia and Botswana where H_z field recordings were available, at periods of 100, 200, 333, 500 and 1000 seconds (Figures 6.12 to 6.16)(see induction arrows in Figures D.3 to D.7).

After tipper strike angle calculation, galvanic distortion of the electric field was removed from the data (using Strike), with the impedance strike angles constrained to the values computed from the tipper data. The removal of galvanic distortion from the impedances ensured that more accurate EM penetration depths could be obtained. NB-depths (Niblett-Bostick depths) were calculated for periods 100, 200, 333, 500 and 1000 seconds using only the TE apparent resistivity curves (see Section 3.2.4) of sites which had reliable responses and smaller than 2 GB-errors (Groom-Bailey errors) at the five periods (Figures 6.12 to 6.16). An average tipper strike angle was obtained from the five values calculated at periods 100, 200, 333, 500 and 1000 seconds (Figure 6.17) by the following guidelines:

1. All tipper strike values at a site that had depth estimates of greater than 50 km were averaged, and the average assigned to the site as the strike angle representing the lithospheric mantle depth range.

2. If none of the five tipper strike values at a site was estimated to sample structure deeper than 50 km then the site was not given a strike value.

3. If however, less than five of the tipper strike values at a site were estimated to only sample crustal structure, and one or more of the other values, unknown in depth, are at larger periods, then an average

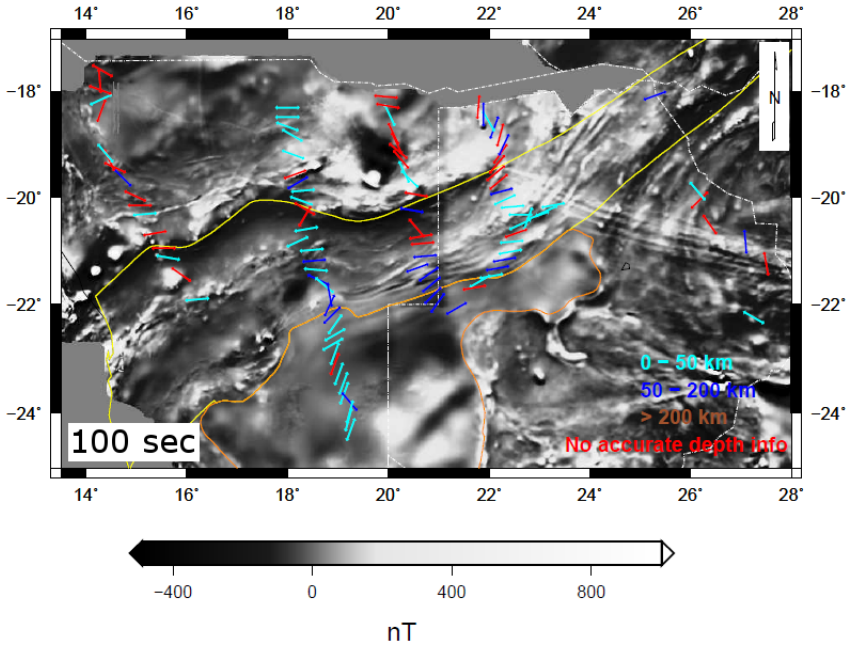


Figure 6.12: *Tipper strike angles calculated at 100 seconds for sites in profiles ETO, DMB, NEN, OKAWIN and ZIM where an H_z field was recorded, and the penetration depth ranges associated with the period.*

of the larger period values was calculated and assigned to the site. It was noted that the average calculated does not necessarily represent strike at lithospheric mantle depths, but does represent strike at depths greater than the crustal depth estimate associated with the longest of the periods where depth was approximated.

4. At sites where all five tipper strike values had unknown depths the average of the five values was calculated and assigned to the site with no depth specification.

It was important to retain tipper strike values even though their depth ranges were unknown, because it was more probable that unreliable responses and GB-errors greater than 2 were caused by noise in, and galvanic distortion of, the electric field rather than magnetic field in the given period range (see Sections 3.5.3 and 3.6.1). Therefore tipper strike values were assumed reliable even in the cases where their depth estimates, if calculated, would have been unreliable.

For comparison, and to provide added strike information at sites where there was uncertainty in depth, impedance strike angles were computed using Strike for the depth range $50 - 200$ km at sites where tipper data were avail-

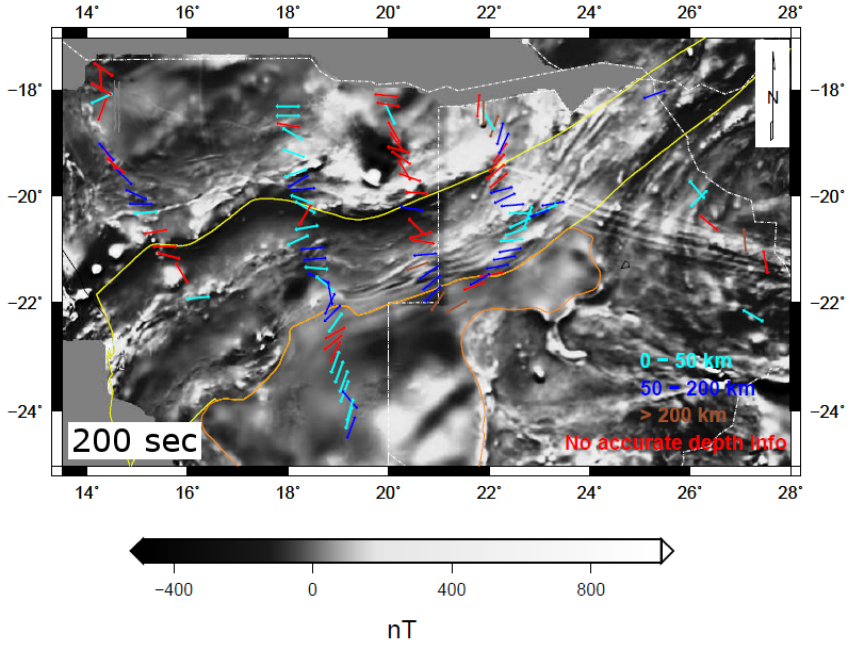


Figure 6.13: *Tipper strike angles calculated at 200 seconds for sites in profiles ETO, DMB, NEN, OKAWIN and ZIM where an H_z field was recorded, and the penetration depth ranges associated with the period.*

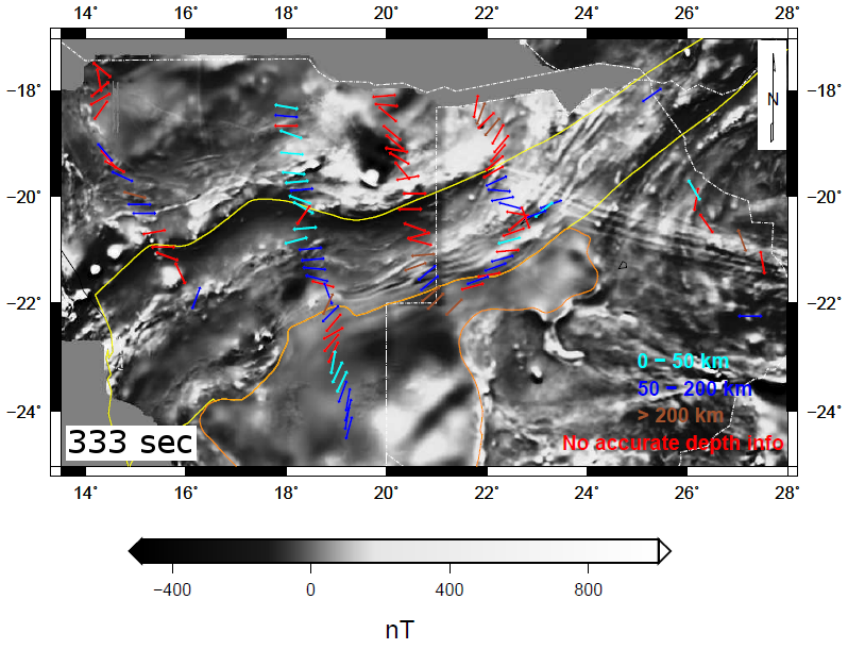


Figure 6.14: *Tipper strike angles calculated at 333 seconds for sites in profiles ETO, DMB, NEN, OKAWIN and ZIM where an H_z field was recorded, and the penetration depth ranges associated with the period.*

able (Figures 6.18 and D.8). Of all the impedance strike angles computed, only ones that had associated GB-errors less than 2 were used to replace

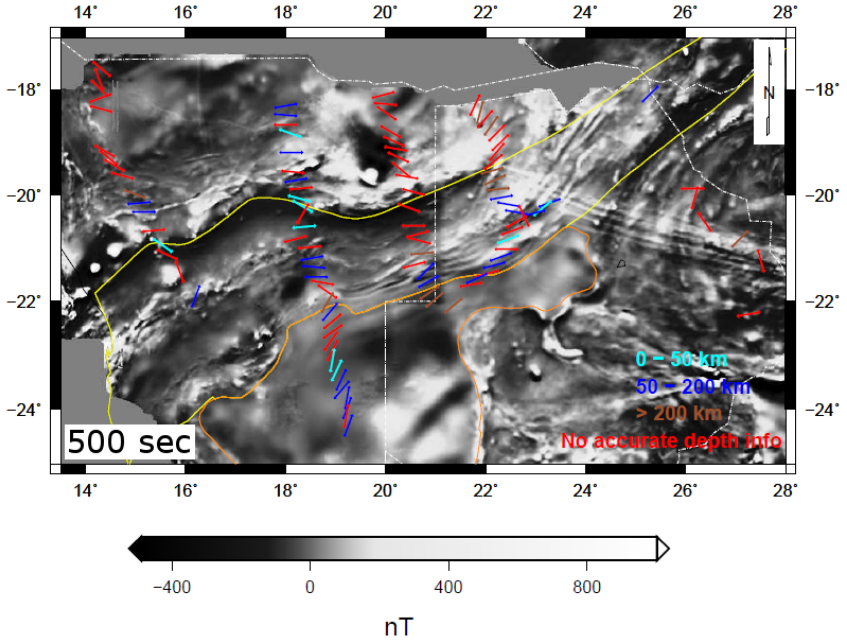


Figure 6.15: *Tipper strike angles calculated at 500 seconds for sites in profiles ETO, DMB, NEN, OKAWIN and ZIM where an H_z field was recorded, and the penetration depth ranges associated with the period.*

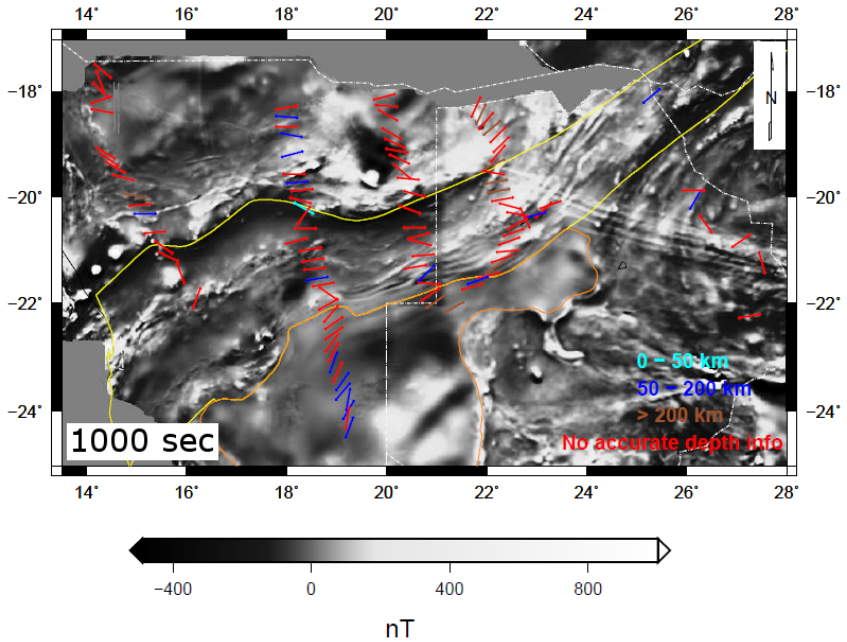


Figure 6.16: *Tipper strike angles calculated at 1000 seconds for sites in profiles ETO, DMB, NEN, OKAWIN and ZIM where an H_z field was recorded, and the penetration depth ranges associated with the period.*

tipper strike angles where depth was unknown, or depth was unknown but constrained to be deeper than a specific crustal value (Figure 6.18). Due to

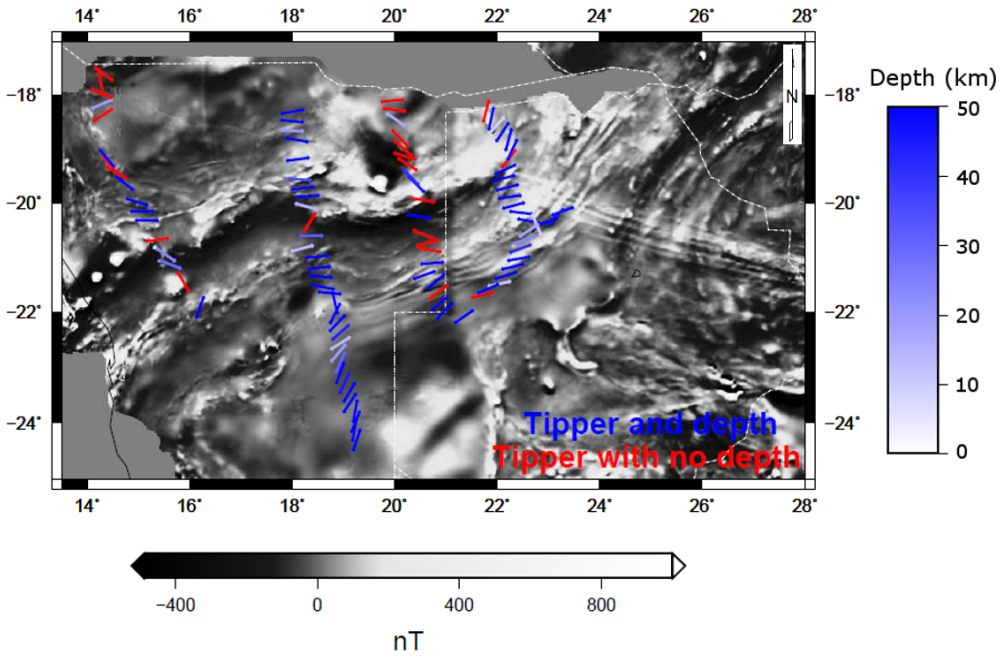


Figure 6.17: *Tipper strike angles obtained after averaging (see text) the five values calculated at 100, 200, 333, 500 and 1000 seconds at each site. The depths below which the strike values apply are indicated.*

diffusion related increase in lateral sensitivity with increasing depth, variations in strike from site to site (separated by approximately 20 km) should be subtle at lithospheric mantle depths. Hence, the substitute impedance strike values were compared with neighbouring tipper values, and, if an angle difference of greater than 45° was observed, the difference was ascribed to the ambiguity in impedance strike calculations and a 90° rotation was applied (Figure 6.18). None of the strike calculations for lithospheric mantle depths up to now were completed for the ZIM profile (Figure 6.1), because there were insufficient tipper data (Figures 6.12 to 6.16) and an inversion result for sub-crustal depths was not available.

The assumptions that all tipper strike angles that are unknown or not well constrained in depth samples structure at lithospheric mantle depths, leads to distinct regions of consistent strike (except for a few outliers) becoming clear. In all, nine regions of relatively consistent strike can be identified (Figure 6.19). The consistency and similarity in strike between two neighbouring sites, in the case where one is unknown in depth and the other is sampling structure at sub-crustal depths, means that both are probably sensing the same depth range (that is, sub-crustal). The ones which did not conform

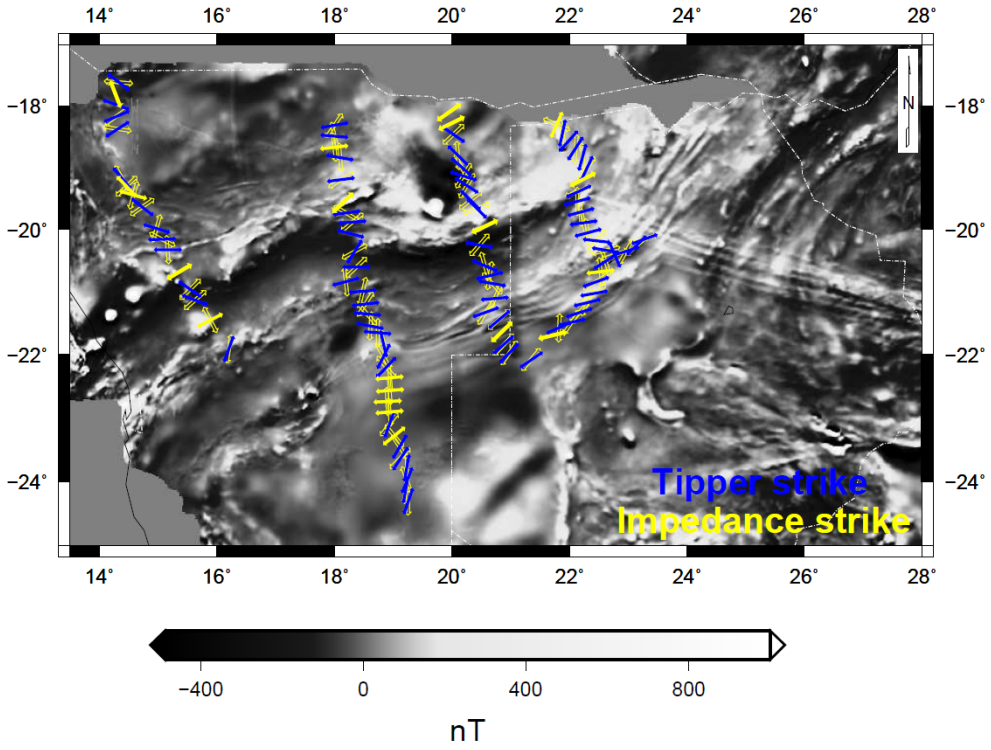


Figure 6.18: *Impedance (yellow) and tipper (blue) strike angles calculated for sites in northern Namibia and Botswana. Empty arrows indicate the original impedance strike angles calculated. Yellow arrows indicate impedance strike angles with GB-errors smaller than 2, that substituted tipper strike angles unknown in depth, or where depth was unknown but constrained to be below a certain crustal depth.*

to its neighbours, together with other outliers present, would be removed by averaging of strike angles in the nine regions.

A jacknife approach was used to calculate an appropriate average strike angle for each of the nine identified regions. Sequentially, each angle value was removed from its group and only the remaining values were used to compute an average and standard deviation. The standard deviations were compared, and the value, that when omitted, produced the lowest standard deviation was not included in the next round of calculations. The same process was repeated until only the two values that produced the lowest standard deviation together remained. In cases where there were a dominant strike and a few outliers with variable strike values present, the resultant plot of standard deviation versus number of values removed took on an L-shape. The average selected for each region was the value associated with the standard deviation at the 'elbow' of the curve. Averages of 132.94°, 89.17°, 88.50°, 20.54°, 58.93°,

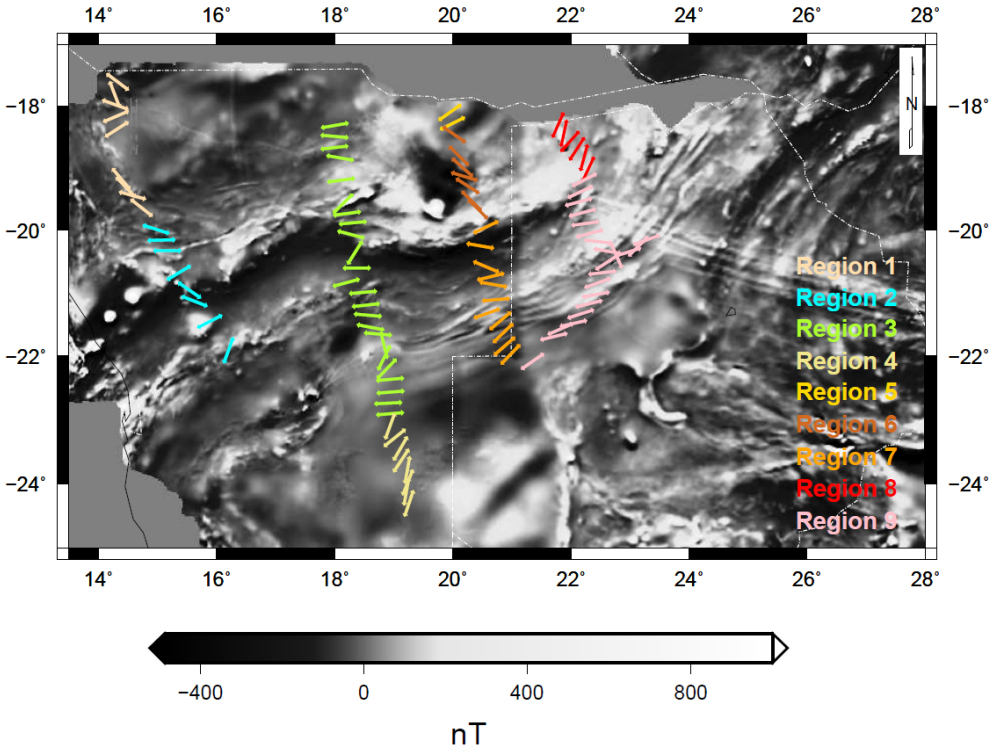


Figure 6.19: *Nine regions identified where strike appears approximately consistent over a number of sites.*

130.83°, 50.63°, 21.75° and 73.02° were selected for regions 1, 2, 3, 4, 5, 6, 7, 8 and 9, respectively (Figure D.9). The relevant assignment of angles and projections of profiles ETO, DMB, NEN and OKAWIN were made using the averages obtained (Figure 6.20).

6.4 Interpolation results

The projected data for both crustal and lithospheric mantle depths were imported onto a grid with cell dimensions 5 km by 5 km by 1 km (Figures 6.21 and 6.22). The horizontal dimensions of cells were made according to the average horizontal spacing between cells in the regional 2D profiles, which meant that information provided by the AMT profiles was aliased. The size of the interpolation kernel was $31 \times 31 \times 31$ cells. Only every fifth resistivity value in the vertical direction was used in calculation.

The interpolation tests showed that the integer b needed to be large (9 was used in testing) to allow for the angle term in equation (6.2) to have a comparable effect to the distance term (even when using a-values as small as

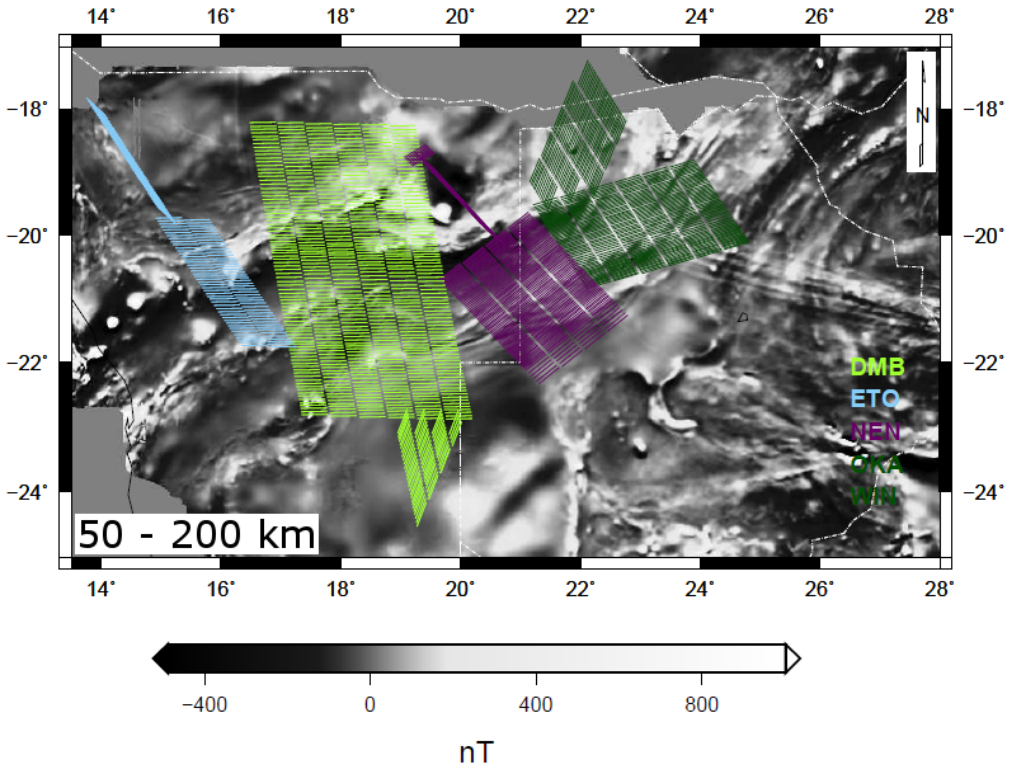


Figure 6.20: *Strike angles assigned to, and projection directions of, profiles ETO, DMB, NEN and OKAWIN for lithospheric mantle depths.*

1). In all the tests a good balance between the contributions of the distance and angle terms was found when $a = 4$ and $b = 9$. The good balance, when choosing $a = 4$ and $b = 9$, was most apparent in the extreme example where two adjacent and parallel profiles were given strike angles that differed by 60°, and the resultant interpolation was still successful (Figure 6.9). No two adjacent profiles in the SAMTEX data (Figures 6.11 and 6.20) contain such great differences in strike and thus the values $a = 4$ and $b = 9$ were also used in the interpolation of the SAMTEX data. Calculations started at a depth of 1 km and continued with the distance between two successive calculations gradually increasing with depth, similar to the increase in vertical cell size with increasing depth in an inversion mesh (see Appendix E for the specific depths used).

Figures 6.23 and 6.24 depict interpolation results of SAMTEX data at depths of 20 km and 120 km, respectively. Artifacts related to vertical smearing in between profiles (Figures 6.6c and 6.10) were apparent at crustal depths, but disappeared deeper into the lithosphere (Figures 6.23 and 6.24).

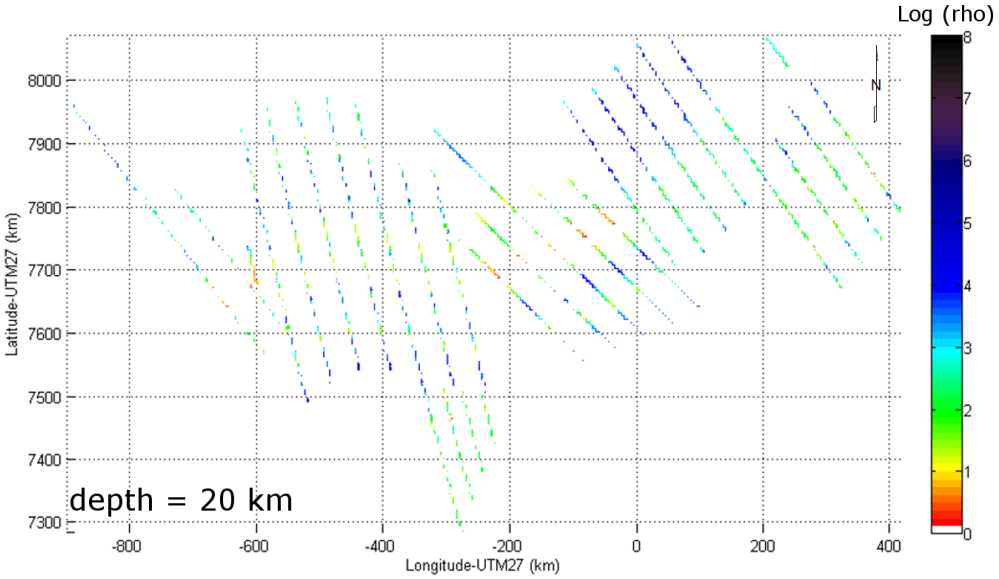


Figure 6.21: *Resistivity values associated with the projected SAMTEX profiles at a depth of 20 km, imported onto the interpolation grid with cell dimensions 5 km by 5 km by 1 km. Projected profiles are separated by 40 km in the direction of regional strike.*

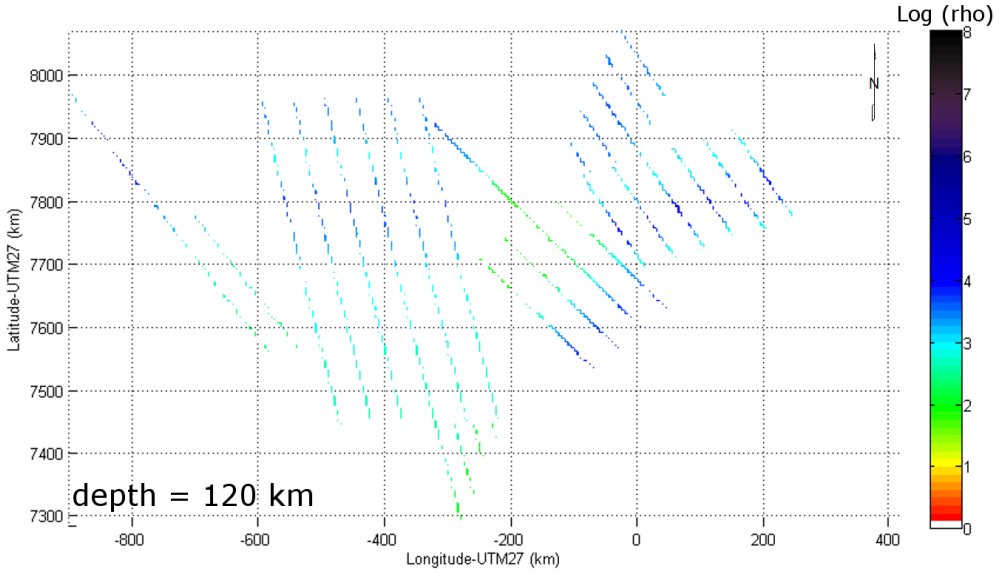


Figure 6.22: *Resistivity values associated with the projected SAMTEX profiles at a depth of 120 km, imported onto the interpolation grid with cell dimensions 5 km by 5 km by 1 km. Projected profiles are separated by 40 km in the direction of regional strike.*

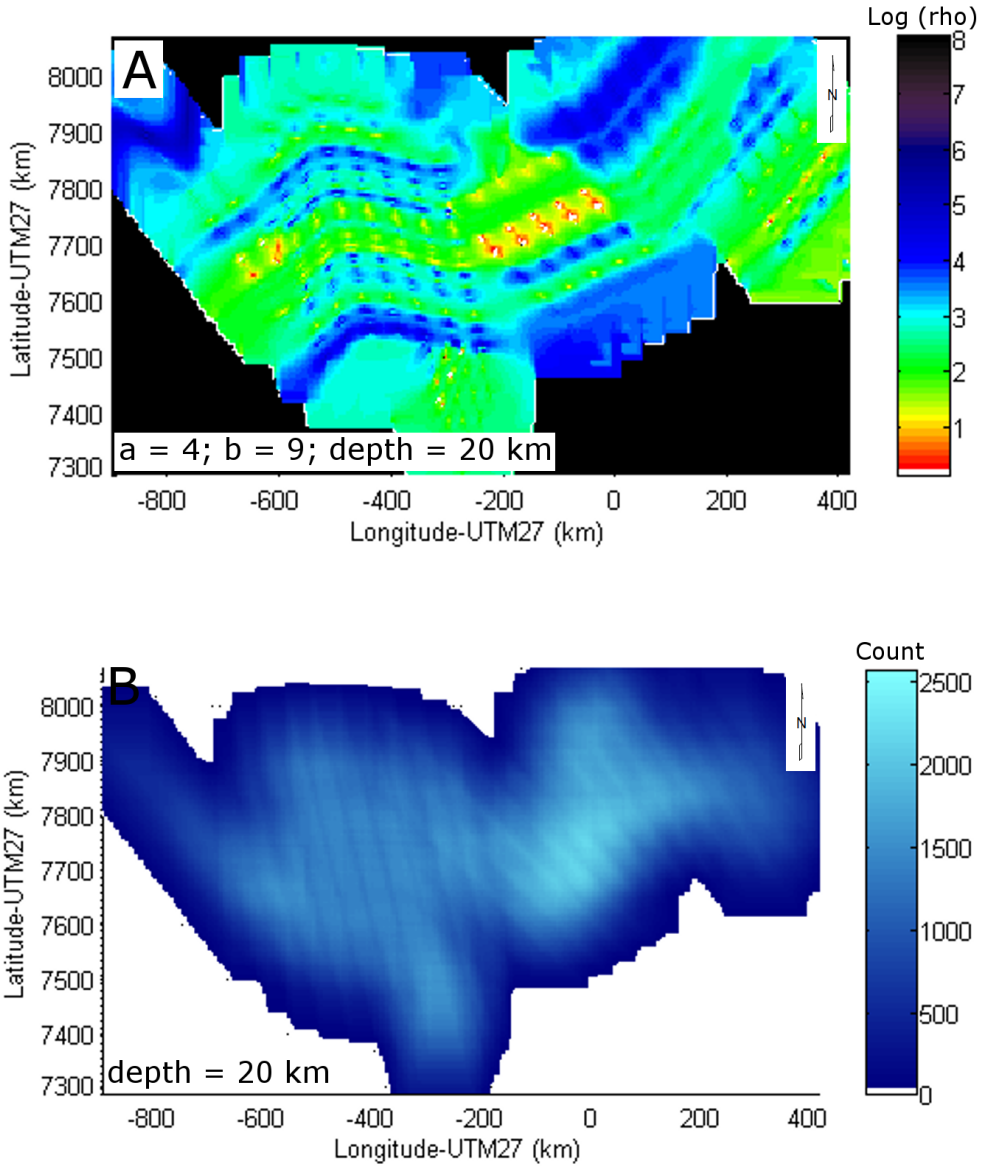


Figure 6.23: *Interpolation results at 20 km depth (a) and the number of resistivity values used in each calculation (b, n in equation 6.2). The cells for which n was 0 were given a resistivity of* 1×10^8 $\Omega.m$ *(a).*

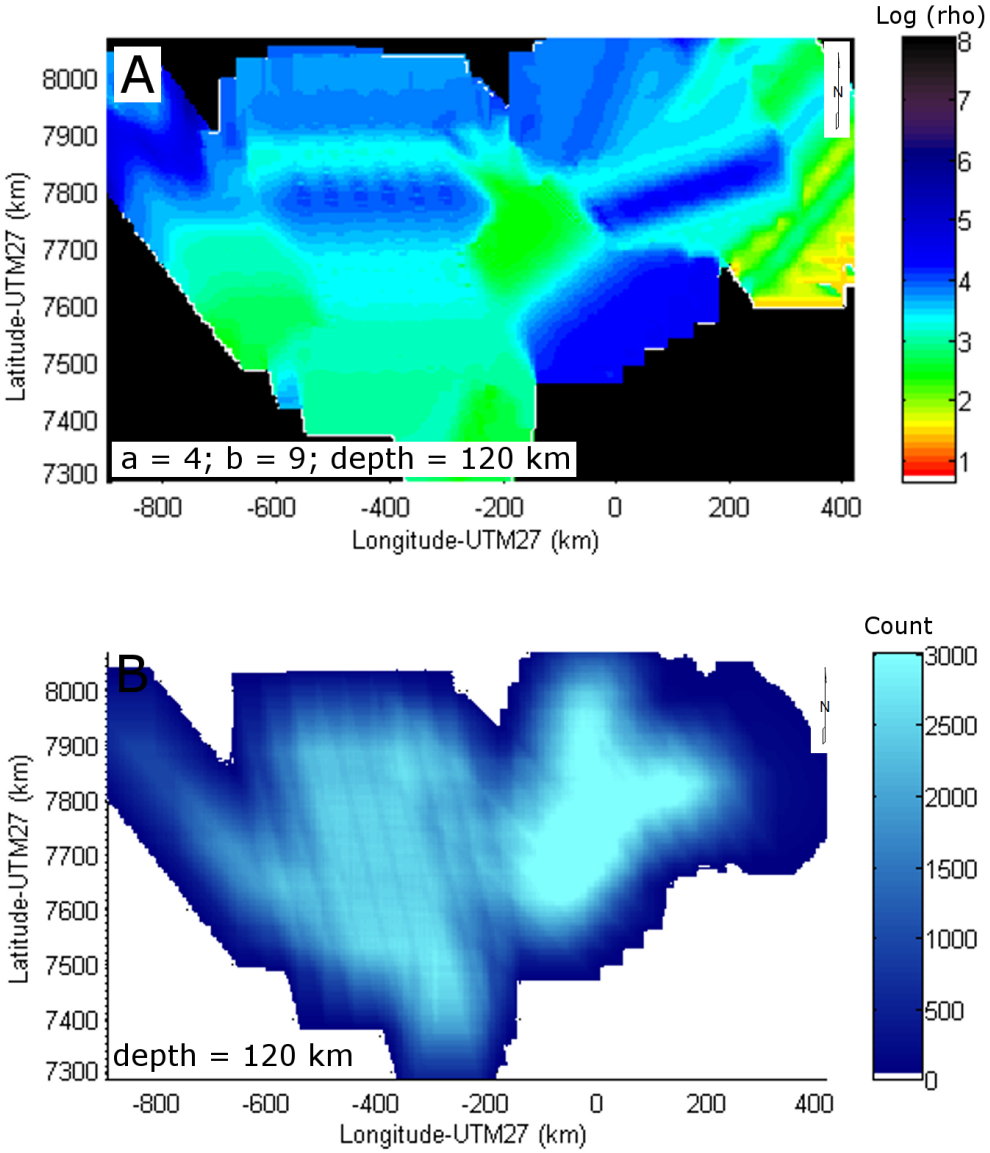


Figure 6.24: *Interpolation results at 120 km depth (a) and the number of resistivity values used in each calculation (b, n in equation 6.2). The cells for which n was 0 were given a resistivity of* 1×10^8 $\Omega.m$ *(a).*

Chapter 7

DC forward modelling

The 3D resistivity model representative of northern Namibia and Botswana produced in Chapter 6, can now be used to investigate the preferential flow of DC current within the Earth between the Otjiwarongo and Katima Mulilo regions. RES3DMOD[1] by Dr. M. H. Loke was the DC forward modelling program used in the current study. The program utilizes the finite difference method (Dey and Morrison, 1979) in calculation, and is able to generate solutions for various electrode configurations, including Schlumberger, Wenner and dipole-dipole. The decrease of potential away from a point of current injection, similar to measurements made with the mise-á-la-masse method (Parasnis, 1967 and Telford et al., 1990, pp. 538-539), can also be extracted from the program's output. The extracted potentials were used in the current study as indicators of return current flow between the Otjiwarongo and Katima Mulilo regions.

7.1 Program input

The input for RES3DMOD encompasses rectangular grids of numbers, each number having an associated resistivity value, at several depth levels, specified in the input file, where the distance between consecutive levels increase with increasing depth. Because only integers $0-9$ were allowed in the input file, the multitude of interpolated resistivity values had to be separated into 10 groups. The separation was done such that each integer had approximately the same number of resistivity values allocated to it (Figure 7.1). After separation, the number of interpolated resistivity values was decreased, because the maximum total number of electrodes allowed in RES3DMOD was 4624.

[1] see `http://www.geoelectrical.com/downloads.php`

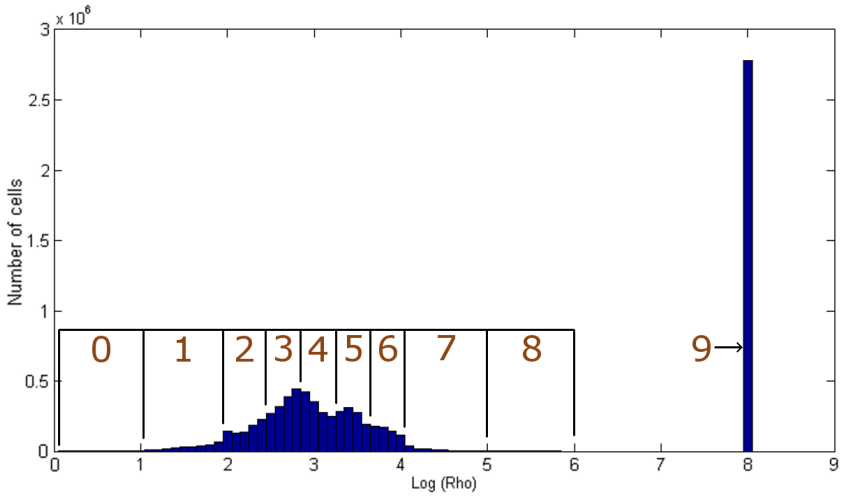


Figure 7.1: *A histogram of the interpolated resistivity values and division of the values into 10 groups.*

In RES3DMOD, electrodes are assigned to the rectangular grid such that, starting at the edges, neighbouring pairs of integers (in both horizontal directions) are separated by one electrode. Hence, in addition to removing interpolated resistivities, the number of integers, in both horizontal directions, was also made even before import.

7.2 Modelling results

When DC current is injected into a homogeneous conductivity region at a point, the lines of equipotential are circular with the injection point at its centre (Parasnis, 1967). In a higher dimensional region, distortion of the circular equipotentials gives an indication of preferential current flow. To observe if the equipotentials would also be affected by the edges of the input grid used, the potential drop-offs, when current was injected in the Otjiwarongo region, of three different sized grids were compared (Figure 7.2a, b and c). The sizes of the three grids were 40 km by 40 km (Figure 7.2a), 80 km by 80 km (Figure 7.2b) and 930 km by 480 km (Figure 7.2c). The latter was the regional scale grid used to investigate return current flow between the Otjiwarongo and Katima Mulilo regions. Only structure at crustal depths $(0 - 50$ km) was used in the forward computations of the three grids.

The results show that there are in fact discernable differences in the solutions when using different sized grids but the same injection points. Thus, care

must be taken when making inferences about calculated potentials close to the edges of models.

The extent to which the return DC current is confined to shallow depths was explored by varying the amount of depth information provided during forward modelling. Different potential drop-offs were obtained when including structure up to mid-crustal ($0-24$ km), crustal ($0-50$ km) and lithospheric mantle depths ($0-200$ km)(Figures 7.3 and 7.4). Forward solutions with different depth information were obtained with current being injected in both the Otjiwarongo (Figure 7.3) and Katima Mulilo regions (Figure 7.4).

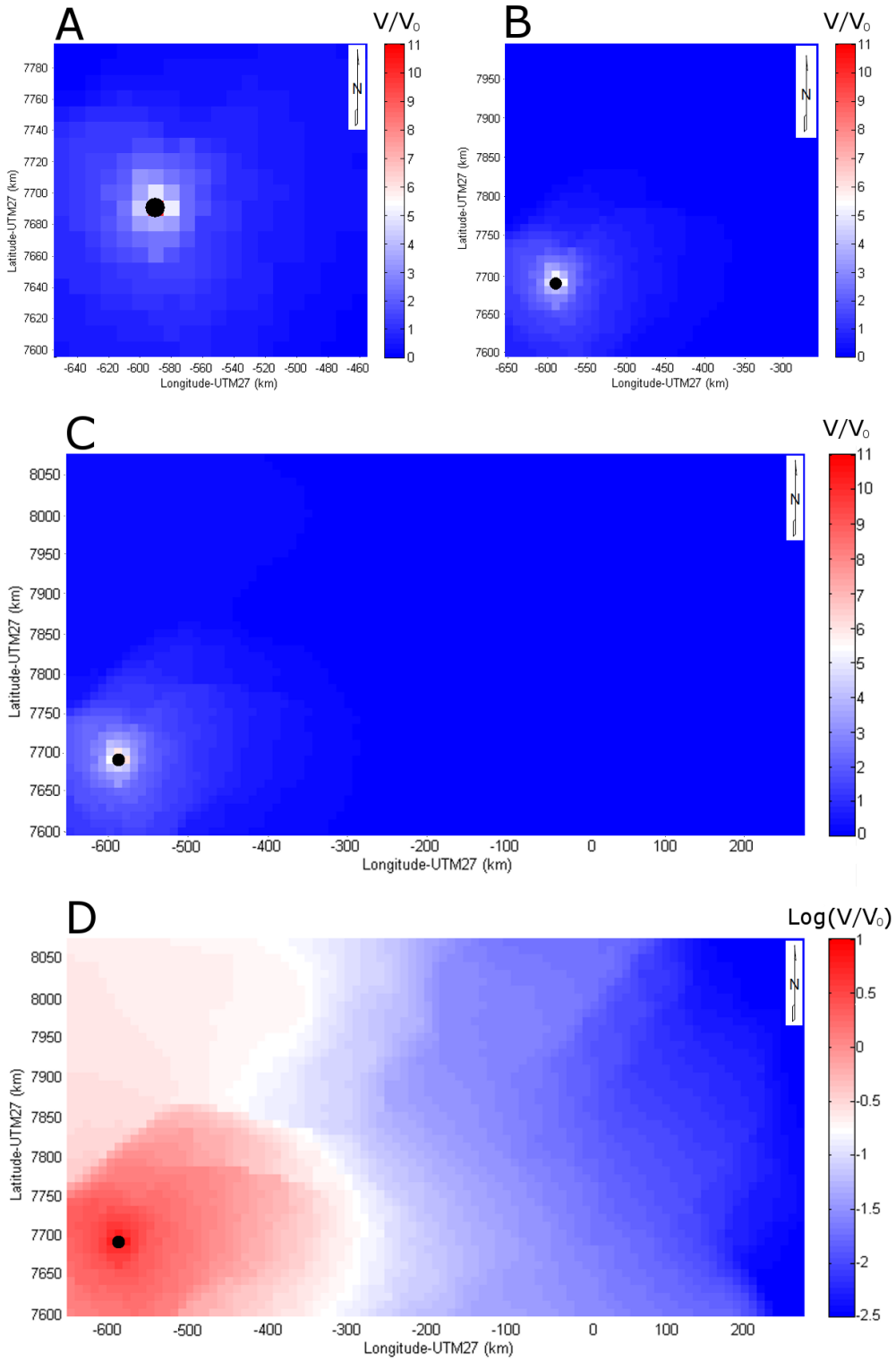


Figure 7.2: *A comparison of normalized potential values (V_0 is the equivalent potential when using a 1 m electrode spacing) where the same injection point (black dot) but different input grid sizes were used (a, b and c). Also, plotting the logarithm of the normalized potentials depicts the prefered flow of the DC current more clearly (d). All calculations were done with only structure at crustal depths included.*

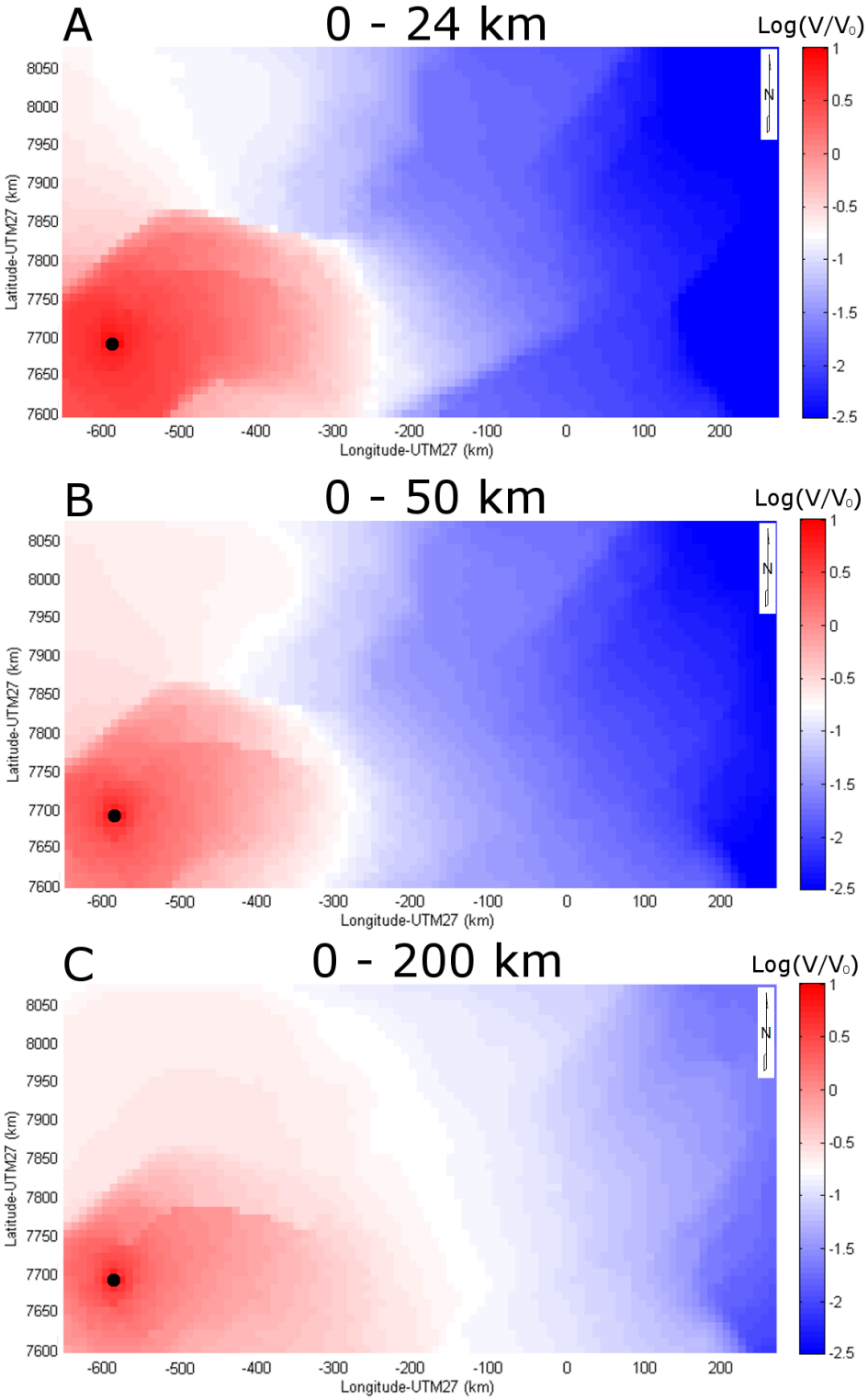


Figure 7.3: *Resulting normalized potential values after current was injected in the Otjiwarongo region (injection point indicated with black dot) and structure up to mid-crustal (a), crustal (b) and lithospheric mantle (c) depths included.*

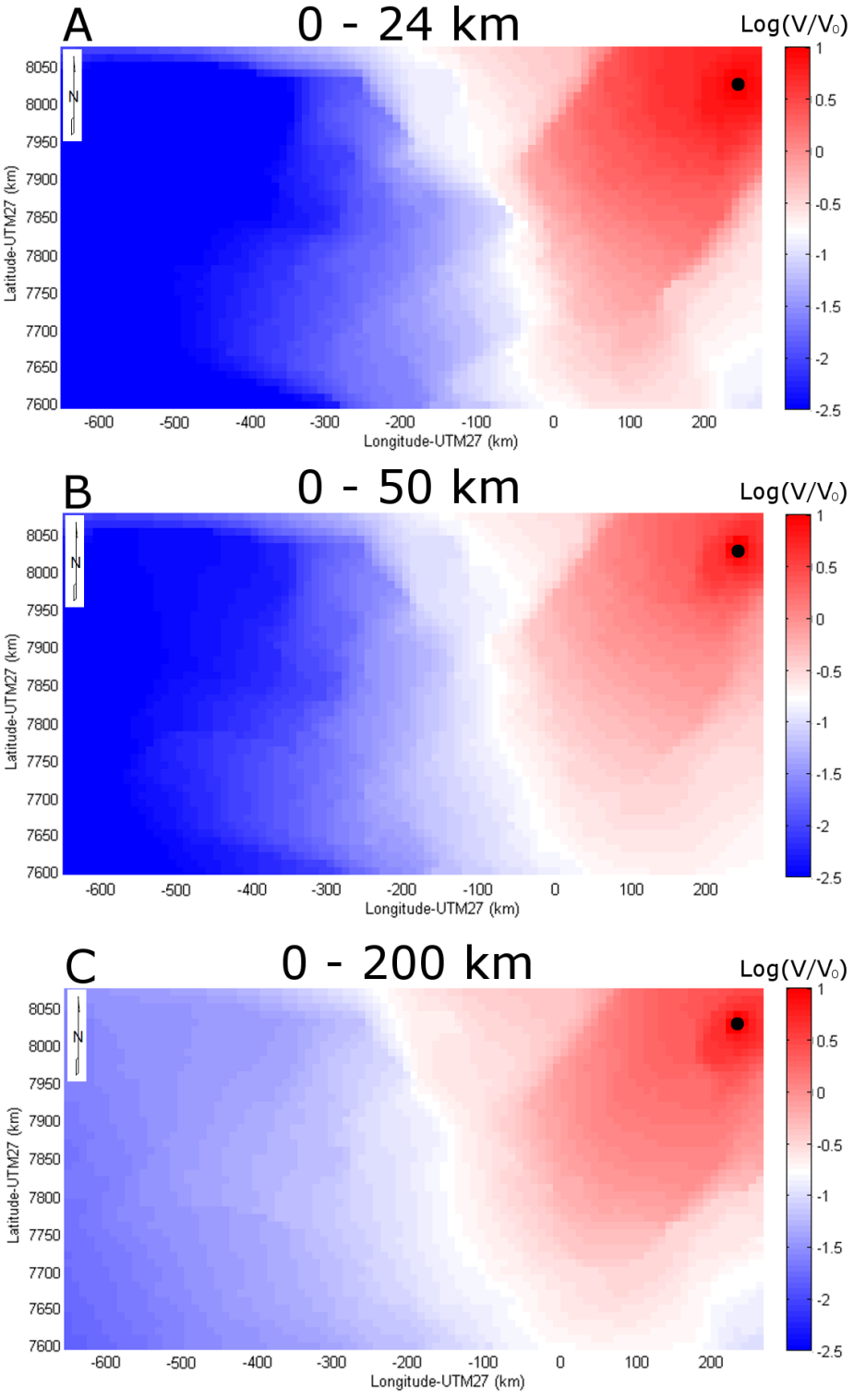


Figure 7.4: *Resulting normalized potential values after current was injected in the Katima Mulilo region (injection point indicated with black dot) and structure up to mid-crustal (a), crustal (b) and lithospheric mantle (c) depths included.*

Chapter 8

Discussion and conclusions

8.1 Placement of earth electrodes

The successful placement of a HVDC earth electrode only depends on the conductivity of rock volumes near the surface and in close proximity to the electrode (Thunehed et al., 2007 and de Beer, 2009, pers. comm.). Therefore, thorough evaluations of conductivity variations in the shallow subsurface associated with the Otjiwarongo and Katima Mulilo regions, especially where AMT data are available, need to be completed before a decision on electrode placement is made.

8.1.1 Otjiwarongo region

Consider the standard grid and uniform grid Laplacian inversion results of the Otjiwarongo region (Figures 5.5 and 5.7). It is clear from the two inversions, which are in agreement, that of all sites included in the inversion, the shallow subsurface is most conductive below sites ELG005 and ELG004. Despite similar structures surrounding sites ELG005 and ELG004 in the two models, the uniform grid Laplacian inversion is used for further testing, because although in the standard grid Laplacian model greater emphasis is placed on resolving shallow structures, and the TM mode responses (providing information about conductivity boundaries) are not weighted down during inversion (see Sections 5.3 and 5.5), sites ELG005 and ELG004 also have higher misfits (compared to neighbouring sites) in the latter model. The robustness of the high conductivity beneath sites ELG005 and ELG004 in Figure 5.7 were tested by assigning high resistivities to all cells above 5 km depth and running the inversion again (using the inversion settings specified

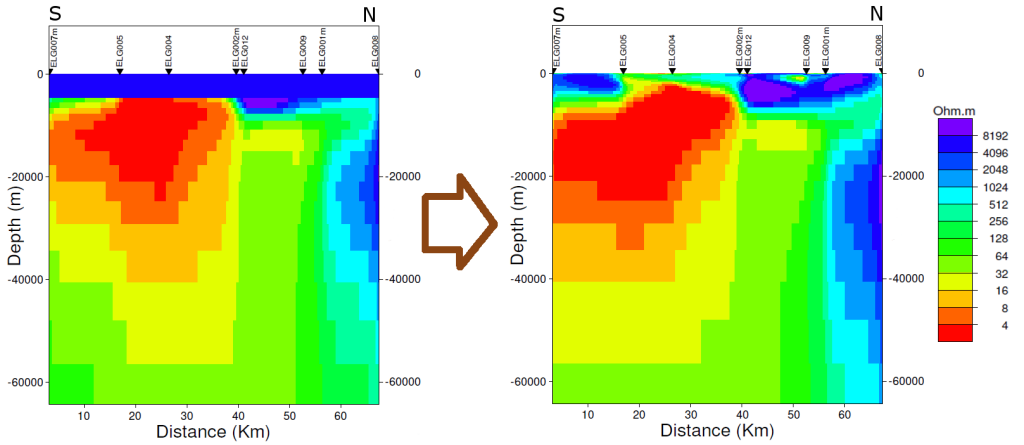


Figure 8.1: *Uniform grid Laplacian inversion result (right) after placing a 5 km thick resistive layer at the top of the original Otjiwarongo inversion model (left).*

in Section 5.5)(Figure 8.1). The resulting model shows that across the profile the conductivity remains the highest beneath sites ELG005 and ELG004 (Figures 8.1).

According to the currently available geological information in the Otjiwarongo region (Figure 1.8), site ELG004 is situated on undifferentiated Damara Sequence (NDA in Figure 1.8), whereas site ELG005 is located on Nosib Group rocks, consisting of quartzite, arkose with conglomerate and ironstone (NNS in Figure 1.8, Tankard et al., 1982, p. 317). It is unclear what the cause of the high conductivity beneath site ELG004 is, whereas the localized ironstone is the most probable cause of high conductivity beneath site ELG005. In addition, from detailed geology (Figure 1.8) and magnetic data (Figure 1.2) it is clear that the Nosib Group rocks are not confined to a small area containing site ELG005, but persist for kilometres in all directions. Hence, for large distances the conductivity is known to be high around (deduced from geology and magnetics) and beneath (observed in the inversion models) site ELG005. Therefore, site ELG005, rather than site ELG004, is proposed as an optimal location to place the HVDC earth electrode in the Otjiwarongo region.

8.1.2 Katima Mulilo region

The selection of an appropriate location for an earth electrode in the Katima Mulilo region is a case of finding the best solution out of a series of good

ones, because most of the shallow subsurface beneath sites included in the inversion is conductive (Figure 5.6). The option regarded as best will be the one where conductivity, determined in a quantitative way, is highest.

To test the robustness of all conductive structures present, resistivities in the shallow subsurface (up to 1 km) were substituted with a thin resistive layer and the inversion (using the inversion settings specified in Section 5.5) was run again (Figure 8.2). The resulting inversion model is similar to the original and both show that beneath sites RAK054, ELZ294, RAK053, ELZ102m and CPV029 the conductivity is highest (Figure 8.2).

Owing to the lack of detailed geological information in the Katima Mulilo region, attributed to the vast Kalahari sediment cover (Moore and Larkin, 2001 and Singletary et al., 2003), geology cannot be used to facilitate the choice of an appropriate electrode location. A choice based solely on the conductivity information gathered from the MT data must be made. Due to the approximate 1D behaviour of data in the AMT frequency range (Figures 4.4 and 4.8), 1D inversion tools can be used to observe conductivity variations with depth below each site. Subsequently, NB-resistivities (equation 3.74) were computed for the AMT sites at depths of 100 m, 200 m, 500 m, 900 m and 1000 m (Figure 8.3). The 1D inversion results show that the conductivities of regions including sites ELZ102m and ELZ103 are consistently high at all depths calculated (Figure 8.3). Other sites also have highly conductive subsurfaces (as expected), but the conductivities are not consistently high at all depths. In addition, at the shallowest depths, the conductivity beneath site ELZ103 is highest.

The shallow subsurface beneath ELZ102m was also indicated as highly conductive in the 2D inversion model. Its neighbouring site in the model, RAK053, which had a similar high conductivity subsurface, is situated, in plan view (Figure 5.1), between it and site ELZ103. In light of the similarities between 1D and 2D inversions of the Katima Mulilo data, regarding the high conductivity shallow subsurfaces beneath sites ELZ102m, RAK053 and ELZ103, the region enclosing the three sites is deemed most appropriate for earth electrode placement.

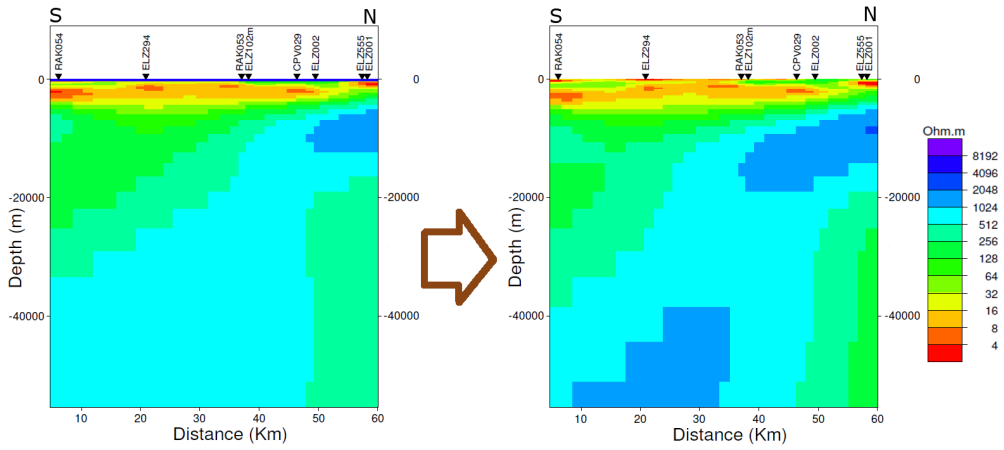


Figure 8.2: *Uniform grid Laplacian inversion result (right) after placing a thin 1 km resistive layer at the top of the original Katima Mulilo inversion model (left).*

8.2 Interpretation of 2D inversion results

8.2.1 Otjiwarongo inversion

The two most prominent conductivity features in the Otjiwarongo region, determined by 2D inversion of the data (Figures 5.5 and 5.7), were a surficial discontinuous resistive layer and a mid-crustal conductor. Both were determined to be robust features.

The Otjiwarongo area is characterized by large volumes of metamorphic rocks and sparse intrusive igneous complexes (Figure 1.8). By combining knowledge of geology and the factors controlling conductivity (see Section 2.1), it can be concluded that resistive shallow rocks as measured, are unfractured (not fluid-filled, van Zijl and de Beer, 1983), and do not contain interconnected highly conductive materials.

The same metamorphic rocks exposed at the surface continue to mid-crustal depths (Gray et al., 2006), but, in contrast, the conductivity, along most of the 2D profile, increases significantly. Of the possible explanations for the observed high conductivity, the presence of large quantities of fluid can be ruled out because the pressure at mid-crustal depths is too high (see Section 2.2). Although there has been volcanic activity in the past (attested by the presence of igneous intrusions) there is none at present. Thus, the presence of

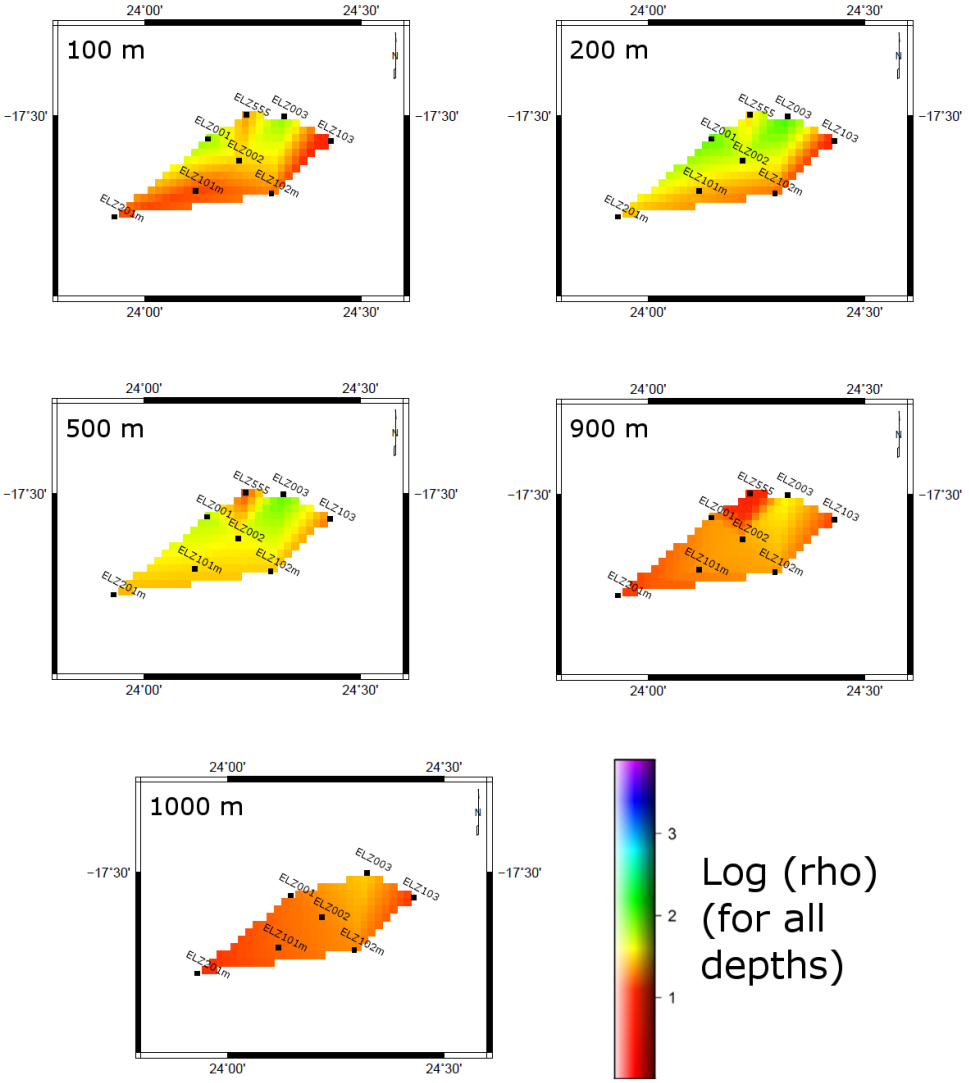


Figure 8.3: *NB-resistivities calculated for the Katima Mulilo AMT sites at depths of 100 m, 200 m, 500 m, 900 m and 1000 m.*

partial melt can also be ruled out as a possible cause of the high conductivity. The relatively low temperatures at mid-crustal depths means that temperature is also an unlikely cause, leaving only the presence of interconnected highly conductive materials as a possible reason for the high conductivity at mid-crustal depths (see Section 2.1).

A comparison of localities of the Otjiwarongo array and the conductive belt in northern Namibia and Botswana, indicates that most of the array overlies the belt (Figure 8.4). The Otjiwarongo conductor is also situated at the same mid-crustal depth range characteristic of the conductive belt. Therefore,

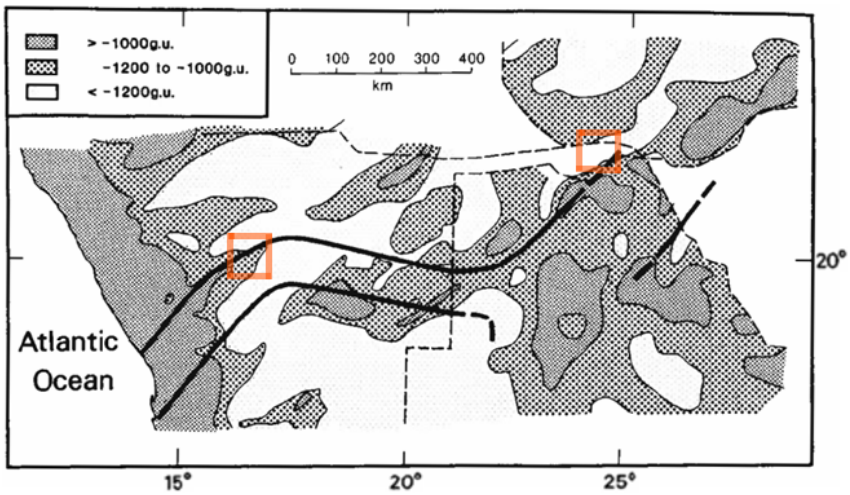


Figure 8.4: *The Otjiwarongo (left square) and Katima Mulilo (right square) study regions relative to the proposed conductive belt (van Zijl and de Beer, 1983).*

it can be confidently concluded that the conductive belt exists below the Otjiwarongo area and the MT data have substantiated its existence. The materials suggested to be the cause of high conductivities observed in the belt, were magnetite (produced by serpentinization of the DMB rocks, van Zijl and de Beer, 1983) and graphite, correlated with marble units present in shear zones (Ritter et al., 2003). In the Otjiwarongo region, marble units (NSWm in Figure 1.8) are also present, and are contained in undifferentiated Swakop Group rocks associated with the regional shear zone traversing the study area. The shear zone manifests itself, on surface, as the Autseib Fault (Figure 8.5), and extends for large distances in the direction of regional DMB strike. Interestingly, the MT profile of Ritter et al. (2003) intersected the same shear zone (Figure 2.7b), and the graphite-model, explaining the high conductivity in the resultant inversion model (Figure 2.7b), was based on the presence of the Autseib Fault and other shear zones (see section 2.4). Hence, it is concluded that interconnected graphite is also associated with marble units in the Otjiwarongo region, and it is the cause of the high conductivity of the mid-crustal conductor.

8.2.2 Katima Mulilo inversion

The most prominent feature in the Katima Mulilo inversion model (Figure 5.6) was a surface conductive layer which varied in thickness. Penetration depths of the EM energy at each site (Figure 5.12) indicated that the

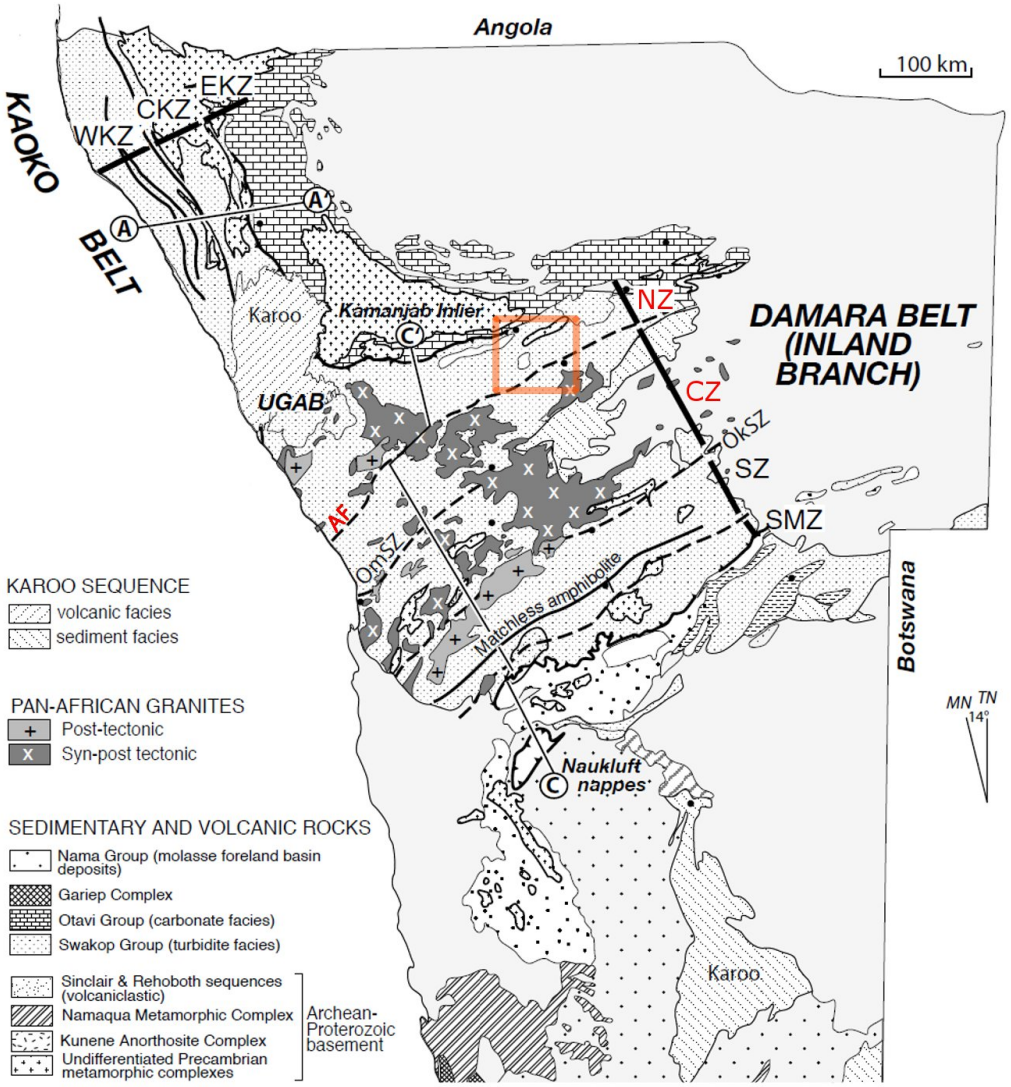


Figure 8.5: *A regional geological map of central and northern Namibia (modified from Gray et al., 2006) showing the Autseib Fault crossing the Otjiwarongo region and separating the Northern (NZ) and Southern (SZ) Zones of the DMB.*

high conductivities measured were not artifacts of inversion (that is, artifacts caused by inadequate penetration of energy at shallow depths), but that high conductivity rocks indeed existed at upper crustal levels. While its existence is beyond doubt, its horizontal continuity is questionable, because, in general, the distance between neighbouring sites is greater than the depth of the conductive layer.

High conductivities at the uppermost subsurface are attributed to porous sediments of the Kalahari Group (see Section 2.2). However, Kalahari sedi-

ments in the Katima Mulilo area have a maximum thickness of $100 - 200$ m (Thomas and Shaw, 1990). Therefore, there exists an alternate reason for the high conductivities observed deeper down. A cause similar to the one responsible for the DMB conductive belt appears unlikely, because the Otjiwarongo area does not coincide with any region covered by the conductive belt (Figure 8.4), and the Katima Mulilo conductive layer is confined to the upper crust, while the belt is a mid-crustal phenomenon. If materials associated with shear zones (Coward and Daly, 1984) in the Katima Mulilo region are the cause of the anomalous conductivity, similar to graphite-bearing shear zones in Namibia, then the shear zones present would have to be near horizontal. However, due to the high grades of metamorphism present in the DMB (which also increases to the north-west, Singletary et al., 2003), it can be deduced that horizontal shear zones are implausible and near vertical ones more realistic.

Clastic and carbonate rocks of the Ghanzi Group, existing within the Northwest Botswana rift, directly underlie the Kalahari sediments (see Section 1.4). It is possible that the clastic and carbonate rocks are fractured and fluid-filled at upper crustal depths, but in Namibia the shallow DMB rocks have been found to be unfractured (van Zijl and de Beer, 1983; Ritter et al., 2003 and Section 8.2.1), and the depositional and deformational histories of DMB rocks in Namibia and Botswana are alike. The Ghanzi Group is, in part, an extension of the Nosib Group, which contains localized ironstone (Tankard et al., 1982, p. 317), that has been found to be conductive (see Section 8.1.1). Ironstone has also been discovered in the mobile belts in Botswana (Hutchins and Reeves, 1980 and Kampunzu et al., 2000). If the assumption is made that ironstone is also present, and confined to, the Ghanzi Group, then the first piece of supporting evidence is the similarity between the thickness of the Ghanzi sequence in northern Botswana, $6 - 7$ km (Kampunzu et al., 2000), and the maximum thickness of the observed conductive layer (approximately 6 km). Consequently, and in light of the limited information available due to the Kalahari sediment cover, the hypothesis is made that ironstone is present in the Ghanzi Group, and it is the cause of the observed high conductivity at upper crustal depths (not including the shallowest depths).

8.3 Interpolation results

In Chapter 6 the assumption was made that due to long range structural trends observed in regional geology and mainly magnetic data, that conductivity would also be continuous over large distances. Imperative evidence for the continuity in conductivity within the DMB was the existence of a conductive belt discovered in the 1970s using geomagnetic arrays (de Beer et al., 1982), which essentially track current flow in interconnected bodies. Trends in regional geological and magnetic data are evidence of structural continuity at crustal depths (Figure 6.11) and not lithospheric mantle depths. However, subsequent tipper and impedance strike analyses of MT data over the lithospheric mantle depth range showed that conductivity structure was linear along large parts of the SAMTEX profiles (Figure 6.19), and thus, because of diffusion related lateral sensitivities, also continuous for large distances away from profiles. Tipper and impedance strike analyses could have been completed for structure at crustal depths as well, but would have been less successful, because at shallow depths MT data give information regarding local, rather than regional, trends in structure.

Apparent from the interpolation results, and 2D inversion models used during interpolation, is the presence of highly conductive structures at mid-crustal depths within the DMB (that is, MT data confirming the conductive belt, Figure 6.23). The conductivities, albeit remaining high, varied from profile to profile, and interestingly, appeared in various regions to be discontinuous along profile (Figure 6.23). Encouragingly, by using trends in regional geology and magnetics as the projection directions for profiles at crustal depths, good continuity was achieved between the high conductivity regions in the various profiles.

8.4 DC return current flow

In the case where the Otjiwarongo-Katima Mulilo HVDC powerline is operated in monopolar mode, large amounts DC current will be injected into the Earth at the electrode locations. One of the aims of the current study was to practically apply the AMT and BBMT data in the Otjiwarongo and Katima Mulilo regions to find suitable locations for the placement of the HVDC earth electrodes. A second more theoretically orientated aim, was to deter-

mine where the DC return current would flow between the two electrodes, after being injected into the Earth.

Following injection, DC current will flow along the paths of least resistance (R)(de Beer, 2009, pers. comm.):

$$R = \frac{\rho l}{A}, \tag{8.1}$$

where ρ is resistivity, l is the distance of flow and A is the cross-sectional area perpendicular to the direction of flow. The translation of equation (8.1) into current flow within a large scale conductivity region, could be observed from the potential values calculated after currents were injected at locations within the Otjiwarongo and Katima Mulilo regions (Figures 7.3 and 7.4). The minimization of ρ in equation (8.1) is apparent in the fact that currents, for $200 - 300$ km away from the injection points (Figures 7.3 and 7.4), flow mostly within the highly conductive parts of the DMB. As more structure was added at depth, the currents, while still mostly flowing within the DMB, became more spread out laterally, indicative of attempts to maximize the vertical cross-sectional area perpendicular to the direction of flow. The preferential flow of DC currents in straight lines, rather than curved, is deducible from the confinement of currents within the DMB over larger distances when injected in the Katima Mulilo region (where the DMB was generally more resistive, Figures 6.23 and 6.24), compared to when injected in the Otjiwarongo region (compare Figures 7.3 and 7.4).

Taking into account equation (8.1) and the calculated potentials, using the interpolated resistivity model, there are a few concluding observations that can be made. Firstly, irrespective of the amount of resistivity-depth information made available, the preferential flow of DC current remains within the conductive DMB for approximately $200 - 300$ km, starting from the injection point and following regional trends in the DMB. However, the possibility that the distance of $200 - 300$ km would become less if resistivity structure at greater than 200 km depth was included cannot be discarded. The aforementioned is verified by the fact that the Otjiwarongo and Katima Mulilo regions are approximately 850 km apart, and subtle potential differences were noted with the addition of conductivity information at greater depth in the current study (Figures 7.3 and 7.4). Secondly, beyond $200 - 300$ km the flow of current commences along no prefered path, as evidenced by the

equal potential values along the perpendicular to the line connecting the Otjiwarongo and Katima Mulilo injection points (Figures 7.3 and 7.4). Invariant potentials have also been measured experimentally along the perpendicular at the centre of the line connecting the Cahora Bassa electrodes, during the powerline's use for deep Schlumberger soundings in the 1970s (van Zijl and Joubert, 1975).

It must be noted that the potential values extracted from the output file after forward modelling, were calculated with the first electrode situated at the injection point and the second placed an infinite distance away. Therefore, in the present case, different potential values (although only slightly different) would be obtained if it was possible to specify that the second electrode in Figure 7.3, for example, be located in the Katima Mulilo region (and vice versa for Figure 7.4). In particular, potential differences would be identifiable in the area surrounding the second electrode, where current starts to gather and return to the surface again. Because of the grid size restrictions in RES3DMOD (see Section 7.1), current flow was partially constrained by limiting the grid size to an area small enough, such that it only includes the Otjiwarongo and Katima Mulilo regions (see Figure 7.2 for effects related to changing the grid size).

Chapter 9

Summary and recommendations

Appropriate locations for the HVDC earth electrodes in the Otjiwarongo and Katima Mulilo regions were selected based on available MT and geological data in the two areas. The locations chosen, that had the most conductive shallow subsurfaces, were the areas surrounding site ELG005 and including sites ELZ102m, RAK053 and ELZ103 in the Otjiwarongo and Katima Mulilo regions, respectively.

2D inversion results of the Otjiwarongo data indicated that most of the shallow subsurface in the area was resistive while highly conductive structures existed at mid-crustal depths (Figures 5.5 and 5.7). It was concluded that the high resistivities of the shallow metasedimentary and meta-igneous rocks meant that the surficial rocks did not contain traces of fluid or other conductive materials. The mid-crustal conductor was shown to form part of the larger conductive belt in the DMB, and the cause of the high conductivity in the belt locally was interconnected graphite associated with marble contained in the existent shear zone.

1D and 2D inversion models representative of the Katima Mulilo subsurface provide evidence for the presence of a conductive layer at upper crustal depths, that varied in thickness, and reached a maximum depth of $6 - 7$ km below site ELZ294 (Figures 8.3 and 5.6). High conductivities at the uppermost subsurface were ascribed to fluid-filled sediments of the Kalahari Group. The most plausible reason for the high conductivity deeper down in layer was hypothesized to be ironstone present in the Ghanzi Group.

The researcher was informed that, in addition to AMT data, helicopter EM surveys were also completed in the Otjiwarongo and Katima Mulilo regions (Thunehed, 2009, pers. comm.). There have also been time-domain EM data acquired south of Katima Mulilo. Unfortunately the EM data in question could not be made available to the researcher during the study period. In future, the EM data should be obtained and can then be used to correct for static shifts in the MT data recorded in the two regions. If any other geophysical data, which focuses on resolving structure deeper down in the crust, are measured close to the towns of Otjiwarongo and Katima Mulilo, then results from analysis of the data can be used to constrain structure during 2D inverse modelling of the MT data.

The array-style site arrangement in both the Otjiwarongo and Katima Mulilo regions is suited for 3D, rather than 2D, inversion of the data. Hence, it is recommended that available 3D inversion codes be used to obtain conductivity models of the Otjiwarongo and Katima Mulilo data, and the results compared to the 2D models obtained in the current study. The comparison can be used to identify and categorize the areas where 3D inversion tools have improved the overall understanding of induction processes within the Earth.

The fact that mid-crustal conductors in both the study by Ritter et al. (2003) and the current one are interpreted to be caused by graphite-bearing marble units confined to major shear zones (Figure 8.5), evokes inferences of interconnected conductive materials associated with shear zones possibly being the cause of the entire DMB conductive belt. Therefore, in future, high resolution electrical and EM studies should be focused on areas within the conductive belt (especially in Botswana) where major shear zones are present, to determine whether or not high conductivities are only confined to the shear zones.

Following inversion of the Otjiwarongo and Katima Mulilo data, the results were used, together with other regional scale MT inversion models in northern Namibia and Botswana, to create a 3D interpolated resistivity model. The interpolation scheme was designed to retain the continuity in conductivity structure deducted from trends in geological and geophysical data (crustal

depths, Figure 6.11) and observed in tipper and impedance strike analyses results (lithospheric mantle depths, Figure 6.19). The interpolation produced good continuity between crustal conductive regions within the various 2D inversion models where MT data have sampled the DMB conductive belt. In addition, some parts of the conductive belt in the interpolated model appeared to be discontinuous along profile (Figure 6.23), supporting the theory that high conductivities within the DMB are restricted to major shear zones.

Potential values extracted from 3D DC forward computations of the interpolated resistivity model, were used as indicators of preferential current flow in the cases where DC current was injected in the Otjiwarongo and Katima Mulilo regions, respectively (Figure 7.3 and 7.4). The potentials showed that for both injections, DC current mostly flowed within the conductive parts of the DMB and followed regional trends for $200 - 300$ km into the subsurface. However, only structure up to 200 km was included in the forward modelling, while the distance between the Otjiwarongo and Katima Mulilo regions was approximately 850 km. Therefore, it is proposed that further modelling tests are undertaken to observe the effects conductivity structure at sub-lithospheric depths has on the flow of return current. Also, a more quantitative analysis needs to be developed which relates the calculated potentials to the exact amount of current flowing per unit volume in regions where preferential flow is apparent. At distances greater than $200 - 300$ km there was no specific path followed by the DC current, as the current increasingly attempted to maximize the vertical cross-sectional area perpendicular to the direction of flow (equation 8.1).

In light of the results and findings in the current study, there are some suggested improvements to the resistivity model used during forward modelling. Firstly, the possibility that high conductivities are only concentrated in shear zones within the DMB, can be incorporated into the 3D model, by assigning low values to the resistivity model (at crustal depths) in areas where shear zones are observed. Also, Weckmann et al. (2003) showed that the conductivities within the major shear zones are anisotropic. Thus, the high conductivity regions within the 3D model can also be made anisotropic, and an anisotropic DC forward modelling code (Li and Spitzer, 2005 and Zhou et al., 2009) can be used to investigate the flow of return current. Secondly, MT inversion results can still be used in the forward model at sub-crustal

depths, because although the data have little resolution (diffusion related), conductivity is intuitively expected to be smoother at mantle depths because of its overall dependence on temperature (see Section 2.3). However, because different regularization parameters were used in producing the 2D models (different researchers) used in interpolation, a way needs to be formulated such that the amount of smoothing is normalized between the various models, before being imported into the 3D grid. Finally, the north-west south-east trending Okavango dyke swarm in Botswana has been shown to be resistive (Miensopust et al., 2010), and due to its intersection with the DMB at crustal depths, it also needs to be included in the future resistivity model.

Appendix A

Acquisition parameters

Table A.1: *Data acquisition parameters for AMT and BBMT sites close to the town of the Otjiwarongo, and, their respective remote reference (RR) sites used during acquisition.*

Site	Type	Latitude	Longitude	Elevation	RR site
ELG001A	AMT	-20.2583 °S	16.3373 °E	1255 m	ELG002A
ELG091A	BBMT	-20.2583 °S	16.3373 °E	1255 m	ELG092A
ELG002A	AMT	-20.3885 °S	16.4874 °E	1347 m	-
ELG092A	BBMT	-20.3885 °S	16.4874 °E	1347 m	ELG091A
ELG003A	AMT	-20.1013 °S	16.2208 °E	1264 m	ELG002A
ELG093A	BBMT	-20.1013 °S	16.2208 °E	1264 m	ELG097A
ELG004B	AMT	-20.4932 °S	16.5845 °E	1464 m	-
ELG005A	AMT	-20.5773 °S	16.5979 °E	1539 m	ELG002A
ELG007A	AMT	-20.6993 °S	16.6077 °E	1594 m	ELG004B
ELG097A	BBMT	-20.6993 °S	16.6077 °E	1594 m	ELG093A
ELG008A	AMT	-20.1423 °S	16.4565 °E	1286 m	ELG011A
ELG009A	AMT	-20.3018 °S	16.2647 °E	1252 m	ELG004B
ELG010A	AMT	-20.2267 °S	16.5257 °E	1346 m	ELG004B
ELG011A	AMT	-20.2798 °S	16.6319 °E	1398 m	ELG004B
ELG012B	AMT	-20.3935 °S	16.3549 °E	1306 m	ELG004B
ELG013A	AMT	-20.5244 °S	16.1548 °E	1286 m	ELG004B
ELG913A	BBMT	-20.5244 °S	16.1548 °E	1286 m	ELG914B
ELG014A	AMT	-20.0863 °S	16.7184 °E	1370 m	ELG004B
ELG914B	BBMT	-20.0863 °S	16.7184 °E	1370 m	ELG913A

Table A.2: *Data acquisition parameters for AMT and BBMT sites close to the town of the Katima Mulilo, and, their respective remote reference (RR) sites used during acquisition. Site CPV026 has latitude = -17.7809 ˚S, longitude = 23.7303 ˚E, and elevation = 972 m.*

Site	Type	Latitude	Longitude	Elevation	RR site
ELZ001A	AMT	-17.5524 °S	24.1459 °E	987 m	ELZ102B
ELZ002A	AMT	-17.5995 °S	24.2177 °E	939 m	ELZ102B
ELZ003A	AMT	-17.5020 °S	24.3226 °E	923 m	ELZ201A
ELZ101A	AMT	-17.6676 °S	24.1181 °E	944 m	ELZ201A
ELZ191A	BBMT	-17.6676 °S	24.1181 °E	944 m	ELZ291A
ELZ102B	AMT	-17.6728 °S	24.2931 °E	929 m	ELZ002A
ELZ192A	BBMT	-17.6728 °S	24.2931 °E	929 m	ELZ294A
ELZ103A	AMT	-17.5564 °S	24.4308 °E	929 m	ELZ003A
ELZ201A	AMT	-17.7239 °S	23.9302 °E	943 m	ELZ101A
ELZ291A	BBMT	-17.7239 °S	23.9302 °E	943 m	ELZ191A
ELZ294A	BBMT	-17.7117 °S	24.5119 °E	931 m	ELZ192A
ELZ555A	AMT	-17.4981 °S	24.2356 °E	952 m	ELZ002A
CPV027	BBMT	-17.7104 °S	23.8605 °E	968 m	CPV026
CPV028	BBMT	-17.6496 °S	24.0627 °E	961 m	CPV029
CPV029	BBMT	-17.6385 °S	24.2124 °E	938 m	CPV028
RAK053	BBMT	-17.6124 °S	24.3964 °E	929 m	RAK054
RAK054	BBMT	-17.8013 °S	24.6190 °E	929 m	RAK053

Appendix B

Recorded MT data

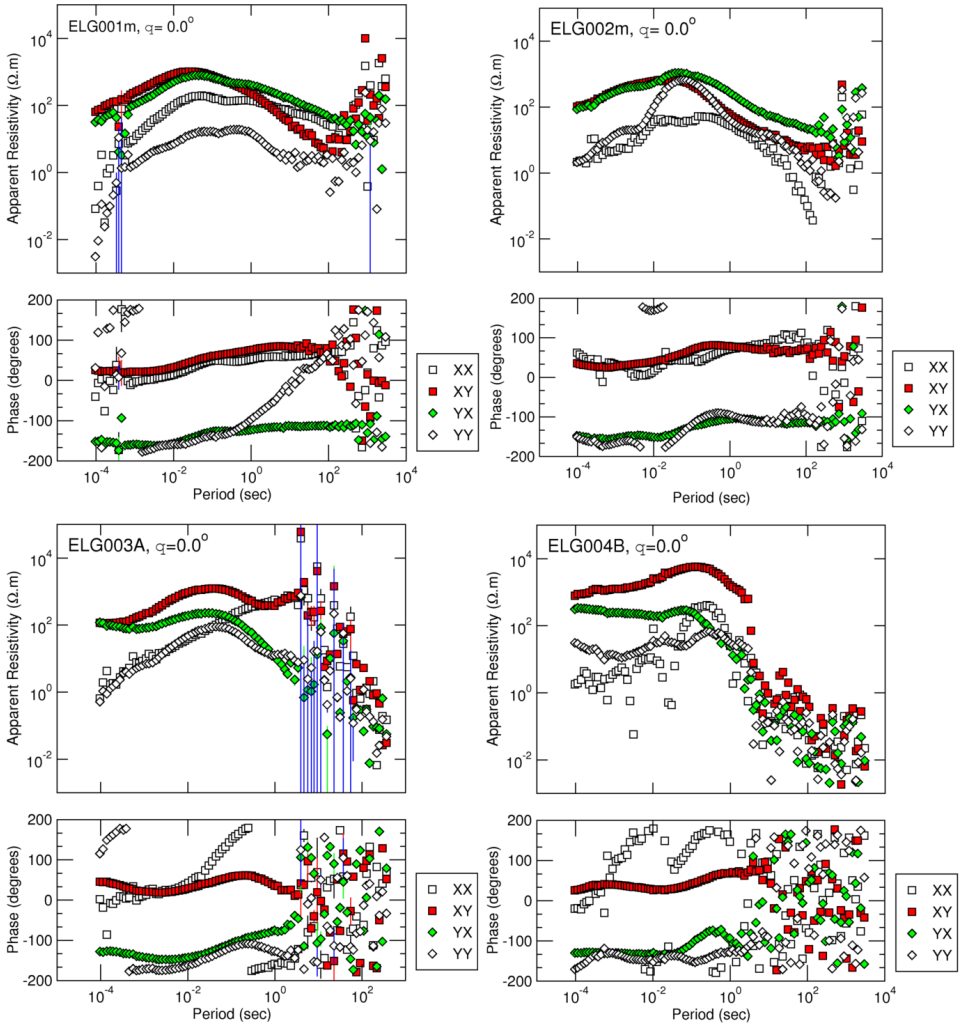


Figure B.1: *MT apparent resistivity and phase curves, rotated to true north and not decomposed, for sites ELG001m, ELG002m, ELG003A and ELG004B. Sites ELG001m and ELG002m consist of merged (m) AMT and BBMT data.*

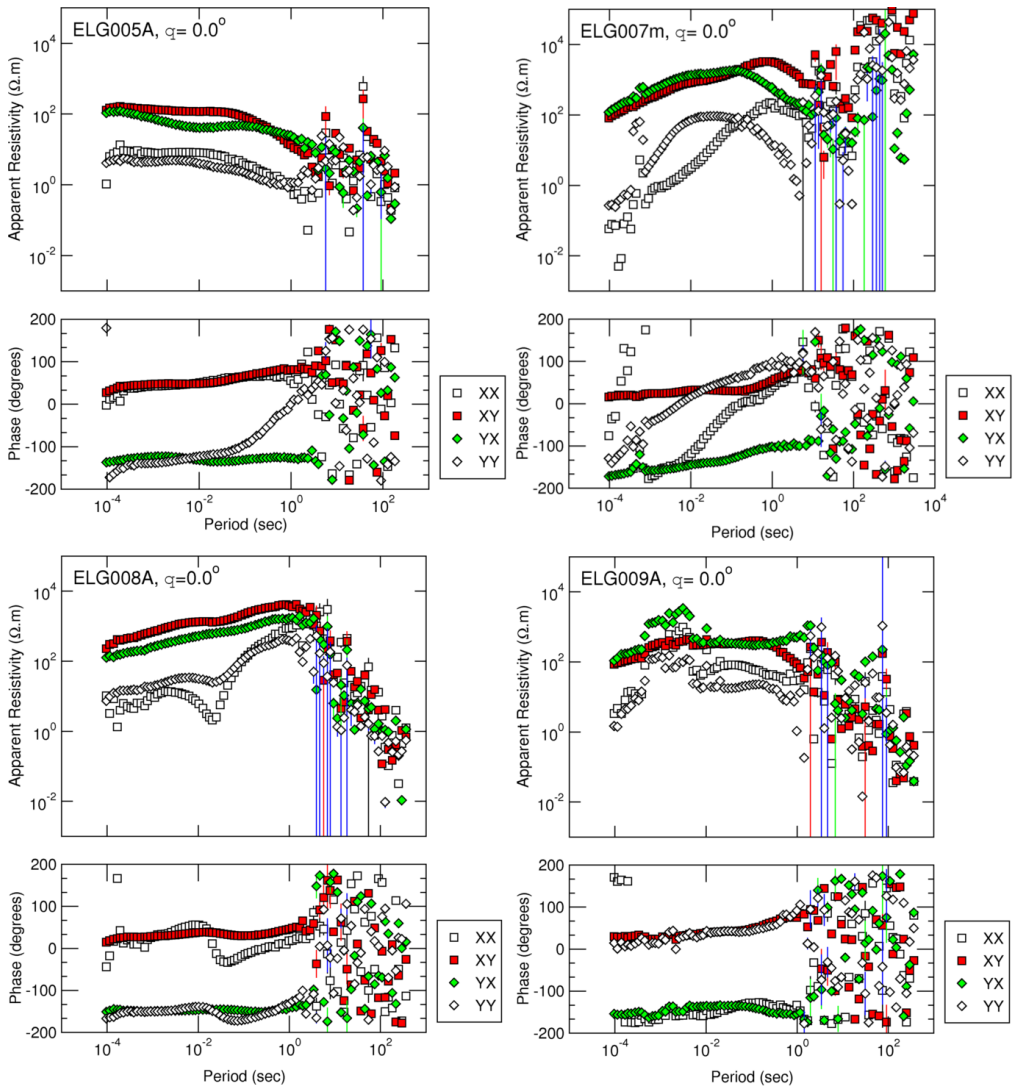


Figure B.2: *MT apparent resistivity and phase curves, rotated to true north and not decomposed, for sites ELG005A, ELG007m, ELG008A and ELG009A. Site ELG007m consists of merged (m) AMT and BBMT data.*

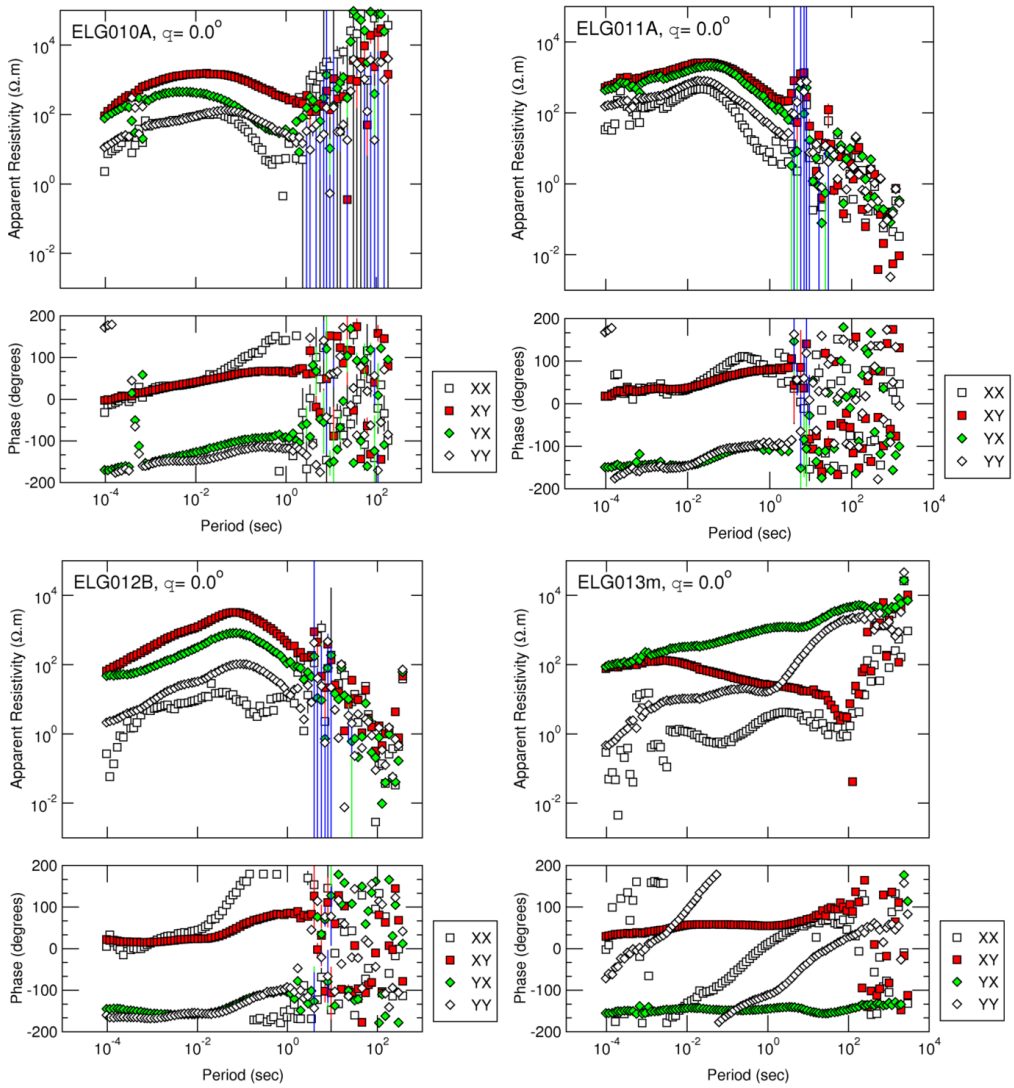


Figure B.3: *MT apparent resistivity and phase curves, rotated to true north and not decomposed, for sites ELG010A, ELG011A, ELG012B and ELG013m. Site ELG013m consists of merged (m) AMT and BBMT data.*

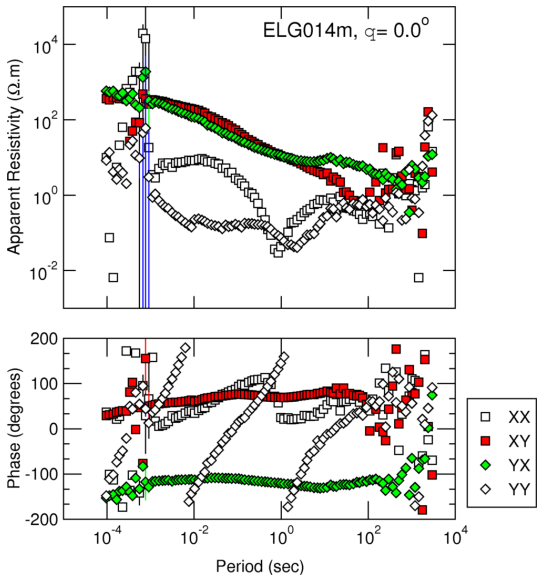


Figure B.4: *MT apparent resistivity and phase curves, rotated to true north and not decomposed, for site ELG014m, which consists of merged (m) AMT and BBMT data.*

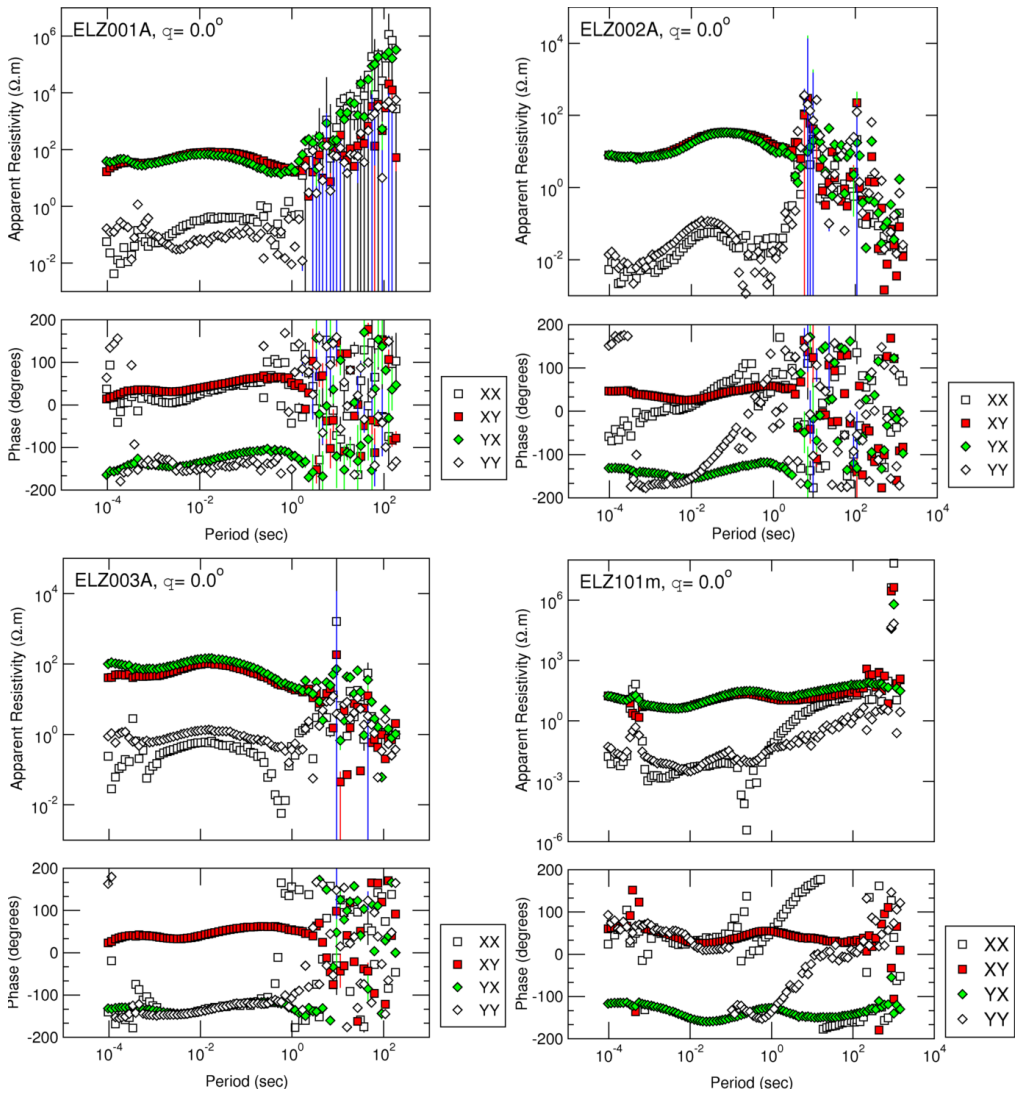


Figure B.5: *MT apparent resistivity and phase curves, rotated to true north and not decomposed, for sites ELZ001A, ELZ002A, ELZ003A and ELZ101m. Site ELZ101m consists of merged (m) AMT and BBMT data.*

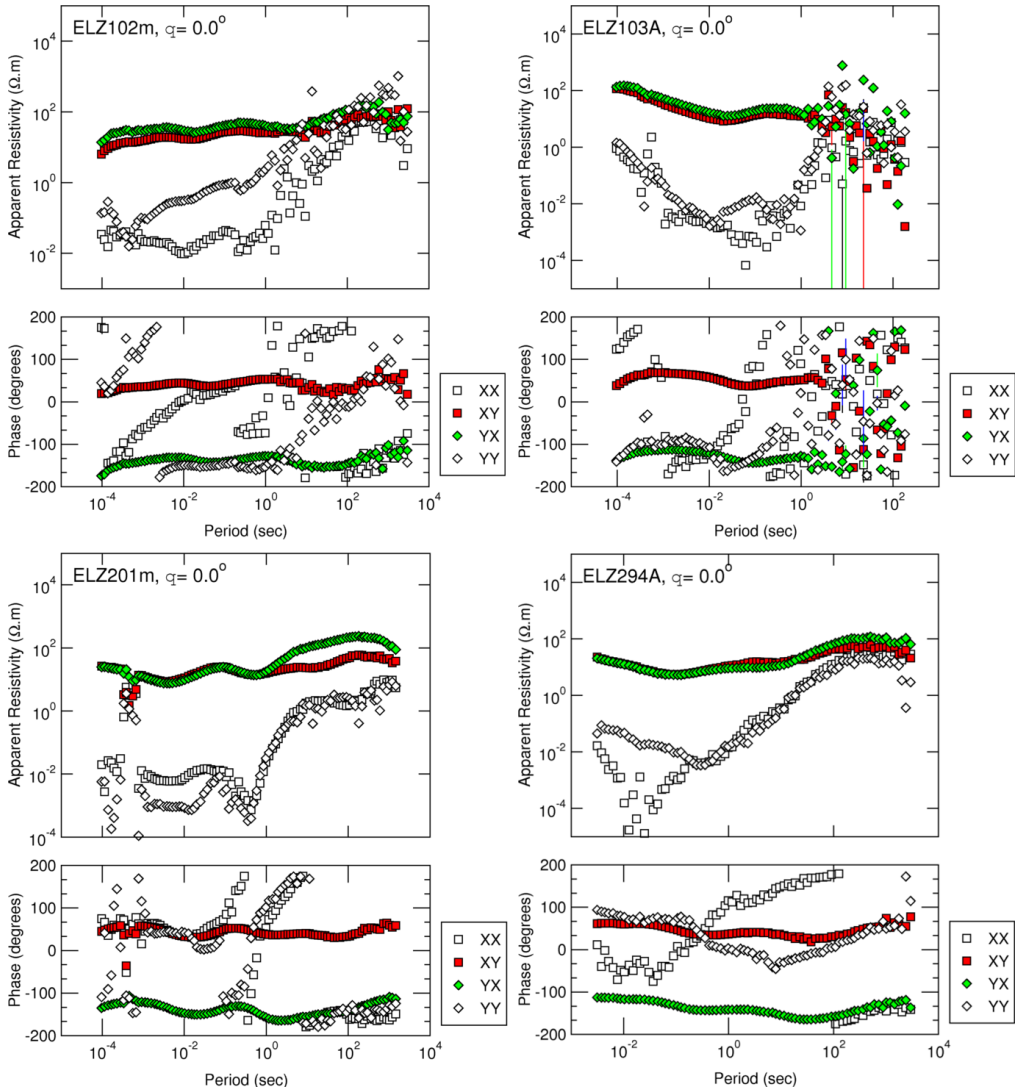


Figure B.6: *MT apparent resistivity and phase curves, rotated to true north and not decomposed, for sites ELZ102m, ELZ103A, ELZ201m and ELZ294A. Sites ELZ102m and ELZ201m consist of merged (m) AMT and BBMT data.*

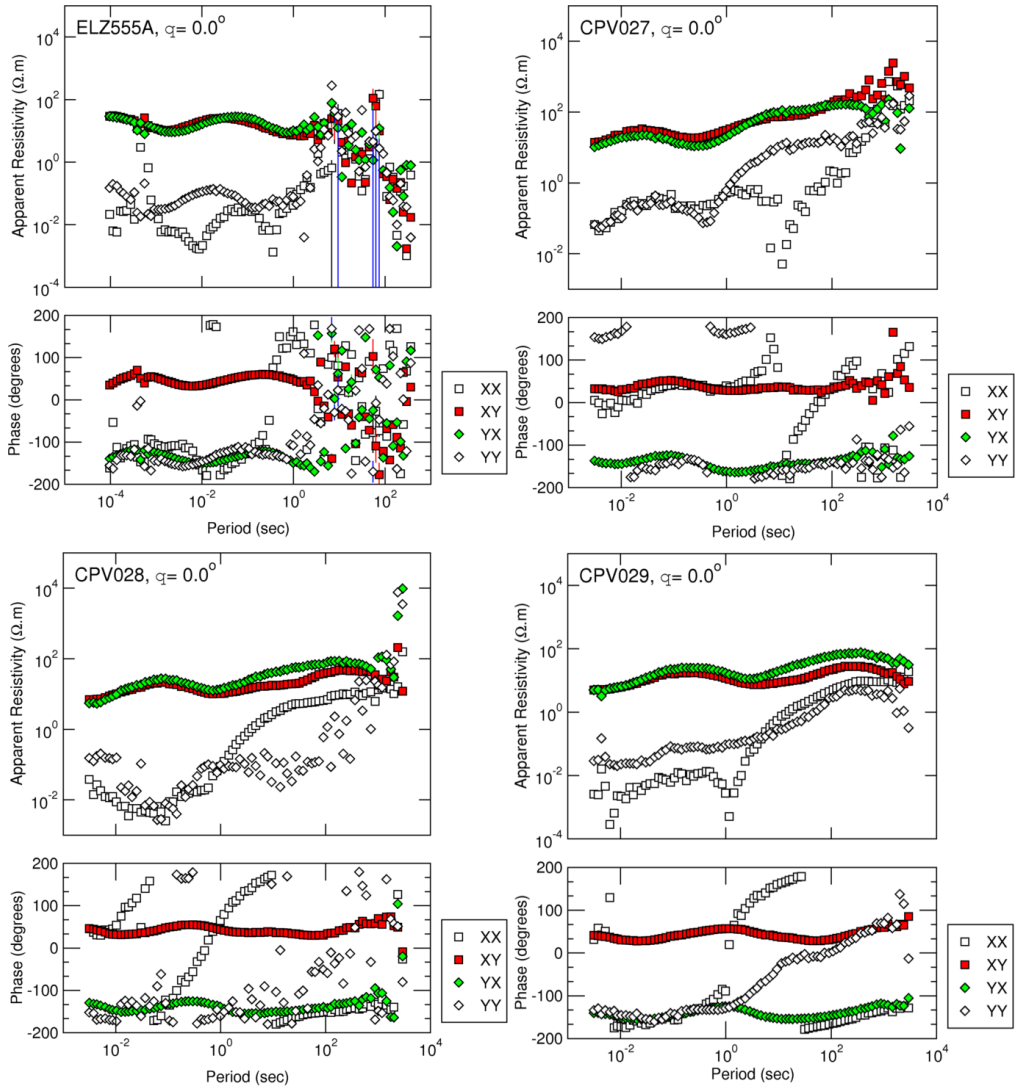


Figure B.7: *MT apparent resistivity and phase curves, rotated to true north and not decomposed, for sites ELZ555A, CPV027, CPV028 and CPV029.*

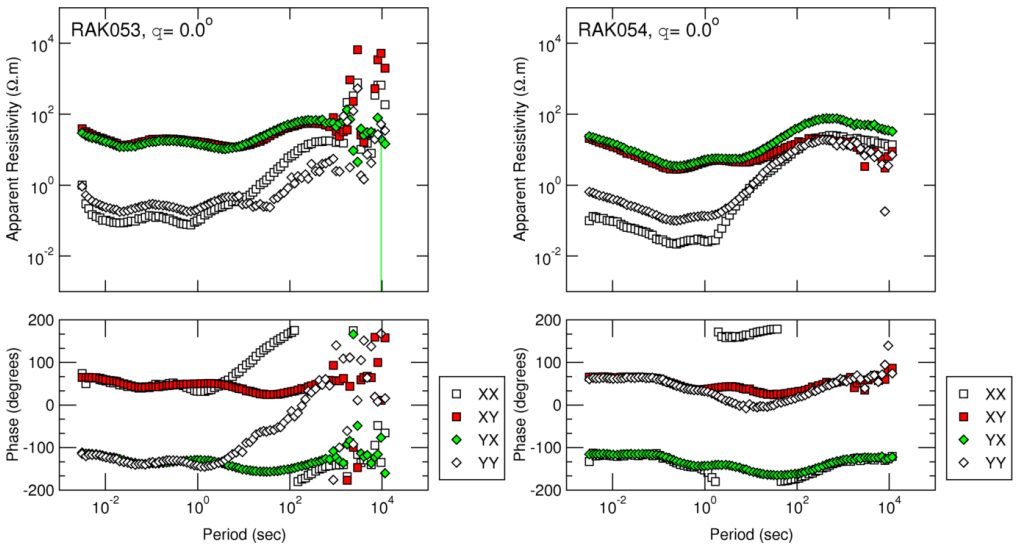


Figure B.8: *MT apparent resistivity and phase curves, rotated to true north and not decomposed, for sites RAK053 and RAK054.*

Appendix C

2D inversion results

The following models depict the effects on 2D inversion results when regularization parameters α and β are varied.

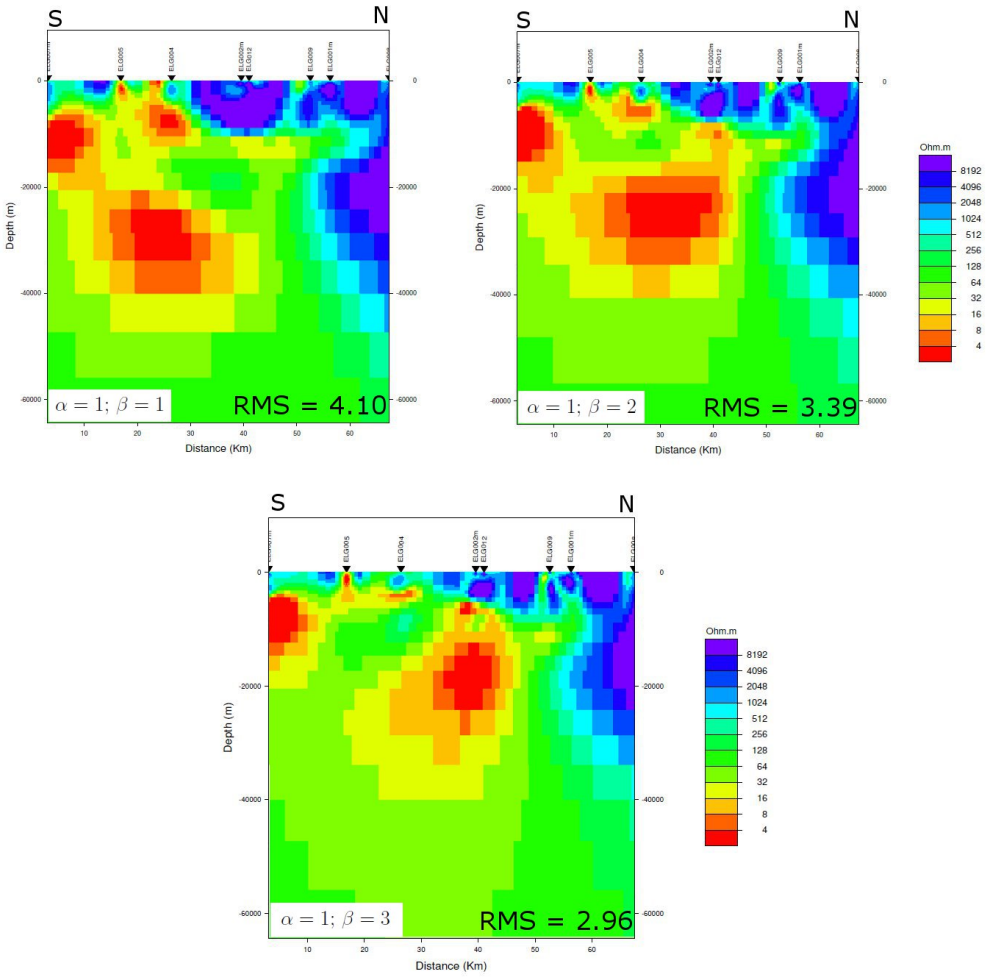


Figure C.1: *Standard grid Laplacian inversion results of the Otjiwarongo data with $\alpha = 1$ and β varied from 1 to 3.*

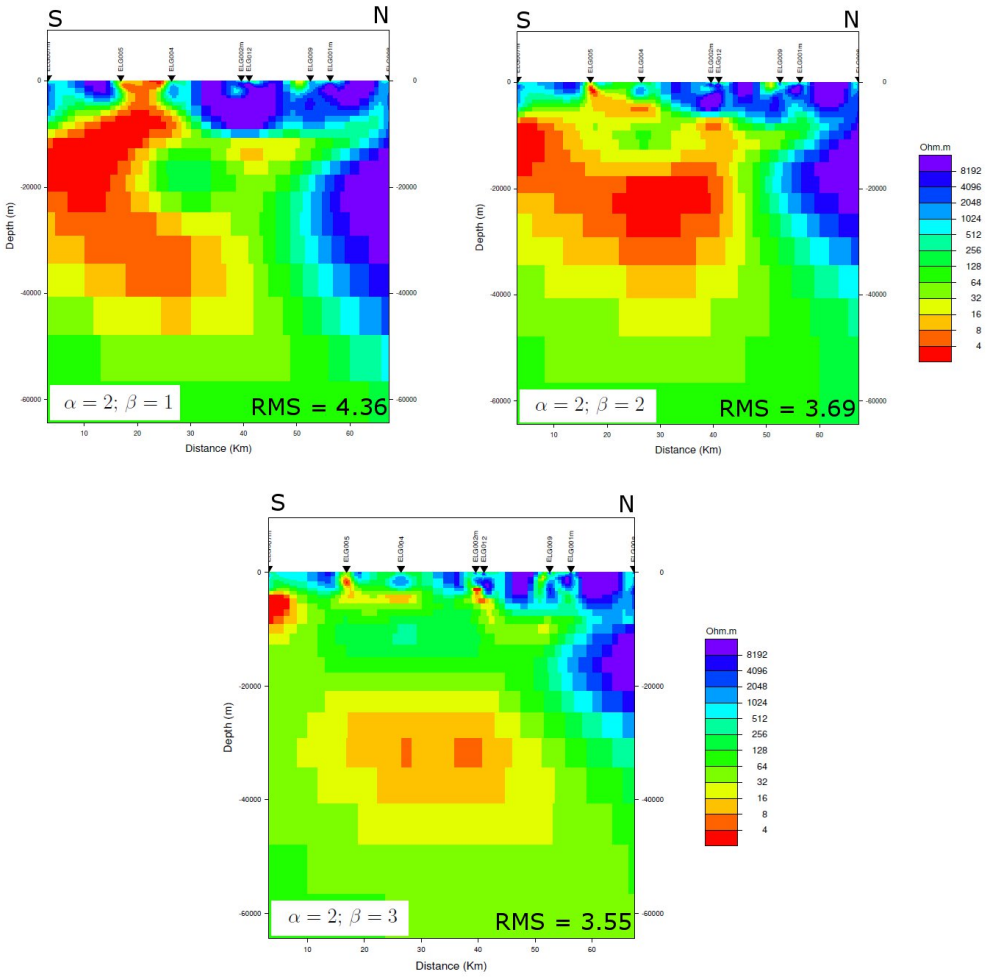


Figure C.2: *Standard grid Laplacian inversion results of the Otjiwarongo data with $\alpha = 2$ and β varied from 1 to 3.*

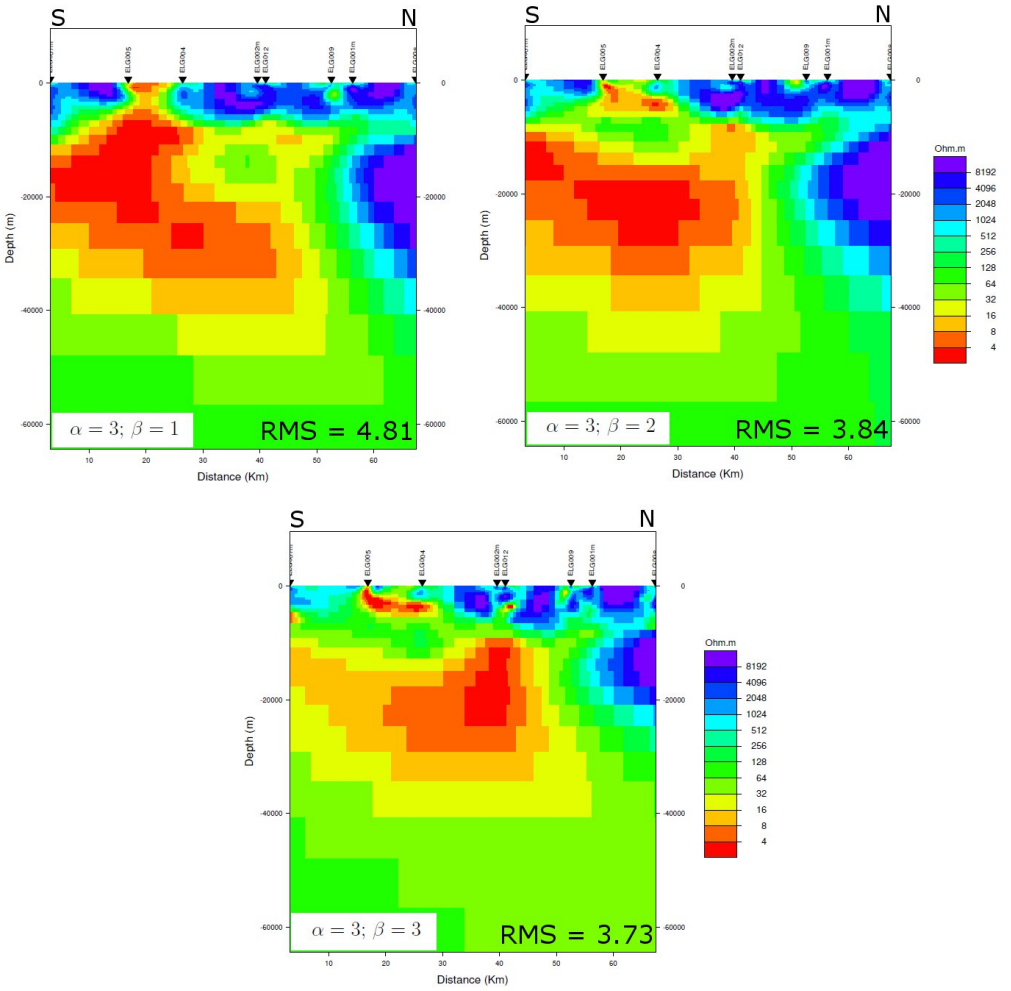


Figure C.3: *Standard grid Laplacian inversion results of the Otjiwarongo data with $\alpha = 3$ and β varied from 1 to 3.*

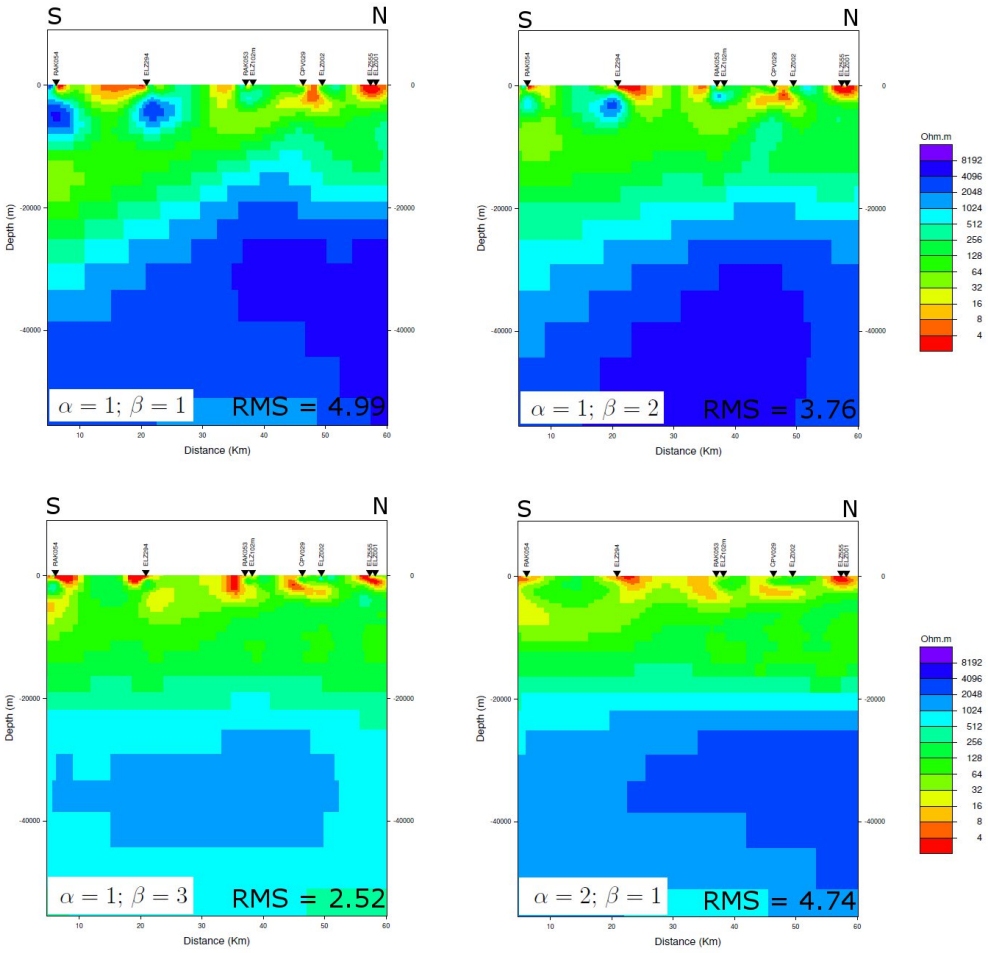


Figure C.4: *Standard grid Laplacian inversion results of the Katima Mulilo data with α and β varied.*

Appendix D

Interpolation material

The following results are supplementary material to the tests completed and data used in calculating an interpolated resistivity model of northern Namibia and Botswana in Chapter 6.

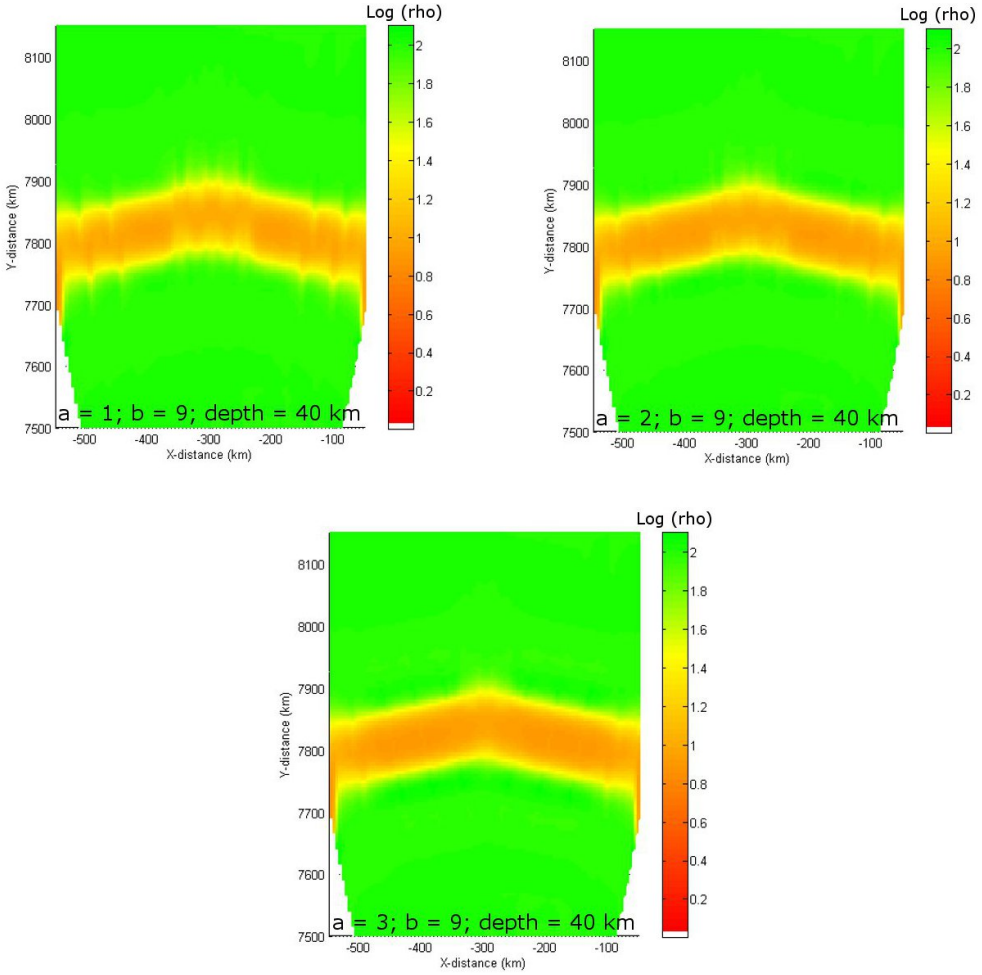


Figure D.1: *Results of the first interpolation test, at 40 km depth, with $b = 9$ and a varied from 1 to 3.*

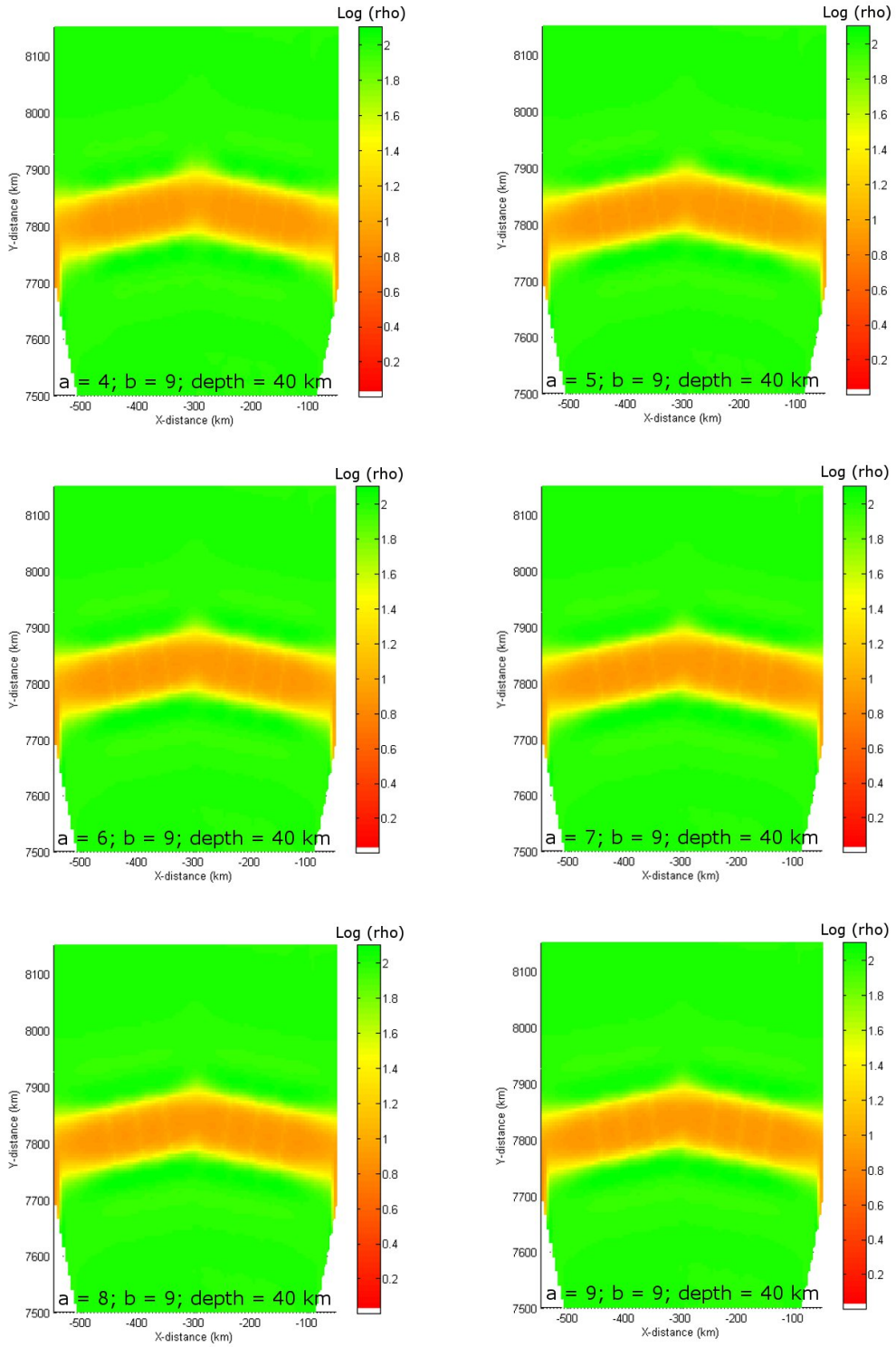


Figure D.2: *Results of the first interpolation test, at 40 km depth, with $b = 9$ and a varied from 4 to 9.*

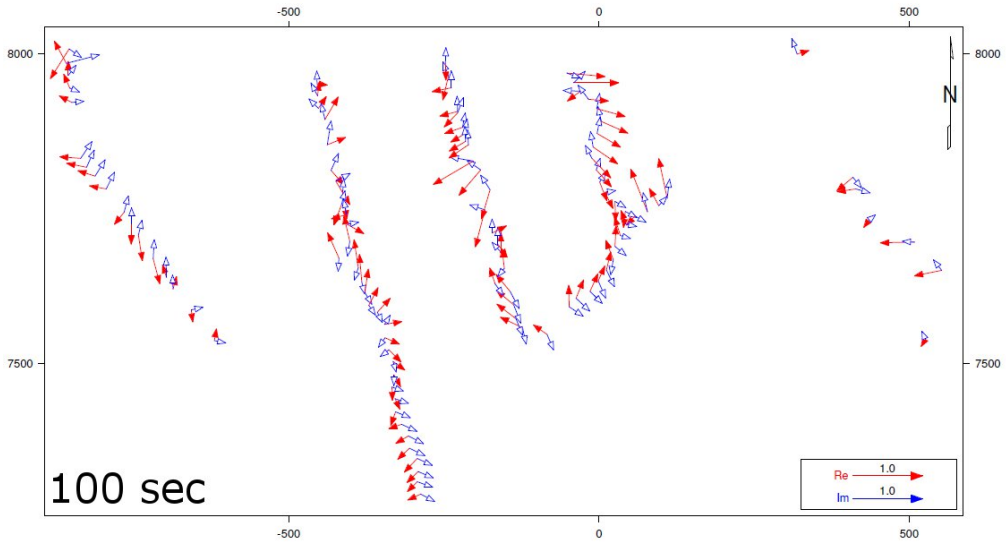


Figure D.3: *Real and imaginary induction arrows at 100 seconds for the MT sites in profiles ETO, DMB, NEN, OKAWIN and ZIM.*

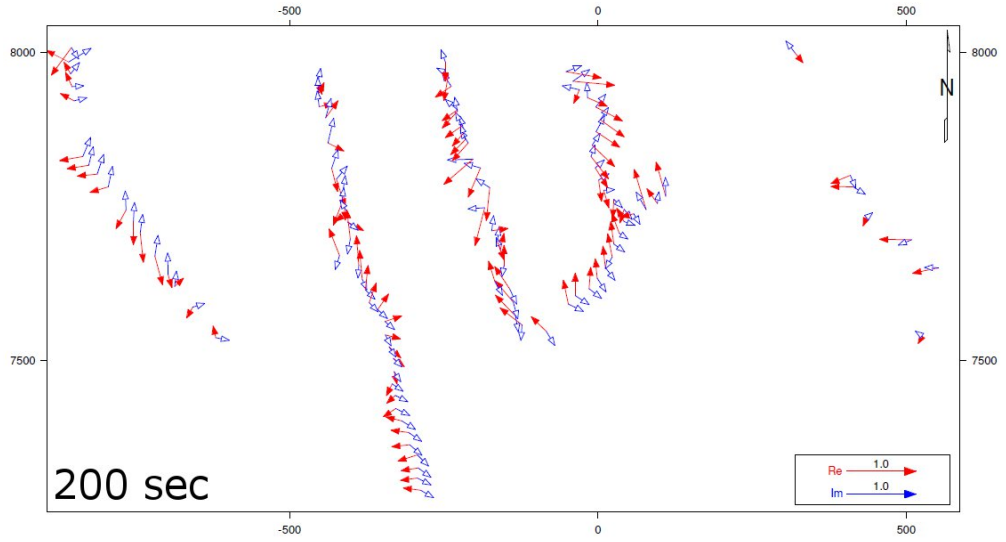


Figure D.4: *Real and imaginary induction arrows at 200 seconds for the MT sites in profiles ETO, DMB, NEN, OKAWIN and ZIM.*

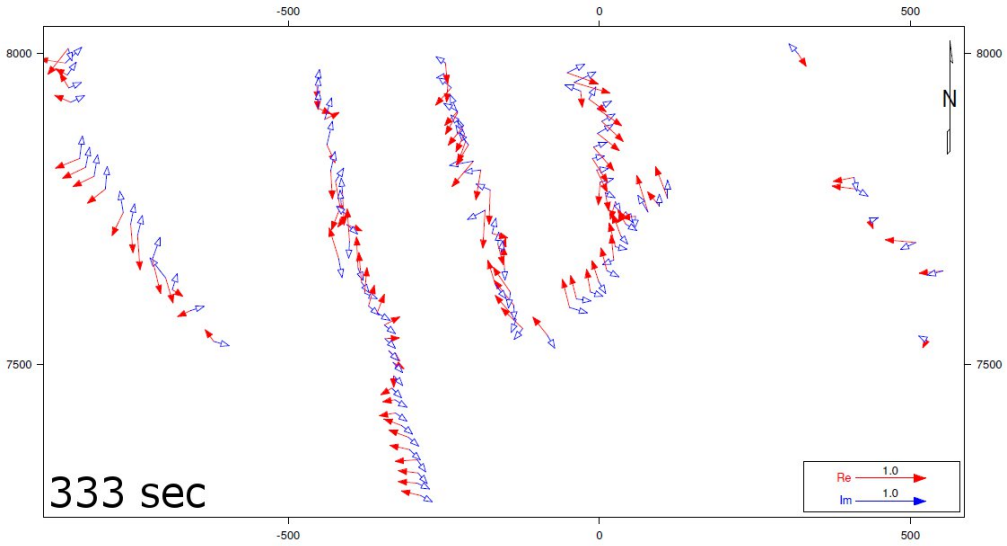


Figure D.5: *Real and imaginary induction arrows at 333 seconds for the MT sites in profiles ETO, DMB, NEN, OKAWIN and ZIM.*

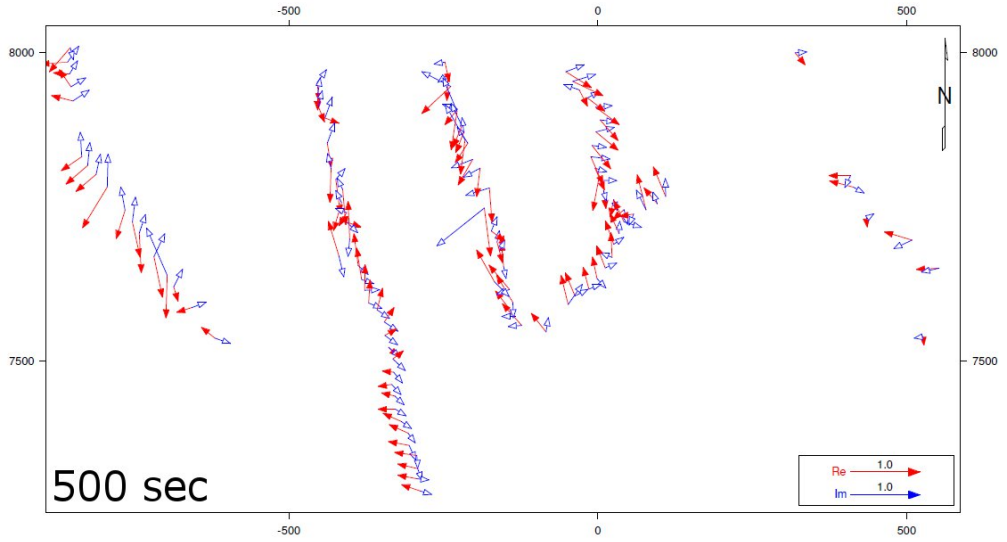


Figure D.6: *Real and imaginary induction arrows at 500 seconds for the MT sites in profiles ETO, DMB, NEN, OKAWIN and ZIM.*

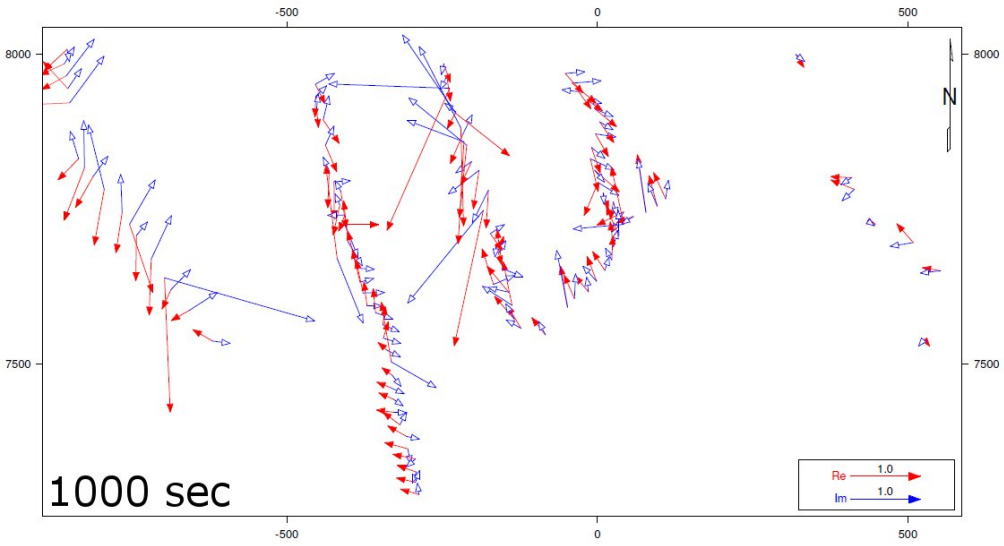


Figure D.7: *Real and imaginary induction arrows at 1000 seconds for the MT sites in profiles ETO, DMB, NEN, OKAWIN and ZIM.*

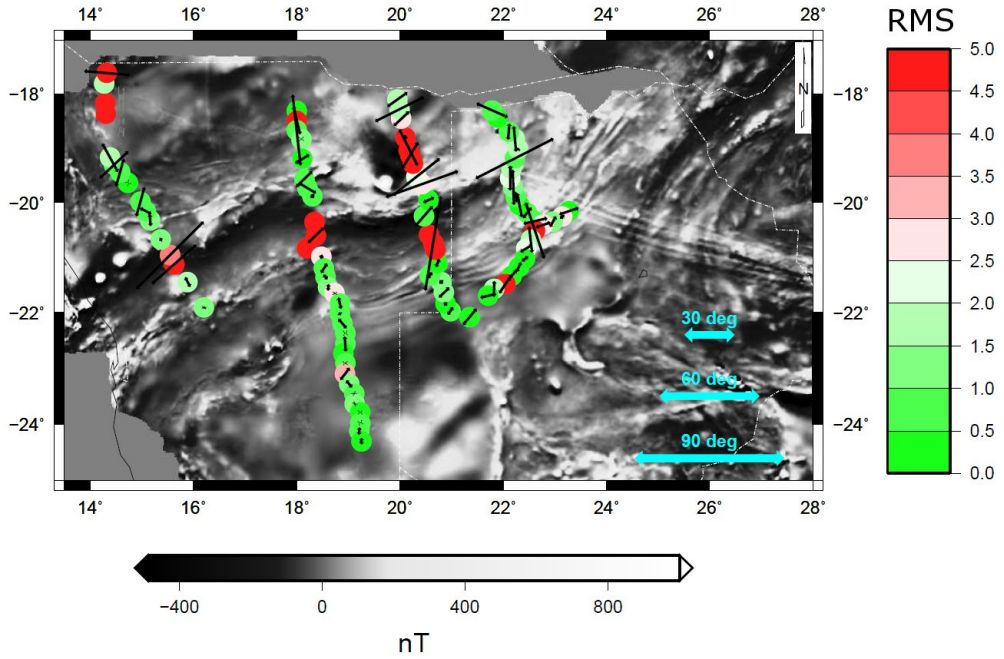


Figure D.8: *Impedance strike angles, phase differences and GB-errors (RMS) calculated for the MT sites in profiles ETO, DMB, NEN, OKAWIN and ZIM over the* $50 - 200$ *km depth range.*

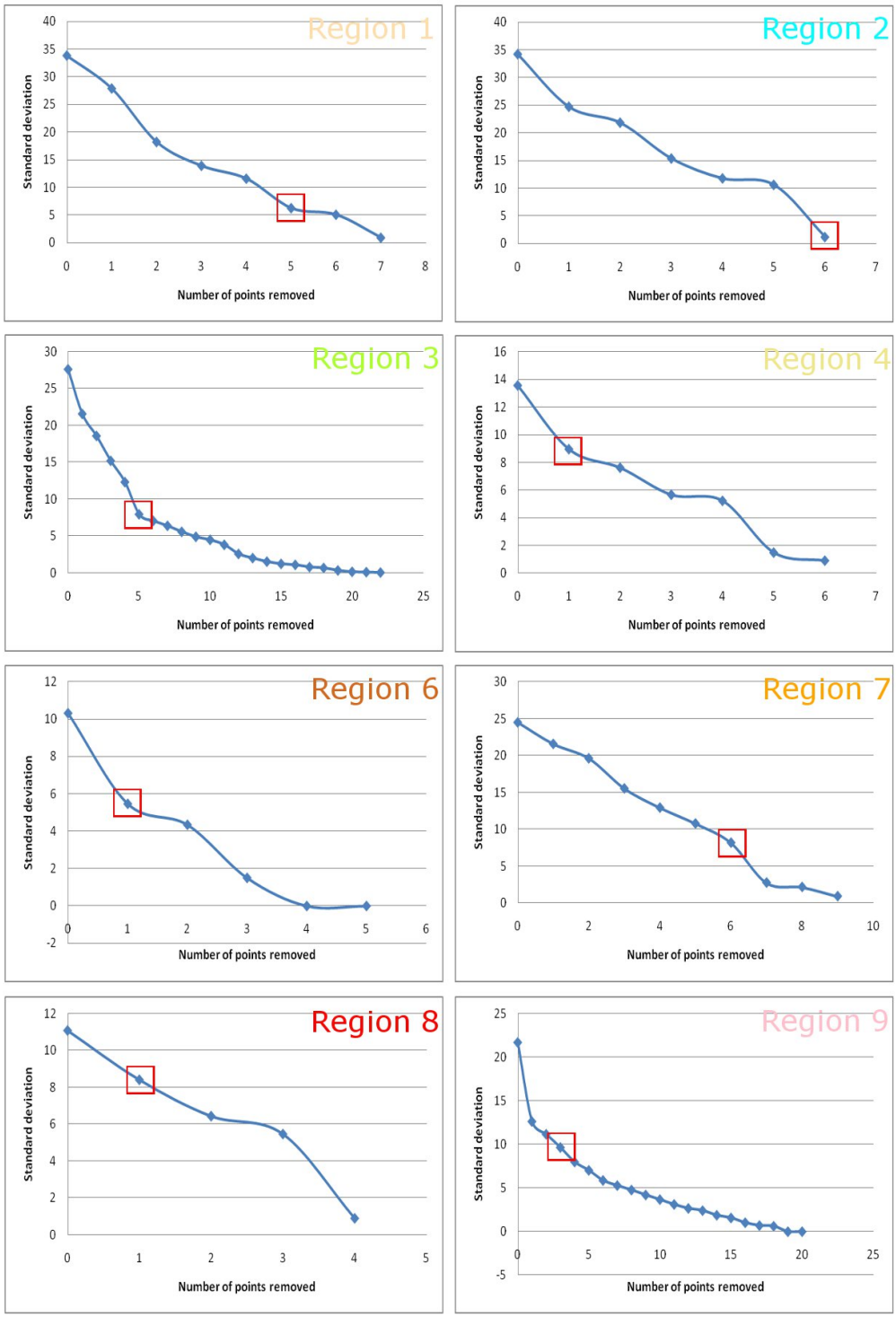


Figure D.9: *Plots of standard deviation versus number of strike values removed for the groups of consistent strike (Figure 6.19) which had more than 2 values. The squares indicate the standard deviation values associated with the averages that were used as projection directions for the various regions at lithospheric mantle depths.*

Appendix E

Interpolation code

The interpolation code used to compute a 3D resistivity model of northern Namibia and Botswana is shown below. The same code was used in the tests done prior to the interpolation of the SAMTEX data. However, variables such as grid size, the size of the interpolation kernel, the values a and b and the depths being calculated were changed.

```
%%% Linear interpolation code for resistivity data
%%% Pieter-Ewald Share
%%% February 2010

clear all;
close all;

% creating a grid

x = [-900:5:420];
y = [7285:5:8070];
z = [0:-1:-200];

[X,Y,Z] = ndgrid(x2,y2,z2);

XC = reshape(X,numel(X),1);
YC = reshape(Y,numel(Y),1);
ZC = reshape(Z,numel(Z),1);

% importing the profile data and assigning each resistivity
```

```
% value to an appropriate cell in the grid

fid = fopen('lithos_all1000.txt');
data = fscanf(fid, '%g %g %g %g %g', [5 inf]);
fclose(fid);

oneval = ones (numel(X),1);

for i = 1:length(data);
[val,c(i,1)] = min(sqrt((XC-oneval*data(1,i)).^2 +
(YC-oneval*data(2,i)).^2 + (ZC-oneval*(data(3,i)/1000)).^2));
end;

value = zeros(size(X));
anglevalue = zeros(size(X));

[iis,jjs,kks] = ind2sub(size(X),c);

for i = 1:length(data);
value(iis(i),jjs(i),kks(i)) = log10(data(4,i));
anglevalue(iis(i),jjs(i),kks(i)) = data(5,i);
end;

% the vertical dimension of grid cells (always 1 km) is smaller
% than the vertical dimension of cells in the inversion model
% at great depth, therefore resistivity values need to be
% copied down if the lower cells are empty

for m = 1:length(x2);
for n = 1:length(y2);
for o = 1:length(z2);
if o == length(z); break; end;
if ((value(m,n,o) > 0) && (value(m,n,o+1) == 0));
value(m,n,o+1) = value(m,n,o);
anglevalue(m,n,o+1) = anglevalue(m,n,o);
end;
end;
```

```
end;
end;

% creating the interpolation kernel with a = 4

distance = zeros(31,31,31);
angle = zeros(31,31,31);

for mr = -15:15;
for nr = -15:15;
ang = atan((0 - mr)./(0 - nr));
for or = -15:15;
dist = (1 + sqrt((mr).^2 + (nr).^2 + (or).^2)).^4;
mmm = mr + 16; nnn = nr + 16; ooo = or + 16;
distance(mmm,nnn,ooo) = dist;
angle(mmm,nnn,ooo) = ang;
if nr == 0; angle(mmm,nnn,ooo) = pi./2; end;
end;
end;
end;

% calculating the interpolation results at specific depths with
% b = 9, and also counting the number of resistivity values
% used in each calculation

result = zeros(size(X)); total = zeros(size(X));

depth = [1 2 3 5 6 8 9 11 14 16 19 21 25 28 32 36 41 46 51 57
64 71 80 88 98 109 121 134 149 164 182 201];
number = 0;
for m = 1:length(x);
for n = 1:length(y);
for o = depth;
sum = 0; count = 0; weighting = 0;
for mr = -15:15;
for nr = -15:15;
for or = -75:5:75;
```

```
mrm = mr + m; nrn = nr + n; oro = or + o;
if (mrm >= 1) && (mrm <= length(x)) && (nrn >= 1) &&
(nrn <= length(y)) && (oro >= 1) && (oro <= length(z));
if value (mrm,nrn,oro) > 0
count = count + 1;
mmm = mr + 16; nnn = nr + 16; ooo = ((or + 75)./5) + 1;
cosine = (sqrt(cos(anglevalue(mrm,nrn,oro) -
angle(mmm,nnn,ooo)).^2)).^9;
if (mmm == 16) && (nnn == 16); cosine = 1; end;
sum = sum + (value (mrm,nrn,oro)./distance
(mmm,nnn,ooo)).*cosine;
weighting = weighting + (1./distance (mmm,nnn,ooo)).*cosine;
end;
end;
end;
end;
end;
if weighting == 0; result (m,n,o) = 0;
else result (m,n,o) = sum./weighting; end;
total (m,n,o) = count; number = number + 1; disp(number);
end;
end;
end;

% saving the interpolation results to file

fid = fopen('interp_all_15kern_d4a9_post.txt','w');
for m = 1:length(x);
for n = 1:length(y);
for o = 1:length(z);
list = [m n o value(m,n,o) anglevalue(m,n,o) result(m,n,o)
total(m,n,o)];
fprintf(fid,'\t%4.0f\t%4.0f\t%4.0f\t%8.4f\t%8.4f\t%8.4f\t%6.0f
\n',list');
end;
end;
end;
```

```
fclose(fid);

% displaying interpolation results at a depth of 20 km

figure(1);
surf(x,y,result(:,:,21)','Edgecolor','none');
view(2);
axis equal;
axis([-900 -420 7285 8070]);
xlabel({'Longitude-UTM27 (km)'});
ylabel({'Latitude-UTM27 (km)'});
load('MyColormaps','mycmap');
set(figure(1),'Colormap',mycmap);
colorbar;
```

References

Árnason, K., Eysteinsson, H., Hersir, G. P., 2010. Joint 1D inversion of TEM and MT data and 3D inversion of MT data in the Hengill area, SW Iceland. Geothermics 39 (1), 13–34. 63

Aster, R., Borchers, B., Thurber, C., 2005. Parameter Estimation and Inverse Problems. Elsevier. 60

Avdeev, D., Avdeeva, A., 2009. 3D magnetotelluric inversion using a limited-memory quasi-Newton optimization. Geophysics 74 (3), F45–F57. 63

Bahr, K., 1988. Interpretation of the magnetotelluric impedance tensor: regional induction and local telluric distortion. Journal of Geophysics 62, 119–127. 59

Bailey, R. C., 1970. Inversion of the geomagnetic induction problem. Proceedings of the Royal Society London A315, 185–194. 61

Bailey, R. C., Edwards, R. N., 1976. The Effect of Source Field Polarization on Geomagnetic Variation Anomalies in the British Isles. Geophysical Journal of the Royal Astronomical Society 45, 97–104. 28

Banks, R. J., Livelybrooks, D., Jones, P., Lonstaff, R., 1996. Causes of high crustal conductivity beneath the Iapetus suture zone in Great Britain. Geophysical Journal International 124 (2), 433–455. 28

Begg, G. C., Griffin, W. L., Natapov, L. M., O'Reilly, S. Y., Grand, S. P., O'Neill, C. J., Hronsky, J. M. A., Poudjom Djomani, Y., Swain, C. J., Deen, T., Bowden, P., 2009. The lithospheric architecture of Africa: Seismic tomography, mantle petrology, and tectonic evolution. Geosphere 5 (1), 23–50. 9

Bendat, J. S., Piersol, A. G., 1971. Random data: Analysis and measurement procedures. John Wiley and Sons, Inc., New York. 51

Berdichevsky, M. N., 1999. Marginal notes on magnetotellurics. Surveys in Geophysics 20, 341–375. 38, 43, 85

Berdichevsky, M. N., Dmitriev, V. I., 2002. Magnetotellurics in the Context of Theory of Ill-Posed Problems. Society of Exploration Geophysicists. 37, 42, 61, 111

Boschi, L., Becker, T. W., Soldati, G., Dziewonski, A. M., 2006. On the relevance of Born theory in global seismic tomography. Geophysical Research Letters 33 (L06302), 1–4. 82

Bostick, F. X., 1977. A simple almost exact method of MT analysis. Workshop on Electrical Methods in Geothermal Exploration, U.S. Geological Survey Contract Number 14080001-8-359. 42

Cagniard, L., 1953. Basic theory of the magneto-telluric method of geophysical prospecting. Geophysics 18, 605–635. 38, 39

Caldwell, T. G., Bibby, H. M., Brown, C., 2004. The magnetotelluric phase tensor. Geophysical Journal International 158, 457–469. 60

Carlson, R. W., Grove, T. L., de Wit, M. J., Gurney, J. J., 1996. Anatomy of an Archean craton: A program for interdisciplinary studies of the Kaapvaal craton, southern Africa. EOS, Transactions of the American Geophysical Union 77 (29), 273–277. 2

Chave, A. D., Jones, A. G., 1997. Electric and Magnetic Field Galvanic Distortion Decomposition of BC87 Data. Journal of Geomagnetism and Geoelectricity 49, 767–789. 58

Chave, A. D., Lezaeta, P., 2007. The statistical distribution of magnetotelluric apparent resistivity and phase. Geophysical Journal International 171 (1), 127–132. 100

Chave, A. D., Smith, J. T., 1994. On electric and magnetic galvanic distortion tensor decompositions. Journal of Geophysical Research 99 (B3), 4669–4682. 56, 57

Chave, A. D., Thomson, J. D., 2004. Bounded influence magnetotelluric response function estimation. Geophysical Journal International 157, 988–1006. 55

Clarke, J., Gamble, T. D., Goubau, W. M., Koch, R. H., Miracky, R. F., 1983. Remote-reference magnetotellurics: equipment and procedures. Geophysical Prosepecting 31, 149–170. 54

Constable, S. C., Parker, R. L., Constable, C. G., 1987. Occams inversion: A practical algorithm for generating smooth models from electromagnetic sounding data. Geophysics 52 (3), 289–300. 62

Coward, M. P., Daly, M. C., 1984. Crustal lineaments and shear zones in Africa: their relationship to plate movements. Precambrian Research 24, 27–45. 12, 135

Daly, M. C., 1986. Crustal shear zones and thrust belts: their geometry and continuity in Central Africa. Philosophical Transactions of the Royal Society of London 317 (A), 111–128. 10, 12

de Beer, J. H., 2009. Personal communication on "HVDC powerlines and DC return currents". 128, 137

de Beer, J. H., Huyssen, R. M. J., Joubert, S. J., van Zijl, J. S. V., 1982. Magnetometer array studies and deep Schlumberger soundings in the Damara orogenic belt, South West Africa. Geophysical Journal of the Royal Astronomical Society 70, 11–29. 24, 25, 136

de Beer, J. H., van Zijl, J. S. V., 1975. An electrical conductivity anomaly and rifting in Southern Africa. Nature 225, 678–680. 24

de Beer, J. H., van Zijl, J. S. V., Huyssen, R. M. J., Hugo, P. L. V., Joubert, S. J., Meyer, R., 1976. A Magnetometer Array Study in South-West Africa, Botswana and Rhodesia. Geophysical Journal of the Royal Astronomical Society 45, 1–17. ix, 24, 25

de Groot-Hedlin, C., 1991. Removal of static shift in two dimensions by regularized inversion. Geophysics 56 (12), 2102–2106. 84

de Groot-Hedlin, C., Constable, S. C., 1990. Occam's inversion to generate smooth, two-dimensional models from magnetotelluric data. Geophysics 53 (12), 1613–1624. 62

de Wit, M. J., Richardson, S. H., Ashwal, L. D., 2004. Kaapvaal Craton special volume - An introduction. South African Journal of Geology 107, 2–6. 1

de Wit, M. J., Roering, C., Hart, R. J., Armstrong, R. A., de Ronde, C. E. J., Green, R. W. E., Tredoux, M., Peberdy, E., Hart, R. A., 1992. Formation of an Archean continent. Nature 357, 553–562. 1

d'Erceville, I., Kunetz, G., 1962. The effect of a fault on the Earth's natural electromagnetic field. Geophysics 27 (5), 651–665. 39

Dey, A., Morrison, H. F., 1979. Resistivity modelling for arbitrary shaped two-dimensional structures. Geophysical Prospecting 27 (1), 106–136. 122

Duncan, P. M., Hwang, A., Edwards, R. N., Bailey, R. C., Garland, G. D., 1980. The development and applications of a wide band electromagnetic sounding system using a pseudo-noise source. Geophysics 45 (8), 1276–1296. 21

Eaton, D. W., Darbyshire, F., Evans, R. L., Grütter, H., Jones, A. G., Yuan, X., 2009. The elusive lithosphere-asthenosphere boundary (LAB) beneath cratons. Lithos 109, 1–22. 22

Egbert, G. D., 1997. Robust multiple-station magnetotelluric data processing. Geophysical Journal International 130, 475–496. 55

Egbert, G. D., Booker, J. R., 1986. Robust estimation of geomagnetic transfer functions. Geophysical Journal of the Royal Astronomical Society 87, 173–194. 55

Evans, R. L., Jones, A. G., Garcia, X., Muller, M. R., Hamilton, M. P., Evans, S., Fourie, C. J. S., Spratt, J., Webb, S. J., Jelsma, H., Hutchins, D., 2011. The Electrical Lithosphere beneath the Kaapvaal Craton, Southern Africa. Journal of Geophysical Research 116 (B04105). 3

Farquharson, C. G., Craven, J. A., 2009. Three-dimensional inversion of magnetotelluric data for mineral exploration: An example from the McArthur River uranium deposit, Saskatchewan, Canada. Journal of Applied Geophysics 68 (4), 450–458. 63

Fischer, G., Schnegg, P. A., Pequiron, M., Le Quang, B. V., 1981. An analytic one-dimensional magnetotelluric inversion scheme. Geophysical Journal of the Royal Astronomical Society 67, 257–278. 62

Fullea, J., Muller, M. R., Jones, A. G., 2011. Electrical conductivity of continental lithospheric mantle from integrated geophysical and petrological

modeling: Application to the Kaapvaal Craton and Rehoboth Terrane, southern Africa. Journal of Geophysical Research 116 (B10202). 3

Gamble, T. D., Goubau, W. M., Clarke, J., 1979. Magnetotellurics with a remote magnetic reference. Geophysics 44 (1), 53–68. 54

Gamble, T. D., Goubau, W. M., Miracky, R., Clarke, J., 1982. Magnetotelluric regional strike. Geophysics 47 (6), 932–937. 111

Garcia, X., Jones, A. G., 2001. Three-Dimensional Electromagnetics. Vol. 35 of Methods in Geochemistry and Geophysics. Elsevier, Ch. 13, editors M. S. Zhdanov and P. E. Wannamaker. 58, 60

Garcia, X., Jones, A. G., 2002. Atmospheric sources for audio-magnetotelluric (AMT) sounding. Geophysics 67 (2), 448–458. 44

Garcia, X., Jones, A. G., 2008. Robust processing of magnetotelluric data in the AMT dead band using the continuous wavelet transform. Goephysics 73 (6), 223–234. 51

Garcia, X., Ledo, J., Queralt, P., 1999. 2D inversion of 3D magnetotelluric data: The Kayabe dataset. Earth, Planets and Space 51, 1135–1143. 98

Gardner, R. B., Stacey, F. D., 1971. Electrical resistivity of the core. Physics of the Earth and Planetary Interiors 4, 406–410. 18

Gauss, C. F., 1839. Allgemeine Theorie des Erdmag. Resultate aus den Beobachtungen des magnetischen Vereins im Jahre 1838. Göttingen: Dieterichsche Buchhandlung, editors C. F. Gauss and W. Weber. 44

Goldstein, M. A., Strangway, D. W., 1975. Audio-frequency Magnetotellurics with a grounded electric dipole source. Geophysics 40 (4), 669–683. 29

Goubau, W. M., Gamble, T. D., Clarke, J., 1979. Magnetotelluric data analysis: removal of bias. Geophysics 43, 1157–1166. 54

Gray, D. R., Foster, D. A., Goscombec, B. C., Passchier, W., Trouwe, R. A. J., 2006. 40Ar/39Ar thermochronology of the Pan-African Damara Orogen, Namibia, with implications for tectonothermal and geodynamic evolution. Precambrian Research 150, 49–72. xiii, 11, 12, 13, 131, 134

Griffiths, D. J., 1999. Introduction to Electrodynamics, 3rd Edition. Prentice-Hall Inc. 31, 34, 36

Groom, R. W., Bahr, K., 1992. Corrections for near surface effects: Decomposition of the magnetotelluric impedance tensor and scaling corrections for regional resistivities: A tutorial. Surveys in Geophysics 13, 341–379. 56, 58

Groom, R. W., Bailey, R. C., 1989. Decomposition of Magnetotelluric Impedance Tensors in the Presence of Local Three-Dimensional Galvanic Distortion. Journal of Geophysical Research 94 (B2), 1913–1925. 59

Hamilton, M. P., 2008. Electrical and seismic anisotropy of the lithosphere with the focus on central southern Africa. Ph.D. thesis, University of the Witwatersrand. 40

Hamilton, M. P., Jones, A. G., Evans, R. L., Evans, S., Fourie, C. J. S., Garcia, X., Mountford, A., Spratt, J. E., the SAMTEX Team, 2006. Electrical anisotropy of South African lithosphere compared with seismic anisotropy from shear-wave splitting analyses. Physics of the Earth and Planetary Interiors 158, 226–239. 3

Han, N., Nam, M. J., Kim, H. J., Lee, T. J., Song, Y., Suh, J. H., 2008. Efficient three-dimensional inversion of magnetotelluric data using approximate sensitivities. Geophysical Journal International 175 (2), 477–485. 63

Hansen, P. C., 1992. Analysis of discrete ill-posed problems by means of the L-curve. SIAM Review 34 (4), 561–580. 82

He, Z., Hu, Z., Luo, W., Wang, C., 2010. Mapping reservoirs based on resistivity and induced polarization derived from continuous 3D magnetotelluric profiling: Case study from Qaidam basin, China. Geophysics 75 (1), B25–B33. 63

Heise, W., Caldwell, T. G., Bibby, H. M., Bennie, S. L., 2010. Three-dimensional electrical resistivity image of magma beneath an active continental rift, Taupo Volcanic Zone, New Zealand. Geophysical Research Letters 37 (L10301). 63

Hermance, J. F., Peltier, W. R., 1970. Magnetotelluric fields of a line current. Journal of Geophysical Research 75 (17), 3351–3356. 47

Hildenbrand, T. G., Berger, B., Jachens, R. C., Ludington, S., 2000. Regional crustal structures and their relationship to the distribution of ore

deposits in the western United States, based on magnetic and gravity data. Economic Geology 95 (8), 1583–1603. 107

Hinze, E., 1982. Laboratory electrical conductivity measurements on mantle relevant minerals. Geophysical Surveys 4, 337–352. 18

Hutchins, D. G., Reeves, C. V., 1980. Regional geophysical exploration of the Kalahari in Botswana. Tectonophysics 69, 201–220. 8, 24, 135

Hutton, R., 1972. Some Problems of Electromagnetic Induction in the Equatorial Electrojet Region. I - Magneto-Telluric Relations. Geophysical Journal of the Royal Astronomical Society 28, 267–284. 47

Hutton, V. R. S., Dawes, G., Ingham, M., Kirkwood, S., Mbipom, E. W., Sik, J., 1981. Recent studies of time variations of natural electromagnetic fields in Scotland. Physics of the Earth and Planetary Interiors 24 (1), 66–87. 21

Jacobs, J., Pisarevsky, S., Thomas, R. J., Becker, T., 2008. The Kalahari craton during the assembly and dispersal of Rodinia. Precambrian Research 160 (1-2), 142–158. 9

Jiracek, G. R., 1990. Near-surface and topographic distortions in electromagnetic induction. Surveys in Geophysics 11, 163–203. 56, 57

Jones, A. G., 1982. On the electrical crust-mantle structure in Fennoscandia: no Moho, and the asthenosphere revealed. Geophysical Journal International 68, 371–388. 21, 48

Jones, A. G., 1983. On the equivalence of the Niblett and Bostick transformations in the magnetotelluric method. Journal of Geophysics 53, 72–73. 42

Jones, A. G., 1993. Electromagnetic images of modern and ancient subduction zones. Tectonophysics 219, 29–45. 21

Jones, A. G., 1999. Imaging the continental upper mantle using electromagnetic methods. Lithos 48, 57–80. 1, 17, 22

Jones, A. G., 2002a. Magnetotelluric Data Processing and Analysis. Presented as a short course for the Society of Exploration Geophysicists. 54

Jones, A. G., 2002b. Magnetotelluric Theory. Presented as a short course for the Society of Exploration Geophysicists. 44

Jones, A. G., 2006. Electromagnetic interrogation of the anisotropic Earth: Looking into the Earth with polarized spectacles. Physics of the Earth and Planetary Interiors 158, 281–291. 37

Jones, A. G., Chave, A. D., Egbert, G., Auld, D., Bahr, K., 1989. A Comparison of Techniques for Magnetotelluric Response Function Estimation. Journal of Geophysical Research 94 (B10), 14201–14213. 55, 65

Jones, A. G., Evans, R. L., Muller, M. R., Hamilton, M. P., Miensopust, M. P., Garcia, X., Cole, P., Ngwisanyi, T., Hutchins, D., Fourie, C. J. S., Jelsma, H., Aravanis, T., Pettit, W., Webb, S. J., Wasborg, J., the SAMTEX Team, 2009. Area selection for diamonds using magnetotellurics: Examples from southern Africa. Lithos 112S, 83–92. 1, 3

Jones, A. G., Ferguson, I. J., 2001. The electric Moho. Nature 409, 331–333. 21

Jones, A. G., Groom, R. W., 1993. Strike-angle determination from the magnetotelluric impedance tensor in the presence of noise and local distortion: rotate at your peril! Geophysical Journal International 113, 524–534. 59

Jones, A. G., Jödicke, H., 1984. Magnetotelluric transfer function estimation improvement by a coherence-based rejection technique. In: 54th Annual International Meeting of the Society of Exploration Geophysicists. Atlanta, Georgia, december 2-6. 55, 65

Jones, A. G., Katsube, T. J., Schwann, P., 1997. The Longest Conductivity Anomaly in the World Explained: Sulphides in Fold Hinges Causing Very High Electrical Anisotropy. Journal of Geomagnetism and Geoelectricity 49, 1619–1629. 28

Jones, A. G., Lezaeta, P., Ferguson, I. J., Chave, A. D., Evans, R. L., Garcia, X., Spratt, J., 2003. The electrical structure of the Slave craton. Lithos 71 (2-4), 505–527. 33

Jones, A. G., Spratt, J., 2002. A simple method for deriving uniform field MT responses in auroral zones. Earth Planets Space 54, 443–450. 47, 48

Jones, F. W., Price, A. T., 1970. The perturbations of alternating geomagnetic fields by conductivity anomalies. Geophysical Journal of the Royal Astronomical Society 20, 317–334. 40

Kampunzu, A. B., Armstrong, R. A., Modisi, M. P., Mapeo, R. B. M., 2000. Ion microprobe U-Pb ages on detrital zircon grains from the Ghanzi Group: implications for the identification of a Kibaran-age crust in northwest Botswana. Journal of African Earth Sciences 30 (3), 579–587. 135

Kao, D., Orr, D., 1982. Magnetotelluric response of a uniformly stratified Earth containing a magnetized layer. Geophysical Journal of the Royal Astronomical Society 70 (2), 339–347. 33

Keller, G. V., 1988. Rock and Mineral Properties. Vol. 1 of Electromagnetic Theory in Applied Geophysics - Theory. Society of Exploration Geophysicists, Ch. 2, editor M. N. Nabighian. 17, 31, 32

Key, R. M., Rundle, C. C., 1981. The regional significance of new isotopic ages from Precambrian windows through the "Kalahari Beds" in northwestern Botswana. Transactions of the Geological Society of South Africa 84, 51–66. 9

Khoza, T. D., Jones, A. G., Muller, M. R., Evans, R. L., Miensopust, M. P., Webb, S. J., Share, P. E., 2011. Lithospheric structure of the Damara Orogen and southern Congo craton: insights from deep probing magnetotellurics, submitted to Geology. 3

Korte, M., Mandea, M., Kotzé, P., Nahayo, E., Pretorius, B., 2007. Improved observations at the southern African geomagnetic repeat station network. South African Journal of Geology 110, 175–186. 25

Koshcheev, L. A., 2003. Environmental characteristics of hvdc overhead transmission lines. In: Third Workshop on Power Grid Interconnection. Vladivostok, Russia, 30 September - 3 October. 8

Kurtz, R. D., Garland, G. D., 1976. Magnetotelluric measurements in eastern Canada. Geophysical Journal of the Royal Astronomical Society 45 (2), 321–347. 21

Kusky, T. M., 1998. Tectonic setting and terrane accretion of the Archean Zimbabwe craton. Geology 26, 163–166. 9

Kuvshinov, A., Utada, H., Avdeev, D., Koyama, T., 2005. 3-D modelling and analysis of Dst C-responses in the North Pacific Ocean region, revisited. Geophysical Journal International 160, 505–526. 18, 20, 23

Labson, V. F., Becker, A., Morrison, H. F., Conti, U., 1985. Geophysical exploration with audiofrequency natural magnetic fields. Geophysics 50 (4), 656–664. ix, 43, 46

Laštovičková, M., 1983. Laboratory measurements of electrical properties of rocks and minerals. Geophysical Surveys 6, 201–213. 18

Ledo, J., 2006. 2-D Versus 3-D Magnetotelluric Data Interpretation. Surveys in Geophysics 27, 111–148. 63

Li, Y., Spitzer, K., 2005. Finite element resistivity modelling for three-dimensional structures with arbitrary anisotropy. Physics of the Earth and Planetary Interiors 150, 15–27. 141

Lin, C.-H., Tan, H.-D., Tong, T., 2011. Three-dimensional conjugate gradient inversion of magnetotelluric full information data. Applied Geophysics 8 (1), 1–10. 63

Majaule, T., Hanson, R. E., Key, R. M., Singletary, S. J., Martin, M. W., Bowring, S. A., 2001. The Magondi Belt in northeast Botswana: Regional relations and new geochronological data from the Sua Pan area. Journal of African Earth Sciences 32, 257–267. 9

Mareschal, M., 1986. Modelling of natural sources of magnetospheric origin in the interpretation of regional induction studies: A review. Surveys in Geophysics 8, 261–300. 47

Marsh, J. S., 1973. Relationships between transform directions and alkaline igneous rock lineaments in Africa and South America. Earth and Planetary Science Letters 18, 317–323. 25

Martin, H., Porada, H., 1977. The intracratonic branch of the Damara Orogen in southwest Africa I. Discussion of geodynamic models. Precambrian Research 5, 311–338. 13

Masters, T. G., Shearer, P. M., 1995. Seismic Models of the Earth: Elastic and Anelastic. Vol. 1 of Global Earth Physics - A Handbook of Physical Constants. American Geophysical Union, Ch. 6, editor T. J. Ahrens. 22

McNeice, G. W., Jones, A. G., 2001. Multisite, multifrequency tensor decomposition of magnetotelluric data. Geophysics 66 (1), 158. 59, 68

McPherron, R. L., 2005. Magnetic pulsations: Their sources and relation to solar wind and geomagnetic activity. Surveys in Geophysics 26, 545–592. 45

Merrill, R. T., McElhinny, M. W., 1983. The Earth's Magnetic Field. Academic Press, London. 44, 45

Miensopust, M. P., Jones, A. G., Muller, M. R., Garcia, X., Evans, R. L., 2010. Lithospheric structures and Precambrian terrane boundaries in northeastern Botswana revealed through magnetotelluric profiling as part of the Southern African Magnetotelluric Experiment. Journal of Geophysical Research 116 (B02401). 3, 142

Miller, R. M., 1983. The Pan-African Damara Orogen of Namibia. Special Publication of the Geological Society of South Africa 11, 431–515. 11, 12

Miller, R. M., 2008. Archaean to Mesoproterozoic. Vol. 1 of The Geology of Namibia. Ministry of Mines and Energy, Geological survey of Namibia. 107, 109

Modie, B. N., 2000. Geology and mineralisation in the Meso- to Neoproterozoic Ghanzi-Chobe Belt of northwest Botswana. Journal of African Earth Sciences 30 (3), 467–474. 11, 12, 13

Moore, A. E., Larkin, P. A., 2001. Drainage evolution in south-central Africa since the breakup of Gondwana. South African Journal of Geology 104, 47–68. 130

Moorkamp, M., Jones, A. G., Eaton, D. W., 2007. Joint inversion of teleseismic receiver functions and magnetotelluric data using a genetic algorithm: Are seismic velocities and electrical conductivities compatible? Geophysical Research Letters 34 (L16311). 63

Muller, M. R., Jones, A. G., Evans, R. L., Grütter, H. S., Hatton, C., Garcia, X. Hamilton, M. P., Miensopust, M. P., Cole, P., Ngwisanyi, T. D., Hutchins, D., Fourie, C. J. S., Jelsma, H. A., Evans, S. F., Aravanis, T., Pettit, W., Webb, S. J., Wasborg, J., the SAMTEX Team, 2009. Lithospheric structure, evolution and diamond prospectivity of the Rehoboth

Terrane and western Kaapvaal Craton, southern Africa: Constraints from broadband magnetotellurics. Lithos 112S, 93–105. 3, 9

Neal, S. L., Mackie, R. L., Larsen, J. C., Schultz, A., 2000. Variations in the electrical conductivity of the upper mantle beneath North America and the Pacific Ocean. Journal of Geophysical Research 105 (B4), 8229–8242. 23

Nguuri, T. K., Gore, J., James, D. E., Webb, S. J., Wright, C., Zengeni, T. G., Gwavava, O., Snoke, J. A., the Kaapvaal Seismic Group, 2001. Crustal structure beneath southern Africa and its implications for the formation and evolution of the Kaapvaal and Zimbabwe cratons. Geophysical Research Letters 28 (13), 2501–2504. 2

Niblett, E. R., Sayn-Wittgenstein, C., 1960. Variation of electrical conductivity with depth by the magneto-telluric method. Geophysics 25, 998–1008. 42, 61

Nover, G., 2005. Electrical Properties of Crustal and Mantle Rocks - A Review of Laboratory Measurements and their Explanation. Surveys in Geophysics 26, 593–651. 16, 17, 18, 19, 20, 22

Olsen, N., 1998. The electrical conductivity of the mantle beneath Europe derived from C -responses from 3 to 720 hr. Geophysical Journal International 133, 298–308. 23

Pádua, M. B., Padilha, A. L., Vitorello, I., 2002. Disturbances on magnetotelluric data due to DC electrified railway: a case study from southeastern Brazil. Earth Planets Space 54, 591–596. 55

Pakhomenko, E. I., Belikov, B. P., Dvorzhak, E., 1973. Influence of serpentinization upon the elastic and electrical properties of rocks. Izv. Earth Physics 8, 101–108. 27

Parasnis, D. S., 1967. Three-dimensional electric mise-á-la-masse survey of an irregular lead-zinc-copper deposit in central Sweden. Geophysical Prospecting 15 (3), 407–437. 122, 123

Parker, R. L., 1980. The Inverse Problem of Electromagnetic Induction: Existence and Construction of Solutions Based On Incomplete Data. Journal of Geophysical Research 85 (B8), 4421–4428. 62

Parker, R. L., 1983. The magnetotelluric inverse problem. Geophysical Surveys 6, 5–25. 61

Parker, R. L., Booker, J. R., 1996. Optimal one-dimensional inversion and bounding of magnetotelluric apparent resistivity and phase measurements. Physics of The Earth and Planetary Interiors 98, 269–282. 62

Parkinson, W. D., 1959. Directions of rapid geomagnetic fluctuations. Geophysical Journal of the Royal Astronomical Society 2 (1), 1–14. 43

Patra, H., Mallick, K., 1980. Geosounding Principles: Time-Varying Geoelectric Soundings. Vol. 14B of Methods in Geochemistry and Geophysics. Elsevier. 36, 38, 39

Patro, P. K., Egbert, G. D., 2008. Regional conductivity structure of Cascadia: Preliminary results from 3D inversion of USArray transportable array magnetotelluric data. Geophysical Research Letters 35 (L20311). 63

Peltier, W. R., Hermance, J. F., 1971. Magnetotelluric fields of a Gaussian electrojet. Canadian Journal of Earth Sciences 8, 338–346. 47

Petiau, G., Dupis, A., 1980. Noise, temperature coefficient and long time stability of electrodes for telluric observations. Geophysical Prospecting 28, 792–804. 49

Pirjola, R. J., 1992. On magnetotelluric source effects caused by an auroral electrojet system. Radio Science 16, 352–357. 47

Pirjola, R. J., 1998. Modelling the electric and magnetic fields at the Earth's surface due to an auroral electrojet. Journal of Atmospheric and Solar-Terrestrial Physics 60, 1139–1148. 47

Pommier, A., Gaillard, F., Pichavant, M., Scaillet, B., 2008. Laboratory measurements of electrical conductivities of hydrous and dry Mount Vesuvius melts under pressure. Journal of Geophysical Research 113 (B05205). 17

Pommier, A., Le-Trong, E., 2011. "SIGMELTS": A web portal for electrical conductivity calculations in geosciences. Computers & Geosciences 37 (9), 1450–1459. 17

Pomposiello, M. C., Booker, J. R., Favetto, A., 2009. A discussion of bias in magnetotelluric responses. Geophysics 74 (4), 59–65. 55

Price, A., 1973. The theory of geomagnetic induction. Physics of The Earth and Planetary Interiors 7 (3), 227–233. 32, 35, 41

Price, A. T., 1962. The theory of magnetotelluric methods when the source field is considered. Journal of Geophysical Research 67 (5), 1907–1918. 46

Ranalli, G., 1987. Rheology of the Earth: Deformation and flow processes in Geophysics and Geodynamics. Allen and Unwim Inc., USA. 22

Rankin, D., 1962. The magneto telluric effect on a dike. Geophysics 27 (5), 666–676. 39

Ritter, O., Haak, V., Rath, V., Stein, E., Stiller, M., 1999. Very high electrical conductivity beneath the Münchberg Gneiss area in Southern Germany: implications for horizontal transport along shear planes. Geophysical Journal International 139 (2), 161–170. 27

Ritter, O., Weckmann, U., Vietor, T., Haak, V., 2003. A magnetotelluric study of the Damara Belt in Namibia 1. Regional scale conductivity anomalies. Physics of the Earth and Planetary Interiors 138, 71–90. ix, 25, 27, 28, 133, 135, 140

Roberts, J. J., Tyburczy, J. A., 1999. Partial-melt electrical conductivity: Influence of melt composition. Journal of Geophysical Research 104 (B4), 7055–7065. 16

Rodi, W., Mackie, R. L., 2001. Nonlinear conjugate gradients algorithm for 2-D magnetotelluric inversion. Geophysics 66 (1), 174–187. 62, 63

Rudervall, R., Charpentier, J. P., Sharma, R., 2000. High Voltage Direct Current (HVDC) Transmission Systems Technology Review Paper. ABB, Sweden. 6, 7, 8

Santos, F. A. M., Trota, A., Soares, A., Luzio, R., Loureno, N., Matos, L., Almeida, E., Gaspar, J. L., Miranda, J. M., 2006. An audio-magnetotelluric investigation in Terceira Island (Azores). Journal of Applied Geophysics 59 (4), 314–323. 29

Schmucker, U., 1973. Regional induction studies: A review of methods and results. Physics of The Earth and Planetary Interiors 7, 365–378. 37, 46

Schmucker, U., 1985. Geophysics of the Solid Earth, the Moon and the Planets. Vol. 5/2b of Landolt-Bornstein: Numerical Data and Functional Relationships in Science and Technology. Springer-Verlag, New York, Ch. 4, editors K. Fuchs and H. Soffel. 42, 45

Schmucker, U., Weidelt, P., 1975. Electromagnetic induction in the earth. Tech. rep., Laboratoriet for anvendt geofysik, Aarhus Universitet. 34, 35

Schwalenberg, K., Rath, V., Haak, V., 2002. Sensitivity studies applied to a two-dimensional resistivity model from the Central Andes. Geophysical Journal International 150, 673–686. 82

Schwarz, G., 1990. Electrical conductivity of the earth's crust and upper mantle. Surveys in Geophysics 11, 133–161. 16, 18, 19

Shankland, T. J., 1975. Electrical conduction in rocks and minerals: Parameters for interpretation. Physics of The Earth and Planetary Interiors 10, 209–219. 17

Shankland, T. J., Ander, M. E., 1983. Electrical Conductivity, Temperatures, and Fluids in the Lower Crust. Journal of Geophysical Research 88 (B11), 9475–9484. 20, 21

Shankland, T. J., Peyronneau, J., Poirier, J.-P., 1993. Electrical conductivity of the Earth's lower mantle. Nature 366, 453–455. 17, 24

Silver, P. G., Chan, W. W., 1988. Implications for continental structure and evolution from seismic anisotropy. Nature 335, 34–39. 1

Simpson, F., 1999. Stress and seismicity in the lower continental crust: A challenge to simple ductility and implications for electrical conductivity mechanisms. Surveys in Geophysics 20, 201–227. 19

Simpson, F., Bahr, K., 2005. Practical Magnetotellurics, 1st Edition. Cambridge University Press. 19, 29, 30, 32, 34, 36, 37, 38, 40, 41, 44, 51, 53, 54, 55, 80

Sims, W. E., Bostick, F. X., Smith, H. W., 1971. The estimation of magnetotelluric impedance tensor elements from measured data. Geophysics 36 (5), 938–942. 52, 53, 54

Singletary, S. J., Hanson, R. E., Martin, M. W., Crowley, J. L., Bowring, S. A., Key, R. M., Ramokate, L. V., Direng, B. B., Krol, M. A., 2003.

Geochronology of basement rocks in the Kalahari Desert, Botswana, and implications for regional Proterozoic tectonics. Precambrian Research 121, 47–71. 8, 10, 13, 130, 135

Siripunvaraporn, W., 2010. Three-dimensional Magnetotelluric Inversion: An Introductory Guide for Developers and Users. In: 20^{th} International Workshop on Electromagnetic Induction in the Earth. Giza, Egypt, 18-24 September. 63

Siripunvaraporn, W., Egbert, G., 2000. An efficient data-subspace inversion method for 2-D magnetotelluric data. Geophysics 65 (3), 791–803. 62

Siripunvaraporn, W., Egbert, G., Lenbury, Y., Uyeshima, M., 2005. Three-dimensional magnetotelluric inversion: data-space method. Physics of the Earth and Planetary Interiors 150, 3–14. 63

Smith, J. T., 1995. Understanding telluric distortion matrices. Geophysical Journal International 122, 219–226. 57, 58

Smith, J. T., 1997. Estimating galvanic-distortion magnetic fields in magnetotellurics. Geophysical Journal International 130, 65–72. 57, 58

Smith, J. T., Booker, J. R., 1988. Magnetotelluric inversion for minimum structure. Geophysics 53 (12), 1565–1576. 62

Smith, J. T., Booker, J. R., 1991. Rapid Inversion of Two- and Three-Dimensional Magnetotelluric Data. Journal of Geophysical Research 96 (B3), 3905–3922. 62

Spies, B. R., 1989. Depth of investigation in electromagnetic sounding methods. Geophysics 54 (7), 872–888. 37

Srivastava, S. P., 1965. Method of interpretation of magnetotelluric data when source field is considered. Journal of Geophysical Research 70 (4), 945–954. 46

Stacey, F. D., Anderson, O. L., 2001. Electrical and thermal conductivities of Fe-Ni-Si alloy under core conditions. Physics of the Earth and Planetary Interiors 124, 153–162. 18

Sternberg, B. K., 1979. Electrical resistivity structure of the crust in the southern extension of the Canadian shield - layered Earth models. Journal of Geophysical Research 84 (B1), 212–228. 21

Sternberg, B. K., Washburne, J. C., Pellerin, L., 1988. Correction for the static shift in magnetotellurics using transient electromagnetic soundings. Geophysics 53 (11), 1459–1468. 59

Sutherland, R., 1999. Basement geology and tectonic development of the greater New Zealand region: an interpretation from regional magnetic data. Tectonophysics 308, 341–362. 107

Swift, C. M., 1967. A magnetotclluric investigation of electrical conductivity anomaly in the southwestern United States. Ph.D. thesis, MIT. 50, 53

Swift, C. M., 1971. Theoretical magnetotelluric and Turam response from two-dimensional inhomogeneities. Geophysics 36 (1), 38–52. 63

Tankard, A. J., Hobday, D. K., Jackson, M. P. A., Hunter, D. R., Eriksson, K. A., Minter, W. E. L., 1982. Crustal Evolution of Southern Africa: 3.8 Billion Years of Earth History. Springer-Verlag, New York. 11, 12, 129, 135

Telford, W. M., Geldart, L. P., Sheriff, R. E., 1990. Applied Geophysics, 2nd Edition. Cambridge University Press. 33, 122

Thomas, D. S. G., Shaw, P. A., 1990. The deposition and development of the Kalahari Group sediments, Central Southern Africa. Journal of African Earth Sciences 10 (1/2), 187–197. 13, 135

Thunehed, H., 2009. Discussion on the HVDC earth electrodes near Otjiwarongo and Katima Mulilo. 140

Thunehed, H., Åström, U., Westman, B., 2007. Geophysical and geological pre-investigations for HVDC-electrodes. In: IEEE PES PowerAfrica 2007 Conference and Exposition. Johannesburg, South Africa, 16-20 July. 7, 8, 128

Turberg, P., Müller, I., Flury, F., 1994. Hydrogeological investigation of porous environments by radio magnetotelluric-resistivity (RMT-R 12-240 kHz). Journal of Applied Geophysics 31 (1-4), 133–143. 29

Tuson, P., 2007. HVDC Strengthening in Southern Africa. In: IEEE PES PowerAfrica 2007 Conference and Exposition. Johannesburg, South Africa, 16-20 July. 7, 9

Unsworth, M. J., Jones, A. G., Wei, W., Marquis, G., Gokarn, S. G., Spratt, J. E., Bedrosian, P., Booker, J., Leshou, C., Clarke, G., Shenghui, L., Chanhong, L., Ming, D., Sheng, J., Solon, K., Handong, T., Ledo, J., Roberts, B., 2005. Crustal rheology of the Himalaya and Southern Tibet inferred from magnetotelluric data. Nature 438, 78–81. 29

Utada, H., Koyama, T., Shimizu, H., Chave, A. D., 2003. A semi-global reference model for electrical conductivity in the mid-mantle beneath the north Pacific region. Geophysical Research Letters 30 (4), 43(1)–43(4). 18, 20

Utada, H., Munekane, H., 2000. On galvanic distortion of regional 3-D MT impedances On galvanic distortion of regional three-dimensional magnetotelluric impedances. Geophysical Journal International 140, 385–398. 56, 60

van Reenen, D. D., Barton Jr., J. M., Roering, C., Smith, C. A., van Schalkwyk, J. F., 1987. Deep crustal response to continental collision: The Limpopo belt of southern Africa. Geology 15, 11–14. 9

van Zijl, J. S. V., de Beer, J. H., 1983. Electrical conductivity of the Damara Orogen and its tectonic significance. Special Publication of the Geological Society of South Africa 11, 369–379. xiii, 24, 26, 27, 131, 133, 135

van Zijl, J. S. V., Joubert, S. J., 1975. A crustal geoelectrical model for South African precambrian granitic terrains based on deep Schlumberger soundings. Geophysics 40 (4), 657–663. 138

Viljanen, A., Pirjola, R. J., Amm, O., 1999. Magnetotelluric source effect due to 3D ionospheric current systems using the complex image method for 1D conductivity structures. Earth Planets Space 51, 933–945. 47

Vozoff, K., 1991. The Magnetotelluric Method. Vol. 2 of Electromagnetic Theory in Applied Geophysics - Application. Society of Exploration Geophysicists, Ch. 8, editor M. N. Nabighian. 34, 37, 43, 44, 48, 50

Wannamaker, P. E., Hohmann, G. W., Ward, S. H., 1984. Magnetotelluric responses of three-dimensional bodies in layered earths. Geophysics 49 (9), 1517–1533. 63, 85

Ward, S. H., Hohmann, G. W., 1988. Electromagnetic Theory for Geophysical Applications. Vol. 1 of Electromagnetic Theory in Applied Geophysics - Theory. Society of Exploration Geophysicists, Ch. 4, editor M. N. Nabighian. 35

Weckmann, U., Jung, A., Branch, T., Ritter, O., 2007. Comparison of electrical conductivity structures and 2D magnetic modelling along two profiles crossing the Beattie Magnetic Anomaly, South Africa. South African Journal of Geology 110, 449–464. 28

Weckmann, U., Ritter, O., Haak, V., 2003. A magnetotelluric study of the Damara Belt in Namibia 2. MT phases over 90°reveal the internal structure of the Waterberg Fault/Omaruru Lineament. Physics of the Earth and Planetary Interiors 138, 91–112. 25, 141

Weidelt, P., 1975. Electromagnetic induction in three-dimensional structures. Journal of Geophysics 41, 85–109. 34, 41

Wiese, H., 1962. Geomagnetische Tiefentellurik. II. Die Streichrichtung der Untergrundstrukturen des elektrischen Widerstandes, erschlossen aus geomagnetischen Variationen. Geofis. Pura Appl. 52, 83–103. 43

Wight, D. E., Bostick, F. X., 1980. Cascade decimation - A technique for real time estimation of power spectra. In: Proc. IEEE Intern. Conf. Acoustic, Speech, Signal Processing. Denver, Colorado, pp. 626–629. 51

Woodford, D. A., 1998. HVDC Transmission. Manitoba HVDC Research Centre, Manitoba, Canada. 6, 7

Xiao, Q., Cai, X., Xu, X., Liang, G., Zhang, B., 2010. Application of the 3D magnetotelluric inversion code in a geologically complex area. Geophysical Prospecting 58 (6), 1177–1192. 63

Xu, Y., Poe, B., Shankland, T., Rubie, D., 1998. Electrical Conductivity of Olivine, Wadsleyite, and Ringwoodite Under Upper-Mantle Conditions. Science 280, 1415–1418. 18

Yoshino, T., Manthilake, G., Matsuzaki, T., Katsura, T., 2008. Dry mantle transition zone inferred from the conductivity of wadsleyite and ringwoodite. Nature 451, 326–329. 18, 23

Zhang, P., Pedersen, L. B., Mareschal, M., Chouteau, M., 1993. Channeling contribution to tipper vectors: A magnetic equivalent to electrical distortion. Geophysical Journal International 113, 693–700. 58

Zhou, B., Greenhalgh, M., Greenhalgh, S. A., 2009. 2.5-D/3-D resistivity modelling in anisotropic media using Gaussian quadrature grids. Geophysical Journal International 176, 63–80. 141